

**Mechanistic studies on Compound I and II
formation in the dye-decolourising peroxidases
from *Streptomyces lividans***

Marina Rožman

A thesis submitted for the degree of PhD Biochemistry

School of Life Sciences
University of Essex

October 2021

Abstract

Iron-containing enzymes can utilise oxygen to carry out a variety of oxidative transformations. In the case of haem peroxidases, their interaction with hydrogen peroxide leads to the formation of two Fe^{IV}-oxo intermediates: Compound I and Compound II, which are the oxidising species in the catalytic cycle. Dye decolourising peroxidases (DyPs) are the most recent family of haem peroxidases to be discovered and are now known to be widely distributed in bacterial and fungal genomes. Based on phylogenetic and structural analysis, DyPs have been placed into three sub-families (types A, B, C/D), which differ predominately in their cellular location, structure and enzymatic activity.

This thesis is focused on three DyPs present in the soil-dwelling bacterium *Streptomyces lividans*: two A-types, DtpA and DtpAa and a B-type, DtpB. Detailed structural and kinetic studies are reported aimed towards deciphering mechanistic intricacies of Compound I and II formation amongst these DyPs. Through a combination of low dose synchrotron X-ray crystallography and zero dose serial femtosecond X-ray crystallography using an X-ray free electron laser (XFEL), high-resolution structures with unambiguous redox state assignment of the ferric and ferryl (Fe^{IV}=O) haem species have been obtained. Experiments using stopped-flow kinetics, solvent-isotope exchange and site-directed mutagenesis combined with the redox state validated DyP structures have provided the first comprehensive kinetic and structural framework for how DyPs can modulate their distal haem pocket Asp/Arg dyad to use either the Asp or the Arg to facilitate proton transfer and rate enhancement of peroxide heterolysis.

Acknowledgements

This PhD thesis would not have been possible without encouragement from some very special people. Many thanks to my patient and inspiring supervisors, loving family and kind lab members.

My most special thanks go to my caring mother, brother and my husband Josip who never stopped supporting and believing in me. You have now been through three degrees with me, and yet you keep pushing me forward. Your guidance and help were invaluable and have shaped the person I am today. Above all else big "thank you" for understanding how important my education is to me.

I want to thank present and past members of the lab 5.08, especially Amanda who introduced me to DyPs and provided support even from her new lab in Cambridge. Many thanks to Neil who became my best friend in the UK- I miss you very much and hope to see you soon, to Ricky, Vinay and Kes for tea and lunch breaks that made my day enjoyable even during the most stressful times. I wish to thank Hannah and Pete for helping me with protein purifications and making the lab such a great place to work.

Many thanks to Mike W. for all the help with stopped-flow experiments and life lessons. Thank you for listening about my troubles and worries, always meeting them with some advice. The love you have for science is contagious and has inspired me to continue walking the path of research.

Finally, I would like to thank my supervisors who have been fundamental for this PhD project, always actively engaged and available to help with the lab work. Thank you, Dima, for helping with the EPR experiments and Mike H. for all the assistance with

crystallography. My biggest thanks go to Jonathan who above everyone else really made this PhD possible. Thank you for being the most supportive supervisor I have had. You have introduced me to research and academia and have been a role model for scientific thinking and reasoning. Your Supervisor of the Year award was absolutely deserved and thus I wish to quote a line I have written to support your nomination:

“I believe that coming to study with Jonathan was one of the best decisions I have ever made, and it has most certainly helped me grow as scientist and a person.”

It has not been left unnoticed that you somehow always had time to listen about any doubts and hardships I had experienced and offered enormous support to Josip and me. It has been the greatest pleasure to work with you and despite the guaranteed stress of doing a PhD, I will always remember my days in 5.08 fondly.

Lastly, I would like to thank Peter Nicholls Scholarship, which provided funding for this PhD. I am truly thankful for every opportunity that has been given to me and I can promise I will do my best to learn more and hopefully to give back to the science community by inspiring new researchers to join this rewarding field.

Table of Contents

Abstract	2
Acknowledgements	3
Table of Figures	8
Table List	11
Chapter 1: Introduction	13
1.1. Haem peroxidases	14
1.2. Haem peroxidases form iron-oxo intermediates	15
1.3. X-ray crystallography approach for probing ferryl intermediates	17
1.4. Dye-decolourising peroxidases	20
1.5. Focus of this thesis	22
Chapter 2: Two A-type dye-decolourising peroxidases in <i>Streptomyces lividans</i> with distinctly different H₂O₂ reactivities	24
2.1. Introduction	25
2.2. Experimental procedures	28
2.2.1. Site-directed mutagenesis of DtpAa and DtpA	28
2.2.4. Stopped-flow absorption kinetics	30
2.3. Results	33
2.3.1. Over-expression and purification of DtpA and DtpAa	33
2.3.2. The electronic absorbance spectrum of DtpAa	35
2.3.3. Validation of the ferric haem state in the crystal structure of DtpAa	37
2.3.4. Comparison of the ferric DtpAa and DtpA X-ray structures determined at 100 K	38
2.3.5. The kinetics of Compound I formation in DtpAa	42
2.3.6. The pH dependence of Compound I formation in DtpA and DtpAa	47
2.3.7. D ₂ O ₂ as a mechanistic probe to study Compound I formation	49
2.3.8. Removal of the distal Asp in DtpAa and DtpA decreases the rate of Compound I formation	52
2.4. Discussion	57
Chapter 3: An Electron Paramagnetic Resonance spectroscopy study to investigate reaction of DtpA from <i>Streptomyces lividans</i> with H₂O₂	66
3.1. Introduction	67
3.2. Experimental procedures	68

3.2.1. Site-directed mutagenesis of DtpAa.....	68
3.2.2. Over-expression and purification of DtpAa	68
3.2.3. Preparation of DtpAa time course samples for EPR measurements	69
3.2.4. EPR spectroscopy and simulation	69
3.2.5. Electron transfer pathways identification using eMap.....	70
3.2.6. Crystallisation, X-ray data collection, structure determination and refinement.....	71
3.2.7. Stopped-flow absorption kinetics	72
3.3. Results.....	74
3.3.1. EPR characterisation of the ferric haem forms of DtpAa	74
3.3.2. The free radical region of DtpAa EPR spectra.....	78
3.3.3. Kinetics of the four spectral components: SigA, SigB, SigC and SigD.....	80
3.3.4. Electron transfer pathway prediction in DtpA and DtpAa.....	82
3.3.5. Crystal structures of tyrosine variants	86
3.3.6. Stopped-flow kinetics of the DtpAa tyrosine variants	87
3.3.7. Monitoring the reaction of the DtpAa tyrosine variants with H ₂ O ₂ by EPR spectroscopy	90
3.4. Discussion	95
Chapter 4: Using Serial femtosecond X-ray crystallography to determine zero dose ferric and ferryl peroxidase structures of DtpB from <i>Streptomyces lividans</i>	105
4.1. Introduction.....	106
4.2. Experimental procedures	110
4.2.1. Over-expression and purification of DtpB	110
4.2.2. Sample preparation.....	110
4.2.3. EPR spectroscopy and simulation	110
4.2.4. Crystallisation and H ₂ O ₂ soaking of DtpB crystals.....	111
4.2.5. Microspectrophotometry and X-ray data collection at 100 K.....	112
4.2.6. Serial femtosecond X-ray crystallography	113
4.2.7. Serial synchrotron crystallography.....	114
4.2.8. DtpB structure determination and refinement	114
4.3. Results.....	119
4.3.1. Over-expression and purification of DtpB	119
4.3.2. The electronic absorbance spectrum of DtpB	120
4.3.3. EPR spectroscopy of Compound I DtpB.....	121
4.3.4. Crystal structures of Fe ^{III} DtpB	122

4.3.5. Crystal structures of Compound I DtpB	127
4.3.6. SSX dose series on Compound I DtpB	131
4.4. Discussion	135
Chapter 5: Exploring the catalytic mechanism of a B-type dye-decolorizing peroxidase from <i>Streptomyces lividans</i>	144
5.1. Introduction	145
5.2. Experimental procedures	146
5.2.1. Site-directed mutagenesis	146
5.2.2. Over-expression and purification	147
5.2.3. Sample preparation	147
5.2.4. Stopped-flow absorption spectroscopy	148
5.2.5. Crystallisation of DtpB variants	148
5.2.6. Serial femtosecond X-ray crystallography	149
5.3. Results	152
5.3.1. Spectral characteristics	152
5.3.2. Compound I formation is enhanced by the distal Arginine in DtpB	156
5.3.3. A “Dry” distal site moderates Compound II formation	161
5.3.4. Compound II formation is proton-coupled	167
5.3.5. SFX crystal structures of D152A and N245A variants	170
5.4. Discussion	172
Summary	181
References	187

Table of Figures

Figure 1. Haem b.

Figure 1.1. Catalytic cycle of haem peroxidases.

Figure 1.2. The Poulos-Kraut mechanism of Compound I formation.

Figure 2. Superposition of the haem environment in DtpA and DtpAa reveals a slight shift of the distal Asp residue, which controls their chemistry.

Figure 2.1. Amino acid sequence alignment of DtpA and DtpAa.

Figure 2.2. Over-expression and purification of DtpAa.

Figure 2.3. Electronic absorbance spectra of DtpAa.

Figure 2.4. Electronic absorbance spectra of DtpAa.

Figure 2.5. $2F_o-F_c$ electron density map contoured at 1.5σ for the haem site of Chain A in DtpAa.

Figure 2.6. X-ray crystal structures determined at 100 K of DtpAa and DtpA in the ferric haem oxidation state.

Figure 2.7. Detection of Compound I (Cmpd I) in DtpAa using stopped-flow absorption spectroscopy (25 °C).

Figure 2.8. Observed pseudo-first order rate constants (k_{obs1} and k_{obs2}) obtained from global fitting of the spectral transitions for the reaction of DtpAa (5 μ M) with increasing H₂O₂ concentrations at pH 7.0 (A) and pH 5.0 (B) at 25 °C.

Figure 2.9. pH dependence profiles for the rate of Compound I formation in DtpAa and DtpA on reacting with a fixed concentration of H₂O₂.

Figure 2.10. The KIE on the formation of Compound I and Compound II in DtpA and DtpAa at pD 7.0 and 25 °C.

Figure 2.11: Absorbance spectra of the Asp variants at pH 7.0.

Figure 2.12. Kinetics of Compound I formation for the distal Asp variants of DtpA and DtpAa at 25 °C.

Figure 2.13. Superposition of the haem environment in DtpA and DtpAa reveals a slight shift of the distal Asp residue.

Figure 2.14. Mechanism of Compound I formation in DtpA and DtpAa.

Figure 3. Predicted electron transfer pathways in DtpAa.

Figure 3.1. EPR spectroscopy of DtpAa.

Figure 3.2. EPR spectra of the free radical region in DtpAa.

Figure 3.3. Kinetics of the four EPR signals identified in the free radical region of the DtpAa EPR spectra after H₂O₂ addition.

Figure 3.4. Results of the eMap analysis for DtpA.

Figure 3.5. Results of the eMap analysis for DtpAa.

Figure 3.6. Electron transfer active aromatic residues within the vicinity of the haem in DtpA and DtpAa.

Figure 3.7. Y345F DtpAa crystal (200 x 150 x 150 μ m) mounted on a loop.

Figure 3.8. Structural superposition of chain A of the Y345F and DM variants with WT DtpAa.

Figure 3.9. Electronic absorbance spectra (pH 5.0) of DtpAa Tyr variants; Y345F and Y345F/F347Y (DM).

Figure 3.10. Compound I formation in DtpAa WT and Tyr variants.

Figure 3.11. EPR spectroscopy of the second time series of DtpAa and the Tyr variants.

Figure 3.12. EPR spectra of the free radical region in the WT DtpAa (second set of samples) and the Tyr variants.

Figure 3.13. Structural superposition of DM DtpAa variant with WT DtpA with residues predicted to play a role in radical formation.

Figure 3.14. Results of the eMap analysis for the DtpAa DM variant.

Figure 3.15. Results of the eMap analysis for the DtpAa Y345F variant.

Figure 4. Approaches used to obtain low dose (A) or zero dose (B) X-ray crystal structures of the *S. lividans* DyPs.

Figure 4.1. DtpB crystals.

Figure 4.2. DtpB purification.

Figure 4.3. Electronic absorption spectrum of Fe^{III}-DtpB and Compound I generated by addition of one-molar equivalent H₂O₂ (pH 5.0).

Figure 4.4. X-band EPR spectra (10 K) of Fe^{III}-DtpB and spectra of four samples frozen at variable times after addition of one-molar equivalent H₂O₂.

Figure 4.5. Electronic absorption spectra of Fe^{III} DtpB crystals.

Figure 4.6. Quaternary structure of DtpB hexamer.

Figure 4.7. Tertiary structure of DtpB.

Figure 4.8. 2F_o-F_c electron density maps contoured at 1.4 σ of the distal pockets of the Fe^{III} state of DtpB in Chain A at 100 K and RT.

Figure 4.9. Electronic absorption spectra of Compound I DtpB crystals.

Figure 4.10. Distal pockets of the Compound I state determined at RT and 100 K.

Figure 4.11. Dose dependent elongation of the Fe-O bond of each chain in DtpB hexamer assembly.

Figure 4.12. Superposition of Chain C haem across selected dose series structures revealing dose-dependent migration of the oxygen from the haem-Fe

Figure 4.13. The SFX haem site structure of Fe^{III}-DtpB and comparison with the redox state validated Fe^{III}-DtpA and Fe^{III}-DtpAa structures.

Figure 5. Absence of water molecule in the haem environment affects the DtpB chemistry.

Figure 5.1. Electronic absorbance spectra of DtpB WT and the D152A, N245A and DM variants.

Figure 5.2. Electronic absorbance spectra of the N245A and DM DtpB variants at pH 5.0 and 7.0, respectively, showing reaction of the ferric enzyme with H₂O₂.

Figure 5.3. Electronic absorbance spectra of the R243A variant of DtpB measured at pH 5.0.

Figure 5.4. Detection of Compound I in WT DtpB and variants using stopped-flow absorption spectroscopy (pH 5.0 and 7.0 at 25 °C).

Figure 5.5. The pH dependence of Compound I formation in WT DtpB and variants.

Figure 5.6. Compound I reduction in WT DtpB.

Figure 5.7. Kinetics of Compound II formation and reduction (pH 7 and 25 °C).

Figure 5.8. Detection of Compound II in DtpB variants using stopped-flow absorption spectroscopy (25 °C).

Figure 5.9. Kinetic isotope effect on Compound I formation in DtpB WT at pH 5.0 or 7.0.

Figure 5.10. Distal pockets of the ferric D152A and N245A variants determined using SFX at room temperature.

Figure 5.11. Water channels connecting the Fe^{IV}=O to the bulk solvent via the distal R243 and the haem propionates in the SFX structure.

Figure 5.12. The catalytic mechanism of Compound II formation in DtpB based on structural and kinetic data.

Figure 6.1. The catalytic mechanism of Compound I formation in DtpA based on structural and kinetic data.

Figure 6.2. The catalytic mechanism of Compound I formation in DtpB based on structural and kinetic data.

Table List

Table 2.1. Crystallographic data processing and refinement statistics for ferric DtpAa (100 K).

Table 2.2. Wavelength absorbance maxima at pH 7.0 for DtpAa and DtpA and the respective distal Asp variants.

Table 3.1. Crystallographic data processing and refinement statistics for DtpAa Y345F and DM variants.

Table 3.2. The principal g-values, rhombicity parameters E/D, individual line widths and Lorentz/Gaussian line shape ratios used in the simulation of the EPR signals of the two HS ferric haem forms of DtpAa.

Table 3.3. Wavelength absorbance maxima at pH 5.0 for DtpAa and the Tyr variants.

Table 4.1. SFX (ambient temperature), composite (100 K) X-ray crystallography and SSX dose series data processing for DtpB in space group $P2_12_12_1$.

Table 4.2. Refinement and validation statistics for SFX (room temperature), composite X-ray crystallography and SSX dose series for DtpB.

Table 4.3. Coordinate bond lengths for the Fe^{III} DtpB haem site.

Table 4.4. Coordinate bond lengths for the Compound I DtpB haem site.

Table 4.5. Wavelength absorbance maxima at pH 7.0 for DtpAa, DtpA and DtpB.

Table 5.1. Mutagenic primer pairs used to generate D152A, N245A, R243A and D152A/N245A DtpB mutations.

Table 5.2. SFX X-ray crystallography data processing for the DtpB D152A and N245A variants in space group $P2_12_12_1$.

Table 5.3. Refinement and validation statistics for the room temperature SFX X-ray crystallography of the DtpB D152A and N245A variants.

Table 5.4. Wavelength absorbance maxima for DtpB and variants measured at pH 5.0 or pH 7.0 for the DM.

Table 5.5. Second-order rate constants (k) and ionisation equilibrium parameters (pK_a) for Compound I formation in WT DtpB and variants.

Table 5.6. Second-order rate constants of Compound II formation and reduction obtained from stopped-flow measurements for DtpB distal Asp and distal Asn variants at pH 5.0/5.8 and 7.0.

Table 5.7. Second-order Compound I reduction rates in H₂O and D₂O at pH(D) 7.0.

Table 5.8. Compound II reduction rates in H₂O and D₂O at pH(D) 7.0 for the DtpB variants studied.

Chapter One

Introduction

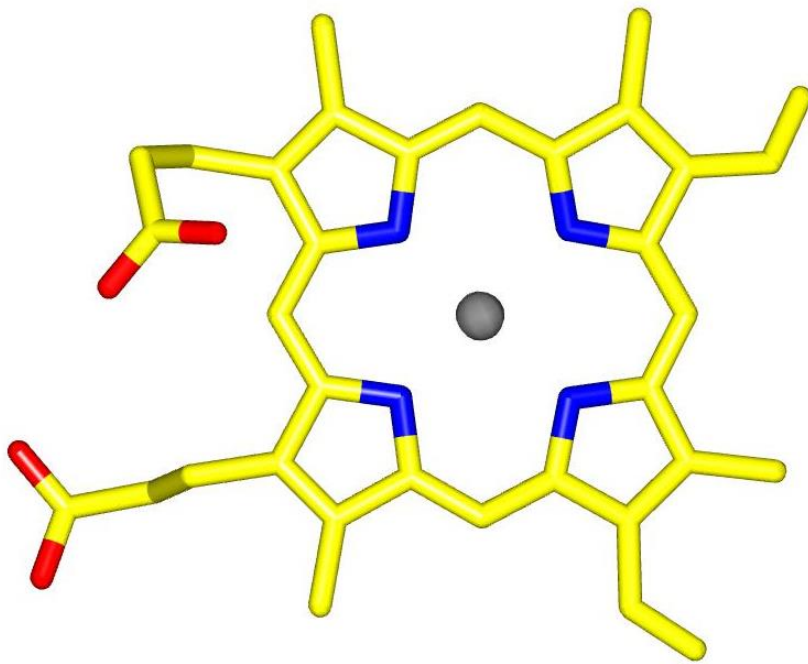


Figure 1. Haem b.

1.1. Haem peroxidases

The countless number of biochemical reactions in living systems are carried out by metalloproteins. A majority of these proteins are haem proteins, *i.e.* they embody iron protoporphyrin IX as the cofactor. A fascinating property of haem containing proteins is that they are involved in a multitude of very diverse functions, including, but not limited to, dioxygen transport or storage, biological electron-transfer and oxidative redox chemistry of organic substrates. The haem cofactor also partakes in circadian clock regulation as a regulator of ion channel activity in cells (Burton *et al.*, 2020; Freeman *et al.*, 2019). Thus, such great diversity of functions attributed to a single cofactor emphasizes the importance of the relationship between structure and function in biology and has encouraged numerous research groups to study the chemistry of haem in various protein environments.

Haem peroxidases are an exemplar model for researching structure/function relationships, as the haem can form somewhat stable catalytic intermediates, often making them easy to capture and study using an array of biophysical methods. Peroxidases encompass a large group of oxidoreductases that, using hydrogen peroxide (H_2O_2) as the electron acceptor, catalyse the oxidation of a substrate (Sugano, 2009). They are found in all living organisms, including bacteria, fungi, plants and mammals. In plants, peroxidases are involved in auxin metabolism, lignin and suberin formation, crosslinking of cell wall components and cell elongation (Welinder, 1992). In mammals, they play a role in biological processes including hormone regulation and immunity (Fawal *et al.*, 2013). Peroxidases are classified in two main superfamilies: the plant peroxidases (non-animal), that also contain evolutionary related haem

peroxidases from fungi and bacteria (Welinder, 1992), and the animal peroxidases. The plant peroxidase superfamily is then subdivided into three classes depending upon the enzyme function and cellular location (Welinder *et al.*, 1992). For example, yeast cytochrome c peroxidase (CcP) and chloroplast ascorbate peroxidase (APX) are intracellular enzymes and represent Class I peroxidases, whereas Class II enzymes include the extracytoplasmic fungal peroxidases such as lignin peroxidase, manganese peroxidase and versatile peroxidase. Similarly, horseradish peroxidase (HRP) and barley grain peroxidase are Class III peroxidases and are extracytoplasmic (Sugano *et al.*, 2007; Welinder, 1992). In addition to these two large superfamilies, four smaller protein families are indexed separately in RedOxiBase (<http://peroxibase.toulouse.inra.fr/>), a peroxidase database: Catalases (Kat), Di-haem cytochrome c peroxidases (DiHCcP), Dye-type peroxidases (DypPrx), and haem Haloperoxidases (HalPrx) (Fawal *et al.*, 2013).

1.2. Haem peroxidases form iron-oxo intermediates

All peroxidases react with H_2O_2 to form high-valent haem species, commonly referred to as ferryl haem (Dunford, 1999; Poulos, 2014). Prior to formation of the first ferryl haem intermediate, H_2O_2 binds to the ferric haem and undergoes heterolytic scission of the O–O bond to form the first ferryl intermediate – Compound I ($[\text{Fe}^{\text{IV}}=\text{O}-\text{R}\cdot]^+$) where R stands for radical site. (Dolphin *et al.*, 1971). Reduction of the Compound I occurs in a single-electron step by an electron supplied by a reducing substrate to yield the second ferryl haem intermediate, Compound II ($\text{Fe}^{\text{IV}}=\text{O}$ or $\text{Fe}^{\text{IV}}-\text{OH}$) (Dunford, 1999; Poulos, 2014). A further one-electron reduction of Compound II returns the haem to the ferric state (Dunford, 1999; Poulos, 2014). The ferryl intermediates are different

among different peroxidases, and therefore catalytic mechanism varies as well. For instance, Compound I in HRP (Aasa *et al.*, 1975), manganese peroxidase (Wariishi *et al.*, 1989), lignin peroxidase (Khindaria and Aust, 1996) and chloroperoxidase (Rutter, 1982), contains a ferryl haem together with a radical on porphyrin ring. On the other hand, Compound I of CcP contains a tryptophan radical (Erman *et al.*, 1989; Mauro *et al.*, 1988; Sivaraja *et al.*, 1989). In addition to peroxidases a large number of haem enzymes (e.g. P450s, NO synthase and catalases) use ferryl haem as part of their catalytic mechanism and thus much effort has been focused on understanding the formation, nature and reactivity of ferryl haem (Hiner *et al.*, 2002; Moody and Raven, 2018).

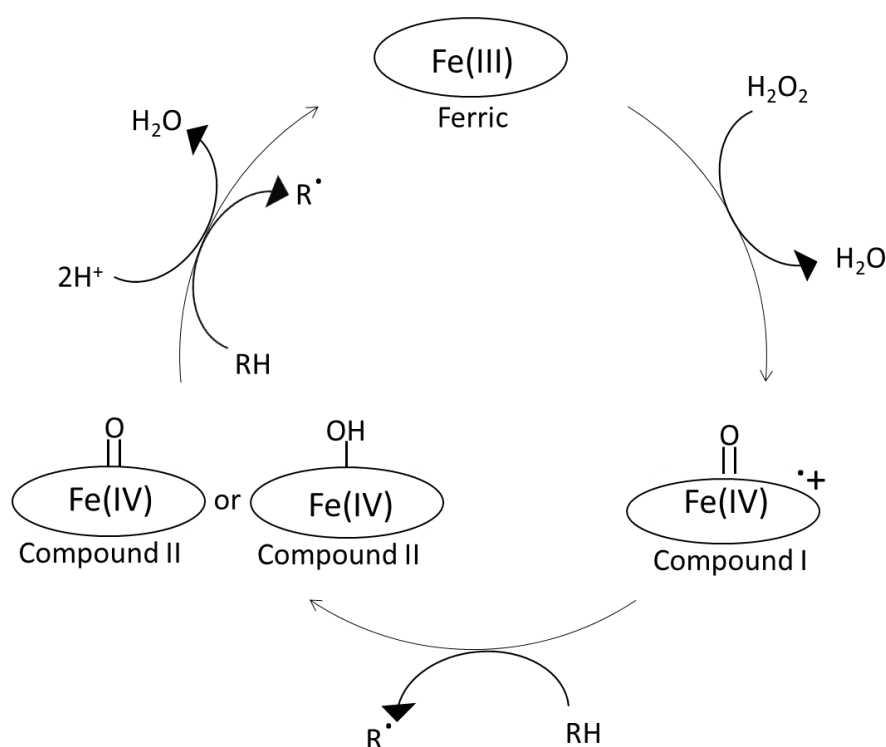


Figure 1.1. Catalytic cycle of haem peroxidases. For the full description see the main text. Variability of Compound II protonation state is depicted: $\text{Fe}^{\text{IV}}\text{-OH}$ for protonated or $\text{Fe}^{\text{IV}}\text{=O}$ for unprotonated species. R stands for substrate.

The chemical nature of as Compounds I and II in peroxidases has attracted much discussion as to whether they are formulated as an unprotonated $\text{Fe}^{\text{IV}}=\text{O}$ or a protonated $\text{Fe}^{\text{IV}}\text{-OH}$ species (Moody and Raven, 2018). The reactivity of these ferryl species is controlled by protonation. There is a long experimental history associated with efforts to assign the chemical nature of these ferryl species using spectroscopy (e.g. EXAFS (Extended X-ray Absorption Fine Structure), resonance Raman and Mössbauer, X-ray crystallography and more recently neutron crystallography, which not only eliminates radiation damage, but also has the advantage of being able to observe nuclear density attributed to proton positions. A detailed history of the experimental efforts to define the nature of ferryl heme has been reviewed by Raven and Moody (Moody and Raven, 2018).

1.3. X-ray crystallography approach for probing ferryl intermediates

With the advent of high brilliance synchrotron radiation sources and their high throughput data collection capabilities, X-ray crystal structure determination of proteins and enzymes has become a relatively routine and increasingly automated process, with the often high-resolution structures obtained used to assist in the interpretation of mechanism. It is now recognised that if the appropriate experimental safeguards in the collection of X-ray diffraction data have not been put in place, there is a danger of a mismatch between the determined structures and mechanism (Pfanzagl *et al.*, 2020b). This is because the high intensity X-rays generated at synchrotron sources are partially absorbed by protein crystals, all of which have a high water content. Radiolysis of this water produces multiple radical species including a large

number of solvated photoelectrons that can cause not only global radiation damage (*i.e.* degradation of the crystalline order and hence diffracting properties of the crystal, which to a certain limit can be countered by cryo-cooling the crystals to 100 K), but also site-specific radiation damage (Burmeister, 2000; Ravelli and McSweeney, 2000; Weik *et al.*, 2000). This site-specific radiation damage can, in the case of metalloenzymes, reduce redox active metals via solvated photoelectrons and hence change the coordination geometry and the coupled protein structure. Thus, site-specific radiation damage is a particular concern for the determination of haem-Fe redox states in peroxidases (Kekilli *et al.*, 2017; Pfanzagl *et al.*, 2020b), with the resting state Fe^{III} and high-valent Fe^{IV} species both exquisitely susceptible to site-specific radiation damage. Such damage can occur at X-ray doses at least three orders of magnitude lower than the 20-30 Mgy range, which is an acceptable absorbed dose limit for global radiation under cryo-cooled conditions (Henderson, 1995; Owen *et al.*, 2006). The very low doses required for redox state changes essentially rule out the effective determination of non-damaged states from single crystals at either cryogenic or room temperature. Lowering the X-ray flux, for example by using an in-house diffractometer or a very attenuated synchrotron beam would require either a greatly increased data collection time (thereby incurring a similar dose as using a more intense source for a shorter time) or accepting a much lower resolution dataset which may not reveal the details of the metal centre environment. Therefore, to capture intact (*i.e.* free of radiation-induced damage) or near-intact structural data from radiation-sensitive Fe^{III} and Fe^{IV} haem species using X-ray crystallography, two general approaches have been developed i) low-dose composite (*i.e.* multi-crystal) structures coupled with single crystal spectroscopy to validate redox state before and after X-ray exposure (near-intact) (Berglund *et al.*, 2002; Chaplin *et al.*, 2019; Gumiero *et al.*, 2011; Lučić *et al.*,

2020a; Lučić *et al.*, 2020b; Mehareenna *et al.*, 2010) and ii) the use of X-ray free electron lasers (XFELs, zero effective dose) (Chreifi *et al.*, 2016; Ebrahim *et al.*, 2019; Lučić *et al.*, 2020b).

With the recent invention of the XFEL, an opportunity has arisen to obtain high resolution structures unlimited by concern regarding the radiation damage. Femtosecond-duration pulses from an XFEL source ensure the formation of diffraction patterns before the onset of radiation damage, eliminating completely site-specific radiation damage (Chapman *et al.*, 2014; Chapman *et al.*, 2011; Neutze *et al.*, 2000; Schlichting, 2015; Spence, 2014). This approach is called serial femtosecond crystallography (SFX) and requires the presentation of a new crystal for each pulse, as the XFEL pulse destroys the crystal. While the X-ray dose is tremendously high in such experiments, with 10 femtosecond pulses there is insufficient time under typical experimental conditions for any radiation damage to be manifested in the observed structure (this principle is termed “diffraction-before-destruction”). Another advantage of the SFX is that data can be collected at room temperature as cryo-cooling is no longer necessary to protect the crystal from global radiation damage. Therefore, SFX affords the opportunity to acquire structures and observe chemistries that are not frozen out, which can be the case with data collection at 100 K (Fraser *et al.*, 2011). In this thesis, both SFX and low-dose composite approach will be explored for determining validated redox-state structures of dye-decolourising peroxidases.

1.4. Dye-decolourising peroxidases

Dye-decolorizing peroxidases (DyPs; EC number 1.11.1.7) are the most recently discovered member of the histidine-haem ligated peroxidase superfamily (Kim and Shoda, 1999). They are widespread in bacterial and fungal genomes (Singh and Eltis, 2015) and represent a distinct haem peroxidase structural family that possess a dimeric $\alpha + \beta$ barrel fold (SCOP 3000089, InterPro Pfam CL0032) capable of binding a single *b*-type haem (Hofbauer *et al.*, 2021; Sugano *et al.*, 2007). DyPs were initially divided into four phylogenetic classes; types A, B, C and D (Ogola *et al.*, 2009), with types C and D later found to be one phylogenetic class and now referred to as C/D-type. The A- and B-types are exclusively found in bacteria whilst the C/D-types are found in bacteria and fungi (Ogola *et al.*, 2009).

A distinguishing feature of the DyP family is the absence of a distal haem pocket His residue, which in non-mammalian peroxidases such as HRP, APX and CcP is part of a highly conserved His-Arg couple that plays a prominent role in Compound I formation (Erman *et al.*, 1993; Howes *et al.*, 1997; Rodríguez-López *et al.*, 2001). The distal His functions as an acid–base catalyst (Figure 1.2), removing the proton from the O^α atom of the bound $Fe^{III}-O_2H_2$ (Poulos and Kraut, 1980; Vidossich *et al.*, 2010), to generate an anionic precursor to Compound I known as Compound 0 ($Fe^{III}-O^\alpha-O^\beta H$) (Baek and Vanwart, 1989; Svistunenko *et al.*, 2007). The proton is then transferred to the O^β atom of Compound 0 to form an oxy-water complex ($Fe^{III}-O-OH_2$) that enables the distal oxygen to leave as a H_2O molecule (Figure 1.2) (Poulos and Kraut, 1980; Vidossich *et al.*, 2010). Thus, heterolysis of the O–O bond is proton assisted. In DyPs a distal Asp-Arg couple is present (Sugano *et al.*, 2007), with the recently identified exception being the DyP from *Cellulomonas bogoriensis* where a Glu replaces the Asp (Habib *et al.*,

2019). Compound I formation in some DyPs argue for the distal Arg being the proton acceptor and donor (Mendes *et al.*, 2015b; Singh *et al.*, 2012), whereas in others the Asp has been reported to serve as the acid–base catalyst (Pfanzagl *et al.*, 2018; Shrestha *et al.*, 2017).

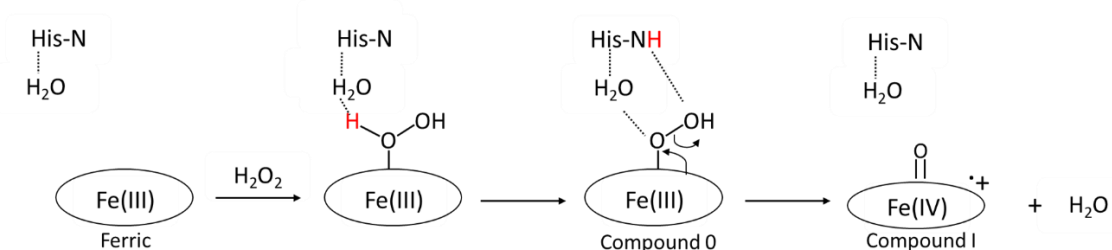


Figure 1.2. The Poulos-Kraut mechanism of Compound I formation. For detailed description see the main text. The H^α proton of H₂O₂ is depicted in red.

Historically, the name DyP derives from the discovery that a C/D-type displayed an ability to oxidise recalcitrant anthraquinone and/or azo-dyes used in the textile industry (Kim and Shoda, 1999). However, it has become apparent that not all DyPs possess an ability to oxidise these redox dyes and thus the initial naming of this family of haem peroxidases is in hindsight rather unfortunate (Yoshida and Sugano, 2015). In fact, the physiological function of DyPs is almost completely unknown, with only a handful of examples illustrating a potential role of fungal C/D-types in lignin oxidation (Liers *et al.*, 2010; Liers *et al.*, 2013) and in the degradation of an antifungal anthraquinone compound (Sugawara *et al.*, 2019). Bacterial DyPs are also associated with 21ncapsuling systems (Contreras *et al.*, 2014; Rahmanpour and Bugg, 2013; Sutter *et al.*, 2008). These proteinaceous nanocompartments are assembled into icosahedral hollow capsids by one type of shell protein, that serve to encapsulate cargo proteins (Giessen, 2016; Giessen and Silver, 2017; Sutter *et al.*, 2008). A recent cryo-EM study

has revealed that oligomeric DyP assemblies (dodecamers) can pack inside a capsid and thus provide a concentrated centre for an antioxidant response in the microbe (Tang *et al.*, 2021).

All DyPs react with H₂O₂ to form the ferryl haem species as described in section 1.2 (Groves, 2006; Moody and Raven, 2018; Winkler and Gray, 2011), which are essential for their oxidative chemistry. Although their physiological substrates remain unknown, many DyPs, in addition to reacting with synthetic dyes, display a wide substrate specificity with artificial electron donors such as ABTS, guaiacol and ferrocyanide (Chaplin *et al.*, 2017). One of the major ambitions of DyPs researchers is to bioengineer them into potent textile waste catalysers. About 7×10^5 metric tons of synthetic dyes is produced annually and 15-20% of it is released into environment as waste (Husain, 2010; Rai *et al.*, 2005). The need for novel treatment strategies, particularly in Eastern societies is widely recognised since synthetic dyes used in the textile industry are poorly biodegradable with physical and chemical processes for the downstream treatment of dye waste expensive and largely ineffective (Kim and Shoda, 1999). The possibility of using biological methods for dye-decolourization became widely popular for its cost, effectiveness and environmental benignity (Chen *et al.*, 2003; Stolz, 2001). Although DyPs are not always great synthetic dyes oxidisers, it might be possible to increase their activity against pollutants through detailed study of their catalytic cycle. Understanding the biochemistry of DyPs is the first step towards rational design of potentially useful biocatalysts for textile waste.

1.5. Focus of this thesis

In the soil-dwelling Gram-positive bacterium, *Streptomyces lividans*, three DyPs are present. Based on sequence analysis, two are classed as A-types, each possessing a signal sequence that locates them in the extracytoplasmic environment. The third is a B-type, which from the absence of a signal sequence remains located in the cytoplasm. The physiological substrates for these *S. lividans* DyPs remain unknown, but one of the A-types (dye-type peroxidase A; DtpA) has been implicated in a copper trafficking pathway that regulates a morphological development step in the life-cycle of *S. lividans* (Petrus *et al.*, 2016). Despite the presence of multiple DyP encoding genes in many bacterial and fungal genomes, comparative reporting of intra-species structural and kinetic properties is sparse (Ahmad *et al.*, 2011; Liu *et al.*, 2011; Liu *et al.*, 2017; Roberts *et al.*, 2011). In this thesis the focus is on a holistic approach using the three *S. lividans* DyPs to decipher through stopped-flow kinetics, electron paramagnetic resonance (EPR) spectroscopy and X-ray based structural approaches the mechanistic intricacies of Compound I and II formation. It presents insights into understanding how different mechanisms of Compound I and II formation can be adopted by DyPs and it highlights several approaches to mitigate against the often insidious effects of X-ray radiation used in crystallographic data collection upon the metal site structure.

Chapter Two

Two A-type dye-decolourising peroxidases in *Streptomyces lividans* with distinctly different H₂O₂ reactivities

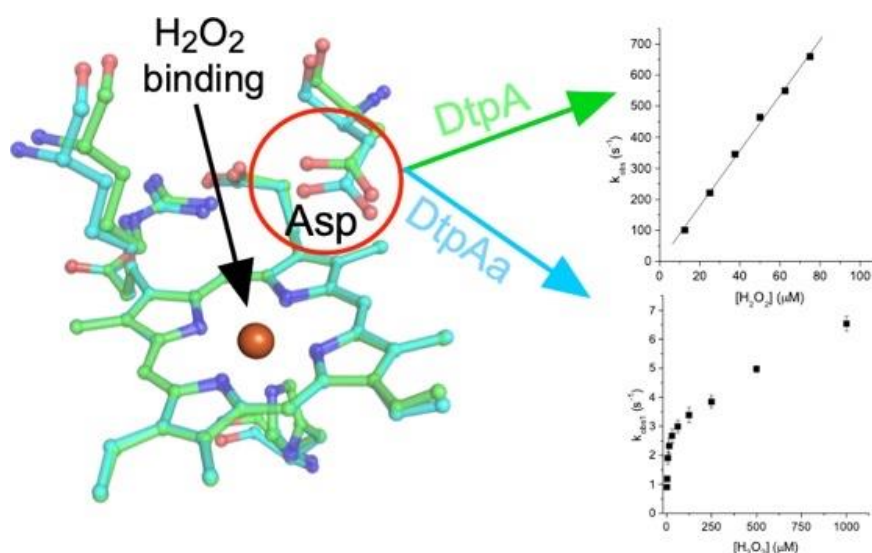


Figure 2. Superposition of the haem environment in DtpA and DtpAa reveals a slight shift of the distal Asp residue, which controls their chemistry.

Results from this Chapter have been published in:

M. Lučić, A. K. Chaplin, T. Moreno-Chicano, F. S. N. Dworkowski, M. T. Wilson, D. A. Svistunenko, M. A. Hough and J. A. R. Worrall A subtle structural change in the distal haem pocket has a remarkable effect on tuning hydrogen peroxide reactivity in dye decolourising peroxidases from *Streptomyces lividans*. *Dalton Transactions*, 2020, 49, 1620-1636.

I acknowledge the work from Dr. Tadeo Moreno-Chicano, Dr. Florian S. N. Dworkowski, Dr. Michael A. Hough and Dr. Jonathan A. R. Worrall who have crystallized DtpAa, collected the structural data and kindly provided the merged data file for me to further analyze.

2.1. Introduction

The genome of the soil-dwelling Gram-positive bacterium *S. lividans* contains three genes encoding for DyPs. Two of these are A-types, referred to as DtpA and DtpAa, and are secreted to the extracytoplasmic environment, with the third, a B-type (DtpB), located in the cytoplasm. DtpA is membrane associated *i.e.* possesses a predicted trans-membrane sequence (Petrus *et al.*, 2016), whereas DtpAa, contains a clear N-terminal peptidase cleavage site suggesting that it is secreted into the extracytoplasmic environment. Amino acid sequence alignment of the two A-type aligned using Clustal Omega (<https://www.ebi.ac.uk/Tools/msa/clustalo/>) and formatted using ESPrpt 3.0 (Figure 2.1) (Robert and Gouet, 2014). SIAS server (http://imed.med.ucm.es/Tools/sias_help.html) reveal a sequence identity of 43%. Both the reason behind the existence of two A-type homologues and their biological function in *S. lividans* are unknown. So far, a detailed structural and mechanistic characterisation of DtpA has revealed that it can rapidly react with H₂O₂ to form Compound I with a second-order rate constant of $8.9 \times 10^6 \text{ M}^{-1} \text{ s}^{-1}$ and possesses the ability to oxidise anthraquinone dyes as well as conventional peroxidase substrates (Chaplin *et al.*, 2017). However, its physiological substrate remains to be discovered.

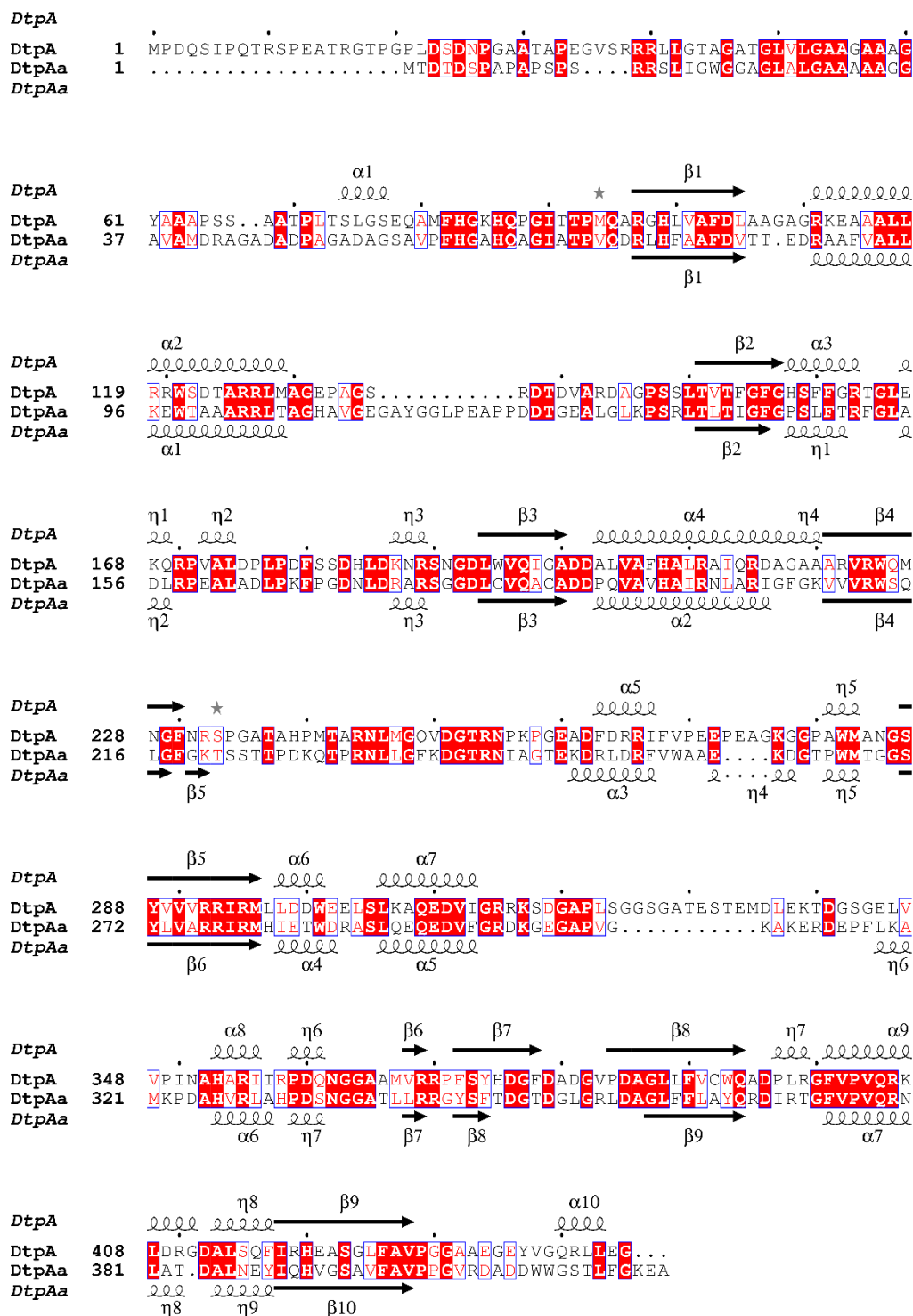


Figure 2.1. Amino acid sequence alignment of DtpA and DtpAa. Residues that are similar between the two homologues are depicted with red colour. Secondary structure elements were determined from the respective X-ray structures of DtpA (PDB 6GZW) and DtpAa (PDB 6TB8) and are depicted as α , β , η standing for α -helix, β -sheet and 3_{10} helix, respectively.

Recently, a serial femtosecond X-ray crystallography study using an X-ray free electron laser (XFEL) has determined the DtpAa structure at room temperature with the haem in the ferric oxidation state (Ebrahim *et al.*, 2019). A key factor for the interpretation of structure/mechanism studies with metalloproteins and enzymes is to ensure that the structures determined are in the redox state generated prior to exposure of X-rays. In the case of peroxidases several strategies have been employed to ensure the redox state of the haem is validated including the metastable Compound I and Compound II intermediates of the peroxidase reaction cycle. These include low-dose composite approach (*i.e.* multi-crystal) coupled with single crystal spectroscopy (Berglund *et al.*, 2002; Chaplin *et al.*, 2019; Gumiero *et al.*, 2011; Kwon *et al.*, 2020; Lučić *et al.*, 2020a; Mehareenna *et al.*, 2010), as well as neutron diffraction (Casadei *et al.*, 2014; Kwon *et al.*, 2016; Kwon *et al.*, 2020) and X-ray free electron lasers (Chreifi *et al.*, 2016; Ebrahim *et al.*, 2019; Kwon *et al.*, 2021). Insights into why *S. lividans* possesses two A-type DyP homologs in the same cellular location and to their biological function, can begin to be addressed through structure and mechanistic studies.

This Chapter reports detailed structural and mechanistic studies of DtpAa as well as further studies on DtpA. It provides insight into the mechanistic features of two A-type DyPs reacting with H₂O₂ through studying the redox validated X-ray structures in combination with stopped-flow reaction kinetics, including deuterium kinetic isotope exchange experiments, the pH dependency of Compound I formation and site-directed mutagenesis to create the distal Asp mutants of DtpAa and DtpA. A mechanism for Compound I formation in DtpAa and DtpA is proposed and discussed.

2.2. Experimental procedures

2.2.1. Site-directed mutagenesis of *DtpAa* and *DtpA*

Two pET28a vectors (Novagen) that served as the template for site-directed mutagenesis were supplied by Dr. Amanda Chaplin. They contained the nucleotide sequences encoding for amino acid residues 48 to 420 of *DtpAa* and 69 to 445 of *DtpA*. The site-directed mutagenesis was carried out using the QuikChange protocol (Stratagene). The following forward and reverse primers to create the D239A mutant and the D251A mutant of *DtpAa* and *DtpA*, respectively, were designed and synthesized (Sigma); D251A-F 5'-GCCAGGTCGCCGGCACCCGCAAC-3', D251A-R 5'-GTTGCGG GTGCCGGCGACCTGGC-3', D239A-F GGCTTCAAGGCCGGCA CCCGCAAC-3', D239A-R CCGAAGTTCCGGCCGTGGGCGTTG-3'. A polymerase chain reaction (PCR) mix consisting of the respective primers (75 ng μL^{-1}), the respective pET28a template (15 ng μL^{-1}), 10 mM dNTPs (Fermentas), Pfu Turbo polymerase (Agilent), 10 \times Pfu buffer (Agilent) and deionised water was prepared and subjected to the following PCR cycle; 95 °C for 3 min; 18 cycles of 95 °C for 1 min, 65 °C for 1 min and 72 °C for 8 min; and 72 °C for 10 min. Clones were corroborated for the presence of the desired mutation by DNA sequencing (Source Bioscience).

2.2.2. Purification of *DtpAa* and *DtpA*

The plasmid containing either the *DtpA* or *DtpAa* insert was transformed into *Escherichia coli* BL21 (DE3) cells. Overnight precultures (low salt LB medium; Melford) were used to inoculate 1.4 L of high salt LB medium (10 g tryptone, 10 g sodium chloride, 5 g yeast extract per litre) with 50 $\mu\text{g mL}^{-1}$ kanamycin and grown at

37 °C, 220 r.p.m. At an OD₆₀₀ of 1.0, the haem-precursor, 5-aminolevulinic acid (250 μM final concentration) and an iron supplement, iron citrate (100 μM final concentration) were added to each flask. Cultures were then induced by adding isopropyl β-D-thiogalactopyranoside (IPTG; Melford) to a final concentration of 500 μM and carbon monoxide (CO) gas was bubbled through the culture for 45 s. Flasks were then sealed and incubated for a further 15 h at 30 °C and 100 r.p.m. Cells were harvested via centrifugation (10 000g, 20 min, 4°C) and the cell pellet resuspended in 50 mM Tris/HCl, 500 mM NaCl (Fisher) and 20 mM imidazole (Sigma) at pH 7.5 (Buffer A). The following purification procedure was used for both DtpA and DtpAa. The resuspended cell suspension was lysed using an EmulsiFlex-C5 cell disrupter (Avestin) followed by centrifugation (22 000 g, 45 min, 4 °C). The clarified supernatant was loaded onto a 5-ml nickel–nitrilotriacetic acid–sepharose column (GE Healthcare) equilibrated with buffer A and eluted by a linear imidazole gradient using buffer B (buffer A with 500 mM imidazole). Fractions were collected (eluate was distinguished based on their intensive red colour), pooled and concentrated using a Centricon (VivaSpin) with a 5 kDa cut-off at 4 °C. Further purification was achieved using a S200 Sephadex size-exclusion column (GE Healthcare) equilibrated with 50 mM sodium acetate, 150 mM sodium chloride, pH 5.0, fractions were collected, pooled and the protein was checked for purity using 15% SDS PAGE gel, then concentrated and stored at -20 °C until required. The D239A and D251A variants were over-expressed and purified in an identical manner to their respective wild-type protein.

2.2.3. Sample preparation

Concentrations of DtpAa and DtpA, as well as variants were determined spectrophotometrically using a Cary 60 UV-Visible spectrophotometer (Agilent) and

an extinction coefficient (ϵ) at 280 nm determined using ProtParam (Gasteiger *et al.*, 2003) of $46,057 \text{ M}^{-1} \text{ cm}^{-1}$ for DtpAa and $37,470 \text{ M}^{-1} \text{ cm}^{-1}$ for DtpA. Buffers used were 50 mM sodium acetate pH 5.0, 150 mM NaCl; 20 mM sodium phosphate 100 mM NaCl, pH 7.0 and a mixed buffer system comprising of 10 mM Tris, 10 mM MES, 10 mM MOPS, 10 mM sodium acetate, 200 mM potassium chloride with the pH adjusted between values of 4 and 10 as required. Enzymes were exchanged into a desired buffer using a PD-10 column (Generon) and concentrated using centrifugal ultrafiltration devices (GE Healthcare). H_2O_2 solutions (Sigma-Aldrich) were prepared from a stock with the final concentration determined spectrophotometrically using an $\epsilon = 43.6 \text{ M}^{-1} \text{ cm}^{-1}$ at 240 nm (Beers and Sizer, 1952). The required deuterated buffers were prepared in 99.9% D_2O (Sigma). Highly concentrated enzymes and H_2O_2 stocks were diluted directly in D_2O and left to equilibrate in the D_2O solutions before experiments were performed.

2.2.4. Stopped-flow absorption kinetics

Transient kinetics of the interaction of H_2O_2 with ferric enzymes was performed using a SX20 stopped-flow spectrophotometer (Applied Photophysics) equipped with either a photomultiplier or a diode-array multi-wavelength unit and thermostatted to 25 °C. Enzyme solutions (10 μM before mixing) were prepared in the appropriate buffer (H_2O or D_2O) and mixed with a series of H_2O_2 (or D_2O_2) concentrations (ranging from 4–10,000 μM before mixing, depending on enzyme used). The overall spectral transitions were monitored using either the photomultiplier or diode array unit and time course were fitted to kinetic models in the Pro-K software (Applied Photophysics) to yield rate constants for Compound I (k_{obs1}) and Compound II formation (k_{obs2}). Rate constants for Compound I formation (k_{obs1}) at various pH values were obtained using 10 μM of

enzyme (before mixing) and a fixed H₂O₂ concentration, which for DtpA was 50 μM, DtpAa 250 μM, D251A 500 μM and D239A 250 μM (all after mixing).

2.2.5. X-ray structure determination and refinement

DtpAa crystals were grown by Dr. Tadeo Moreno-Chicano and X-ray diffraction and single crystal spectroscopic data were collected at 100 K at the Swiss Light Source (SLS) beamline X10SA by Dr. Jonathan A.R. Worrall, Dr. Tadeo Moreno-Chicano and Dr. Mike Hough in September 2018, together with absorbance spectra measured prior to and following X-ray data collection using the MS3 on-axis microspectrophotometer (Fuchs *et al.*, 2014). A multi-crystal approach was used to obtain a complete low-dose composite dataset for the ferric DtpAa structure. A total of 13 spectroscopically-validated diffraction data wedges were merged using the in house go2gether.com script in the XDS package (Kabsch, 2010) and the merged data was provided for refinement and structure analysis in this Chapter. The merged data was refined against a starting model of the serial femtosecond X-ray crystallography (SFX) room temperature structure of DtpAa (PDB code 6I43) (Ebrahim *et al.*, 2019). Refinement of the cryo-cooled structure was carried out initially using Refmac5 (Murshudov *et al.*, 1997) in the CCP4i suite and subsequently in PHENIX (Liebschner *et al.*, 2019), with model building between refinement cycles in Coot (Emsley *et al.*, 2010). Riding hydrogen atoms were added during refinement. The structure was validated using the Molprobit server (Davis *et al.*, 2007), the JCSG Quality Control Server and tools within Coot (Emsley *et al.*, 2010). A summary of data collection and refinement statistics are given in Table 2.1. The X-ray absorbed dose was estimated using Raddose-3D (Zeldin *et al.*, 2013). To reflect the beam profile used, a weighted average of doses calculated for top hat and Gaussian profiles was calculated and doses were estimated for the range of

crystal dimensions used. Estimates of bond length error for the iron-water and iron-proximal His bonds were derived using the Online_DPI server (Kala Sekar *et al.*, 2015) based on the estimated coordinate error as previously described (Gurusaran *et al.*, 2013).

Table 2.1. Crystallographic data processing and refinement statistics for ferric DtpAa (100 K). Values in parenthesis refer to the outermost resolution shell.

Space group	P2 ₁
Unit cell (Å)	a=71.4, b=67.59, c= 72.9, β = 105.5°
Resolution (Å)	48.71 - 1.80
Outer shell (Å)	1.84 - 1.80
Unique reflections	61725 (3542)
Mn (I/SD)	6.3 (1.6)
CC _{1/2}	0.989 (0.683)
Completeness (%)	99.4 (96.1)
Redundancy	4.5 (2.9)
R _{cryst}	0.1513
R _{free}	0.1991
RMS dev. bond lengths (Å)	0.009
RMS dev. bond angles (°)	1.000
Ramachandran favoured (%)	98.19
PDB accession code	6TB8

2.3. Results

2.3.1. Over-expression and purification of DtpA and DtpAa

An example of a purification for DtpAa is shown in Figure 2.2. Both A-type DyPs and their variants over-expressed well in *E. coli* as evidenced by the pink cell pellet on harvesting (Figure 2.2A). Using a Ni²⁺-NTA sepharose column a single peak at 280 nm eluting at ~ 35 % buffer B (Figure 2.2B) was observed. This peak contained fractions that were orange/brown in colour and from SDS-PAGE analysis showed a major band running at ~ 40 kDa, consistent with the expected molecular weight for DtpA (~ 40.5 kDa) and DtpAa (~ 42.8 kDa) (Fig. 2.2E). A final purification step was carried out using an S200 size-exclusion column, which produced a single peak with an elution volume of ~ 75 ml (Figure 2.2C and D). Fractions eluting from this column were checked by SDS-PAGE and showed some minor lower molecular weight contaminants, but the most intense band was observed at ~40 kDa, consistent with the purified peroxidase (Figure 2.2E).

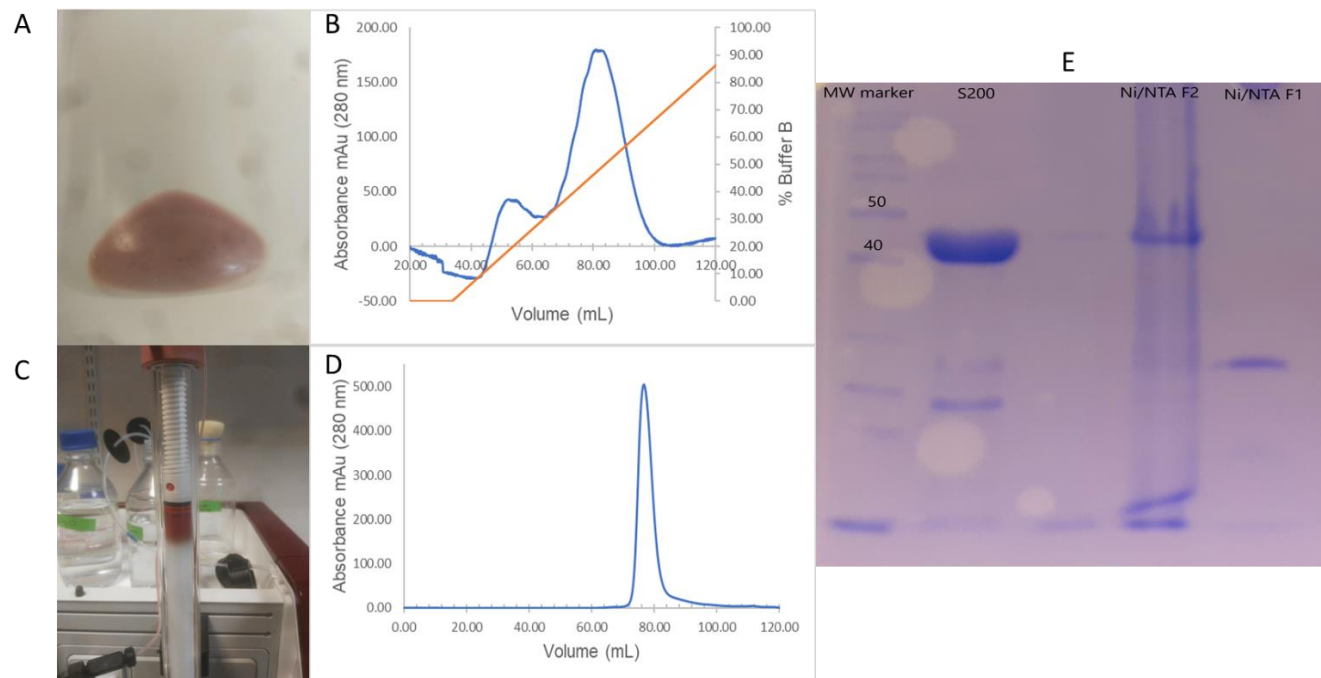


Figure 2.2. Over-expression and purification of DtpAa. Both A-types were over-expressed in identical manner and shown similar profile. A) Pink cell pellet after spinning 1.4 L cultures. B) Ni²⁺-NTA profile of DtpAa showing an absorbance peak (mAu) at 280 nm in blue at ~35 % buffer B shown in orange. C) DtpAa loaded on S200 column. D) S200 size-exclusion sephadex column absorbance 280 nm (mAu) profile of DtpAa eluting at ~ 75 mL. E) Coomassie stained 15 % SDS-PAGE gel analysis of DtpAa fractions from an S200 size-exclusion sephadex column and Ni²⁺-NTA His-trap column. A single protein band between 40-50 kDa that can be identified as DtpAa is present in Ni²⁺-NTA fraction 2 (eluted at ~35 % buffer B) and in S200 fraction.

2.3.2. The electronic absorbance spectrum of DtpAa

The electronic absorbance spectrum of purified DtpAa at pH 7.0 is shown in Figure 2.3, with the peak maxima wavelengths reported in Table 2, alongside those of DtpA for comparison. The spectrum is consistent with a high-spin (HS) ferric haem species (as per the peak maxima wavelengths), which upon addition of one-equivalent H_2O_2 , leads to a decrease in the Soret band intensity and a red shift in wavelength, coinciding with the appearance of α and β bands of equal intensity and a further low intensity charge transfer band in the red region (Figure 2.3 and Table 2.2). No further changes to the spectrum are observed on subsequent additions of H_2O_2 . Comparison with the wavelength maxima of the high-valent haem intermediates generated during the peroxidase cycle in DtpA i.e. Compound I ($[(\text{Fe}^{\text{IV}}=\text{O})\text{por}\bullet^+]$) and Compound II ($\text{Fe}^{\text{IV}}=\text{O}$) (Table 2) (Chaplin *et al.*, 2017; Petrus *et al.*, 2016), suggests the spectrum generated on addition of H_2O_2 to DtpAa is consistent with a Compound II species. It was previously reported that on stoichiometric addition of H_2O_2 to DtpA, a Compound I absorbance spectrum forms (Chaplin *et al.*, 2017). Therefore, in contrast for DtpAa, Compound II forms without any detectable Compound I formation in the static absorbance experiment, suggesting the possibility of an unstable Compound I species that decays rapidly to Compound II (*vide infra*).

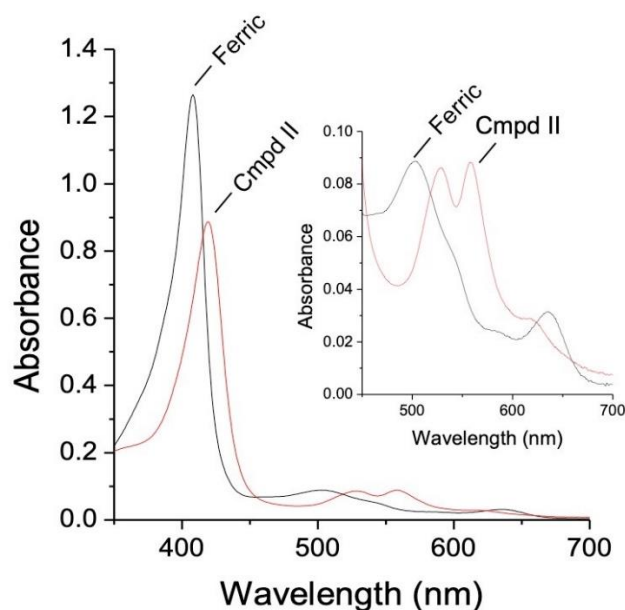


Figure 2.3. Electronic absorbance spectra of DtpAa. Solution spectra at pH 7.0 with the ferric and Compound II species, the latter formed following addition of one molar equivalent of H_2O_2 per molar haem, indicated. *Inset* a zoom-in of the α/β band region.

Table 2.2. Wavelength absorbance maxima at pH 7.0 for DtpAa and DtpA and the respective distal Asp variants.

Protein	Ferric (nm)	Compound I (nm)	Compound II (nm)
DtpAa	406, 500, 540 (sh) ^a , ~ 588, 630	^c 403, 534, 588, 614, 641	416, 527, 557, 620
DtpA ^b	406, 502, 540 (sh), 635	399, 530, 557, 614, 644	419, 528, 557, 621
D239A DtpAa	410, 504, 569, 636, 687	n.d.	418, 528, 556, 632, 686
D251A DtpA	408, 501, 542 (sh), ~ 589, 635	^c 400, 539, 588, 605, 638	418, 528, 558, 615, 638

^aShoulder (sh)

^bValues taken from (Chaplin *et al.*, 2017).

^cValues taken from global fitting of the spectral transitions observed upon mixing with H_2O_2 in stopped-flow spectrophotometer.

2.3.3. Validation of the ferric haem state in the crystal structure of DtpAa

To compare the structures of DtpAa and DtpA, determined by X-ray crystallography, it is important that the oxidation state of the haem in the structure is validated. The spectroscopically-validated X-ray crystal structure of ferric DtpA has been determined previously (Chaplin *et al.*, 2019). Prior to X-ray diffraction data collection, an absorbance spectrum at 100 K of a DtpAa crystal was acquired using the on-axis UV-vis microspectrophotometer at the SLS (Figure 2.4). Identical electronic absorbance bands to those of the ferric DtpAa in solution are observed (Figure 2.3B), indicating a ferric DtpAa species in the crystal. To mitigate against X-ray induced photo-reduction of the ferric DtpAa crystal, a multi-crystal strategy was employed whereby 20° wedges (a total of 200 images each of 0.1° oscillation) were collected per ferric DtpAa crystal, with absorbance spectra recorded prior to and following the measurement of each data wedge and examined to ensure that the spectrum of the ferric form remained largely intact (Figure 2.4).

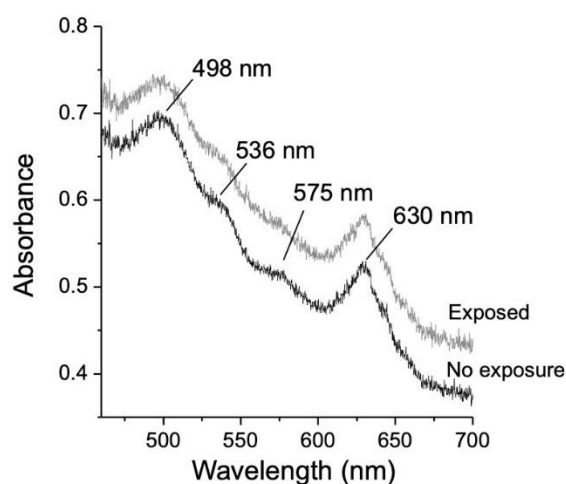


Figure 2.4. Electronic absorbance spectra of DtpAa. The α/β band region of a crystal of ferric DtpAa recorded at 100 K before (no X-ray exposure) and after exposure to X-rays following collection of a 20° data wedge.

2.3.4. Comparison of the ferric DtpAa and DtpA X-ray structures determined at 100 K

The validated ferric DtpAa X-ray structure was determined to 1.80 Å resolution (Table 1), with two DtpAa monomers (chains A and B) found in the crystallographic asymmetric unit (all bond-lengths and B-factors reported herein refer to chain A). Electron density was visible for residues 55-416 in chain A and 56-417 in chain B. The overall monomer fold of DtpAa consists of two ferredoxin-like folds (composed of $\beta\alpha\beta\beta\alpha\beta$ secondary structure), to create two domains in which one houses the *b*-type haem (Figure 2.5 and 2.6A). A comparison of the tertiary structures of DtpAa and DtpA illustrates the structural homology of the core $\beta\alpha\beta\beta\alpha\beta$ fold between these two A-type DyPs, with changes in helical content and loop insertions and/or deletions contributing to the variation in structural shape (Figure 2.6A). Most notable are two extended loop sections incorporating residues 113 and 125 in DtpAa and residues 337 and 347 in DtpA (Figure 2.6A and Figure 2.1 reporting a primary sequence alignment).

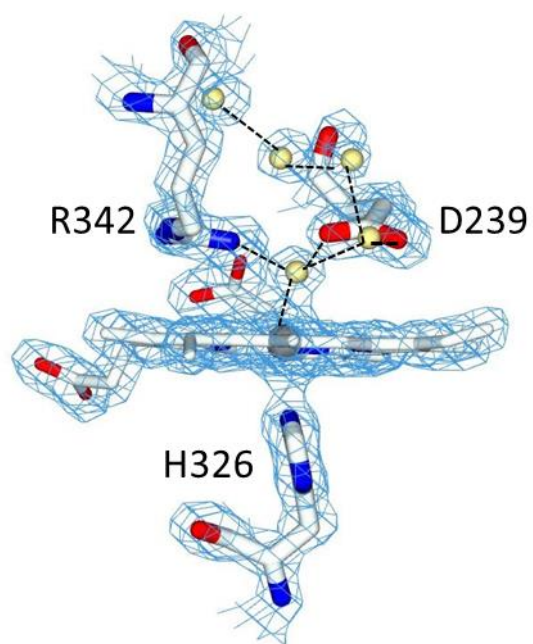


Figure 2.5. $2F_o-F_c$ electron density map (blue) contoured at 1.5σ for the haem site of Chain A in DtpAa. Water molecules are depicted as yellow spheres.

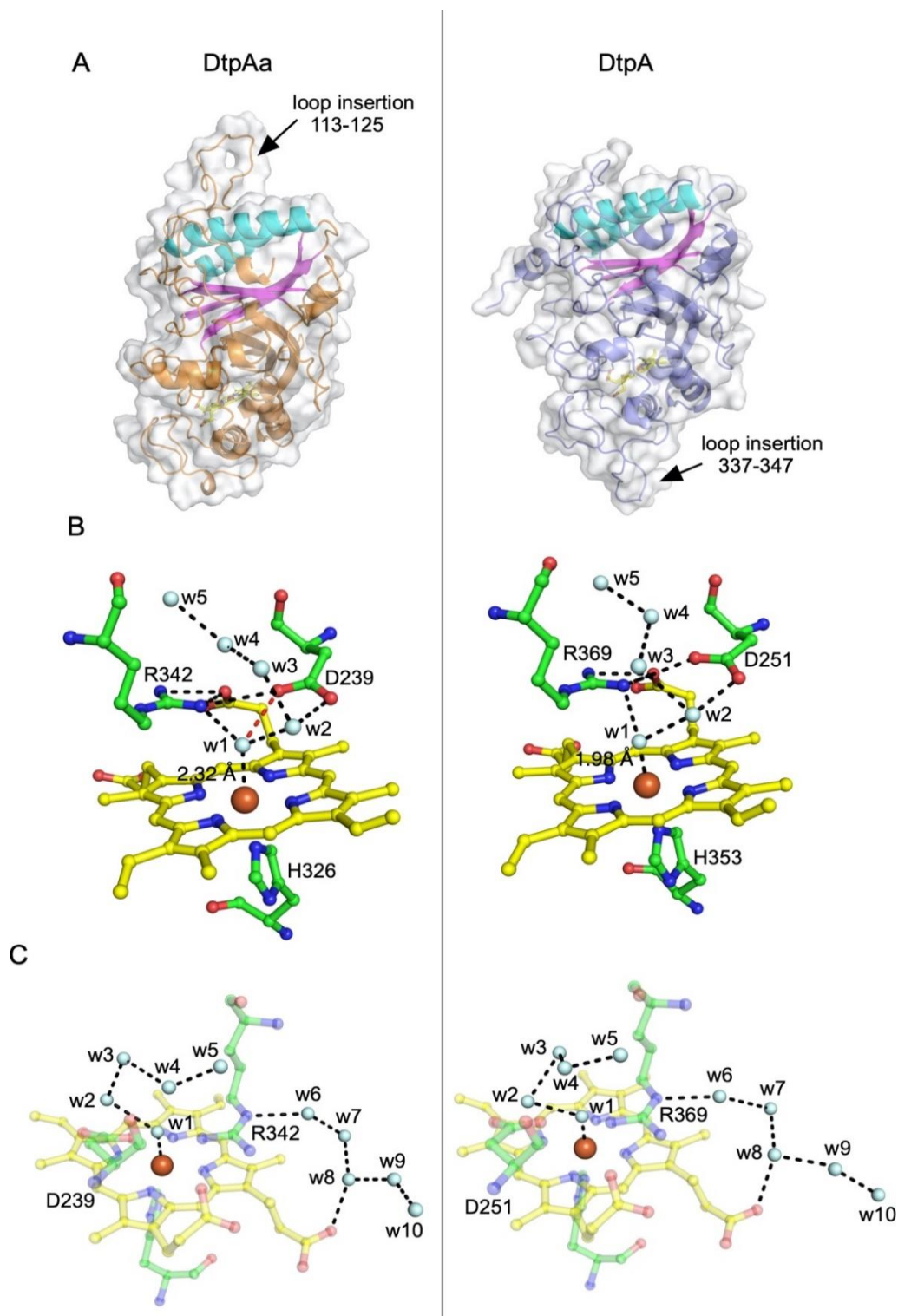


Figure 2.6. X-ray crystal structures determined at 100 K of DtpAa and DtpA (Chaplin *et al.*, 2019) in the ferric haem oxidation state. A) Cartoon of the overall structure and surface representation. The fold for one of the ferredoxin-like domains in each structure is highlighted. B) Haem pocket environment, with H₂O molecules shown as cyan spheres (w). C) Extended H₂O network originating in the distal haem pocket and connecting to the enzyme surface.

The electron-density map for DtpAa is consistent with the ferric haem being six-coordinate, with axial coordination from a proximal His residue, (His326 N^{δ1}-Fe bond $2.19 \pm 0.13 \text{ \AA}$) and a distal H₂O (w1) molecule (B-factor 12.6 \AA^2) (Figure 2.6B and 2.5). The distal Fe^{III}-OH₂ bond length ($2.32 \pm 0.13 \text{ \AA}$) is significantly longer in DtpAa compared to in DtpA ($1.98 \pm 0.096 \text{ \AA}$, B-factor 11.5 \AA^2), despite the ferric nature of the haem in both structures. The highly conserved distal haem pocket residues, Asp239 and Arg342, participate in several hydrogen-bonding (H-bonding) interactions, including to each other and in the case of Arg342 to the haem propionate-6 (Figure 2.6B and 2.5). Of particular note is that the O^{δ1} atom of Asp239 H-bonds (2.72 \AA) with w1 in the ferric DtpAa structure (red-dashed line Figure 2.6B). This H-bonding interaction is absent in ferric DtpA, where a distance of 4.15 \AA from the O^{δ1} atom of Asp251 and w1 is observed (Figure 2.6B).

In DtpAa a clear positional shift in the side chain of Asp239 towards the haem is noted, permitting the H-bonding interaction with w1, and may concomitantly assist in lengthening the Fe-OH₂ distal bond-length (Figure 2.5B). Therefore, in DtpAa, the distal H₂O is H-bonded by both the distal Asp and Arg residues (Figure 2.5B), with a shorter H-bond length between the Nⁿ¹ atom of Arg342 and w1 (2.77 \AA) compared to 3.01 \AA in DtpA. All other H-bonding interactions with Asp239 and Arg342 in DtpAa are mirrored in DtpA (Figure 2.5B).

The distal w1 forms the base of an extended H-bonded H₂O network reaching upwards from the distal pocket (Figure 2.5B); w1 is H-bonded to w2 (2.76 \AA ; B-factor 14.6 \AA^2), w2 H-bonded to w3 (2.52 \AA ; B-factor 19.5 \AA^2), w3 H-bonded to w4 (3.13 \AA ; B-factor 13.5 \AA^2) and w4 H-bonded to w5 (2.81 \AA ; B-factor 10.1 \AA^2). A similar H₂O network

is found in the ferric DtpA structure (Figure 2.5B), but it is notable that w3 and w4 occupy different spatial positions (Figure 2.5B) and have a significantly shorter H-bonding distance of 2.81 Å, compared to 3.10 Å in DtpAa. In both DtpAa and DtpA, w5 is positioned at a surface opening, that has dimensions sufficient to enable H₂O₂ to enter, but not bulky organic substrates such as synthetic dyes.

A second H-bonded H₂O channel leading from the distal side of the haem to the solvent exterior is present in ferric DtpAa (Figure 2.5C). The N^ε atom of Arg342 H-bonds with w6 (2.77 Å; B-factor 12.8 Å²), which is the start of a H-bonded H₂O chain that extends out perpendicular from the Arg342 side chain ending at w10 located at a second surface opening (Figure 2.5C). Within this H₂O network, w8 participates in a H-bonding interaction with the O^{δ2} atom (2.69 Å) of the haem propionate-7. Thus, both haem propionates participate in polar interactions that stem from the distal side of the haem. In ferric DtpA, an identical H-bonded H₂O channel is observed (Figure 2.5C). Therefore, both the distal Arg and Asp residues are central components of two extensive H-bonding H₂O networks in both these ferric A-type DyPs.

2.3.5. *The kinetics of Compound I formation in DtpAa*

Rapid mixing of H₂O₂ with ferric DtpAa was carried out using a stopped-flow spectrophotometer operating in diode-array mode. Spectral transitions on mixing with H₂O₂ were observed that are consistent with the presence of an intermediate species, in going from the ferric species to Compound II. At pH 7.0, global analysis of the full spectral data using a sequential mechanism of $a \rightarrow b \rightarrow c$ (*i.e.* a = ferric, b = intermediate and c = Compound II) reveals the spectrum of the intermediate species, which possesses features consistent with a Compound I ($[(\text{Fe}^{\text{IV}}=\text{O})\text{por}^{\bullet+}]$) species.

Notably, the Soret band displays ~ 50 % decrease in absorbance together with a blue shift, with additional wavelength features in the red region of the spectrum that correlate with the Compound I spectrum of DtpA (Table 2, Figure 2.7A and 2.7B). Figure 2.7A also depicts the kinetic traces at three wavelengths with their fits to the same model (*i.e.* $a \rightarrow b \rightarrow c$) and using the rate constants taken from the global fit (see Figure 2.8). The residuals to the fits illustrate the model used for global analysis adequately describes both kinetic and spectral data (inset Figure 2.7A inset). Thus stopped-flow kinetics confirms that Compound I is formed following addition of H_2O_2 , but rapidly decays to Compound II.

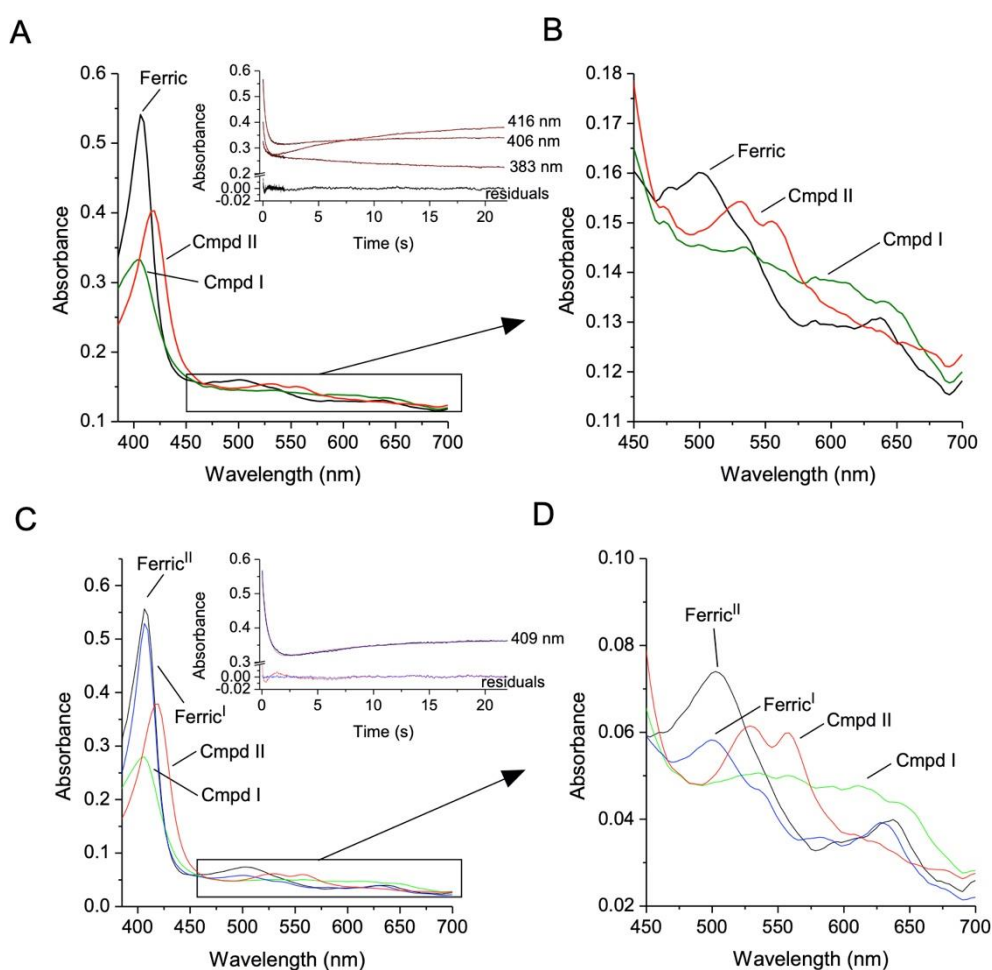


Figure 2.7. Detection of Compound I (Cmpd I) in DtpAa using stopped-flow absorption spectroscopy (25 °C). Spectra obtained from global fitting of the observed spectral transitions upon mixing H_2O_2 (62.5 μM) with ferric DtpAa (5 μM) at pH 7.0 (A and B) and at pH 5.0 (C and D) according to models described in the main text. The haem species identified by global analysis are labelled. Insets A and C show kinetic traces at the specified wavelengths along with their fits and residuals to models described in the text. The kinetic trace in the inset of (C) has been fitted to two models as indicated by the blue and red residuals.

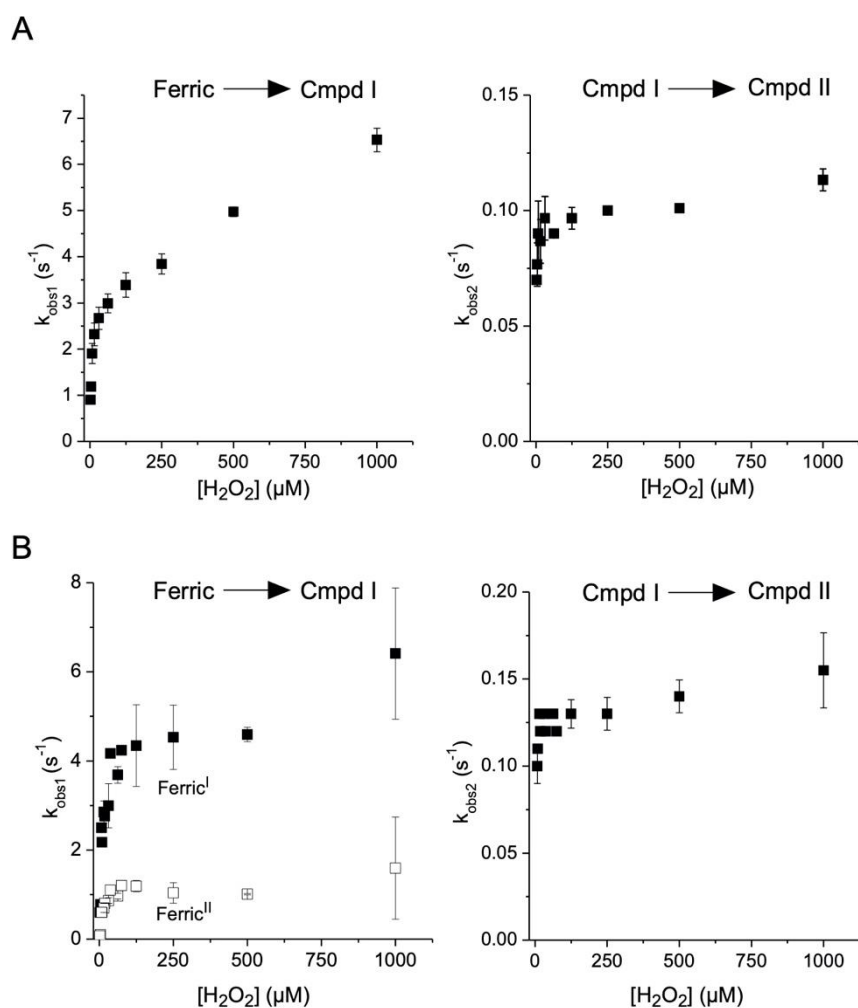


Figure 2.8. Observed pseudo-first order rate constants (k_{obs1} and k_{obs2}) obtained from global fitting of the spectral transitions for the reaction of DtpAa (5 μM) with increasing H₂O₂ concentrations at pH 7.0 (A) and pH 5.0 (B) at 25 °C. k_{obs1} is assigned to the formation of Compound I (Cmpd I) from the HS ferric species and k_{obs2} is assigned to the formation of Compound II (Cmpd II) from Compound I. At pH 5.0 two HS ferric species, Ferric^I and Ferric^{II} exist giving rise to two k_{obs1} rates.

Pseudo-first order rate constants for ferric to Compound I (k_{obs1}) and Compound I to Compound II (k_{obs2}) obtained from the global fitting are plotted as a function of increasing $[H_2O_2]$ in Figure 2.8A. For k_{obs1} a non-linear dependence on $[H_2O_2]$ for Compound I formation is observed, with a steep increase in k_{obs1} values at low $[H_2O_2]$, followed by a more gradual increase at higher $[H_2O_2]$ (Figure 2.8A). This behaviour is in stark contrast to DtpA, where a linear dependence on k_{obs1} with increasing $[H_2O_2]$ between 12.5 and 75 μM is observed at pH 7.0 enabling a second-order rate constant of $8.9 \times 10^6 M^{-1} s^{-1}$ to be determined (Chaplin *et al.*, 2017). The linear dependence of $[H_2O_2]$ therefore indicates for DtpA that the binding of H_2O_2 to the ferric haem is rate limiting Compound I formation. For k_{obs2} little dependence on $[H_2O_2]$ is observed (Figure 2.8B), yielding a limiting rate constant for the decay of Compound I to Compound II of $\sim 0.1 s^{-1}$.

At pH 5.0 the global analysis of the full spectral data required a different model to account for the spectral transitions observed. The data now imply the existence of two ferric species reacting at different rates with H_2O_2 to form an intermediate and therefore a model of $a \rightarrow c; b \rightarrow c; c \rightarrow d$ (*i.e.* $a = \text{ferric}^I$, $b = \text{ferric}^{II}$, $c = \text{intermediate}$ and $d = \text{Compound II}$) was used to yield the spectra shown in Figure and 2.7C and D. This kinetic model reveals that two ferric forms of DtpAa are present (ferric^I and ferric^{II} with a ratio of 50:60 *i.e.* ferric^I comprises 45% of the starting ferric DtpAa), with each form reacting with H_2O_2 at different rates to form a common intermediate assigned as Compound I, which then decays to Compound II (Figure 2.7C and 2.7D). The inset to Figure 2.7C shows a fit to the model $a \rightarrow c; b \rightarrow c; c \rightarrow d$ and to the simpler $a \rightarrow b \rightarrow c$ model (used at pH 7.0), with the accompanying residuals demonstrating that the

model incorporating two ferric forms (blue line inset Figure 2.7C) provides a more satisfactory description of the kinetics observed.

Pseudo-first order rate constants for Compound I formation obtained from the global fitting are plotted against $[\text{H}_2\text{O}_2]$ in Figure 2.8B. The k_{obs1} values for the two ferric species reveal an initial dependence on H_2O_2 concentration, with ferric^I exhibiting similar k_{obs1} values to those determined at pH 7.0, whereas Compound I formation from ferric^{II} is ~ 2 -times slower (Figure 2.7B). At higher H_2O_2 concentrations both k_{obs1} values become rate limited. The decay of Compound I to Compound II again displays little H_2O_2 concentration dependence with a k_{obs2} value of $\sim 0.15 \text{ s}^{-1}$ determined (Figure 2.8B). Overall, these results appear to suggest that the kinetics of Compound I formation in DtpAa are rate limited at low $[\text{H}_2\text{O}_2]$ by binding of H_2O_2 to the haem with a second, rate limit being observed at higher $[\text{H}_2\text{O}_2]$.

2.3.6. The pH dependence of Compound I formation in DtpA and DtpAa

The pH dependence on the rate of Compound I formation for both DtpAa and DtpA on reacting with H_2O_2 was explored (Figure 2.9A and 2.9B). For DtpAa a bell-shaped pH profile is observed with k_{obs1} values increasing between pH values 4 and 7, followed by decreasing k_{obs1} values between pH 7 and 10. This behaviour indicates that two ionisation processes are detected with apparent $\text{p}K_{\text{a1}}$ and $\text{p}K_{\text{a2}}$ values of 4.87 ± 0.15 and 8.19 ± 0.16 , respectively, determined from fitting the data in Figure 2.9A to a two proton ionisation equilibria equation (Equation 2.1)

$$k_{\text{obs1}} = k_0 + \frac{\Delta k_1(10^{\text{pH}-\text{p}K_{\text{a1}}}) + \Delta k_2(10^{2\text{pH}-\text{p}K_{\text{a1}}-\text{p}K_{\text{a2}}})}{1 + (10^{\text{pH}-\text{p}K_{\text{a1}}}) + (10^{2\text{pH}-\text{p}K_{\text{a1}}-\text{p}K_{\text{a2}}})} \quad (2.1)$$

where k_{obs1} is the observed pseudo-first order rate constant, k_0 rate of the protonated form at zero pH and, Δk is the difference in rate between protonated and unprotonated forms.

For DtpA the pH profile again reveals an increase in k_{obs1} values as the pH is increased from 4 to 6 leading to a plateau between pH 6 and 10 (Figure 2.9B). A fit of the data in Figure 2.9B to a single ionisation equilibrium equation yields an apparent pK_{a1} of 4.44 ± 0.15 . Thus, Compound I formation in both DtpA and DtpAa shares a common acidic ionisation equilibrium with a pK_{a} of ~ 4.5 , which could possibly be assigned to an ionisable protein residue. In this respect both DtpAa and DtpA possess an Asp residue in the distal haem pocket, that has been strongly implicated in acting as an acid-base catalyst across the DyP sub-families. Alternatively, the possibility exists that the pK_{a} is that of the haem bound H_2O_2 .

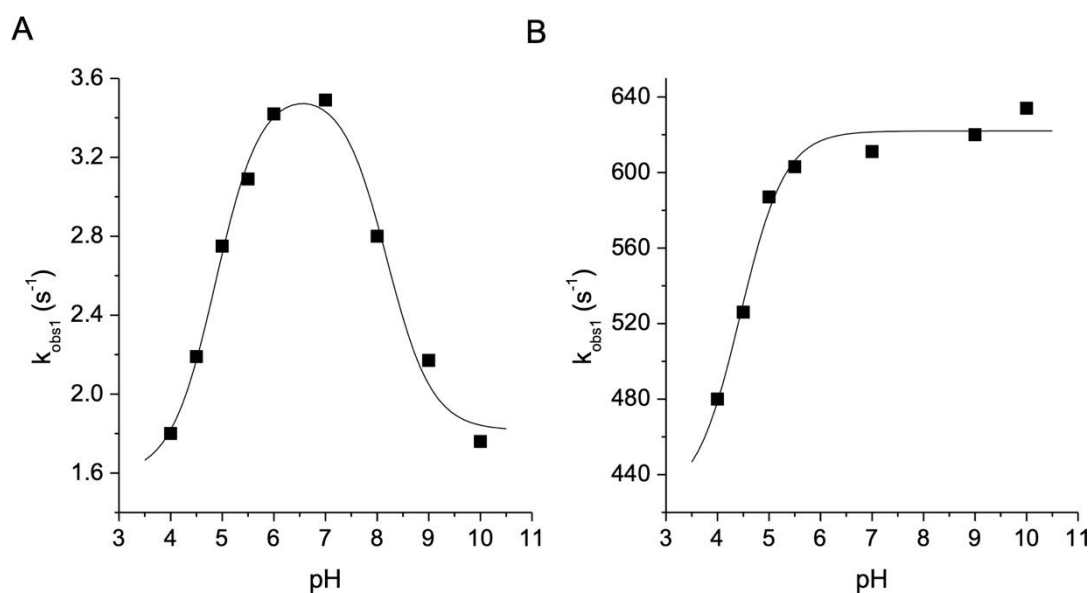


Figure 2.9. pH dependence profiles for the rate of Compound I formation in DtpAa (A) and DtpA (B) on reacting with a fixed concentration of H₂O₂. Pseudo-first order rate constants (k_{obs1}) were obtained from global fitting of the spectral transitions at a determined pH. For DtpAa (A) the data were fitted to a two-proton ionisation equilibria equation (Equation 2.1) and for DtpA (B) a single-proton ionisation equilibrium equation.

2.3.7. D₂O₂ as a mechanistic probe to study Compound I formation

Kinetic isotope effect (KIE) is the change in the reaction rate of a chemical reaction when one of the atoms in the reactants is replaced by one of its isotopes (Atkins, 2018). The reaction rate can be influenced by an isotopic exchange even if it is an atom of the solvent, rather than that of a reactant that has been exchanged for one of its isotopes. Such an effect is called kinetic solvent isotope effect (sKIE). The most common exchange studied in enzyme reaction mechanisms is from H₂O to D₂O. The sKIE is then described as ratio of rate constants for the reactions involving light (H₂O) and heavy (D₂O) solvent.

To investigate further the mechanism of Compound I formation, H₂O₂ was substituted with D₂O₂. As Compound I formation is associated with the breakage and formation of

an O-H bond, then using D₂O₂ will reveal if these steps are rate limiting. For these experiments both DtpA and DtpAa were exchanged into a D₂O buffer (*i.e.* the solvent used) and D₂O₂ was used rather than H₂O₂, therefore a kinetic isotope effect (KIE) instead of a solvent KIE (sKIE) is used to describe Compound I formation.

At pD 7.0 a linear dependence of k_{obs1} on increasing [D₂O₂] was observed with DtpA enabling a second-order rate constant (k_{D}) of $1.1 \pm 0.5 \times 10^7 \text{ M}^{-1}\text{s}^{-1}$ for Compound I formation to be determined (Figure 2.10A), which is identical within error to the value determined in H₂O ($k_{\text{H}} = 8.9 \pm 0.3 \times 10^6 \text{ M}^{-1}\text{s}^{-1}$) (Chaplin *et al.*, 2017). Thus, for DtpA the $k_{\text{H}}/k_{\text{D}} = 0.8$ (*i.e.* < 1) indicating no KIE. For DtpAa a similar kinetic profile with D₂O₂ as with H₂O₂ is observed (Figure 2.10B), but now the k_{obs1} values decrease with an average $k_{\text{obs1H}}/k_{\text{obs1D}} = 1.8$ indicating a KIE for DtpAa (Figure 2.10B). For k_{obs2} (decay of Compound I to Compound II) a limiting rate constant with D₂O₂ is observed as with H₂O₂ with the average $k_{\text{obs2H}}/k_{\text{obs2D}} = 0.9$ meaning no KIE (Figure 2.10C). Together, these results confirm that for DtpAa the rate determining step for Compound I formation is proton-transfer, following binding of H₂O₂ to the ferric haem, whereas for DtpA the absence of a KIE suggests that proton-transfer is faster than H₂O₂ binding.

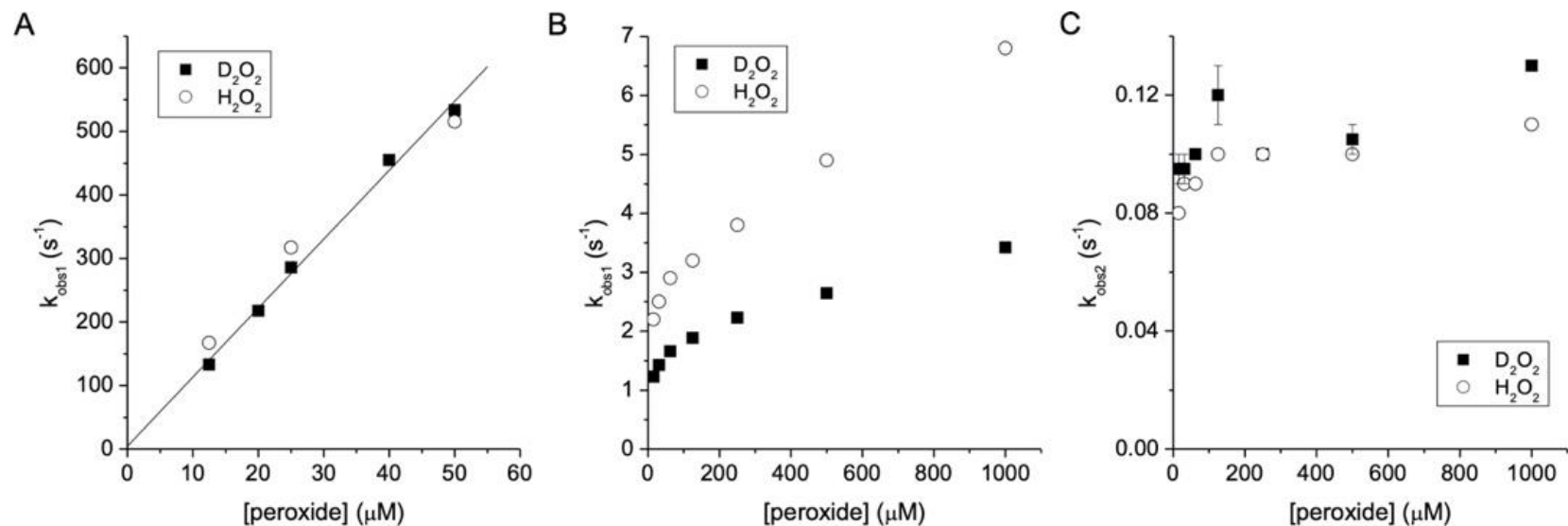


Figure 2.10. The KIE on the formation of Compound I and Compound II in DtpA and DtpAa at pD 7.0 and 25 °C A) Pseudo first-order rate constants (k_{obs1}) plotted against [D₂O₂] obtained from monitoring the formation of Compound I at 406 nm for DtpA (5 μM). The filled squares (D₂O₂) are fitted to a linear function to obtain a second-order rate constant, and the open circles represent data points at comparative [H₂O₂]. B and C) Pseudo-first order rate constants (k_{obs1} and k_{obs2}) obtained from global fitting of the spectral transitions for the reaction of DtpAa (5 μM) with increasing [D₂O₂] (filled squares) and comparative [H₂O₂] (open circles). k_{obs1} is assigned to the formation of Compound I and k_{obs2} is assigned to the decay of Compound I to Compound II.

2.3.8. Removal of the distal Asp in DtpAa and DtpA decreases the rate of Compound I formation

To address the role of the distal Asp in the mechanism of Compound I formation, the D251A and D239A variants of DtpA and DtpAa, respectively, were prepared. Addition of one-equivalent of H_2O_2 to the ferric form of either variant results in the appearance of a spectrum consistent with a Compound II species (Figure 2.11 and Table 2.2). Thus, in contrast with wild-type DtpA in which a Compound I spectrum forms and slowly decays back to the ferric form (Chaplin *et al.*, 2017), the removal of the distal Asp may suggest destabilisation of Compound I.

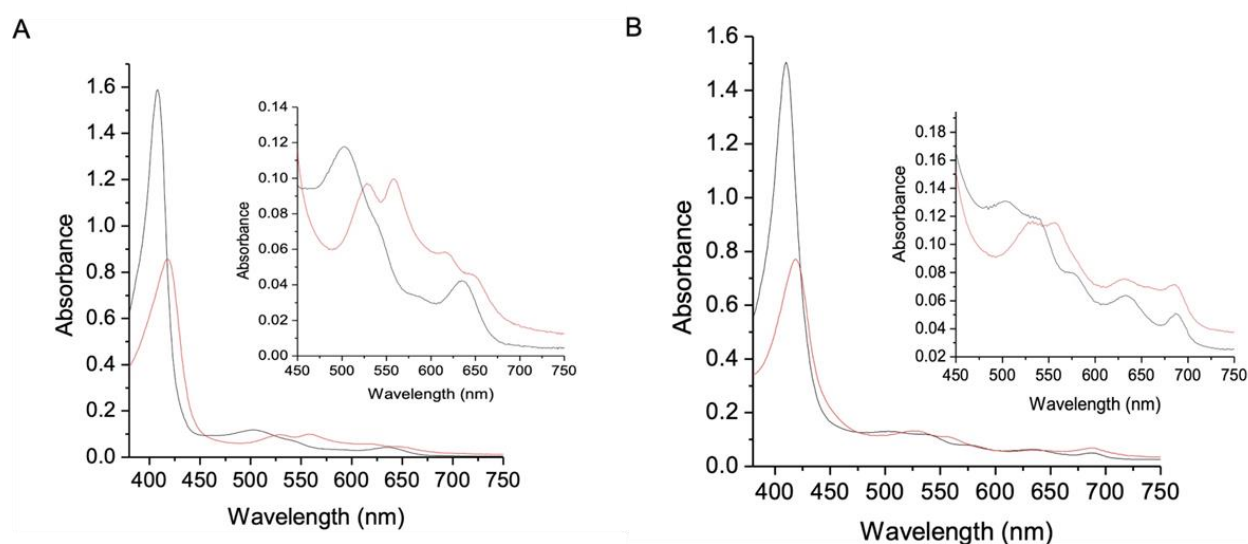


Figure 2.11: Absorbance spectra of the Asp variants at pH 7.0. A) The D251A DtpA variant and B) the D239A DtpAa variant. The black spectra indicates the ferric form and the red spectra following addition of one molar equivalent of H_2O_2 . Insets show a close-up of the Q-bands.

Stopped-flow kinetics revealed spectral transitions on mixing with H_2O_2 that were consistent with the presence of an intermediate species assigned as Compound I before

decaying to Compound II (Figure 2.11). It is notable that for both Asp variants the k_{obs1} values are on the order of a few per second and therefore comparable to wild-type DtpAa. At pH 5.0 the D251A variant displays a linear dependence of k_{obs1} values with $[\text{H}_2\text{O}_2]$ yielding a second-order rate constant of $4.27 \pm 0.07 \times 10^3 \text{ M}^{-1} \text{ s}^{-1}$, 4-orders of magnitude slower than wild-type DtpA and thus providing a clear indication that the distal Asp in DtpA accelerates the reaction with H_2O_2 . For k_{obs2} little dependence on $[\text{H}_2\text{O}_2]$ is observed (Figure 2.12B), yielding a limiting rate constant for the decay of Compound I to Compound II of $\sim 0.08 \text{ s}^{-1}$, a kinetic parameter not possible to determine directly for wild-type DtpA, but maybe inferred to be $\sim 0.005 \text{ s}^{-1}$ by using a previously reported value of $t_{1/2} = 2.5 \text{ min}$ for the decay of Compound I to the form the ferric species in a mechanism in which intermediate Compound II is populated at a low level (Chaplin *et al.*, 2017).

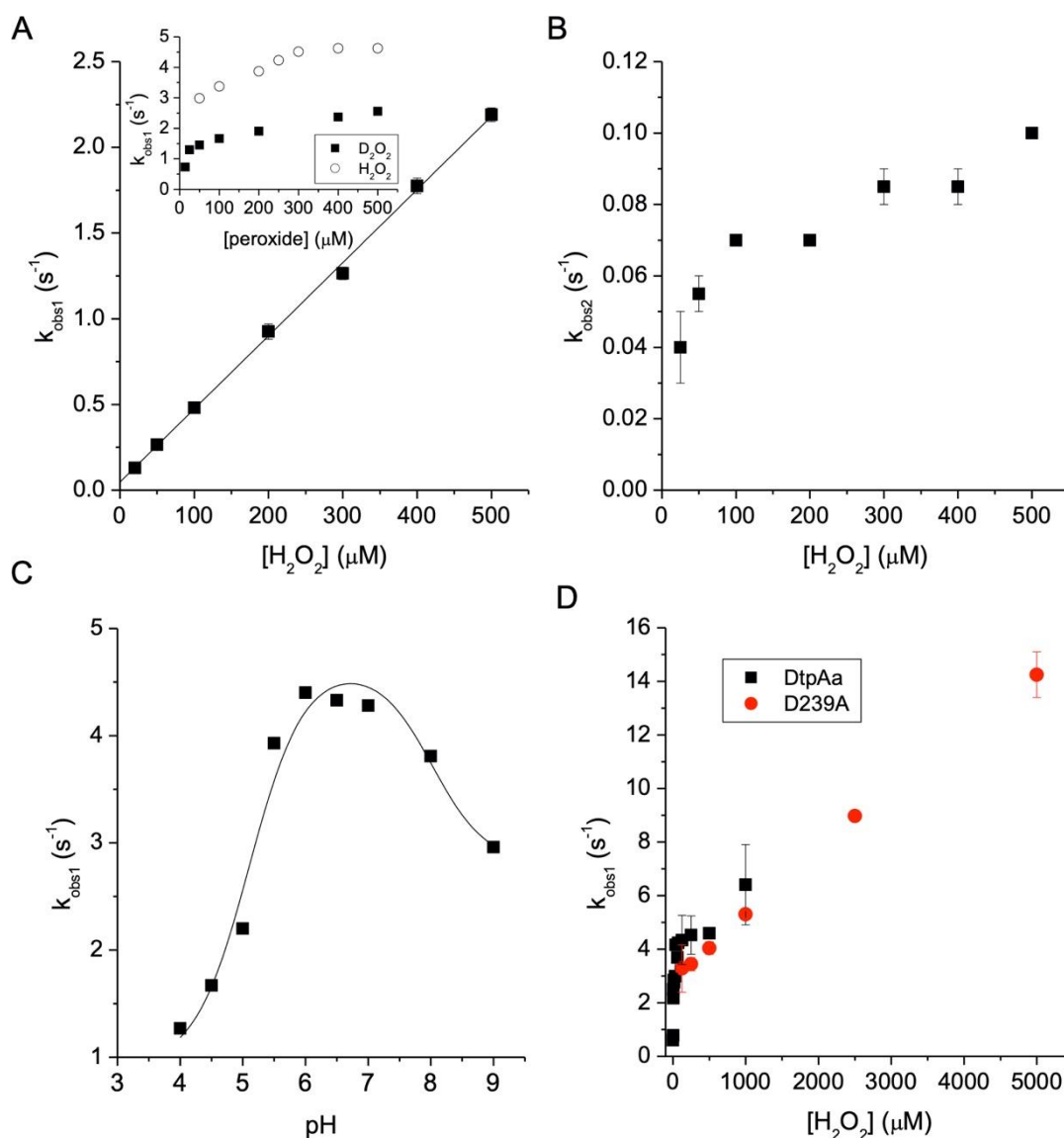


Figure 2.12. Kinetics of Compound I formation for the distal Asp variants of DtpA and DtpAa at 25 °C. Pseudo first-order rate constants (k_{obs1} and k_{obs2}) were obtained from global fitting of the spectral transitions for the reaction of H_2O_2 or D_2O_2 . A) Plot of k_{obs1} values against $[\text{H}_2\text{O}_2]$ for the D251A variant of DtpA (5 μM) at pH 5.0 and inset pH 7.0. The data points are fitted to a linear function to obtain a second-order rate constant for Compound I formation. B) The k_{obs2} values plotted as a function of $[\text{H}_2\text{O}_2]$ for the decay of Compound I to Compound II in the D251A variant of DtpA at pH 5.0. C) The pH dependence of Compound I formation for the D251A variant using a fixed $[\text{H}_2\text{O}_2]$ of 500 μM , with the data fitted to Equation 2.1. D) Overlay of the k_{obs1} values for the D239A variant and wild-type DtpAa at pH 5.0.

In both the wild-type DtpA and the D251A variant, the rate of Compound I formation is greater than the rate of its decay (DtpA with 50 μM H_2O_2 $k_{\text{obs1}}/k_{\text{obs2}} = 5 \times 10^4$ and for the D251A variant 500 μM H_2O_2 $k_{\text{obs1}}/k_{\text{obs2}} = 25$). The maximal fraction of the total protein appearing as the intermediate Compound I, $[\text{CmpdI}]_{\text{max}}$, may be calculated from equation 2.2

$$[\text{CmpdI}]_{\text{max}} = \left(\frac{k_{\text{obs2}}}{k_{\text{obs1}}} \right)^{\left(\frac{k_{\text{obs2}}}{k_{\text{obs1}} - k_{\text{obs2}}} \right)} \quad (2.2)$$

Therefore, for DtpA, the $k_{\text{obs1}}/k_{\text{obs2}}$ ratio shows that Compound I is essentially maximally formed, *i.e.* 100% of the enzyme is in this form prior to decay, while for the D251A variant the $k_{\text{obs1}}/k_{\text{obs2}}$ shows that Compound I maximally comprises 88% of the enzyme. Thus, in both enzymes, Compound I is essentially fully formed and thereafter decays, in the D251A variant 16-fold faster than in the wild-type DtpA, consistent with our suggestion that removal of the distal Asp residue destabilises Compound I in the D251A variant.

At pH 7.0, the k_{obs1} values for the D251A variant become rate limited at high $[\text{H}_2\text{O}_2]$, and substitution with D_2O_2 gives an average $k_{\text{obs1H}}/k_{\text{obs1D}} = 2.0$ indicating a KIE (inset Figure 2.12A). The pH dependence of Compound I formation for the D251A variant is shown in Figure 2.12C, and notably displays two ionisation equilibria for which a $\text{p}K_{\text{a1}} = 5.10 \pm 0.21$ and $\text{p}K_{\text{a2}} = 8.02 \pm 0.50$ are calculated. Thus, in the absence of the distal Asp an acidic ionisation equilibrium remains with a $\text{p}K_{\text{a}}$ comparable to that of wild-type DtpA, and a second ionisation equilibrium is apparent that was not present in the wild-type enzyme.

For the D239A variant of DtpAa, the kinetics of Compound I formation could be followed at pH 5.0 but not at pH 7.0 owing to the rapid decay of Compound I to Compound II resulting in no clear assignment of an intermediate with Compound I spectral features. Therefore, a complete pH profile for Compound I formation could not be determined for the D239A DtpAa variant. However, for pH values between 5.0 and 6.0, where Compound I could be detected, k_{obs1} values show an increase as noted in DtpA and its D251A variant as well as wild-type DtpAa. At pH 5.0 the k_{obs1} values are of a similar order to wild-type DtpAa and the kinetic profile is strongly comparable to the wild-type enzyme (Figure 2.12D). Thus, it can be concluded that in DtpAa removal of the distal Asp is of little consequence to the kinetics of Compound I formation.

2. 4. Discussion

Haem peroxidases are typically crystallised in the ferric resting state but are extremely susceptible to X-ray driven reduction during crystallographic data collection. Amongst the more than 50 deposited structural coordinates of DyP members in the PDB, there is a dearth of supporting information regarding the haem oxidation state for these depositions (Chaplin *et al.*, 2019). The absence of this information does not therefore allow for confident comparison of haem pocket structures to be made within the DyP sub-families and makes structure guided mechanistic insights problematic. As part of this Chapter, the cryo-cooled (100 K) X-ray structure of DtpAa has been unambiguously determined to be in the ferric haem oxidation state, thus enabling comparison with the cryo-cooled ferric DtpA structure (Chaplin *et al.*, 2019) and also the room temperature XFEL structure of ferric DtpAa (Ebrahim *et al.*, 2019).

In both the XFEL and 100 K DtpAa structures the bond-length for the haem bound distal H₂O molecule is significantly longer than in the ferric DtpA structure (Figure 2.5). Notably, the side chain position of the distal Asp in both DtpAa structures is identical, but differs significantly from DtpA where the side chain O^{δ1/2} atoms are further away from the distal haem face and do not participate in a H-bond interaction with the haem bound distal H₂O molecule, which is the case in ferric DtpAa (Figure 2.13). This subtle change in side chain position has significant consequences for H₂O₂ reactivity and will be discussed further. Both DtpAa structures have an extensive network of distal H-bonded H₂O networks arranged around the Asp-Arg couple, which are superimposable and we therefore conclude that no temperature dependent haem pocket changes in the ferric DtpAa structures are apparent.

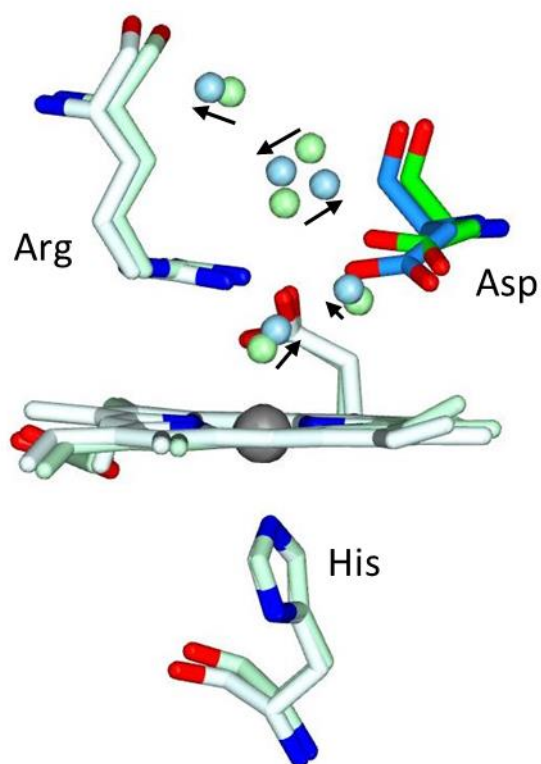


Figure 2.13. Superposition of the haem environment in DtpA (light green and green) and DtpAa (light blue and blue) reveals a slight shift of the distal Asp residue. The distal Asp is accentuated in both A-types with darker colour. Water molecules are depicted as spheres, with green spheres belonging to the DtpA and blue to the DtpAa. Black arrows indicate shift of position of water molecules from DtpA to DtpAa.

A mechanism which can provide a consistent picture of Compound I formation in DtpAa and DtpA is depicted in Figure 2.14. The mechanism comprises six steps. Step

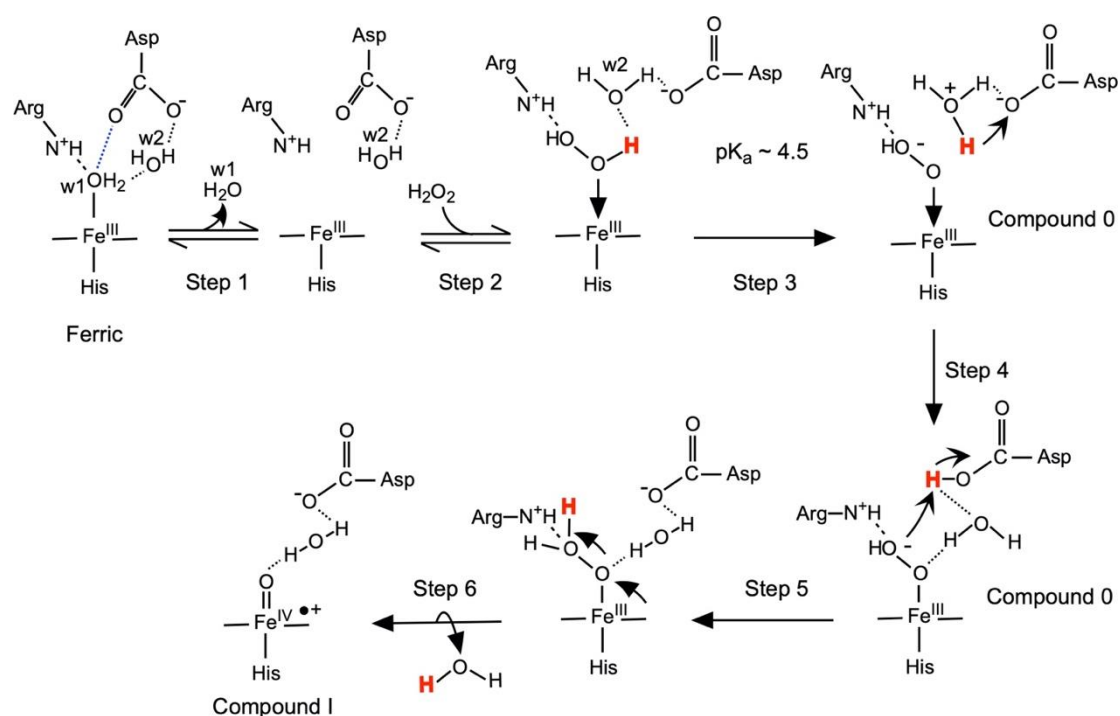


Figure 2.14. Mechanism of Compound I formation in DtpA and DtpAa. For a description of the individual steps see the main text. The H^α proton of H₂O₂ is depicted in red, and the blue H-bond between the distal Asp and the haem bound H₂O molecule (w1) is only present in ferric DtpAa.

1 is the dissociation of the distal H₂O molecule from the ferric haem, step 2 is the second order binding of peroxide to the ferric haem to form the neutral Compound 0 complex (Fe^{III}-OH^α-OH^β), step 3 is the dissociation of the H^α proton to form the anionic Compound 0 complex (Fe^{III}-O^α-OH^β), step 4 is the association of the H^α proton with the distal Asp, step 5 comprises the movement of the H^α proton from the Asp to the OH^β and step 6 is the heterolysis of the O-O bond and electron transfer to form Compound I. Within the framework of the structural, kinetic and thermodynamic results described in the Results section, the mechanism depicted in Figure 2.14 forms

the basis for the following discussion on the different kinetic behaviours observed for DtpA and DtpAa upon reaction with H₂O₂.

By validating the ferric X-ray structures of both DtpAa and DtpA, the requirement for step 1 is accounted for. Both enzymes display an extensive network of H-bonded H₂O molecules that communicate with the distal Asp-Arg couple (Figure 2.5). For H₂O₂ to bind (step 2) the distal haem bound H₂O must be displaced. In DtpA the linear dependence of the rate of Compound I formation on [H₂O₂] is an indication that the rate determining step in our mechanism of Compound I formation is the binding of H₂O₂ to the ferric haem (step 2). As binding of H₂O₂ to DtpA is rapid, this indicates that the ferric haem site is labile, *i.e.* the H₂O dissociation (step 1) does not impede the binding of H₂O₂ (step 2). Were the preceding H₂O dissociation step to be rate limiting, there would be no linear dependency of the rate constant on H₂O₂ concentration. Replacement of H₂O₂ with D₂O₂ revealed no KIE and thus indicates that proton-transfer (steps 4 and 5) is much faster than H₂O₂ binding (step 2). Furthermore, the data show that the rate of Compound I formation in both DtpA and DtpAa is pH dependent. Both enzymes share an ionisation equilibrium with an apparent pK_a of ~4.5. Notably, an acidic ionisation process is also observed in the distal Asp variant of DtpA (and can be inferred for the distal Asp variant of DtpAa), suggesting that the observed pK_a cannot be attributed to the distal Asp. In this respect it has been reported that binding of H₂O₂ to the ferric haem in peroxidases to form the Fe^{III}-OH^α-OH^β complex, promotes the ionisation of H₂O₂ by decreasing the pK_a of the free H₂O₂ from ~11.5 to ~5.5 in the haem bound state (Erman *et al.*, 1993; Rodriguez-Lopez *et al.*, 2001). Such a decrease in the pK_a is consistent with a simple calculation of $\Delta G_{el} = 1347(q_1q_2)/\epsilon D$, where ΔG_{el} is the electrostatic interaction free energy (kJ/mol at 298 K), q₁ and q₂ are

the charges on the iron porphyrin and the proton (unity in both cases), ϵ is the appropriate dielectric constants and D is distance of the charges in Å (a value of 2 Å has been used) (Schulz and Schirmer, 1979). Moore suggests a reasonable value for ϵD is approximately 40 (Moore, 1983). Given this, ΔG_{el} is calculated to be 34 kJ/mol, which equates to a change in pK_a of 6 pH units. Thus, a decrease in the pK_a of H_2O_2 from 11.5 to 5.5 on binding to the haem is consistent with theoretical calculations. Therefore, the acidic pK_a observed in the present studies is attributed to the deprotonation/protonation of the H_2O_2 bound to the haem, which is common to all the enzymes studied. Incidentally, two recent studies with B-type DyPs have indicated that the pK_a of the distal Asp is $\ll 4$ (Pfanzagl *et al.*, 2018; Shrestha *et al.*, 2017), and therefore in the mechanism Asp is depicted as being in an anionic state (Figure 2.14). However, to account for the experimental observations, that an acidic ionisation process occurs for both A-type DyPs with and without the distal Asp residue, the mechanism proposes that the H^α proton of the $Fe^{III}-OH^\alpha-OH^\beta$ complex deprotonates to first form a hydronium ion (step 3). Subsequently, in the case of DtpA, the H^α proton is then transferred from the hydronium ion onto the distal Asp transiently (step 4), followed by transfer to the OH^β (step 5) prior to heterolysis of the O-O bond. As noted by the absence of a KIE, these proton-transfer steps in DtpA are highly optimised and are faster than the initial H_2O_2 binding.

For the D251A variant of DtpA, the linear dependence on the rate of Compound I formation at pH 5.0 with $[H_2O_2]$ (Figure 2.12A) is a further indication that the rate determining step is the binding of H_2O_2 to the ferric haem (step 2). The second-order rate constant is now 2000-fold lower than for wild-type DtpA, suggesting that the distal Asp is important for facilitating favourable H_2O_2 binding to form the initial Fe^{III} -

$\text{OH}^\alpha\text{--OH}^\beta$ complex (step 2). The slightly elevated $\text{p}K_a$ for the H^α in the $\text{Fe}^{\text{III}}\text{--OH}^\alpha\text{--OH}^\beta$ complex in the absence of the Asp, as compared to the wild-type enzyme (5.10 vs 4.44, respectively), serves to illustrate that the distal Asp also tunes the ionisation properties of the haem bound H_2O_2 . At pH 5.0, proton-transfer in the D251A variant remains efficient *i.e.* faster than H_2O_2 binding, despite the absence of the Asp. In DtpA and DtpAa, two extensive networks of H-bonded H_2O molecules that communicate with the Asp and the Arg residue are a dominating feature of the distal pocket (Figure 2.5B and C). In other peroxidases such as APX or CcP (Bonagura *et al.*, 2003; Sharp *et al.*, 2003), the distal pocket H_2O network is notably less extensive. It is well documented that H_2O networks in proteins can facilitate proton transfer (Ishikita and Saito, 2014). Recent insights into the contribution of H_2O networks to proton movement/transfer have highlighted the importance of the directionality of the H-bonded H_2O network, *i.e.* chains of H_2O molecules linked in donor-acceptor configurations that are highly favoured for proton-transfer (Hassanali *et al.*, 2013). For example, a recent work stresses the importance of a chain of water molecules in APX that is connected to the surface (Kwon *et al.*, 2020). These water molecules are not rigid, they can adjust slightly in both orientation and location, creating an additional path for protons moving into the active site and demonstrating the complexity and significance of such channels (Kwon *et al.*, 2020). In the absence of the Asp and w2, for the D251A variant steps 4 and 5 in the mechanism still occur but the ‘substitute’ for w2 in the variant is not optimally configured for proton-transfer from the hydronium ion to the OH^β , but nevertheless is faster than H_2O_2 binding at pH 5.0 (step 2). At pH 7.0, the $k_{\text{obs}1}$ for Compound I formation in the D251A variant approaches a rate limit, indicating that proton-transfer is becoming rate limiting, confirmed by substitution with D_2O_2 . Thus, in the D251A variant, whether H_2O_2 binding or proton-transfer is rate limiting is finely

balanced and this balance can be perturbed through changes in pH or substitution by D_2O_2 .

For DtpAa, the kinetics observed are considerably different from those for DtpA. Compound I formation in DtpAa appears to be initially $[H_2O_2]$ dependent, indicating that step 2 in the mechanism is rate limiting. However, as $[H_2O_2]$ increases, the rate limit transfers to step 4 and 5 (*i.e.* proton-transfer), which is corroborated upon substituting H_2O_2 with D_2O_2 (Figure 2.10B). Thus, for DtpAa as noted for the D251A DtpA variant, there appears to be a fine balance in the kinetic phases that distinguish the events determining the rate limiting steps in the mechanism of Compound I formation. Furthermore, the dependence of k_{obs1} values at low $[H_2O_2]$, when H_2O_2 binding may be considered as being rate limiting for DtpAa, are now a few per second, ~100-fold lower than for DtpA, leading to the conclusion that DtpAa is a poor peroxidase. In fact the k_{obs1} values for DtpAa are comparable with the D251A variant of DtpA and the D239A variant of DtpAa, revealing that even when the distal Asp is present, the rate of Compound I formation is clearly suppressed compared to DtpA. Why might this be? The structural data reveal a subtle positional change of the distal Asp side chain in DtpAa (Figure 2.13), whereby it encroaches towards the distal haem face enabling a H-bond interaction between the haem bound H_2O molecule and the $O^{\delta 1}$ atom of the Asp (Figure 2.5). Now, the haem bound H_2O molecule in DtpAa has an additional interaction compared to DtpA, where despite the shorter $Fe^{III}-OH_2$ bond length, the absence of an additional constraint imposed directly by the distal Asp makes an argument for a more labile haem bound H_2O in DtpA. Therefore, at low $[H_2O_2]$, when H_2O_2 binding may be considered as being rate limiting for DtpAa, the much decreased k_{obs1} values compared to DtpA, could arise as a consequence of a decreased

lability of the distal haem bound H₂O in DtpAa, resulting in the rate being limited by the H₂O dissociation (step 1). However, as noted, low $k_{\text{obs}1}$ values are also observed for both Asp variants, where although no structural information is available to inform whether a haem bound water is present, the absence of the Asp, makes the lability of the H₂O argument less compelling. A further possibility to consider is that the repositioning of the Asp in DtpAa imposes steric constraints, that could lead to hindering the rate of H₂O₂ binding and its stabilisation in the Fe^{III}-OH^α-OH^β complex and decrease the efficiency of (rapid) proton-transfer (steps 4 and 5) through the Asp side chain not being optimally orientated to ensure such transfer. The binding of H₂O₂ to the ferric haem is decreased in the H42L variant of HRP, which has been explained through steric impediment of the Leu side chain and importantly for the stringent requirement of H-bonding between the distal His42 and the Fe^{III}-OH^α-OH^β complex (Rodriguez-Lopez *et al.*, 2001). Thus, the Asp in DtpAa possibly impedes optimal stabilisation of the Fe^{III}-OH^α-OH^β complex and optimal proton-transfer (steps 4 and 5), whereas in DtpA the Asp position is optimised for rapid H₂O₂ binding and proton-transfer. The similarity of rates with the Asp variants supports this proposal. Therefore, the structural repositioning of the distal Asp in DtpAa tips the balance between rate limiting steps from H₂O₂ binding to proton-transfer.

Comparison of the pH dependencies of $k_{\text{obs}1}$ for DtpA, DtpAa and the D251A variant of DtpA, reveal significant differences above pH 7.0. For DtpA, the rate constant is pH independent above pH 7.0 indicating that the rate limit remains H₂O₂ binding and proton transfer is rapid and efficient, suggesting that the finely tuned structure within the haem pocket that delivers the proton for O-O scission remains intact. In the case of DtpAa, in which as discussed the Asp is not optimally positioned for proton-transfer,

above pH 7.0 a second ionisation equilibrium with a pK_a of 8.19 is observed. Similarly, the DtpA D251A variant displays a second ionisation equilibrium with a pK_a of 8.0, which is not the case for the wild-type DtpA. Both DtpAa and the DtpA D251A variant exhibit a KIE showing that proton-transfer is rate limiting and thus the distal pocket is not tuned for optimal proton movement as it is in DtpA. Thus, where a KIE is seen, an ionisation process above pH 7.0 is observed. This may arise from an ionisable group that competes for the hydronium ion proton and thus decreases the fraction of the enzyme entering the productive route to Compound I. In DtpA this postulated group is unable to compete in this manner because of the finely tuned architecture of the pocket as discussed above.

In conclusion, a common mechanism for Compound I formation in two A-type DyPs is influenced by a subtle structural change in the distal haem pocket, which affects the steric approach of H_2O_2 and the way protons are moved in the haem pocket. Remarkably, this difference would appear to account for DtpA reacting rapidly and efficiently with H_2O_2 as opposed to the extremely poor reactivity for DtpAa. Furthermore, the study of these enzymes implies that the pH dependency observed in the acid region is determined not by an ionisable protein residue(s) but by the pK_a of the haem bound peroxide. From a functional perspective these findings serve to advance the notion that not all DyP members possess efficient peroxidase reactivity despite the fold and architecture of the haem pocket being similar. As a corollary to this notion, DtpA will therefore be the dominant sensor of H_2O_2 in *S. lividans*, whereas a function, other than as a peroxidase for DtpAa, awaits elucidation.

Chapter Three

An Electron Paramagnetic Resonance spectroscopy study to investigate reaction of DtpA from *Streptomyces lividans* with H₂O₂

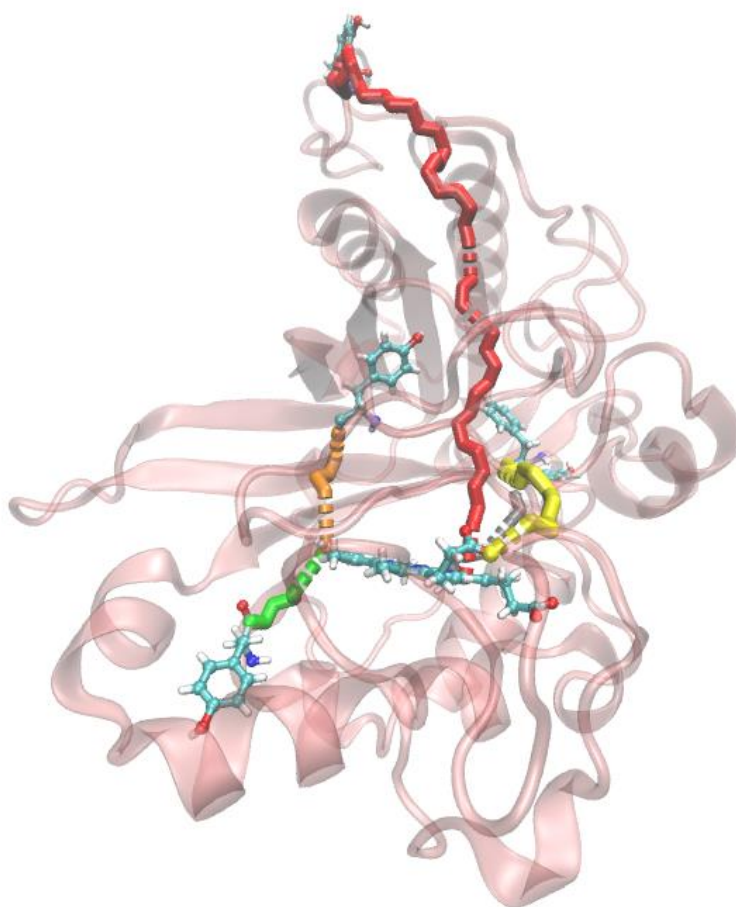


Figure 3. Predicted electron transfer pathways in DtpAa.

Some of the results presented in this Chapter have been published in:

M. Lučić, A. K. Chaplin, T. Moreno-Chicano, F. S. N. Dworkowski, M. T. Wilson, D. A. Svistunenko, M. A. Hough and J. A. R. Worrall A subtle structural change in the distal haem pocket has a remarkable effect on tuning hydrogen peroxide reactivity in dye decolourising peroxidases from *Streptomyces lividans*. *Dalton Transactions*, 2020, 49, 1620-1636.

3.1. Introduction

This Chapter focuses on using Electron Paramagnetic Resonance (EPR) spectroscopy to explore and assign the paramagnetic species that form upon reaction of DtpAa with H₂O₂. The transient paramagnetic species detected in haem peroxidases following addition of H₂O₂ often include the Compound I intermediate in which the porphyrin is oxidised ($[\text{Fe}^{\text{IV}}=\text{O-por}\cdot]^+$), Compound ES, as identified in CcP in which a ferryl and a tryptophan radical form ($[\text{Fe}^{\text{IV}}=\text{O-Trp}\cdot]^+$), as well as Compound II species whereby an internal the one-electron reduction of Compound I occurs through oxidation of a nearby tyrosine or tryptophan to form a tyrosyl or tryptophanyl radicals. Redox-active Tyr and Trp residues have an important role in transfer of electrons over large distances ($>30 \text{ \AA}$) in many redox enzymes where they act as an intermediate electron donors or acceptors (Dempsey *et al.*, 2010). In haem containing Cytochrome P450s, they can form “chains” connecting the haem with protein surface. These chains can have a catalytic role and be implicated in electron transfer (ET) pathway between the haem and a reductant (substrate) (Chaplin *et al.*, 2019) and/or form a radical escape route to protect the enzyme from oxidative stress caused by formation of highly oxidising redox cofactors such as the ferryl haem. In DyPs, access to the haem site is too restricted for bulky substrates, such as dyes, to be oxidized (Strittmatter *et al.*, 2013). Thus a mechanism for oxidation of substrates that proceeds through long-range ET from surface sites has been proposed (Strittmatter *et al.*, 2013). In DtpA an entry port for ET from a substrate to the haem has been identified as tyrosyl radical on Y374. However, sequence alignment of DtpA and DtpAa indicates that Y374 is substituted by Phe in DtpAa (Figure 2.1). This chapter therefore investigates alternative ET pathways in DtpAa.

3.2. Experimental procedures

3.2.1. Site-directed mutagenesis of *DtpAa*

A pET28*adtpAa* vector served as the template for site-directed mutagenesis using the QuikChange protocol (Stratagene). The following forward and reverse primers were used to create Y345F and Y345F/F347Y (DM) mutants:

Y345F-F 5'-GCTGCGCCGCGGCTTCTCCTTCACCGACGGCA-3',

Y345F-R 5'-TGCCGTCGGTGAAGGAGAAGCCGCGGGCGCAGC-3',

DM-F 5'-GCTGCGCCGCGGCTTCTCCTATAACCGACGGCA-3',

DM-R 5'-TGCCGTCGGTATAGGAGAAGCCGCGGGCGCAGC-3'.

A PCR mix consisting of the respective primers (75 ng/μL), the template (15 ng/μL), 10 mM dNTPs (Fermentas), *Pyrococcus furiosus* (*Pfu*) Turbo polymerase (Agilent), 10 x *Pfu* buffer (Agilent), 8% DMSO and deionised H₂O was prepared and subjected to the following PCR cycle; 95 °C for 3 min; 16 cycles of 95 °C for 1 min, 58 °C for 1 min and 72 °C for 8 min; 72 °C for 15 min. Clones were corroborated for the presence of the desired mutation by DNA sequencing (Eurofins).

3.2.2. Over-expression and purification of *DtpAa*

DtpAa was over-expressed in *Escherichia coli* BL21(DE3) cells and purified as reported in Chapter 2. Following purification, *DtpAa* was stored in -20 °C in 50 mM sodium acetate, 150 mM NaCl, pH 5.0. For experiments carried out at pH 7.0, *DtpAa* was exchanged into a desired buffer using a PD-10 column (Generon). The Y345F and

DM variants were over-expressed and purified in an identical manner as the WT DtpAa.

3.2.3. Preparation of DtpAa time course samples for EPR measurements

Time series of DtpAa (WT and the variants) samples following H₂O₂ addition were prepared in two ways. The first procedure required addition of a small volume aliquot of a stock H₂O₂ solution to a much greater volume of 40 μM DtpAa sample to give a 1:10 ratio of final concentrations (DtpAa:H₂O₂), from which aliquots were drawn and frozen in methanol kept on dry ice (~195 K). This method provided the freezing time (*i.e.* the reaction time) from 11 s and upwards. The second procedure to enable sub 10 s sample preparation required the stock H₂O₂ solution to be inserted by a Hamilton syringe into the tip of a plastic tubing connected at the other end to another syringe. Thus, the H₂O₂ loaded tubing was then used to draw in a DtpAa sample preloaded to an EPR tube rapidly followed by releasing the mixture back to the EPR tube and frozen in the methanol. This method provided freezing times from 4 s.

3.2.4. EPR spectroscopy and simulation

Wilmad SQ EPR tubes (Wilmad Glass, Buena, NJ) with OD = 4.05 ± 0.07 mm and ID = 3.12 ± 0.04 mm (mean \pm range) were used. The same peroxidase solution frozen in a set of these tubes yielded very similar intensities of EPR signals (ferric haem); with only ~1–3% random error. In total, two sets of time series samples were prepared for WT DtpAa and one for each of the Tyr variants. The first series of DtpAa EPR spectra was measured on a Bruker EMX EPR spectrometer. For the second series of WT DtpAa, and both Tyr variants all EPR spectra were measured on a Bruker ELEXSYS E500 EPR spectrometer. Both EPR spectrometers were operating in continuous wave

(CW) regime, at X-band (9 GHz microwave frequency), and 100 kHz field modulation frequency. An Oxford Instruments liquid helium system were used to measure the low-temperature (10 K) EPR spectra. EPR spectra of a blank sample (frozen water) measured at the same set of instrumental conditions were subtracted from the spectra to eliminate the background baseline EPR signal. Spectra deconvolution and measurements of the intensities of spectral components in the first time dependence set of DtpAa samples were performed by using the procedure of spectra subtraction with variable coefficient (Svistunenko *et al.*, 2006). Quantitative estimates of the concentrations of the paramagnetic centres were performed by comparison of the second integrals of either the simulated EPR signals (high-spin (HS) ferric forms) or extracted spectral components (four signals in $g=2$ region) with a reference to known total concentration of the ferric haem in the sample. The simulations and spectra extractions were performed by Dr. Dimitri Svistunenko using WinEPR SimFonia (Bruker).

3.2.5. Electron transfer pathways identification using eMap

Putative electron transfer (ET) pathways in DtpA and DtpAa were identified using the online software eMap (Tazhigulov *et al.*, 2019). The eMap analysis is based on a coarse-grained version of the Pathways model (Balabin *et al.*, 2012) in which ET pathway between donor and acceptor is described as a series of through-space, through-hydrogen bond and through-covalent bond tunneling events. Each of these events is assigned a quantitative ‘penalty’ and thus a final score is calculated to identify the most likely ET pathway. For DtpA, the structure with PDB accession code 6GZW (Chaplin *et al.*, 2019) (ferric DtpA structure obtained at 100 K) was uploaded to eMap. To keep the consistency, 6TB8 (Lučić *et al.*, 2020a) was selected for DtpAa (ferric DtpAa structure obtained at 100 K). ET pathways were assessed for both chain A and chain B

in the crystallographic asymmetric unit of both DyPs and keeping the calculation parameters set as the default (Tazhigulov *et al.*, 2019). Haem, together with Tyr and Trp residues, was selected as the ET-active moiety.

3.2.6. Crystallisation, X-ray data collection, structure determination and refinement

Y345F and DM DtpAa variants were crystallised using the hanging drop vapour diffusion method at 18 °C. 1.2 µl of protein solution at 15 mg mL⁻¹ was mixed with an equal volume of reservoir solution containing 100 mM HEPES pH 7.5, and 20% (w/v) PEG 4000 (Sigma). Crystals grew within two days in various shapes and sizes but single rhombohedron crystals (approximately 200 x 150 x 150 µm) were used for diffraction. Crystals were cryo-protected in solution containing 20 % (v/v) glycerol (Fisher), 100 mM HEPES pH 7.5 and 20 % (w/v) PEG 4000 (Sigma) and flash-cooled by plunging into liquid nitrogen. X-ray diffraction data were collected at 100 K at the Diamond Light Source (DLS) beamline i04 at a wavelength of 0.9795 Å. Diffraction data obtained from crystals were processed automatically in xia2 (Winter, 2010) and scaled and merged using Aimless (Evans and Murshudov, 2013) in the CCP4i2 suite. Both structures were refined using Refmac5 (Murshudov *et al.*, 1997) in the CCP4i2 suite (Potterton *et al.*, 2018) with ferric DtpAa WT (PDB code 6TB8 (Lučić *et al.*, 2020a)) used as the input model and with model building between refinement cycles in Coot (Emsley *et al.*, 2010). Riding hydrogen atoms were added during refinement. The structures were validated using the Molprobtity server (Davis *et al.*, 2007), the JCSG Quality Control Server and tools within Coot (Emsley *et al.*, 2010). A summary of data collection and refinement statistics are given in Table 3.1.

Table 3.1. Crystallographic data processing and refinement statistics for DtpAa Y345F and DM variants. Values in parenthesis refer to the outermost resolution shell.

	Y345F	DM
Space group	P2 ₁	P2 ₁
Unit cell (Å)	a=72.02, b=67.79, c=73.02, β =105.65 °	a=71.04, b=68.13, c=73.05, β =105.42 °
Resolution (Å)	70.32 - 1.23	70.42 - 1.27
Outer shell (Å)	1.25 - 1.23	1.29 - 1.27
Unique reflections	191401 (7298)	174917 (7242)
Mn (I/SD)	8.2 (1.6)	9.0 (0.6)
CC _{1/2}	0.996 (0.356)	0.999 (0.339)
Completeness (%)	97.8 (75.8)	99.0 (83.0)
Redundancy	4.8 (2.8)	5.0 (3.7)
R _{cryst}	0.162	0.186
R _{free}	0.180	0.209
RMS dev. bond lengths (Å)	0.013	0.013
RMS dev. bond angles (°)	1.842	1.852
Ramachandran favoured (%)	96.81	96.39

3.2.7. Stopped-flow absorption kinetics

Transient kinetics of the interaction of H₂O₂ with ferric enzymes was performed using a SX20 stopped-flow spectrophotometer (Applied Photophysics) equipped with a diode-array multi-wavelength unit and thermostatted to 25 °C. Enzyme solutions (10 μM before mixing) were prepared in 50 mM sodium acetate, 150 mM NaCl, pH 5.0 and mixed with a series of H₂O₂ concentrations ranging from 62.5 to 2,000 μM before mixing. The overall spectral transitions were monitored using the diode array unit and time course of absorbance at specific wavelengths were fitted to kinetic models in the

Pro-K software (Applied Photophysics) to yield rate constants for Compound I (k_{obs1}) and Compound II formation (k_{obs2}).

3.3. Results

3.3.1. EPR characterisation of the ferric haem forms of DtpAa

The low-temperature (10 K) EPR spectra of ferric DtpAa (Figure 3.1A), reveal features typical for a high-spin (HS) ferric haem in the $g=6$ region as well as at the $g=2$. It is clear that the HS spectrum at pH 5.0 comprises of two forms, while the spectrum at pH 7.0 only one of the forms is present (Figure 3.1A), thus consistent with the findings from the stopped-flow experiments described in Chapter 2 (Ferric^I and Ferric^{II}; see Figure 2.7 and 2.8). Upon addition of 10-fold excess of H₂O₂ to DtpAa, a series of samples were frozen at variable times and an EPR spectrum at each time point recorded (Figure 3.1B). Spectral changes in the $g=6$ and $g=2$ regions were observed. Analysis of the HS ferric haem spectra ($g=6$) using spectra subtraction with variable coefficient procedure (Svistunenکو *et al.*, 2006) enables the deconvolution of the HS ferric haem spectrum into two clear components, defined as HS_{narrow} and HS_{wide} (Figure 3.1A and 3.1B). These two species are typical of many HS ferric haem ($S=5/2$) proteins and peroxidases, when the haem experiences a departure from the axial (tetragonal) symmetry and the principal g -values along two ‘perpendicular’ directions (in the haem plane) become unequal. The g -values of the HS ferric haem can be found from the second order spin Hamiltonian

$$\mathcal{H} = \beta g B S + D(S_z^2 - S(S + 1)/3) + E(S_x^2 - S_y^2) \quad (3.1)$$

where B is external magnetic field, D describes a tetragonal component of the spin Hamiltonian, or axial zero field splitting component, and E , if present at all, introduces a rhombic component (Scholes, 1969). For most cases of non-zero rhombicity ($E \neq 0$), when $E \ll D$, the principal g -values are well approximated as:

$$g_x = 6.00 - 24 E/D, g_y = 6.00 + 24 E/D, g_z = 2.00 - 34E^2/D^2 \quad (3.2)$$

Thus, the zero field splitting rhombicity parameter E/D can be determined from the two g-values in the g=6 area:

$$E/D = (g_y - g_x)/48 \quad (3.3)$$

The E/D parameter can take values from zero for completely axial (tetragonal) haem to a theoretical maximal value of 1/3 for completely rhombic case (Blumberg *et al.*, 1968). In practice the E/D parameters for different haem proteins and enzymes (peroxidases and catalases) fit an approximate interval of 0 - 0.06 (Peisach *et al.*, 1971). The E/D values of the HS ferric haem forms detected in DtpAa, two at pH 5.0 and one at pH 7.0, are reported in Table 3.2, together with the g-values from which they have been calculated.

Table 3.2. The principal g-values, rhombicity parameters E/D, individual line widths and Lorentz/Gaussian line shape ratios used in the simulation of the EPR signals of the two HS ferric haem forms of DtpAa.

	g ₁	g ₂	g ₃	E/D	ΔH ₁ , G	ΔH ₂ , G	ΔH ₃ , G	Lorentz/Gaus sian ratio
HS _{narrow}	6.025	5.804	1.999	0.0046	15	15	15	0.1
HS _{wide}	6.220	5.510	1.992	0.0148	20	20	20	0.1
HS _{wide, pH7}	6.210	5.505	1.992	0.0147	23	25	25	0.1

The two pure line shapes of the HS_{narrow} and HS_{wide} species were used to determine their respective contributions in each EPR spectrum associated with different reaction times following addition of H₂O₂ (Figure 3.1C). To express the HS_{narrow} and HS_{wide}

signals intensities in terms of species concentration *i.e.* μM HS haem, the two signals were simulated (Figure 3.1A and 3.1B) and the resulting line shapes double-integrated over the full range of magnetic field values of the signal (from 900 to 4600 G). This allows the kinetic curves presented in Figure 3.1C to be replotted in terms of HS haem species concentration (Figure 3.1D). Figure 3.1D supports the view that the $\text{HS}_{\text{narrow}}$ and HS_{wide} species are both present and that H_2O_2 reacts with the $\text{HS}_{\text{narrow}}$ form (less rhombic) rapidly, while the HS_{wide} form reacts in two phases to form Compound I; the majority at a rate comparable to that of the $\text{HS}_{\text{narrow}}$ species and a minority species more slowly. At ~ 3 min, when all H_2O_2 is consumed, the ferric haem forms starts to recover, keeping the proportion of the $\text{HS}_{\text{narrow}}$ and the HS_{wide} forms (the HS_{wide} form dominating). At 9 min, the proportion of the HS_{wide} and $\text{HS}_{\text{narrow}}$ is very close to that observed in the control sample before H_2O_2 addition, *i.e.* $\text{HS}_{\text{wide}} / \text{HS}_{\text{narrow}} \sim 4/3$ *i.e.* $\text{HS}_{\text{narrow}}$ comprising 43% of the starting ferric DtpAa.

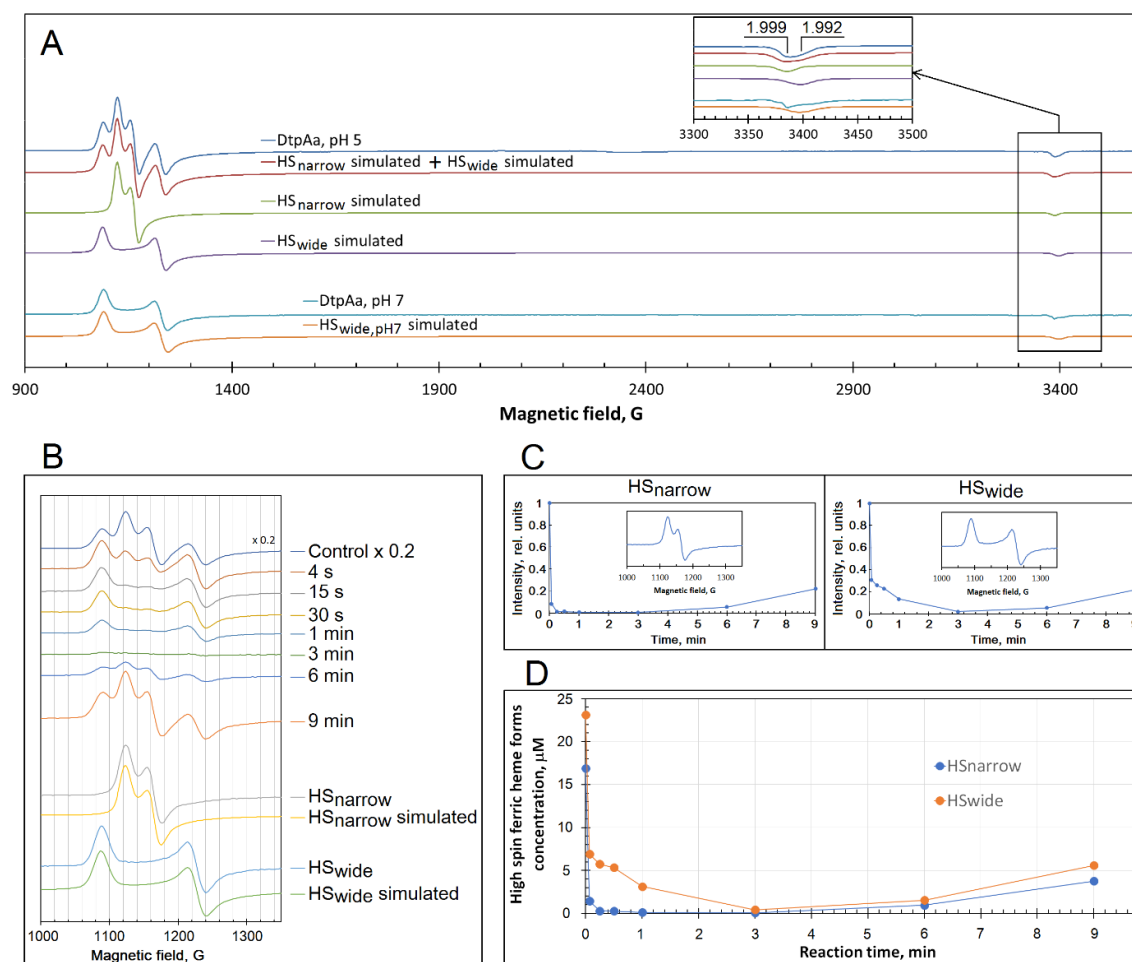


Figure 3.1. EPR spectroscopy of DtpAa. A) The 10 K EPR spectra of 40 μM DtpAa at pH 5.0 and 7.0 and their simulations. The pH 5.0 spectrum can be represented as a sum of two HS ferric haem signals, whereas the spectrum of DtpAa at pH 7.0 exhibits just one form (further details of the simulated spectra in B and Table 3.1). B) The change in line shape of the g_{\perp} area of the HS ferric haem EPR signal ($g \sim 6$) on time following addition of a 10-fold molar excess of H_2O_2 to DtpAa at pH 5. Analysis of the EPR signals allowed extraction of two pure line shapes as follows: $\text{HS}_{\text{narrow}} = \text{Control} - 3.3 \times 4 \text{ s}$; $\text{HS}_{\text{wide}} = 4 \text{ s} - 0.084 \times \text{Control}$. The simulations of these two line shapes ($\text{HS}_{\text{narrow}}$ simulated and HS_{wide} simulated) have been performed by using the parameters reported in Table 3.2 C) The kinetics of the two DtpAa HS ferric forms following reaction with H_2O_2 at pH 5.0; the two signals intensities are normalised to 1.00 in the control sample (before addition of H_2O_2). D) The kinetic dependences of the two HS ferric haem forms, as reported in (C), expressed in concentration. Note the sum of the two forms concentrations in the control ($t = 0$) is 17 μM ($\text{HS}_{\text{narrow}}$) plus 23 μM (HS_{wide}), equal to the protein concentration units of 40 μM used in the experiment.

3.3.2. *The free radical region of DtpAa EPR spectra*

A ~500 G wide magnetic field window was used to record detailed changes in the free radical region of the EPR spectra. A control sample was measured (40 μ M DtpAa) which yielded a slightly asymmetrical EPR spectrum caused by two HS ferric haem forms (Figure 3.2A). Shortly after addition of a 10-fold molar excess of H₂O₂ (0.07 min), an unusual EPR spectrum was recorded, comprised of a wide signal with a hyperfine structure (Figure 3.2A). The intensity of the spectrum is decreasing over the first minute of the reaction, with a concomitant emergence of a free radical EPR signal at $g=2.003$, the latter dominating the EPR spectra at the reaction times from 3 min. The procedure of spectral subtraction with variable coefficient method (Svistunenko *et al.*, 2006) applied to the whole array of the DtpAa EPR spectra, some of which are shown in Figure 3.2A, was used to extract four EPR signals labelled SigA, SigB, SigC and SigD (Figure 3.2B).

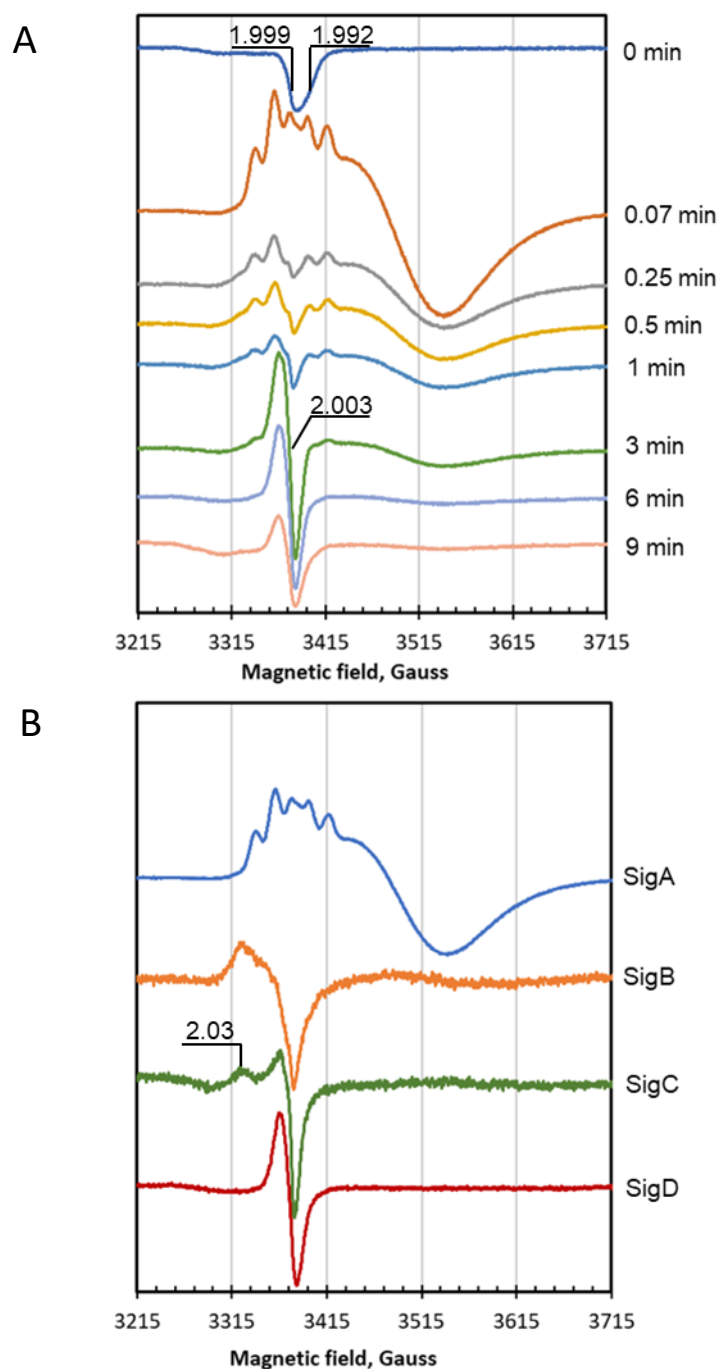


Figure 3.2. EPR spectra of the free radical region in DtpAa. A) Spectral changes in the free radical region upon addition of H_2O_2 recorded at different freezing times, obtained at 10 K. B) The spectral components contributing to the wide EPR spectrum obtained using spectral subtraction with variable coefficient method (Svistunenکو *et al.*, 2006). The component were obtained as follows: SigA = 4 s – 0.23 x Control; SigB = 15 s – 0.61 x 4 s – 0.145 x 1 min; SigC = 1 min – 0.61 x 4 s – 0.392 x 4 s; SigD = 6 min – 0.337 x 3 min.

The most dominant feature is the SigA, a wide signal with a hyperfine structure. The unusual shape of spectrum recorded at 4 s timepoint is caused mostly by this species. SigB is another signal extracted from the array of spectra - it is characterized by a highly asymmetric line shape. SigC represents a canonical EPR line shape of a peroxy radical (ROO•) – with a main feature, likely to be a combination of two components with close but not identical g-values around $g \sim 2.004$, and a distinct ‘parallel’ component at $g \sim 2.03$ (Svistunenko, 2001). The fourth signal extracted from DtpAa spectra, SigD, is a symmetrical singlet that has a g-value of 2.003 and a widths of ~ 18 G and has been previously described as multi-site protein radical (Rajagopal *et al.*, 2013).

3.3.3. Kinetics of the four spectral components: SigA, SigB, SigC and SigD

Extraction of the four signals allowed for description of kinetics for each species. Quantitative estimates of the concentrations were performed by comparison of the second integrals of each signal with a reference to known total concentration of the ferric haem in the sample. Figure 3.3. shows how intensity of each signal changes over time.

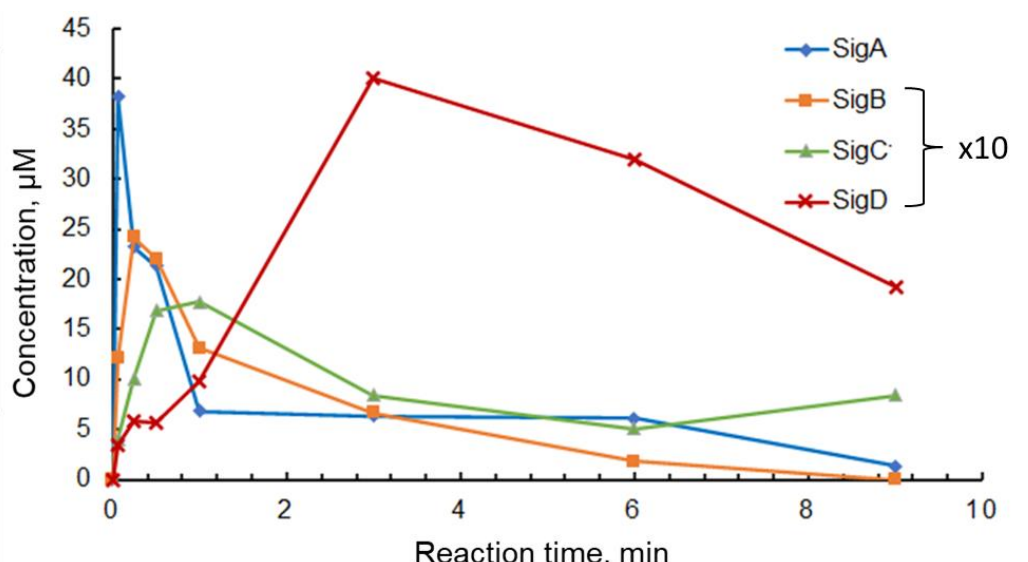


Figure 3.3. Kinetics of the four EPR signals identified in the free radical region of the DtpAa EPR spectra after H_2O_2 addition. The signal intensities of the components have been expressed in μM of corresponding paramagnetic species as described in the text. The concentrations of the species producing signals SigB, SigC and SigD were multiplied by 10 for better viewing.

At the first measured time point (4 s), SigA is the most prevalent species. Its formation is the immediate effect of ferric haem state oxidation by H_2O_2 and coincides with the sharp drop of signal intensity at $g=6$ caused by the HS ferric haem. In addition to SigA, traces of SigB-D are also present in this sample, out of which SigB is the highest concentration (Figure 3.3). The intensity of SigB is rising over the first 15 s, simultaneously with decrease of SigA. However, at any time point, concentration of SigB is much lower than initial SigA concentration. It reaches its maximum between 4 and 15 s when it accounts for approximately <10% of signal coming from radical species. Decrease of SigB concentration is then followed by rise of SigC intensity, reaching its maximum between 1 and 3 minutes, closely followed by SigD.

3.3.4. Electron transfer pathway prediction in DtpA and DtpAa

A recent EPR study has shown that upon formation of Compound I in DtpA, its decay (reduction) over time in the absence of a substrate results in a pristine tyrosyl radical located on Y374, identifying it as a putative entry port for ET from a substrate to the haem (Chaplin *et al.*, 2019). Using eMap (Tazhigulov *et al.*, 2019) and the ferric DtpA structure as input (PDB code 6GZW) ET pathways were predicted. In DtpA, three Tyr and six Trp residues are present. eMap calculations are in agreement with the experimental study, identifying the ET pathway between haem and Y374 as the shortest and thus the most likely (Figure 3.4). Additionally, the software flags W301 as a possible electron donor, however, the presence of a tryptophanyl radical was never confirmed experimentally (Chaplin *et al.*, 2019) and reasons behind this will be discussed later. For DtpAa, using the ferric structure (PDB code 6TB8) the ET pathways predicted are shown in Figure 3.5.

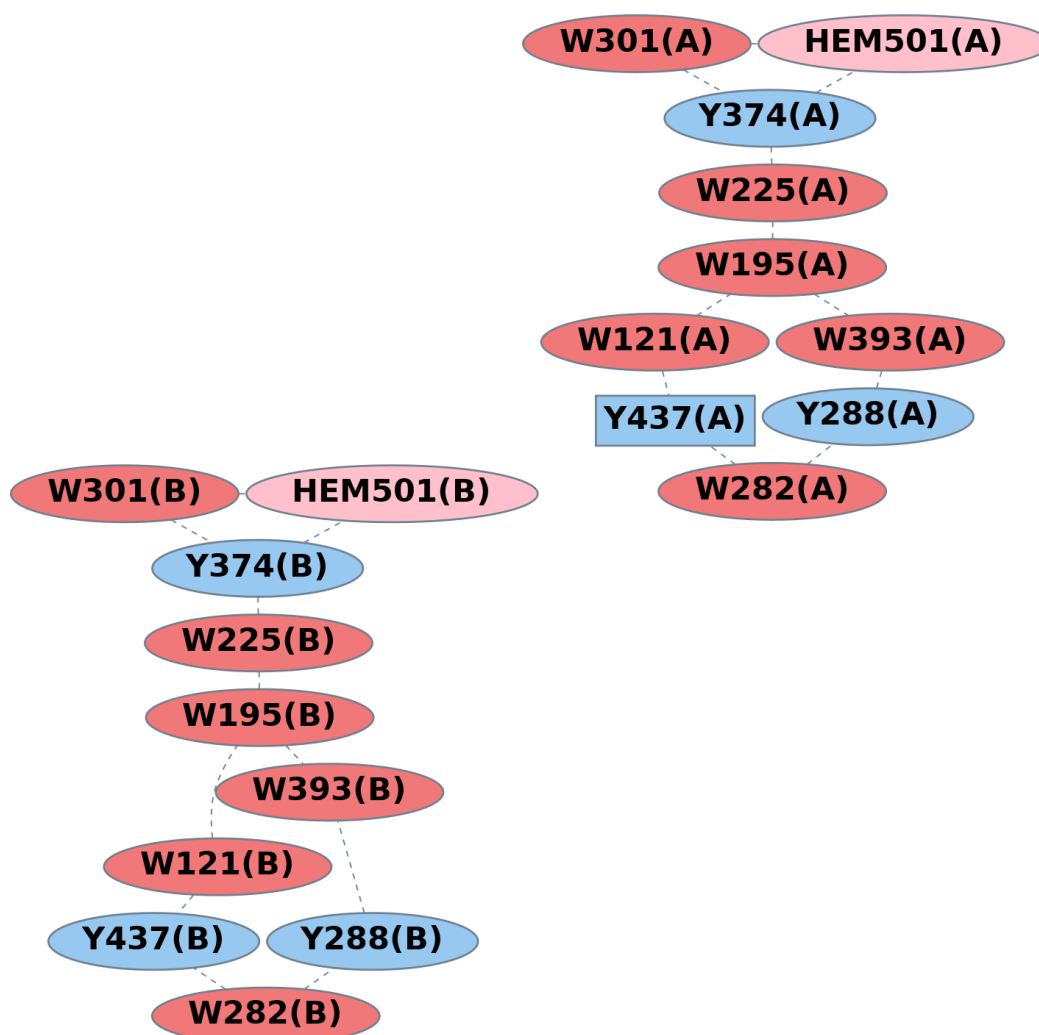


Figure 3.4. Results of the eMap analysis for DtpA. Putative ET pathways between haem and Tyr/Trp residues in DtpA for chains A and B. Ellipse represents surface buried and rectangle surface-exposed residues. Dashed lines represent transfer path from one residue to another.

In DtpAa, five Tyr and six Trp residues are present. Unlike in DtpA, where all Tyr and Trp residues communicate with the haem directly or indirectly, it would appear that in DtpAa only Y389 and W285 are directly involved (Figure 3.5). Notably, an interchain ET contact from Y116 is also identified (Figure 3.5).

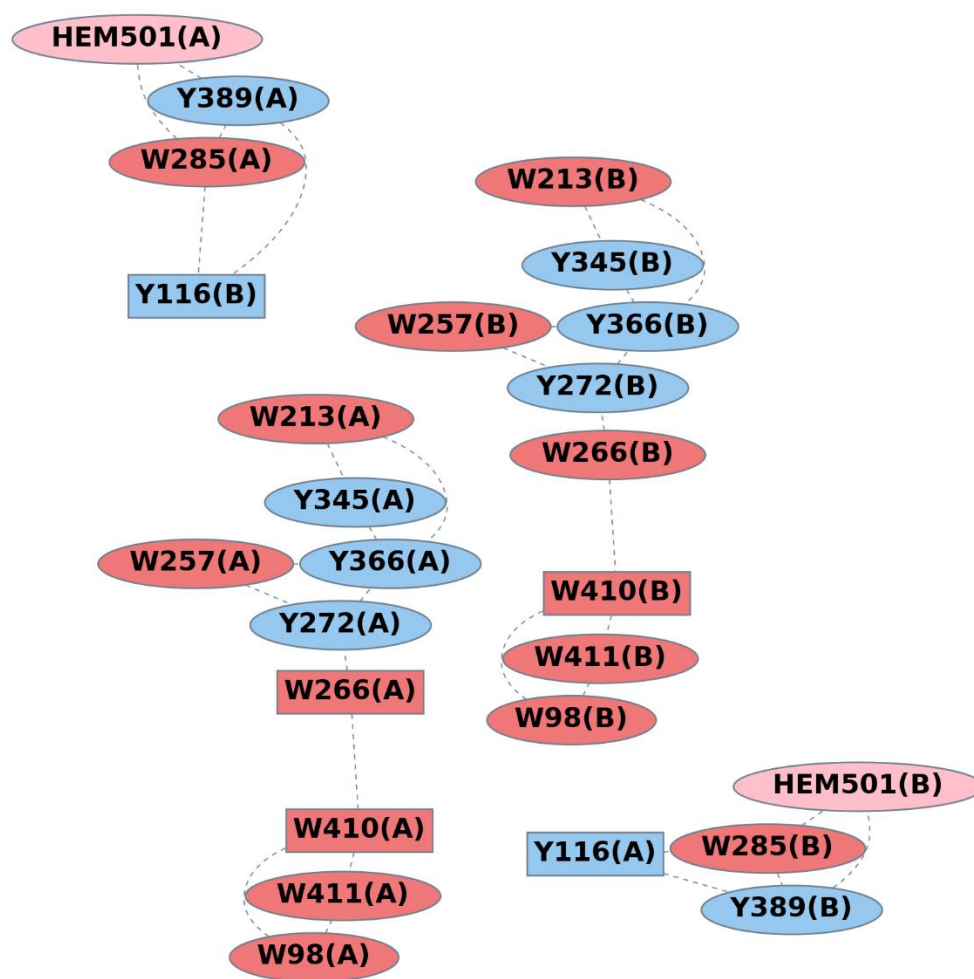


Figure 3.5. Results of the eMap analysis for DtpAa. Putative ET pathways between haem and Tyr/Trp residues in DtpAa for chains A and B. Ellipse represents surface buried and rectangle a surface-exposed residues. Dashed lines represent transfer path from one residue to another.

From sequence analysis, Y389 of DtpA is not homologous to Y374 in DtpA, which has been identified as the electron donor in DtpA (Chaplin *et al.*, 2019). Instead, Y389 is located on the proximal side of the haem, as opposed to the distal haem position found for Y374 in DtpA, and close to a Trp residue that is conserved in all A-type DyP sequences (Chaplin *et al.*, 2019) (W301 in DtpAa and W285 in DtpA; Figure 3.6). In DtpA, a Phe (F417) is present instead of Y389 (Figure 3.6). Furthermore, the ET active

Y374 in DtpA is replaced by an ET inactive Phe (F347) in DtpAa and thus, a homologous entry port for ET transfer to the one in the DtpA, does not exist in DtpAa (Figure 3.6). Interestingly, an additional Tyr (Y345) is found in DtpAa close to the F347 with its side chain facing in the opposite direction (Figure 3.6). In the homologous position to Y345, a Phe is found in DtpA. Thus, where a Phe-Ser-Tyr sequence motif is found in DtpA, the reverse motif is present in DtpAa.

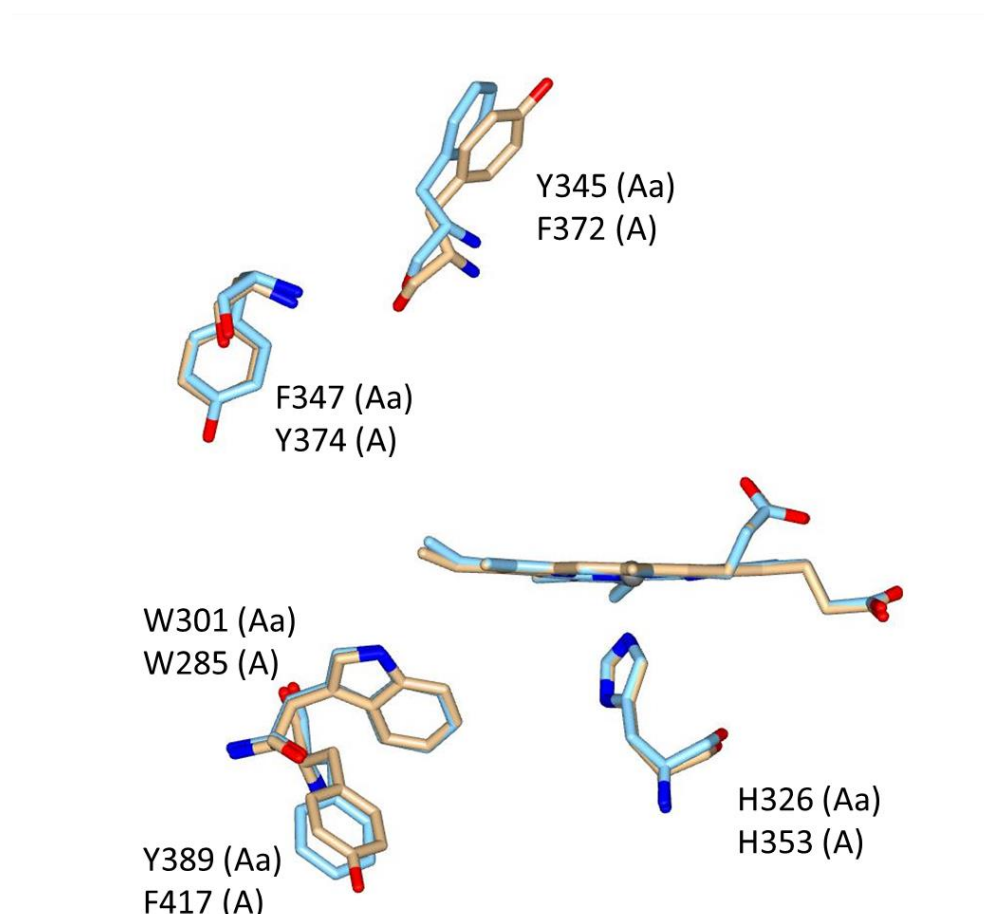


Figure 3.6. Electron transfer active aromatic residues within the vicinity of the haem in DtpA (A) and DtpAa (Aa). Structural superposition of DtpA (6GZW, pale blue) and DtpAa (6TB8, wheat).

3.3.5. Crystal structures of tyrosine variants

To explore further the effect of the Tyr-Ser-Phe sequence motif on the EPR and ET properties of DtpAa following H_2O_2 addition, the Y345 and F347 residues were mutated, to mimic the DtpA motif. Two variants were created, Y345F and a double mutant (DM) (Y345F/F347Y) that has a Tyr structurally homologues to Y374 in DtpA (Figure 3.6). Rhombohedron crystals of both variants were obtained, with an example of a crystal shown in Figure 3.7. These crystals were used to measure crystallographic data and the respective structures were solved to 1.23 Å (Y345F) and 1.27 Å (DM).

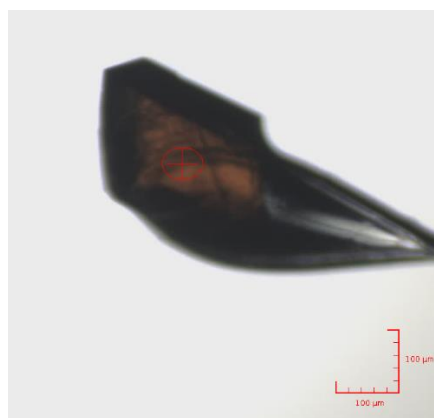


Figure 3.7. Y345F DtpAa crystal (200 x 150 x 150 μm) mounted on a loop.

Using the refined crystal structures of the two variants the Phe-Ser-Tyr motif region was analysed and compared to the WT structure. Figure 3.8 shows the superposition of WT DtpAa and the two variants, where it can be observed that replacing either a Tyr for a Phe or vice versa does not alter the position that the side chain adopts in the respective structure. A slight repositioning of the neighboring D358 between the structures is noted (Figure 3.8). This Asp communicates with Y347, present only in DM, via a water molecule (Figure 3.8), and this interaction is also noted in the crystal

structure of DtpA with Y374. No other structural differences between WT and the two variants were apparent in this region.

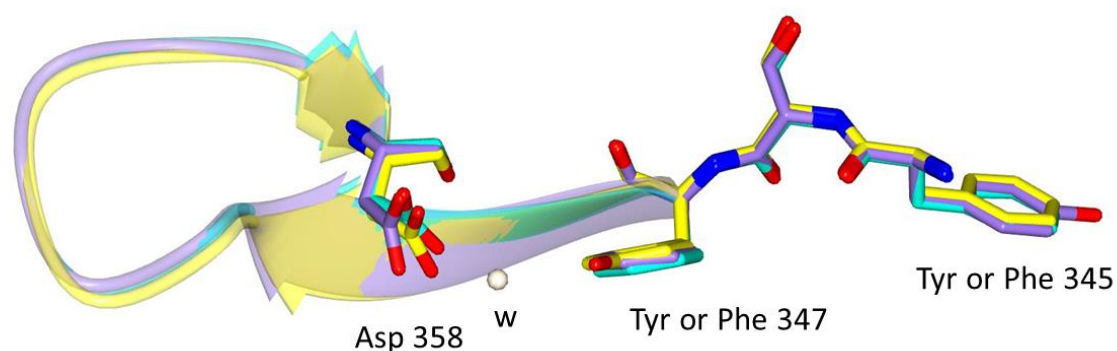


Figure 3.8. Structural superposition of chain A of the Y345F (cyan) and DM (yellow) variants with WT DtpAa (purple, PDB code 6TB8). Mutated Tyr residues are represented as sticks together with the neighboring Asp residue. In the DM structure, a water molecule is found to bridge between Y347 with D358 and is depicted as a wheat coloured sphere.

3.3.6. Stopped-flow kinetics of the DtpAa tyrosine variants

Electronic absorbance spectra of each Tyr variant, before and after the addition of one-equivalent H_2O_2 are reported in Figure 3.9. with Table 3.3 listing peak maxima wavelengths for each spectrum alongside those of WT for comparison. The spectra of both variants are consistent with HS ferric haem species with a 4 nm red shift of Soret band from the WT spectrum (Table 3.3). Addition of one-equivalent H_2O_2 to both variants leads to the same changes reported for the WT in Chapter 2, *i.e.* a Soret band intensity decrease and a red shift in wavelength, coinciding with the appearance of α

and β bands of equal intensity, indicating the presence of a Compound II species. Pure Compound I electronic absorbance spectrum was not detected in either variant without rapid mixing using a stopped-flow spectrophotometer (*vide infra*), although spectral features of Compound I can be detected in the DM, that are mixed with a Compound II species (Figure 3.9). This stipulates that although repositioning of Tyr did not result in an increase of Compound I half-life ($t_{1/2}$) - to be similar to that in DtpA (~ 2.5 min (Chaplin *et al.*, 2017)), the observation of a mixed intermediate species under the time scales of these static absorbance experiments does indicate that the life-time of Compound I is altered. To investigate this further stopped-flow reaction kinetics were undertaken. Upon mixing of the ferric Tyr variants with H_2O_2 two HS ferric species found in the WT enzyme were once more observed. For both variants the spectral transitions were most consistent with a model $a \rightarrow c$; $b \rightarrow c$; $c \rightarrow d$ (*i.e.*, $a = \text{Ferric}^I$, $b = \text{Ferric}^{II}$, $c = \text{Compound I}$ and $d = \text{Compound II}$) previously used for DtpAa (see Chapter 2) and fitted accordingly. Pseudo-first order rate constants were obtained for Compound I formation from the global fitting and are plotted as a function of increasing H_2O_2 in Figure 3.10. There is no significant difference in rates between the WT and either variant. The two ferric forms react slowly and at different rates to form a common intermediate – Compound I. This process is initially dependent on $[H_2O_2]$ but becomes rate limited at higher concentrations. Thus, introduction of Tyr to the same position as Y374 in DtpA has not increased the Compound I formation rate. The decay of Compound I to Compound II again displays little H_2O_2 concentration dependence in Tyr variants, as it was previously described for the WT, with a k_{obs2} value determined to be between 0.1 and 0.15 s^{-1} .

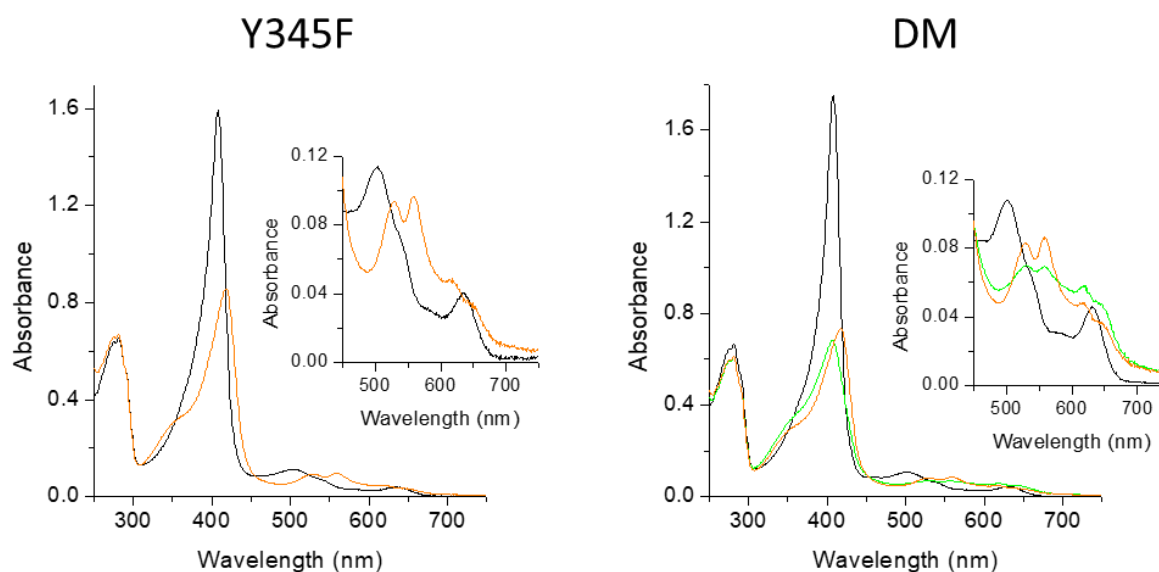


Figure 3.9. Electronic absorbance spectra (pH 5.0) of DtpAa Tyr variants; Y345F and Y345F/F347Y (DM). Ferric species (black spectrum) and Compound II species (orange spectrum) are shown the latter formed following addition of one molar equivalent of H_2O_2 per molar haem, indicated. In DM only, an additional spectrum (green) is present which appears to be a mixture of Compound I and II species. *Insets* show a close-up of the Q-band region.

Table 3.3. Wavelength absorbance maxima at pH 5.0 for DtpAa and the Tyr variants.

Protein	Ferric (nm)	Compound II (nm)
DtpAa	408, 499, 588, 630	419, 527, 558, 617
Y345F DtpAa	410, 511, 637	422, 533, 558, 622
DM DtpA	410, 508, 630	417, 524, 555, 624

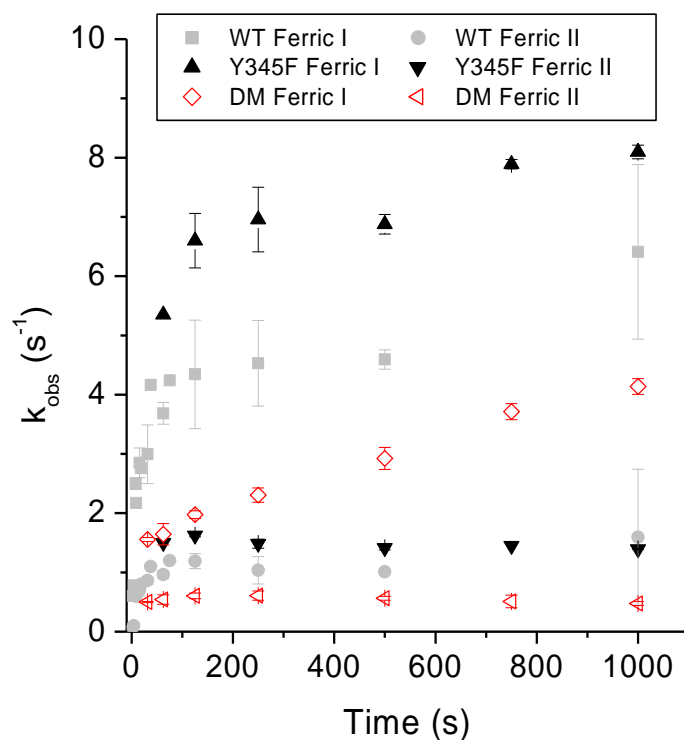


Figure 3.10. Compound I formation in DtpAa WT and Tyr variants. Observed pseudo-first order rate constants (k_{obs}) obtained from global fitting of the spectral transitions for the reaction of DtpAa and Tyr variants (5 μM) with increasing H_2O_2 concentrations at pH 5.0 at 25 $^\circ\text{C}$. At pH 5.0 two HS ferric species, Ferric^I and Ferric^{II} exist giving rise to two k_{obs} rates for Compound I formation.

3.3.7. Monitoring the reaction of the DtpAa tyrosine variants with H_2O_2 by EPR spectroscopy

Time series samples of the Tyr variants following activation with H_2O_2 for EPR analysis were prepared together with a new set of WT DtpAa samples. Figure 3.11A shows the 10 K EPR spectra of the WT and Tyr DtpAa variants with Figure 3.11B focusing on the change occurring at the $g=6$ region (HS ferric haem) before and 5 s after addition of 10-fold molar excess of H_2O_2 . First thing to note is that the two HS

ferric forms observed, in the first time series recorded and from the stopped-flow kinetics, is present. For the two Tyr mutants the ferric haem EPR spectra are very similar to that of the WT, with two HS haem ferric forms again present at pH 5.0 (Figure 3.11A and B) and only one form at pH 7.0 for Y345F (spectrum of DM at pH 7.0 was not recorded; Figure 3.11C). Within 5 s of adding H₂O₂, differences are observed for the mutants in the g=6 region. For the the Y345F variant, where a Tyr has been removed, a notably different spectrum from that observed for the WT DtpAa is now observed whereby the narrow HS ferric form signal is significantly lower, implying that removal of Tyr345 makes a significant difference to the ferric haem oxidation to Compound I. Interestingly, when a Tyr is introduced at position 347 (*i.e.* the DM), the 5 s spectrum is now more similar to that of the WT (Figure 3.11B). This suggests that in the Phe-Ser-Tyr motif it is not so important where the Tyr is located to maintain a similar kinetics of the ferric haem conversion to Compound I.

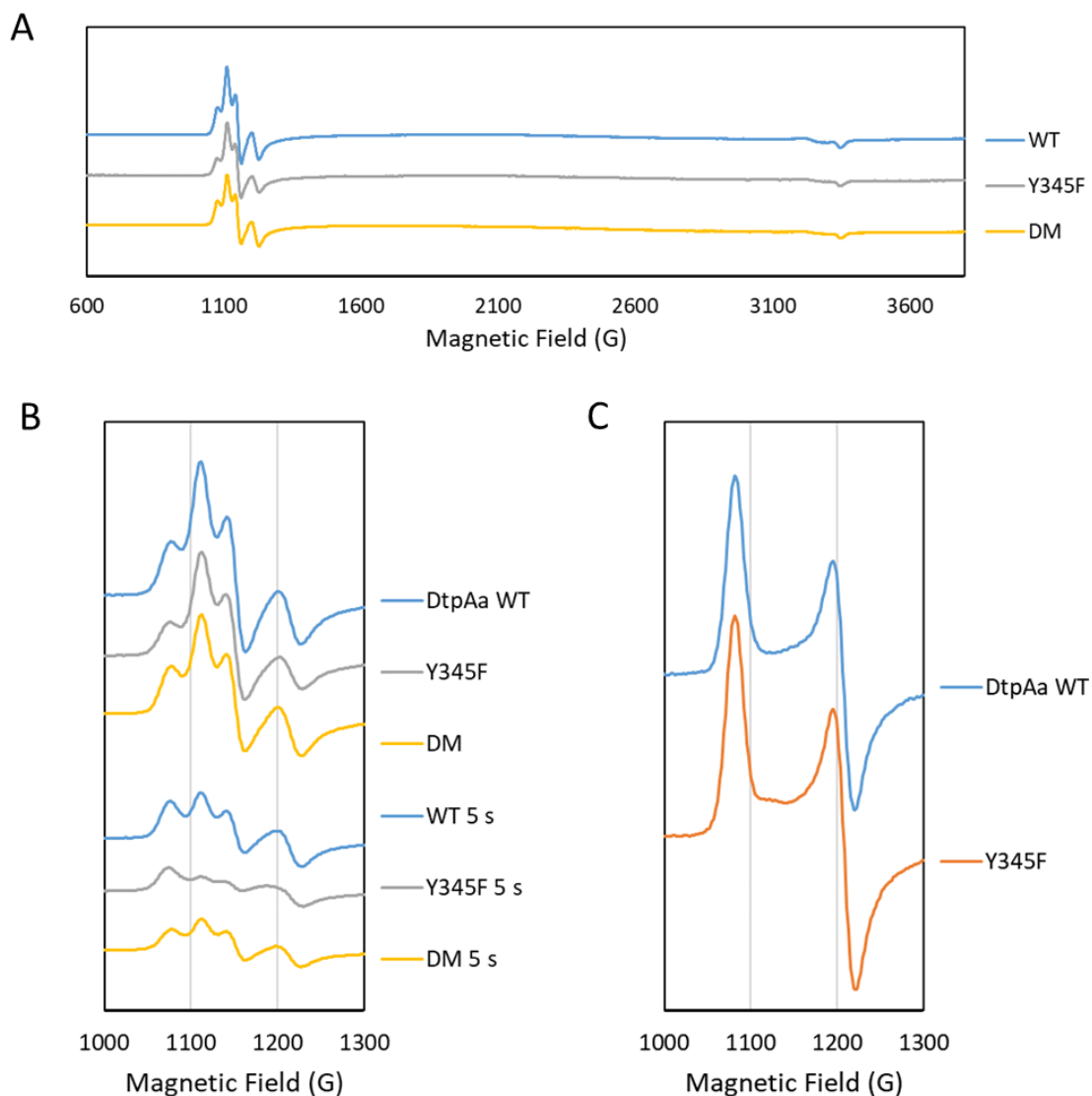


Figure 3.11. EPR spectroscopy of the second time series of DtpAa and the Tyr variants. A) The 10 K EPR spectra of 40 μ M DtpAa and Tyr variants at pH 5.0. B) Comparison of g~6 area line shape of the HS ferric haem EPR signal of DtpAa WT and Tyr variants. EPR spectra recorded before addition of a 10-fold molar excess of H₂O₂ to DtpAa at pH 5.0 and 5 s after the addition. C) The g~6 region of 10 K EPR spectra of 40 μ M DtpAa and Y345 variant at pH 7.0.

A similar pattern appears to be the case when viewing the free radical region of the EPR spectra (Figure 3.12). The wide signal (SigA), which is now lacking the hyperfine feature we observed in the earlier series, seems to evolve much slower in the single mutant Y345F. In the DM, however, it appears much earlier, reaching a maximal intensity at 15 s. In line with this, the SigB signature, prominent in the earliest time point of the WT series (5 s, Figure 3.12), is much lower in the single mutant, with a much stronger multi-site free radical (SigD), whereas in the double mutant, SigB is back to a similar to the WT's intensity at the earliest time point with practically no SigD. While these observations can only invoke speculative rationalisation, it appears that the double mutant, in which the Tyr residue have been removed from its native site and inserted to another, is more similar, as far as the EPR phenomenology is concerned, to the WT than the variant in which the tyrosine was bluntly removed.

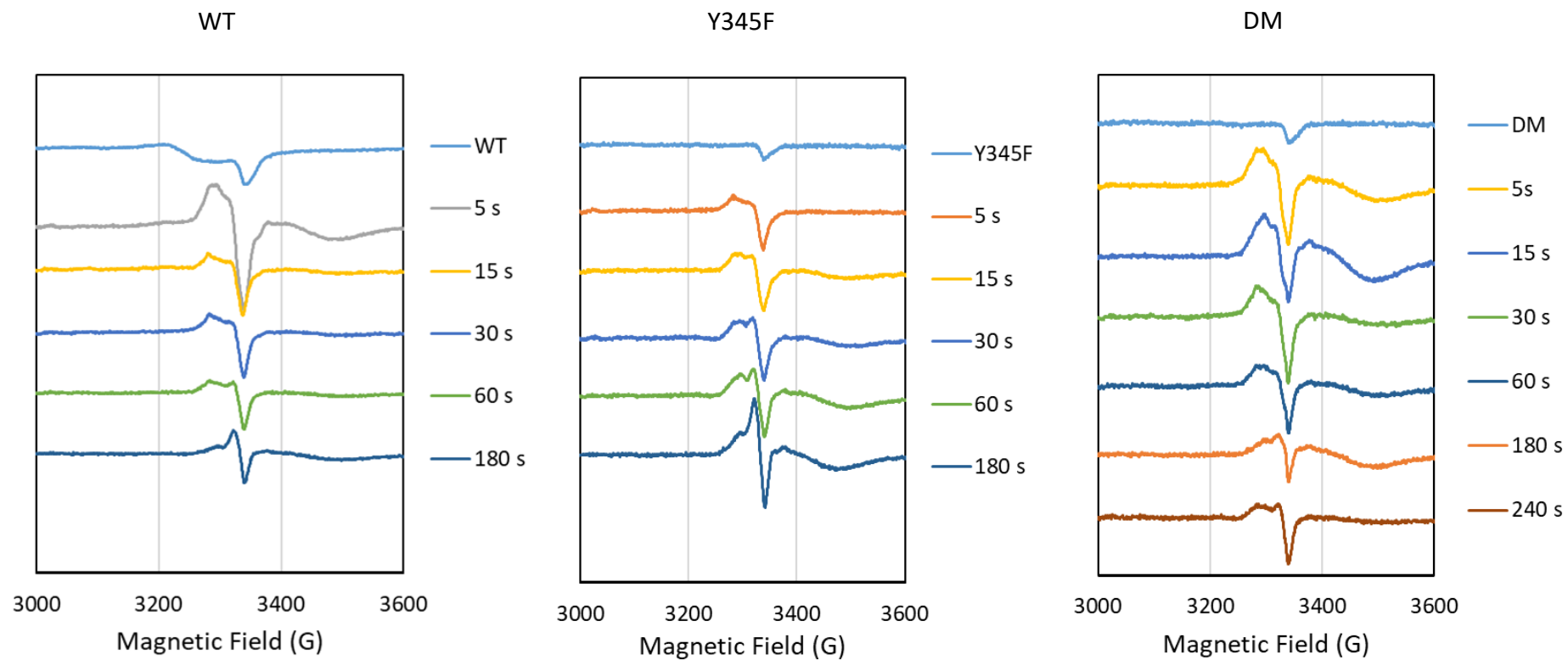


Figure 3.12. EPR spectra of the free radical region in the WT DtpAa (second set of samples) and the Tyr variants. Spectral changes in the free radical region upon addition of H_2O_2 recorded at different freezing times, obtained at 10 K.

3.4. Discussion

Two forms of DtpAa are observed by EPR spectroscopy at pH 5.0, Ferric^I and Ferric^{II}, which have distinct properties. Ferric^I has the narrower splitting of the two g-perpendicular components of the HS g=6 signal, resulting in E/D = 0.005, a value close to cytochrome *c* oxidase and the other form, ferric^{II} has a E/D = 0.015 which is similar to HRP (Peisach *et al.*, 1971). While rhombicity of HS_{wide} is ~3 time greater than of HS_{narrow}, both forms fit well the previously reported range of E/D in haem proteins (Peisach *et al.*, 1971). In a recent study with a genetically engineered myoglobin, a clear correlation is drawn between the ligand arrangement in the distal site of the haem, seen in the crystal structure, and the rhombicity detectable in the EPR spectra, with the E/D value changing from 0.002 to 0.042.(Chand *et al.*, 2018) Therefore, in simple terms the EPR of DtpAa may be accounted for by proposing that a haem pocket acid group is deprotonated at pH 7.0 (only one form) and at pH 5.0 exists in approximately 50 % deprotonated/protonated forms. The negative charge on this deprotonated acid group perturbs the electronic structure of the haem iron rendering this asymmetry of the otherwise axial g-tensor at pH 7.0. A combination of two electronic structures with different degrees of rhombicity (departure from the axial) at pH 5.0, result from the co-existence of the charged and neutral species. The more rhombic form (seen at pH 7.0 and termed ferric^{II} at pH 5.0) has the HS_{wide} spectrum, while ferric^I seen at pH 5.0 is the more axial HS_{narrow} spectrum. The presence of two electronic structures is also evident from the g=2 region of spectrum, where a slightly asymmetrical signal was recorded coming from two distinguishable species.

Upon addition of H₂O₂, a decrease in HS signal intensity occurs with two HS species reacting at a different rate; ferric^I reacts more rapidly with H₂O₂ compared to ferric^{II}.

Although this cannot be seen directly in the EPR experiments, because the appropriate time range is not accessible (*i.e.* within 2 s, see stopped-flow kinetics in Chapter 2), EPR does reveal that there are kinetic differences between ferric^I and ferric^{II} (Figure 3.1). Simultaneously with the decrease in ferric form, an unusual wide free radical signal arises at $g=2$ which has been deconvoluted to four components: SigA, SigB, SigC and SigD. Contribution of each component can be measured in each time point allowing for description of each components kinetics.

Immediately after addition of H_2O_2 to the sample, SigA becomes the most dominant species accounting for > 90% of paramagnetic species present at the first time point (4 s after reaction was started, Figure 3.3). Thus, SigA formation seems to be the immediate effect of ferric haem state oxidation by H_2O_2 suggesting that SigA derives from Compound I. This Compound I signal is very different from the Compound I detected in DtpA that is narrow and has a characteristic sharp maximum at $g=1.9996$ (Chaplin *et al.*, 2019). The EPR spectrum of Compound I is found to vary significantly among numerous peroxidases and globins for which it has been reported (Benecky *et al.*, 1993; Chaplin *et al.*, 2019b; Hillar *et al.*, 2000; Ivancich *et al.*, 2001; Ivancich *et al.*, 2003; Ivancich *et al.*, 1997; Khindaria and Aust, 1996; Matsui *et al.*, 1999; Patterson *et al.*, 1995; Rutter *et al.*, 1984; Schulz and Schirmer, 1979). The variation is attributed to the changeable contribution of the exchange parameter J to the spin Hamiltonian that describes the interaction between the ferryl iron electron spin $S=1$ and porphyrin cation radical spin $S'=1/2$ (Chaplin *et al.*, 2019).

SigB is the second most abundant species present at the earliest time point measured. A SigB-like spectrum was described previously (Ivancich *et al.*, 2001) to correspond

to a Compound I intermediate in CcP. In CcP Compound I contains a radical on a nearby Trp residue (W191) and thus its similarity with SigB suggests that, in DtpAa following addition of peroxide, a transient tryptophanyl radical is formed that is coupled with an Fe^{IV}=O haem. DtpAa houses a nearby tryptophan residue on the proximal side of the haem pocket (Figure 3.6) which was also identified using the eMap software (Tazhigulov *et al.*, 2019) to be involved in a possible ET pathway to the haem (Figure 3.5). This tryptophan residue is conserved amongst DyP family (Chaplin *et al.*, 2019; Linde *et al.*, 2015). In two DyPs, an A-type from *Thermomonospora curvata* DyP (*TcDyP*) and a C/D-type DyP from *Auricularia auriculajudae* (*AauDyP*), a mixed Trp/Tyr radical signal has been recorded and the corresponding residues have been identified as plausible free radical sites (Linde *et al.*, 2015). However, these are protein radicals that evolve from Compound I decay and are not a feature of Compound I itself. In DtpA Compound I decays to a pristine tyrosyl radical despite the presence of homologous tryptophan (Chaplin *et al.*, 2019). DtpA lacks a conserved dyad motif found in *TcDyP* and *AauDyP* that might be essential in radical stabilization. This dyad motif comprises two tryptophan residues arranged perpendicular to one another possibly providing a type of coupling that allows for free radical transfer/stabilization and its detection by EPR spectroscopy (Chaplin *et al.*, 2019). In DtpA, one of the Trp residues (W285) is present (Figure 3.6) but a non-redox active Phe is found in the place of the second Trp. However, DtpAa does possess a redox active residue, albeit a Tyr rather than Trp (Figure 3.6). The presence of the Tyr389-Trp285 couple might therefore be sufficient to stabilize a radical on tryptophanyl and account for the observation of SigB. Thus, DtpAa Compound I might be a mixed species, one of which is a CcP-like Compound I with a tryptophanyl radical.

In the early measured time points, Compound I is the most prevalent species. It decays quickly over the first minute of reaction, along with SigC formation. SigC is distinguishable by a bell-shaped line at $g=2.03$ which is a characteristic feature of the g_z component of a peroxy radical (ROO^*) (Becker *et al.*, 1988; Hedberg and Ehrenberg, 1968; Schlick and Kevan, 1979; Svistunenko, 2001). Such radicals are not specific to any residue, rather they are often formed on carbon centered radicals once they interact with molecular oxygen. These radicals might be seen as a variation of the multi-site protein radical (SigD), which have subsequently reacted with O_2 . SigD is a singlet previously described as multi-site protein radical, *i.e.* it results from superimposition of signals from many different protein-bound radicals (Rajagopal *et al.*, 2013). In the absence of a substrate, ferryl haem (*i.e.* Compound I) can oxidatively damage the host protein due to its high oxidation potential. In P450s, chains of Tyr/Trp residues provide charge shuttling pathways that lead out from the heme to the protein surface, where the oxidising equivalent can be quenched by reductants (Gray and Winkler, 2018). In peroxidases, such a charge/radical escape routes are structurally less obvious and the radicals that form from the catalytic ferryl heme can end up being site non-specific *i.e.*, the result of oxidative damage to the protein. Growth of SigD intensity throughout time series points towards such oxidative damage of DtpAa in absence of a substrate.

In contrast, some peroxidases can form a pristine and stable Tyr or Trp radical, which can have a catalytic role or be implicated in an ET pathway between the haem and a reductant, such as DtpA (Chaplin *et al.*, 2019). In the absence of a substrate, Compound I in DtpA extracts an electron from Y374 to form a stable pristine tyrosyl radical (Chaplin *et al.*, 2019). Under physiological conditions, ET from a Tyr (YOH) is

coupled to proton transfer resulting in the formation of a neutral YO•, that can be observed EPR. The question that arises is why Y374 forms the YO• and not the other two Tyr residues present in DtpA? The answer may lie in the fact that Y374 can deprotonate its oxidised form (YOH•+) to become the EPR observable neutral YO•, much more efficiently than the other Tyr residues. Nearby proton acceptors such as His, Glu, Asp will facilitate formation of YO• and donate back a hydrogen-bond that upshifts the formal potential of YO• by as much as 200 mV (Yee *et al.*, 2019). Such an uplift in potential has beneficial consequences for ET with a donor. Structured H₂O molecules have also been implicated as proton acceptors, whereas bulk water is usually unable to support rapid proton transfer back to the YO• owing to an unfavourable pK_a difference (Yee *et al.*, 2019). In the DtpA crystal structure (Chaplin *et al.*, 2019), an Asp (D385) and a H₂O molecule are in the vicinity of the Y374 phenol ring with the H₂O acting as a hydrogen-bonding bridge between the phenol and the carboxylate group (Figure 3.13). The other two Tyr residues in DtpA do not have a nearby amino acid proton acceptor or a scaffolded water molecule.

In DtpAa, no presence of a tyrosyl radical was detected. DtpAa has five Tyr residues, none of which have a suitable proton acceptor nearby. However, the D385 found near the phenol ring of Y374 in the X-ray crystal structure of DtpA is conserved in DtpAa (D358) (Figure 3.13). Thus, substitution of the F347 in DtpAa with a Tyr (equivalent to Y374 in DtpA) was attempted to test whether presence of nearby proton acceptor could predict radical sites in haem enzymes. Two variants were created: Y345F/F347Y (DM) that has Tyr in homologous position to Y374-DtpA and a Y345F where a Tyr near F347 was replaced by a Phe (mutation also present in DM) to remove any effects possibly arising from two neighboring Tyr residues, rather than proton acceptor

coupled Tyr. Structures of both variants were inspected and an additional structural water bridging newly introduced Y347 to the conserved D358 was found, which could act as a proton acceptor if $\text{YOH}^{\bullet+}$ was formed from Y347 (Figure 3.13). Thus, changes in enzyme ET pathways and in mechanism of formation of ferryl intermediates resulting from F347Y mutation should be present.

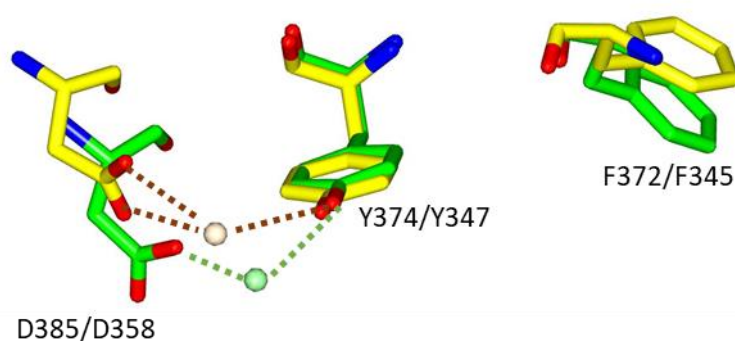


Figure 3.13. Structural superposition of DM DtpAa variant (yellow) with WT DtpA (green) (PDB code 6GZW (Chaplin *et al.*, 2019)) with residues predicted to play a role in radical formation indicated (DtpA/DM DtpAa numbering). Water bridging Y374 to D385 in DtpA is depicted as a pale green sphere, while water bridging Y347 to D358 in DM DtpAa is shown as a wheat sphere.

Indeed a drastic change in ET pathways is predicted by eMAP (Tazhigulov *et al.*, 2019) (Figure 3.14). An additional ET path is now identified, connecting the haem with newly introduced Y347. Moreover, this Tyr now serves as a main node in newly established communication network between all Tyr/Trp residues and the haem, similarly as Y374 in DtpA (Figure 3.4). This comprehensive network is not present in Y345F variant, it has kept the structure present in DtpAa WT with only Y389 and W285 (from the same

chain as the haem) serving as ET nodes (Figure 3.15). However, eMap analysis can only suggest that spatial shift of Tyr location is sufficient to re-establish the ET network as it does not consider the presence or absence of proton acceptor in vicinity of these residues. Thus, kinetics of the variants were inspected using stopped-flow and EPR spectroscopy in hope to shed light on this issue.

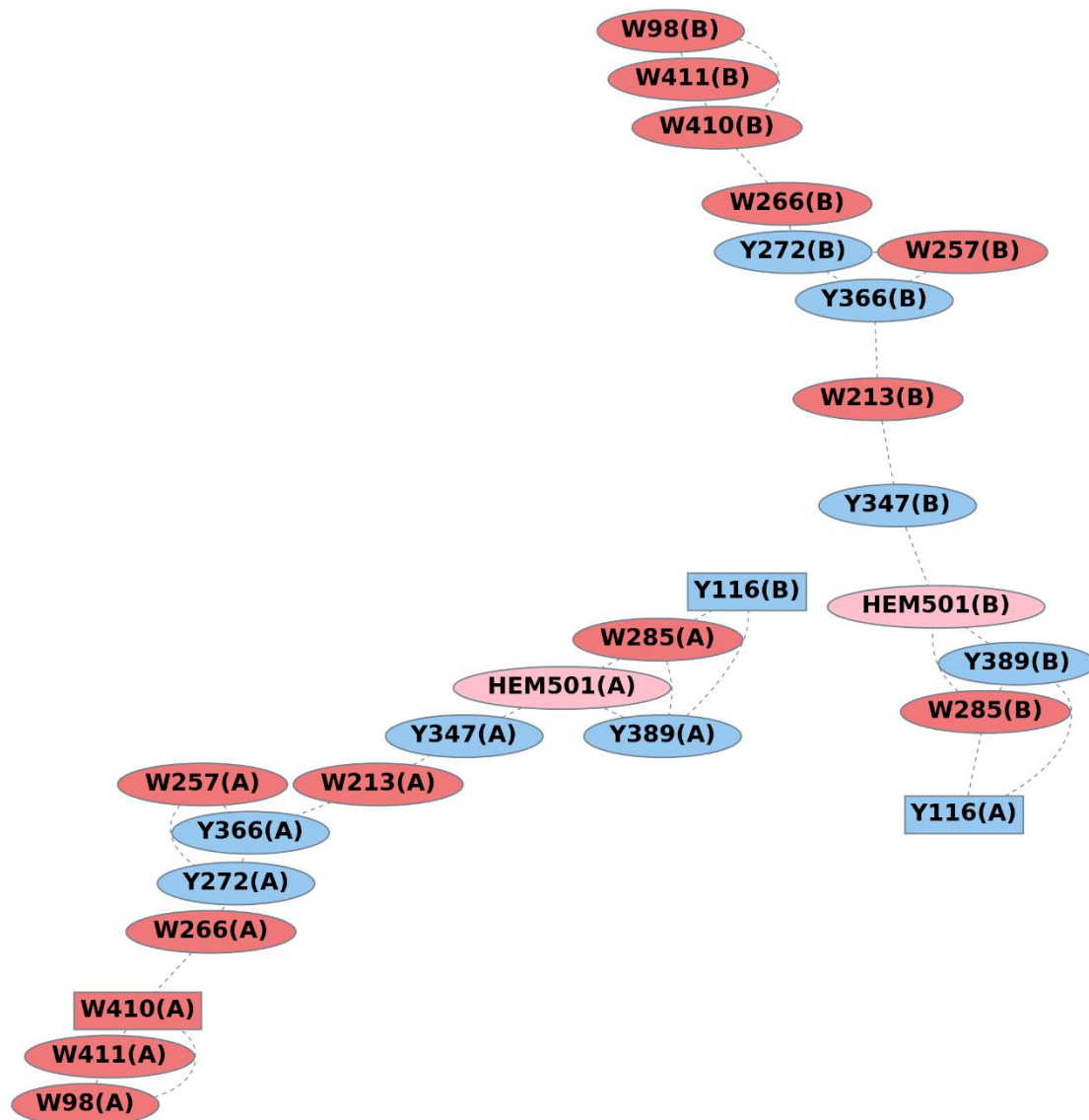


Figure 3.14. Results of the eMap analysis for the DtpAa DM variant. Putative ET pathways between haem and Tyr/Trp residues in the DM obtained by uploading the DM structure eMap. An ellipse represents surface buried and a rectangle a surface-exposed site. Dashed lines represent ET paths from one residue to another.

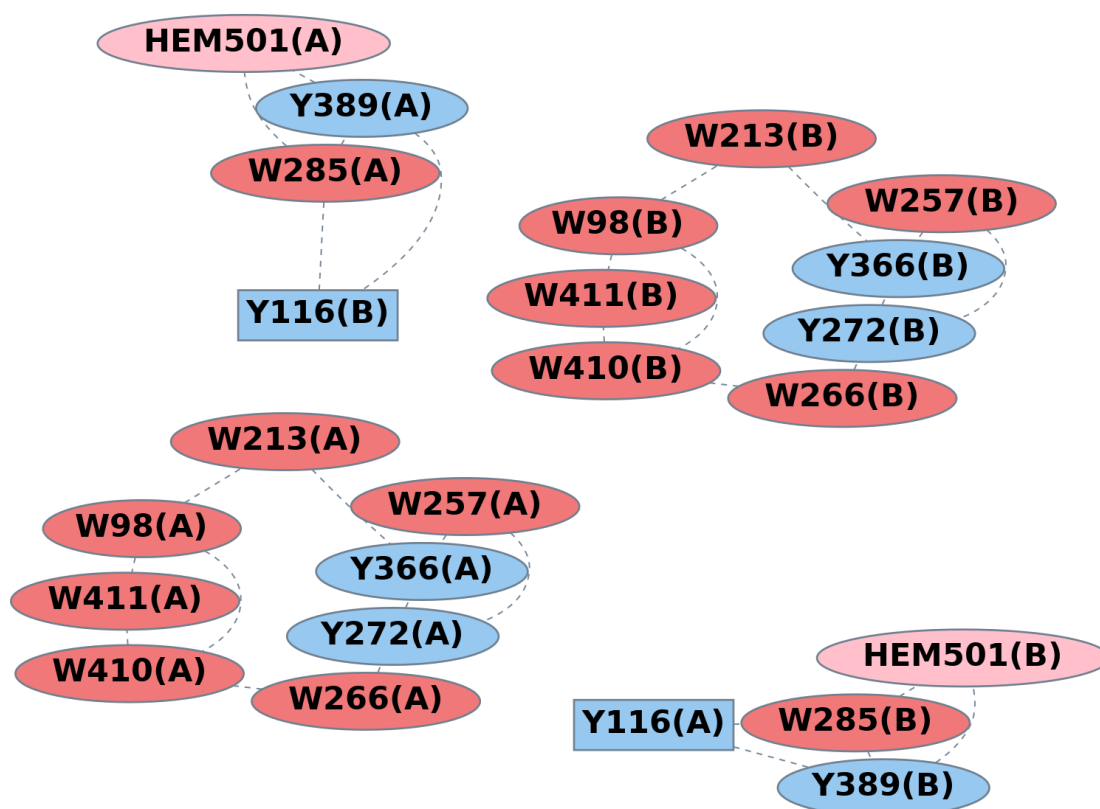


Figure 3.15. Results of the eMap analysis for the DtpAa Y345F variant. Putative ET pathways between haem and the Tyr/Trp residues in the Y345F obtained by uploading the Y345F structure to eMap. An ellipse represents a surface buried and a rectangle a surface-exposed site. Dashed lines represent ET paths from one residue to another.

Compound I is an unstable species in DtpAa that quickly decays to Compound II in WT and Y345F variant. In the DM its half lifetime is slightly prolonged, but it is still too short to allow capturing of an unmixed species without rapid mixing of ferric enzyme and H_2O_2 in the stopped-flow spectrometer. Its formation in both variants is still inefficient, with a rate of $<10 \text{ s}^{-1}$. Rate of Compound I decay to Compound II also remains unchanged from the WT, suggesting that kinetics of Compound I and II formation in DtpAa are not influenced by nearby Tyr residues. However, that does not exclude very likely changes in free radical escape routes caused by the mutations which

could be identified using EPR spectroscopy. If Y347 was to donate an electron to the Compound I haem, an EPR spectra of tyrosyl radical would be detected. Thus, EPR spectra of time series were measured for both variants but are not discussed in this thesis. Further analysis is required, including deconvolution of spectral components from the spectra and, if presence of a tyrosyl radical is confirmed, fitting of the experimental spectra to a simulated tyrosyl radical spectrum (Chaplin *et al.*, 2019; Svistunenko and Cooper, 2004). At this moment, only a comment can be made on spectra recorded 3 min after addition of H₂O₂. In WT and Y345F variant, the line shape of free radical signal (featureless singlet) suggests that the radicals have migrated to multiple amino acids, instead of residing on a specific site. In the DM, the singlet does not become a prevalent species until 4 min time point, implying that Y347 introduction has somewhat delayed a chaotic radical movement through the protein and thus slowed down the oxidative stress on the enzyme. The exact reason for this change remains unknown and further work is required in hope to elucidate the role of F347Y mutation in DtpAa.

Chapter Four

Using Serial femtosecond X-ray crystallography to determine zero dose ferric and ferryl peroxidase structures of DtpB from *Streptomyces lividans*

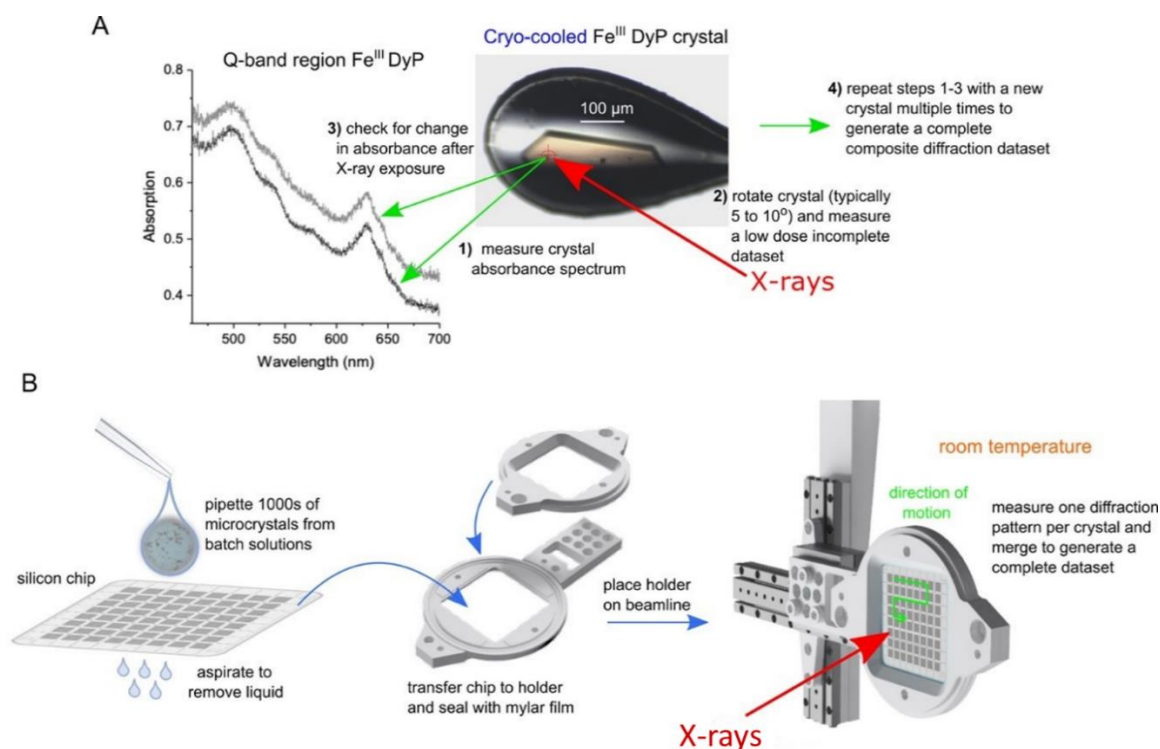


Figure 4. Approaches used to obtain low dose (A) or zero dose (B) X-ray crystal structures of the *S. lividans* DyPs.

Results from this Chapter have been published in:

M. Lučić, D. A. Svistunenko, M. T. Wilson, A. K. Chaplin, B Davy, A. Ebrahim, D. Axford, T. Tosha, H. Sugimoto, S. Owada, F. S. N. Dworkowski, I. Tews, R. Owen, M. A. Hough and J. A. R. Worrall. Serial femtosecond zero dose crystallography captures a water-free distal haem site in a dye-decolourising peroxidase to reveal a catalytic role for an arginine in Fe^{IV}=O formation. *Angewandte Chemie International Edition*, 2020, 59:21656-21662.

I acknowledge the work from Dr. Michael A. Hough, R. O. and Dr. Jonathan A. R. Worrall kindly provided the merged data file for me to further analyze.

4.1. Introduction

Capturing structures of intact (free of specific radiation damage) redox states in metalloenzymes, whilst challenging, is critical for assigning the chemistry of the metal in the catalytic cycle. Substantial efforts have been made to define the chemical nature and thus reactivity of the high-valent $\text{Fe}^{\text{IV}}\text{-O}$ intermediates in iron-containing enzymes, commonly referred to as ferryl (Winkler and Gray, 2011). Many haem enzymes use ferryl species as part of their catalytic cycle, where haem peroxidases are a prominent example (Dunford, 1999; Moody and Raven, 2018; Poulos, 2014; Sivaraja *et al.*, 1989).

X-ray and resonance Raman approaches have focused on measuring the $\text{Fe}^{\text{IV}}\text{-O}$ bond-length and strength, which for $\text{Fe}^{\text{IV}}\text{=O}$ is shorter and stronger than $\text{Fe}^{\text{IV}}\text{-OH}$ species (Moody and Raven, 2018). However, a major complication has been the sensitivity of the haem-Fe to reduction caused by the incident X-rays and lasers (Moody and Raven, 2018). X-rays interact with protein crystals to generate large numbers of solvated photoelectrons, and the effects manifest first in electron rich sites such as metals to rapidly change, for example, the electronic state of the haem-Fe and with it the structure of the active site. This poses a serious limitation to obtaining damage-free structures of redox enzymes at sufficiently high resolutions that the enzyme mechanism can be defined at the chemical level, such as changes resulting from one-electron reduction or the geometry and position of the chemical substrate. Alternative approaches have been sought to obtain intact (undamaged) or near-intact structural data of radiation-sensitive Fe^{III} and Fe^{IV} haem species. These include low-dose composite (*i.e.* multi-crystal) X-ray structures coupled with single crystal spectroscopy (near-intact) (Berglund *et al.*, 2002; Chaplin *et al.*, 2019; Gumiero *et al.*, 2011; Kwon *et al.*, 2020; Lučić *et al.*, 2020a; Meharena *et al.*, 2010), as well as neutron diffraction (Casadei *et al.*, 2014; Kwon *et*

al., 2016; Kwon *et al.*, 2020) and structures determined by X-ray free electron lasers (XFELs zero dose) (Chreifi *et al.*, 2016; Ebrahim *et al.*, 2019; Kwon *et al.*, 2021) to obtain fully intact structures.

Serial femtosecond crystallography (SFX) using XFELs allows diffraction data of a crystal to be collected with femtosecond exposure times that can outrun the effects on the structure of X-ray induced photoreduction/radiation damage (Chapman *et al.*, 2014; Chapman *et al.*, 2011; Ilme, 2015; Neutze *et al.*, 2000; Spence, 2014). Crystal structures determined in this way preserve the redox state of the metal site and can be considered pristine (*i.e.* free of radiation-induced damage) (Chapman *et al.*, 2011; Chreifi *et al.*, 2016a; Schlichting, 2000). As the XFEL pulse destroys the crystal, a new crystal is required for each pulse, explaining the need for serial methods that use many thousands of microcrystals. Efficient sample delivery systems are therefore essential for SFX experiments. Delivering the sample using crystal injector is a common strategy. A thin stream of crystals is produced by ejecting a crystals suspended in high-viscosity carrier matrix through a small orifice, which then flows orthogonally to the XFEL beam and intersects it at defined distance (Chapman *et al.*, 2011; Martiel *et al.*, 2019). This approach requires plenty of sample manipulation steps, including transfer and loading of crystals and resuspension of the crystal slurry into the viscous matrix, that can damage them. Therefore, alternative, fixed-target methods have been developed (Ebrahim *et al.*, 2019; Lučić *et al.* 2020b; Moreno-Chicano *et al.*, 2019).

In this Chapter a SFX approach has been applied where a silicon fixed-target chip containing 25,600 apertures is used to trap microcrystals ($\leq 50 \mu\text{m}$) of the target protein or enzyme (Ebrahim *et al.*, 2019; Moreno-Chicano *et al.*, 2019). An advantage of this

delivery system is that SFX data may be collected at ambient temperature, as opposed to experiments at cryogenic temperatures (100 K) where structural states are frozen out, and chemistry is slowed (Fraser *et al.*, 2011). Ambient temperature crystallography is particularly challenging due to a greatly increased susceptibility to the observed effects of radiation damage in comparison to that which occurs at 100 K (de la Mora *et al.*, 2020; Gotthard *et al.*, 2019). The application of chip-based approach to determine pristine structures of haem-Fe redox states in peroxidases under ambient temperatures is therefore attractive (Ebrahim *et al.*, 2019; Moreno-Chicano *et al.*, 2019), but requires the ferryl species to be stable throughout the duration of the SFX experiment (typically < 20 min using the silicon fixed-target chip system).

Additionally, the chip-based approach is an attractive sample delivery method for serial synchrotron X-ray crystallography (SSX). With the appearance of XFELs, an interest in serial X-ray crystallography has grown, naturally leading towards desire to perform experiments using serial approaches at synchrotrons. Using SSX one can spread the total dose required for structure determination over a large number of crystals with each crystal being subjected to an extremely limited dose (Owen *et al.*, 2017). However, what makes SSX attractive is its availability and low-cost compared to XFELs. Although it does not allow collection of zero-dose structures, it provides an efficient and ‘quick’ way to collect near intact structural data despite the long duration of exposure to X-rays in comparison to an XFEL pulse. A direct comparison of SSX and XFEL methods has been reported for DtpAa (Ebrahim *et al.*, 2019), by ensuring near-identical conditions for the two experiments. This research highlights subtle changes to the active site caused by radiation damage. Specifically, it was found that the haem

Fe bound water molecule moves further away from the iron centre with increasing dose and that the distance it moves is linearly dependant on the dose (Ebrahim *et al.*, 2019).

This Chapter focuses first on determining damage-free (zero dose) structures of the Fe^{III} and Fe^{IV} redox states of the B-type DyP from *Streptomyces lividans*, DtpB, using SFX. This is followed by determining the Fe^{III} and Fe^{IV} structures of DtpB at 100 K using a combination of a multi-crystal microspectrophotometry approach as well as an SSX structure of Fe^{IV} DtpB. Together these structures allow for a thorough comparison of the three different approaches to assess changes in the distal pocket of DtpB caused by increasing dose.

4.2. Experimental procedures

4.2.1. Over-expression and purification of DtpB

DtpB was successfully over-expressed and purified following the same procedure used for DtpA and DtpAa (see Chapter 2).

4.2.2. Sample preparation

DtpB was exchanged into a desired buffer using a PD-10 column (Generon) and concentrated using centrifugal ultrafiltration devices (Vivaspin GE Healthcare). Enzyme concentration was determined by UV-visible spectroscopy (Varian Cary 60 UV-visible spectrophotometer) using an extinction coefficient (ϵ) at 280 nm of 111,450 $\text{M}^{-1} \text{cm}^{-1}$ determined using ProtParam (Gasteiger *et al.*, 2003). H_2O_2 solutions (Sigma-Aldrich) were prepared from a stock with the final concentration determined spectrophotometrically using an $\epsilon = 43.6 \text{ M}^{-1} \text{cm}^{-1}$ at 240 nm (Gasteiger *et al.*, 2003).

4.2.3. EPR spectroscopy and simulation

Wilmad SQ EPR tubes (Wilmad Glass, Buena, NJ) with OD = 4.05 ± 0.07 mm and ID = 3.12 ± 0.04 mm (mean \pm range) were used. Samples frozen in a set of these tubes yielded very similar intensities of EPR signals; with only ~1-3% random error. All EPR spectra were measured on a Bruker EMX EPR spectrometer (X-band) at a modulation frequency of 100 kHz. A Bruker resonator ER 4122 (SP9703) and an Oxford Instruments liquid helium system were used to measure the low-temperature (10 K) EPR spectra. EPR spectra of a blank sample (frozen water) measured at the same set of instrumental conditions were subtracted from the DtpB spectra to eliminate the background baseline EPR signal. Spectra deconvolution into two components and measurements of the intensities of these components in the time dependence set of

samples were performed by using the procedure of spectra subtraction with variable coefficient (Svistunenko *et al.*, 2006). Quantitative estimates of the concentrations of the paramagnetic centres were performed by comparison of the second integrals simulated EPR signals with a reference to known total concentration of the ferric haem in the sample. Simulation was performed by WinEPR SimFonia (Bruker).

4.2.4. Crystallisation and H₂O₂ soaking of DtpB crystals

Various crystal sizes of ferric DtpB were grown under batch conditions and were used accordingly for SFX, SSX or conventional X-ray studies. Microcrystals for SFX and SSX (Figure 4.1A) were grown by mixing in microfuge tubes a 1:1 v/v ratio of a solution containing 6-10 mg/ml DtpB in 50 mM sodium acetate, 150 mM NaCl pH 5 with a precipitant solution consisting of 150 mM MgCl₂, 150 mM HEPES, 20% PEG 4000 with the pH adjusted to 7.5, to give a final volume of 200 µl. Crystals (~10 x 8 µm) grew at room temperature within a 24 - 48 h period and displayed no signs of deterioration over several months. Larger crystals (Figure 4.1C) (~400 x 100 µm) for conventional cryo-cooled X-ray crystallography were obtained by mixing 1:1 v/v solutions of 6-10 mg/ml DtpB in 50 mM sodium acetate, 150 mM NaCl pH 5 with a precipitant solution consisting of 100 mM MgCl₂, 100 mM HEPES pH 7.5, 16% PEG 4000. Crystals grew within 48 h and were stable for many months. To generate Compound I in the microcrystals a stock solution of H₂O₂ was added to a 200 µl microcrystal containing suspension to a final concentration of 600 µM (Figure 4.1B). Larger crystals for cryo-crystallography were removed from the batch solution by pipette and transferred to a drop consisting of H₂O₂ (final concentration 600 µM), 20% w/v glycerol (cryo-protectant) in mother liquor on a siliconized cover slip for 30 s before flash-cooling by plunging into liquid nitrogen.

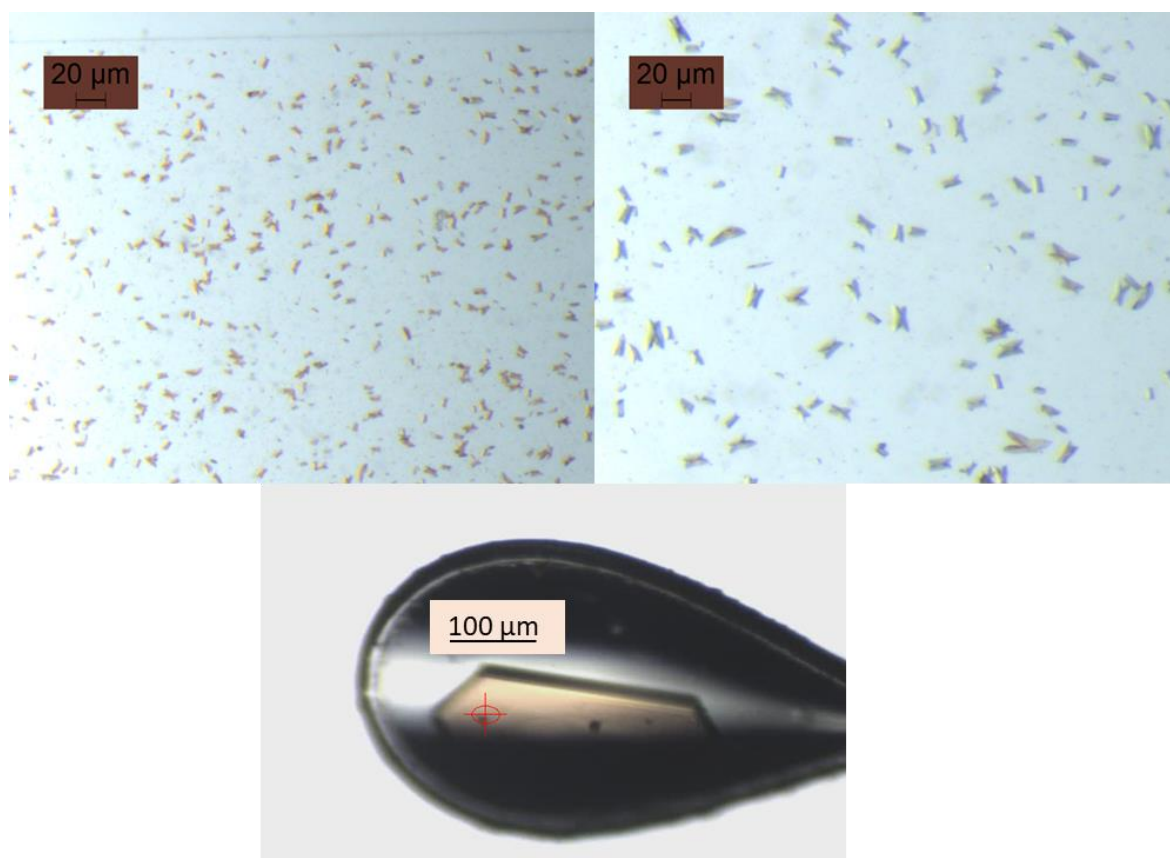


Figure 4.1. DtpB crystals. A) DtpB microcrystals. B) DtpB microcrystals after addition of H₂O₂. C) Example of a large DtpB crystal (300 x 100 μm).

4.2.5. Microspectrophotometry and X-ray data collection at 100 K

Crystals of ferric and H₂O₂ soaked DtpB were cryo-protected in mother liquor containing 20% w/v glycerol and flash-cooled in liquid nitrogen. X-ray diffraction and single crystal spectroscopic data at 100 K were collected at the Swiss Light Source (SLS) beamline X10SA. The MS3 on-axis microspectrophotometer (Fuchs *et al.*, 2014) was used to measure absorbance spectra of ferric DtpB and H₂O₂ soaked DtpB crystals in the range of 450 to 700 nm. Each spectrum was the result of 50 accumulations of 100 ms exposures. Spectra were measured prior to and following X-ray data collection and a dose limit was selected such that minimal changes occurred to the spectrum of

the ferric and ferryl forms during data collection from each crystal. A multi-crystal approach was performed to obtain a complete low-dose composite dataset for the ferric and ferryl DtpB structures. A total of 21 (ferric DtpB) and 13 (ferryl DtpB) spectroscopically-validated diffraction data wedges were merged using the in house go2gether.com script in the XDS package (Kabsch, 2010). X-ray absorbed doses were estimated using Raddose-3D (Zeldin *et al.*, 2013). To reflect the beam profile used, a weighted average of doses calculated for top hat and Gaussian profiles was calculated and doses were estimated for the range of crystal dimensions used.

4.2.6. Serial femtosecond X-ray crystallography

Silicon fixed-target chips with either 12 or 14 μM apertures at their narrowest opening and a nominal capacity of 25,600 were loaded with 200 μl of microcrystal suspension within a humidity enclosure and sealed between two layers of 6 μm thick Mylar. This approach has been described in more detail previously (Moreno-Chicano *et al.*, 2019). To obtain the ferryl structure, Compound I was prepared fresh by adding H_2O_2 directly to the microcrystal suspension. SFX data were measured at SACLA beamline BL2 EH3 using an X-ray energy of 11 keV, a pulse length of 10 fs, beam size 1.6 x 1.6 μm and a repetition rate of 30 Hz. Chips were translated within the interval between X-ray pulses, ensuring that the chip had stopped at the centre of each crystal position (the centre of the aperture) and was exposed only once to X-rays, before moving to the next pulse interval. Data was typically collected from all 25,600 positions on a chip in < 15 min using the SACLA MPCCD detector (Kameshima *et al.*, 2014). SFX data were processed by Dr. Mike Hough and Dr. Robin Owen using the CHEETAH pipeline (Barty *et al.*, 2014) and CrystFEL (White *et al.*, 2016) with scaling and merging using the *Partialator* program.

4.2.7. Serial synchrotron crystallography

Data collection at beamline I24, Diamond Light Source was carried out using an unattenuated X-ray beam of energy 12.8 keV. A dose series was measured upon addition of H₂O₂ to the crystal slurry using the same silicon fixed-target chip method as described for the SFX. The crystals used for SSX belonged to the same crystallization batch as the ones used for SFX. Sequential diffraction patterns at each crystal position in the chip were collected with an exposure time of 10 ms and subsequently binned into one dataset per dose interval as described before (Ebrahim *et al.*, 2019) by Dr. Danny Axford (Diamond Light Source). Absorbed doses were estimated using RADDPOSE-3D (Zeldin *et al.*, 2013) with dose increments corresponding to the total dose accumulated within the exposure time of the first image. In total, 8 sequential doses were collected. The data were indexed using *DIALS* (Winter *et al.*, 2018) and scaling and merging was performed by Dr. Danny Axford using *PRIME* (Uervirojnangkoorn *et al.*, 2015).

4.2.8. DtpB structure determination and refinement

The ferric SFX structure was solved with help of Dr. Mike Hough, Dr. Robin Owen and Dr. Jonathan A. R. Worrall by molecular replacement using MrBUMP (Keegan and Winn, 2008) and BUCCANEER (Cowtan, 2006). The search model identified by MrBUMP for molecular replacement was a B-type dye-decolourising peroxidase from *Rhodococcus jostii* (3QNR) (Singh *et al.*, 2012). Initial refinement of the structure was carried out in PHENIX (Liebschner *et al.*, 2019), using torsion-angle simulated annealing to eliminate model bias and completed using Refmac5 (Murshudov *et al.*, 1997) in the CCP4i2 suite (Potterton *et al.*, 2018). Model building between refinement

cycles was performed in Coot (Emsley *et al.*, 2010). Riding hydrogen atoms were added during refinement. The ferryl DtpB SFX structure, ferric and ferryl 100 K and SSX structures were determined from a starting model of the ferric SFX structure, with the same simulated annealing and refinement procedures used. No restraints were placed on the Fe-N^{ε2}His and Fe-O distances. All structures were validated using the Molprobit server (Davis *et al.*, 2007), the JCSG Quality Control Server and tools within Coot (Emsley *et al.*, 2010). A summary of data collection and refinement statistics are given in Table 4.1 and Table 4.2, respectively.

Table 4.1. SFX (ambient temperature), composite (100 K) X-ray crystallography and SSX dose series data processing for DtpB in space group $P2_12_12_1$. Values in parenthesis refer to the outermost resolution shell. The effective absorbed X-ray dose for the SFX structures is assigned as zero due to the femtosecond duration of the X-ray pulse. As is standard practice for SFX data, (White *et al.*, 2012) the metrics R_{split} and $CC_{1/2}$ are used to assess data quality and resolution limit in place of conventional crystallographic metrics such as R_{merge} or $I/\sigma(I)$. For the SSX structures, a range between the lowest and highest dose is given, with the first value representing dose 1 and the second value dose 8 (the highest dose).

	SFX ferric	SFX ferryl	Composite ferric	Composite ferryl	SSX ferryl
Chips used	4	5	-	-	1
Wavelength (Å)	1.13	1.13	0.8	0.8	0.97
Effective absorbed X-ray dose (kGy)	0	0	11.4	11.3	48.4-387.2
Number of crystals	26223	57909	21	13	23518; 16846
Unit cell dimensions (Å)	86.7, 121.6, 199.0	86.3, 121.1, 198.5	85.8, 120.3, 196.0	85.4, 119.9, 194.2	86.7, 121.6, 199.0

Resolution (Å)	13-1.85	13-1.75	49-1.99	48-1.85	40.05-1.75; 40.13 - 2.72
Number of reflections	175001	207440	138290	159520	212461; 57840
R _{split}	0.136 (0.678)	0.109 (0.887)	-	-	0.142 (0.794); 0.115 (0.782)
CC _{1/2}	0.976 (0.569)	0.984 (0.423)	0.97 (0.50)	0.95 (0.51)	0.975 (0.50); 0.993 (0.52)
R _{merge}	-	-	0.227 (1.02)	0.179 (0.567)	-
R _{pim}	-	-	0.088 (0.472)	0.101 (0.451)	-
(I)/sd(I)	-	-	7.5 (2.1)	4.4 (1.2)	-
Multiplicity	518 (360)	1943 (1359)	6.9 (5.0)	3.1 (1.9)	64.25 (9.84); 140.46 (12.25)
Completeness (%)	100 (100)	100 (100)	99.2 (97.1)	94.2 (79.8)	100 (99.8); 100 (99.5)
Wilson B-factor (Å ²)	26.9	28.4	28.2	22.2	26.9; 34.57

Table 4.2. Refinement and validation statistics for SFX (room temperature), composite X-ray crystallography and SSX dose series for DtpB. Values in parenthesis refer to the outermost resolution shell. For the SSX structures, a range between the lowest and highest dose is given, with the first value representing dose 1 and the second value dose 8 (the highest dose).

	SFX ferric	SFX ferryl	Composite ferric	Composite ferryl	SSX ferryl
Number of reflections	174340	206723	138089	159452	212461; 57840
Resolution (Å)	13-1.85	13-1.75	49-1.99	47.6-1.85	40.05-1.75; 40.13 - 2.72
R_{work}	0.159	0.167	0.176	0.189	0.209; 0.225
R_{free}	0.192	0.199	0.218	0.232	0.238; 0.281
RMSD bond lengths (Å)	0.012	0.011	0.009	0.009	0.009; 0.003
RMSD bond angles (°)	1.7	1.6	1.6	1.6	1.6; 1.3
Solvent atoms	810	880	1142	1195	408; 3
Ramachandran most favoured (%)	97	97	97	97	98; 97
PDB accession code	6YRJ	6YRD	6YRC	6YR4	Not deposited

4.3. Results

4.3.1. Over-expression and purification of DtpB

An example of a purification for DtpB is shown in Figure 4.2. DtpB over-expressed well in *E. coli* using the method described in Chapter 2. It was purified using Ni²⁺-NTA Sepharose column followed by S200 size-exclusion column. SDS-PAGE analysis of Ni²⁺-NTA elution showed a major band running at ~ 35 kDa, consistent with the expected molecular weight for DtpB monomer (Figure 4.2B), which is absent in the flow-through. Size-exclusion produced a single peak with an elution volume of ~ 70 mL (Figure 4.2A) which was checked using SDS-PAGE revealing a single band running at ~ 35 kDa, consistent with high-purity DtpB.

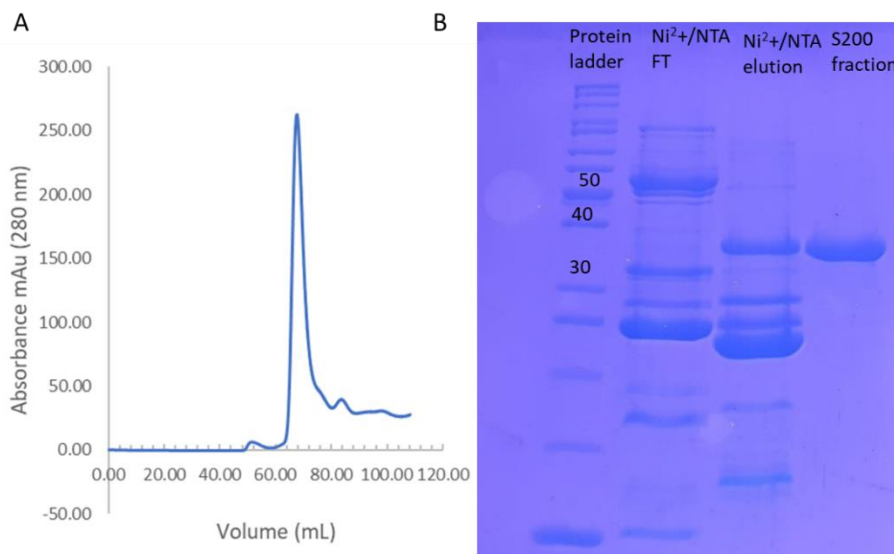


Figure 4.2. DtpB purification. A) S200 size-exclusion Sephadex column absorbance 280 nm (mAu) profile of DtpB eluting at ~ 70 mL. B) Coomassie stained 15 % SDS-PAGE gel analysis of eluted DtpB fractions. A protein band between 30-40 kDa that can be identified as DtpB is present in Ni²⁺-NTA elution together with impurities. The impurities were removed using S200 column, resulting in a single band in the S200 fraction.

4.3.2. The electronic absorbance spectrum of DtpB

DtpB has an electronic absorbance spectrum typical for a high-spin (HS) Fe^{III}-haem featuring a Soret band at 400 nm a Q band at 502 nm, and a charge transfer band at 638 nm (Figure 4.2). Addition of one-molar equivalent of H₂O₂ to Fe^{III}-DtpB leads to rapid formation of a green-coloured species, associated with a 2 nm blue wavelength shift to 398 nm and a flattening of the Soret band in the electronic absorbance spectrum (Figure 4.3). In Q-band region, three new peaks arise at 577 nm, 612 nm and 648 nm (Figure 4.3). These changes are typical for a Compound I species carrying a porphyrin π -cation radical. No further change in the electronic absorbance spectrum following addition of H₂O₂ to DtpB is observed for > 1 h at room temperature (RT), indicating DtpB forms a highly stable Compound I species.

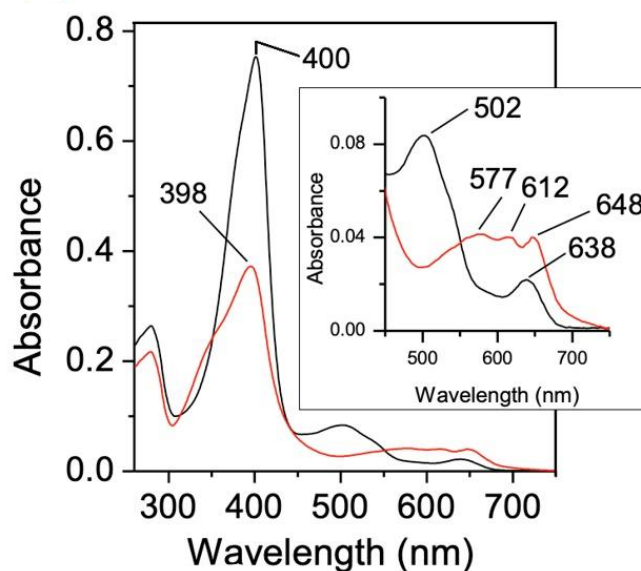


Figure 4.3. Electronic absorption spectrum of Fe^{III}-DtpB (black) and Compound I (red) generated by addition of one-molar equivalent H₂O₂ (pH 5.0). Wavelength (nm) absorbance maxima are indicated. Inset, magnified Q-band region.

4.3.3. EPR spectroscopy of Compound I DtpB

EPR spectroscopy of Fe^{III}-DtpB reveals spectral features typical of a HS Fe^{III}-haem (Figure 4.4). On addition of one-molar equivalent of H₂O₂ to Fe^{III}-DtpB a series of samples were frozen at variable time points and EPR spectrum recorded. After 4 s the HS Fe^{III}-haem signal has all but disappeared (> 1 % of the initial concentration) with a new signal appearing at the g=2 position and a possibly related component at g=2.07. The g=2 signal has a strongly asymmetric line-shape that does not change in intensity over a 30 min period and shows no saturation with microwave power (*inset* Figure 4.4.). Together these features are typical of a highly stable Compound I species carrying a porphyrin π -cation radical.

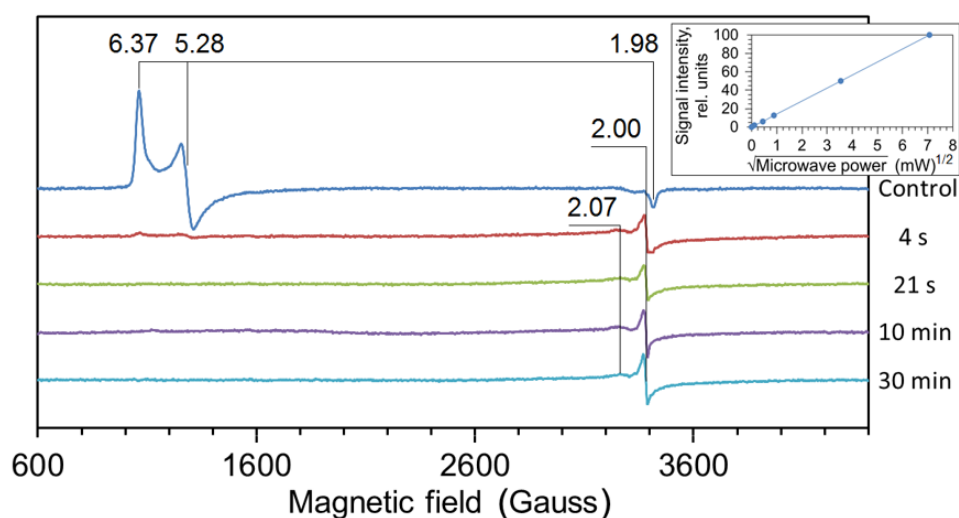


Figure 4.4. X-band EPR spectra (10 K) of Fe^{III}-DtpB (control) and spectra of four samples frozen at variable times after addition of one-molar equivalent H₂O₂. The principle g-values in each spectrum are indicated with the zero field splitting rhombicity parameter $E/D = 0.023$. *Inset*, dependence of the g=2 Compound I signal on microwave power.

4.3.4. Crystal structures of Fe^{III} DtpB

Two validated crystal structures of resting state (ferric) DtpB were obtained, one using the SFX approach on microcrystal slurries loaded on silicon chips and the other by careful on-line monitoring of absorption spectra of larger crystals during data collection, to create a composite low dose data set. For the latter, haem redox state in the crystals was corroborated through analysis of larger DtpB crystals suitable to obtain electronic absorbance spectra at 100 K (Fuchs *et al.*, 2014). Identical electronic absorbance bands to those for Fe^{III} -DtpB in solution were observed in the crystals (Figure 4.5).

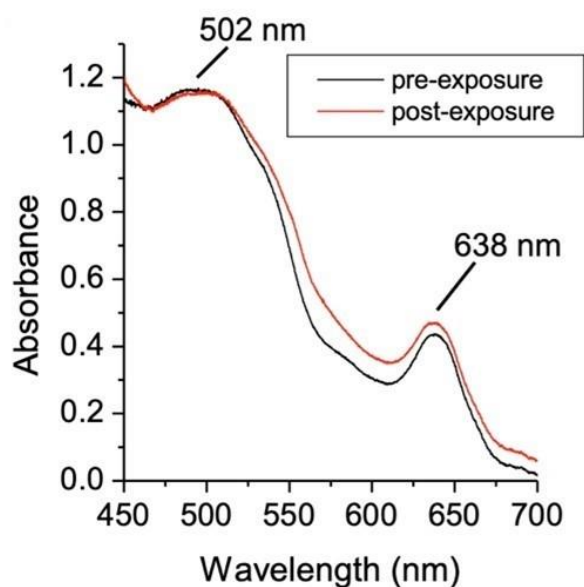


Figure 4.5. Electronic absorption spectra of Fe^{III} DtpB crystals. The α/β band region recorded at 100 K using the on-axis UV-vis microspectrophotometer MS3 at beamline X10SA of the Swiss Light Source. The spectra of pre and post X-ray exposure following collection of a 10° data wedge are shown.

SFX data for Fe^{III} microcrystals of DtpB were collected using the SACLA XFEL beamline BL2 EH3 with help of Brad Davy, Dr. Danny Axford, Dr. Takehiko Tosha, Dr. Hiroshi Sugimoto, Dr. Shigeki Owada, Dr. Ivo Tews and Dr. Robin Owen. The RT SFX structure and 100 K structure of Fe^{III} DtpB were determined to 1.85 Å and 1.99 Å resolution, respectively (Table 4.1 and 4.2), and reveals a hexamer assembly with each monomer displaying a typical DyP two-domain ferredoxin fold (Figure 4.6 and 4.7)

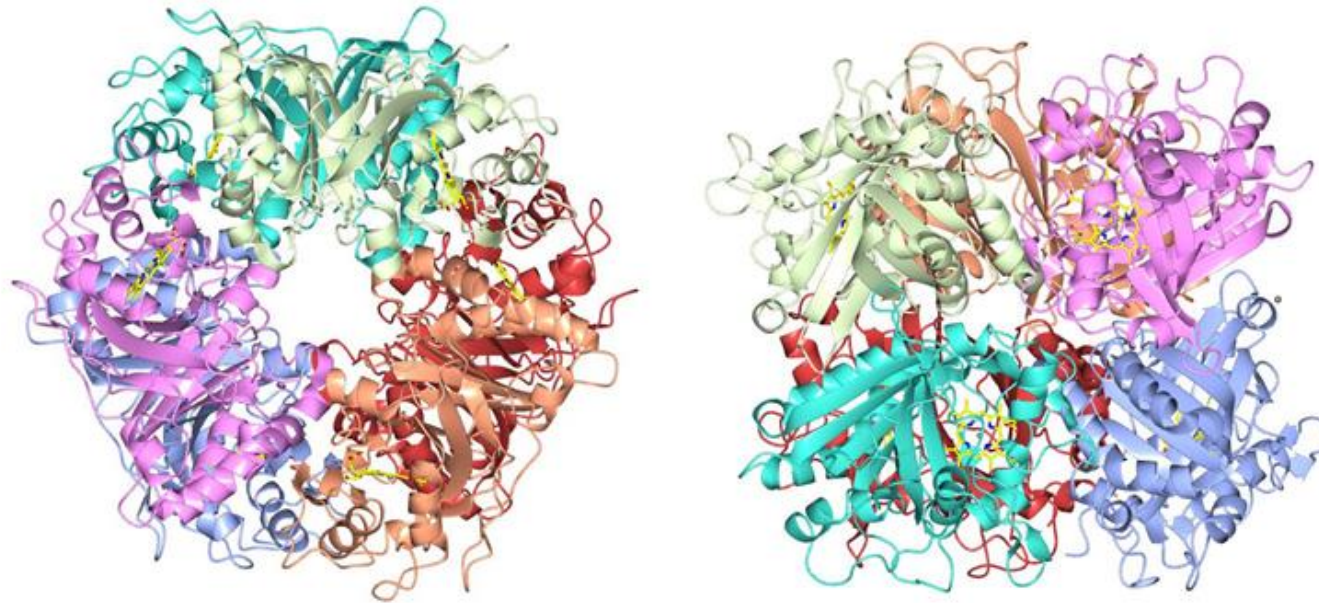


Figure 4.6. Quaternary structure of DtpB hexamer. The RT SFX structure of DtpB hexamer presented at two different angles. Each chain is coloured differently: A: ice blue, B: pale green, C: pink, D: salmon, E: turquoise and F: crimson. The haems are shown in yellow sticks.

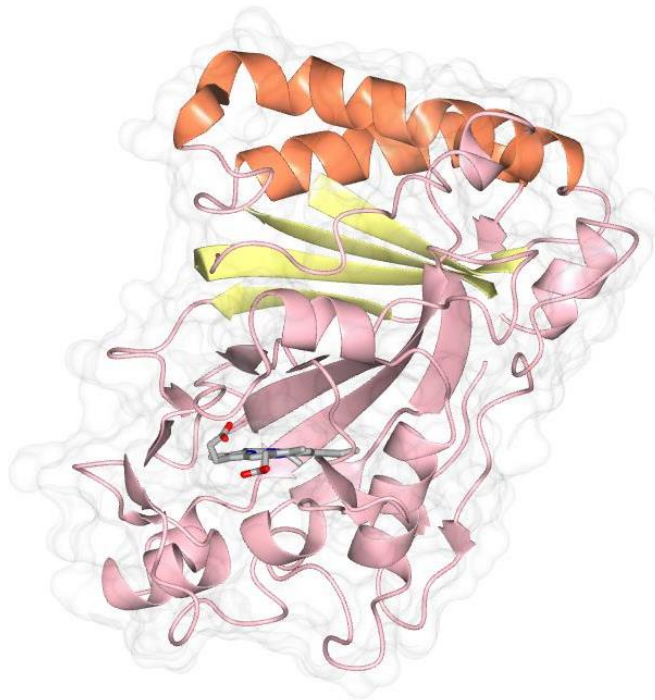


Figure 4.7. Tertiary structure of DtpB. The fold for one of the ferredoxin-like domains is highlighted and the haem is shown in sticks.

Both SFX and spectroscopically validated 100 K composite structure reveal penta-coordinate haem-Fe with axial coordination from a proximal His residue (His225). The distal haem site comprises of highly conserved distal haem pocket residues Arg and Asp (Arg243 and Asp152) and, an additional Asn245 protruding towards haem-Fe (Figure 4.7). A comparison between the haem architecture in the two structures will be made with an assumption that the haem in both is in its ferric state. The effective absorbed dose for both structures (0 kGy for SFX and 11.4 kGY for the composite structure (Table 4.1)) is lower than 40 kGy, a dose reported to be sufficient to cause a

50% reduction of the haem iron redox state independent of oxidation state (*i.e.* Fe^{III} or Fe^{IV}) for cryo-cooled haem protein crystals (Pfanzagl *et al.*, 2020a). Therefore, it is not surprising that there is no significant difference in haem pocket site architecture between RT and 100 K structures (Figure 4.8) as supported by the Fe-His coordinate bond lengths for the haem site (Table 4.3).

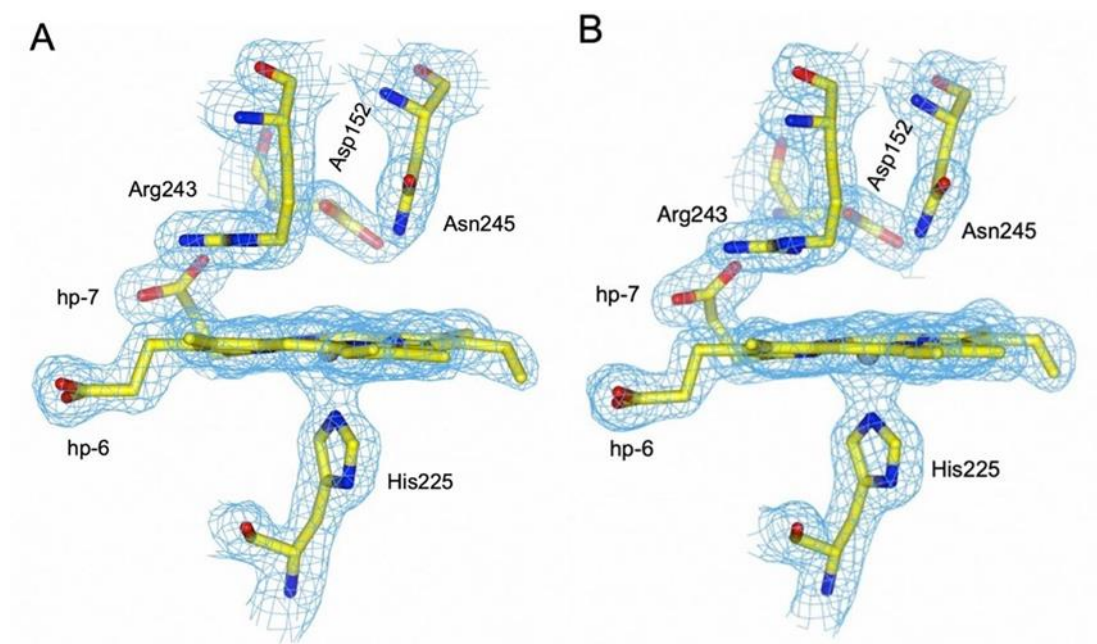


Figure 4.8. $2F_o-F_c$ electron density maps (blue) contoured at 1.4σ of the distal pockets of the Fe^{III} state of DtpB in Chain A at A) 100 K and B) RT.

Table 4.3. Coordinate bond lengths for the Fe^{III} DtpB haem site. The mean distance for haem in each chain of the hexamer is reported together with the associated standard deviation in parentheses.

Chain	SFX ferric Fe-N ^ε His (Å)	Composite ferric Fe-N ^ε His (Å)
A	2.05	2.09
B	2.10	2.10
C	2.04	2.09
D	2.03	2.09
E	2.02	2.01
F	2.00	2.06
Mean distance	2.04 (0.03)	2.07 (0.03)

4.3.5. Crystal structures of Compound I DtpB

Addition of H₂O₂ to both DtpB microcrystals for SFX experiments and large DtpB crystals for 100 K experiments resulted in an instant colour change from brown to green, consistent with Compound I formation. The haem redox state in the crystals was corroborated in the same manner as for Fe^{III} structures, through analysis of larger DtpB crystals suitable to obtain electronic absorbance spectra at 100 K (Fuchs *et al.*, 2014). Identical electronic absorbance bands to those for Compound I in solution were observed in the crystals (Figure 4.9). SFX data for Compound I microcrystals of DtpB were collected using the SACLA XFEL beamline BL2 EH3.

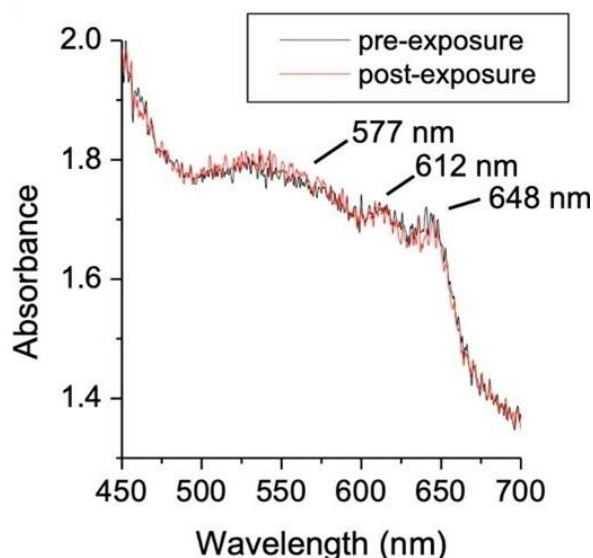


Figure 4.9. Electronic absorption spectra of Compound I DtpB crystals. The α/β band region recorded at 100 K using the on-axis UV-vis microspectrophotometer MS3 at beamline X10SA of the Swiss Light Source. The spectra of pre and post X-ray exposure following collection of an 8° data wedge are shown.

The RT SFX structure and 100 K structure of Compound I DtpB were determined to 1.75 Å and 1.85 Å resolution, respectively (Table 4.1 and 4.2). The SFX structure of the H₂O₂ soaked DtpB revealed a new electron density peak on the distal side of the haem-Fe in each of the six DtpB monomers that make up the hexamer assembly (Figure 4.10A). An oxygen atom has been modelled in each of the chains. Notably, the distance between haem-Fe and the oxygen varies between chains (Table 4.4). The shortest distance is found in chain A at 1.65 ± 0.10 Å (Figure 4.10A), with the mean distance averaged over all six monomers being 1.82 Å (Table 4.4). Notably, other five chains of the hexamer assembly favour longer bond length, closer to the average value (Table 4.4).

A composite Compound I X-ray structure at 100 K was determined to assess temperature effects. The effective absorbed dose was calculated to be 11.3 kGy (Table 4.1), which is again lower than 40 kGy required to reduce 50% of haem-Fe. Composite structure further confirmed the presence of an oxygen atom bound to the haem-Fe, with variability in bond length between chains of the hexamer. A short Fe-O bond of $1.65 \pm 0.14 \text{ \AA}$ is present in chain A, with the mean distance in all six monomers being 1.76 \AA (Figure 4.10B and Table 4.4). A longer Fe-O bond length was again recorded in Chains B – F, with values closer to the average 1.76 \AA (Table 4.4).

The presence of an oxo group enables a new distal site H-bond network to be established on forming Compound I as illustrated in Figure 4.10. A small inwards movement of the Asn245 side chain with respect to its position in the Fe^{III} state is a direct result of the side chain amide H-bonding to the oxo group (2.78 \AA mean value, Table 4.4) (Figure 4.10). Similarly, a subtle rotation of the guanidinium group of Arg243 occurs through H-bonding of the N^{n1} atom to the oxo group (2.82 \AA mean value, Table 4.4) (Figure 4.10).

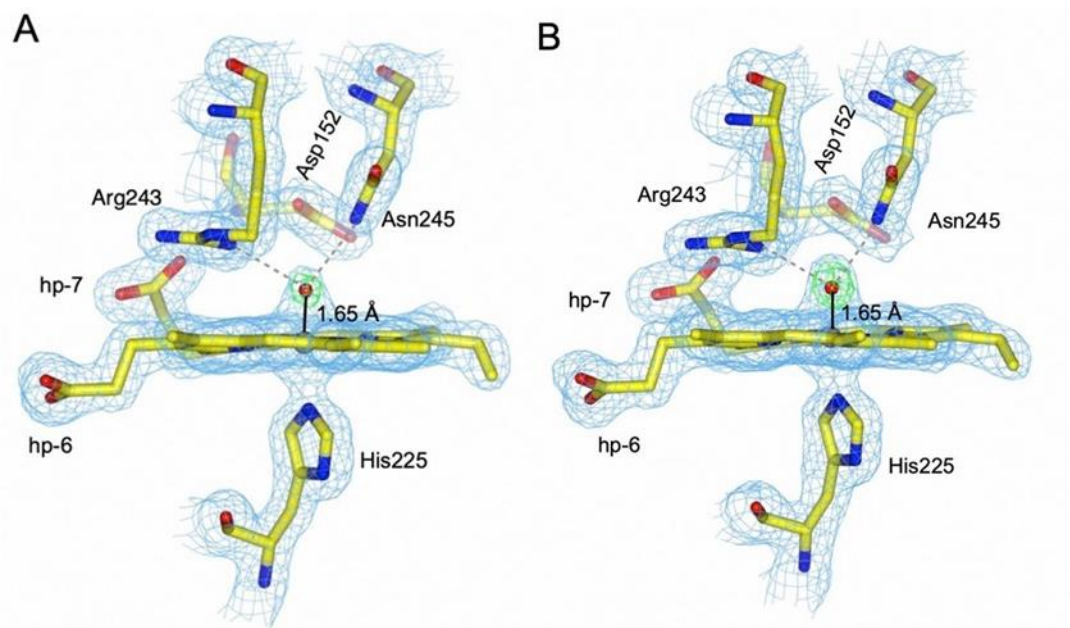


Figure 4.10. Distal pockets of the Compound I state determined at A) RT and B) 100 K. $2F_o-F_c$ electron density maps (blue) contoured at 1.4σ . The F_o-F_c omit map (green) is also shown, contoured at A) $\pm 10 \sigma$ and B) $\pm 7.5 \sigma$. This was calculated after refinement omitting the oxygen atom (red sphere). The Fe-O coordination bond is shown as a solid black line and H-bond interactions involving the O atom are indicated with grey dashed lines.

Table 4.4. Coordinate bond lengths for the Compound I DtpB haem site. Distances for the distal triad of Asp152, Arg243 and Asn245 to the oxo in the ferryl structures are measured from the closest O^δ atom of Asp152, the Nⁿ¹ atom of Arg243 and the side-chain amino group of Asn245. The mean distance for the six chains in the hexamer is reported together with the associated standard deviation in parentheses.

Chain	SFX ferryl					Composite ferryl				
	Fe-N ^ε His (Å)	Fe=O (Å)	Fe=O-Asp (Å)	Fe=O-Arg (Å)	Fe=O-Asn (Å)	Fe-N ^ε His (Å)	Fe=O (Å)	Fe=O-Asp (Å)	Fe=O-Arg (Å)	Fe=O-Asn (Å)
A	2.08	1.65	4.39	2.89	2.96	2.09	1.65	4.33	2.94	2.84
B	2.13	1.89	4.95	2.83	2.72	2.16	1.81	4.19	3.00	2.66
C	2.11	1.89	4.25	2.76	2.67	2.14	1.75	4.12	2.86	2.70
D	2.08	1.85	4.28	2.86	2.78	2.16	1.83	4.21	2.69	2.68
E	2.06	1.83	4.43	2.79	2.77	2.10	1.84	4.16	2.66	2.76
F	2.12	1.80	4.28	2.79	2.80	2.07	1.70	4.37	2.77	2.98
Mean distance	2.10 (0.02)	1.82 (0.08)	4.43 (0.24)	2.82 (0.04)	2.78 (0.09)	2.12 (0.04)	1.76 (0.07)	4.23 (0.09)	2.82 (0.12)	2.77 (0.11)

4.3.6. SSX dose series on Compound I DtpB

The effect of accumulated dose on the Fe-O bond length of Compound I DtpB was investigated using SSX. Compound I was chosen as the target to monitor dose dependent following of Fe-O distance as previously described for DtpAa (Ebrahim *et al.*, 2019). In DtpAa dose dependent migration of water coordinating the haem was followed, instead of oxygen (Ebrahim *et al.*, 2019). Since resting state DtpB is ‘dry’, such method was not applicable to Fe^{III}-DtpB and thus, Fe^{IV} was chosen. The SSX was carried out at Diamond Light Source beamline I24 using the same chip and translation system as used for SFX at SACLA. In total, 8 dose-resolved structures were obtained from a single fixed target, with a dose increment of 48.4 kGy. Notably, already the first

dose is higher than 40 kGy implicating that less than 50% of Fe^{IV}-DtpB is present in any SSX structure (Pfanzagl *et al.*, 2020a).

Looking into the Fe^{IV}-haem environment, an increase in Fe-O bond length with accumulated dose is evident, however, with a significant difference between chains of the hexamer assembly (Figure 4.10). For example, in Chain B, the oxygen density peak disappears quickly, already after the second exposure of the soaked crystals to the beam (*i.e.*, after accumulated dose is higher than 96.8 kGy) (Figure 4.11). The Fe-bound oxygen is present for the longest time in Chain C, “surviving” all eight doses (387.2 kGy) and migrating from 1.89 ± 0.08 Å Fe-O distance measured in SSX structure to 2.55 ± 0.39 Å measured in dose 8 structure (Figure 4.11 and 4.12). Chain C is followed by Chain A and F where the oxygen “survived” 193.6 kGy, Chain D (145.2 kGy) and Chain E (145.2 kGy) (Figure 4.10). Figure 4.12 serves as illustration of oxygen migration from the haem-Fe using Chain C as a model.

Consistent with the prediction that even at dose 1 there is less than 50% of Fe^{IV}-haem present, it is apparent that measured Fe-O bond length is longer in SSX structures than in zero dose SFX structure (Figure 4.11). At dose 1, the bond length varies in range between 1.86 Å and 1.96 Å. Bond length elongation is the most accentuated in Chain A, the chain with the shortest zero-dose bond length, with an initial increase of 0.26 Å after 48.4 kGy that levels off with additional exposure.

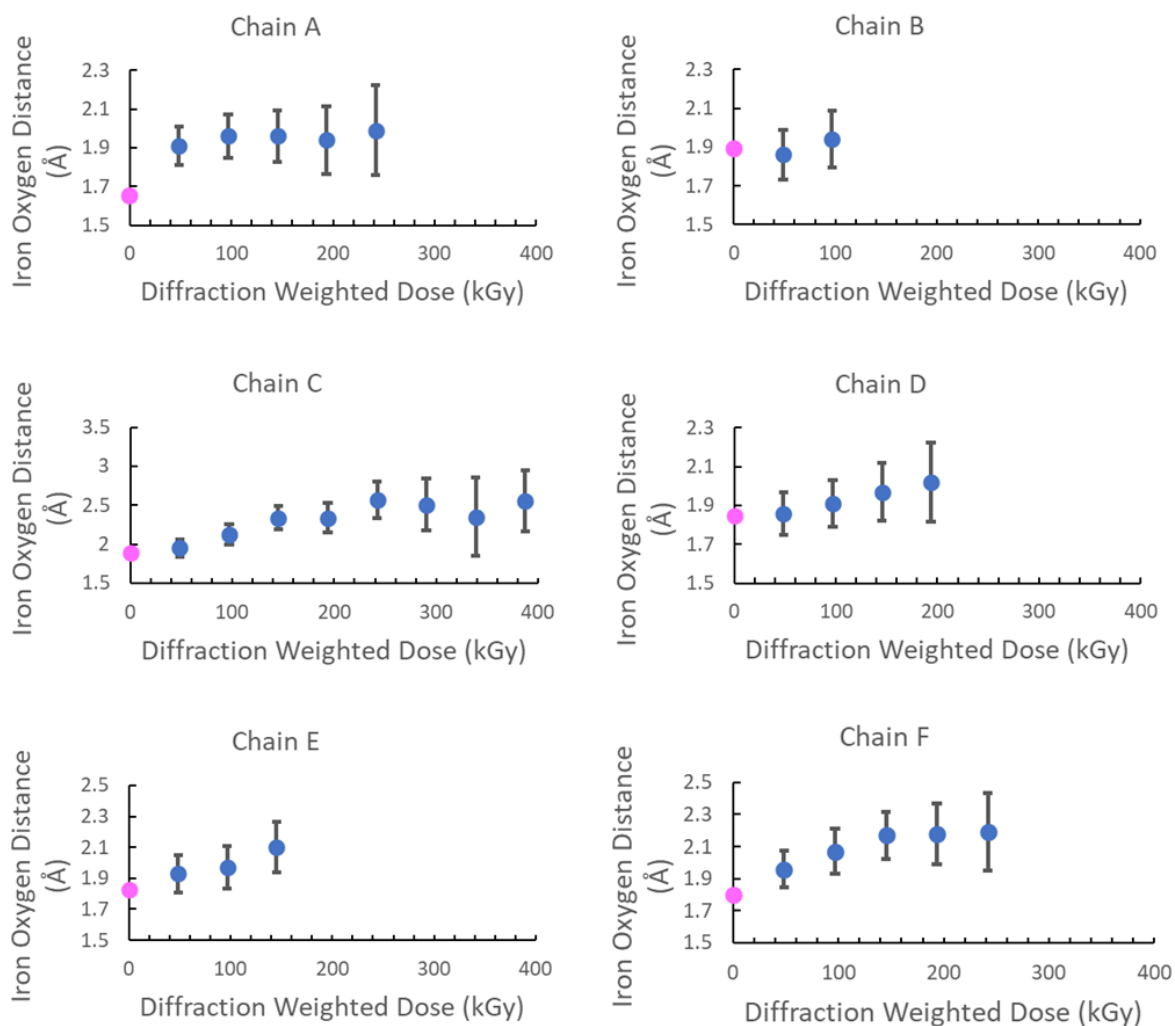


Figure 4.11. Dose dependent elongation of the Fe-O bond of the each chain in DtpB hexamer assembly. For each chain, measured Fe-O distance is plotted as function of dose. Fe-O bond length obtained from the SFX structure for the relevant chain is plotted as the zero-dose point (pink dot). Error bars shown are the estimated standard uncertainty in bond length obtained from the DPI value of the Fe and O atoms (Kala Sekar *et al.*, 2015).

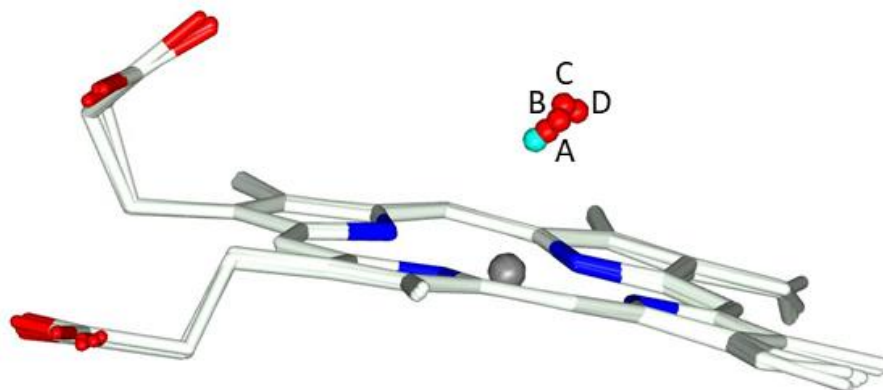


Figure 4.12. Superposition of Chain C haem across selected dose series structures revealing dose-dependent migration of the oxygen from the haem-Fe. The SFX oxygen is shown in cyan and SSX in red as follows: A) 96.8 kGy, B) 145.2 kGy, C) 242 kGy, D) 387.2 kGy.

4.4. Discussion

DtpB was successfully over-expressed and purified using the procedure previously established for DtpAa (see Chapter 2). After purification, spectral characteristics of DtpB resting and transient states were assessed and compared to DtpA (Chaplin *et al.*, 2017) and DtpAa from *S. lividans* as shown in Table 4.5.

Table 4.5. Wavelength absorbance maxima at pH 7.0 for DtpAa, DtpA and DtpB.

Protein	Ferric (nm)	Compound I (nm)	Compound II (nm)
DtpAa	406, 500, 540 (sh) ^a , ~ 588, 630	^c 403, 534, 588, 614, 641	416, 527, 557, 620
DtpA ^b	406, 502, 540 (sh), 635	399, 530, 557, 614, 644	419, 528, 557, 621
DtpB	400, 502, 542, 638	398, 577, 612, 648	n.d.

^aShoulder (sh)

^bValues taken from (Chaplin *et al.*, 2017).

^cValues taken from global fitting of the spectral transitions observed upon mixing with H₂O₂ in stopped-flow spectrophotometer.

Upon addition of H₂O₂ to the Fe^{III}-DtpB, DtpB retains characteristic spectral transition to Compound I (Fe^{IV}-DtpB). It was found that Fe^{IV}-DtpB is a highly stable species (>1 hour) making it an attractive model to study using different X-ray approaches, including even the chip based SFX approach. Data collection for this approach takes >15 min *i.e.*, it is impossible to obtain structures of short-lived catalytic intermediates using this method. However, the highly stable DtpB Compound I permits such structural investigation. In addition to SFX, DtpB is an ideal candidate for SSX and

composite low-dose cryo-crystallography. In this Chapter, three methods have been applied in attempt to obtain redox state validated Fe^{III}-DtpB and Fe^{IV}-DtpB structures. Detailed description and comparison of obtained structures follows.

Firstly, resting state Fe^{III}-DtpB distal haem site was inspected (Figure 4.8). No immediate differences were observed between the 100 K structure (dose 11.4 kGy) and the zero-dose SFX structure. SSX approach was not used on ferric DtpB. Fe^{III}-DtpB revealed several differences when compared with the other redox state validated Fe^{III} structures of the *S. lividans* DyPs, DtpA (Chaplin *et al.*, 2019) and DtpAa (Ebrahim *et al.*, 2019; Lučić *et al.*, 2020a) (Figure 4.13). The haem-Fe in DtpB is penta-coordinate and sits out of the porphyrin plane towards the proximal His225 ligand. Such a distortion results in a short Fe^{III}-N^δ-His bond-length (2.05 ± 0.11 Å in chain A) compared to 2.19 Å reported in Fe^{III}-DtpA and Fe^{III}-DtpAa (Chaplin *et al.*, 2019; Ebrahim *et al.*, 2019; Lučić *et al.*, 2020a). The N^ε of His225 is H-bonded to the O^{δ2} atom of Asp287, an interaction that imparts significant imidazolate character in histidine ligated haem peroxidases resulting in increased electron-donating ability (Poulos, 2014). Fe^{III}-DtpA and Fe^{III}-DtpAa have a hexa-coordination haem geometry with a H₂O molecule occupying the distal coordination position, which forms the base for an extensive H-bonded H₂O network connecting the distal haem-Fe to bulk solvent (Chaplin *et al.*, 2019). This H₂O network communicates with the distal Asp (Figure 4.13), which in DtpA is optimised for rapid proton movement and Compound I formation (Lučić *et al.*, 2020a). The distal haem site in the immediate vicinity of the Asp/Arg couple of Fe^{III}-DtpB is thus ‘dry’, which has the effect of isolating Asp152 from communication with the haem. Moreover, once peroxide is bound the absence of the H₂O-Asp unit makes the distance directly from an O^δ atom of Asp152 to the Fe^{III}-

HOOH complex $\sim 3.5 \text{ \AA}$ which would not be optimal for either direct proton abstraction or delivery to Compound 0 ($\text{Fe}^{\text{III}}\text{-OOH}^-$). The absence of a distal haem-Fe H_2O chain in $\text{Fe}^{\text{III}}\text{-DtpB}$ coincides with the protrusion into the distal site of Asn245, with its side chain amide occupying the spatial position where a H_2O molecule (w2, Figure 4.13) is located and H-bonded to the distal Asp in the $\text{Fe}^{\text{III}}\text{-DtpA}$ and $\text{Fe}^{\text{III}}\text{-DtpAa}$ structures. This H_2O -Asp unit facilitates rapid formation of Compound I in DtpA (Lučić *et al.*, 2020a). Asn245 therefore adds a steric impediment to the distal site in DtpB, and consequently prevents the formation of the haem-Fe H_2O networks observed in DtpA and DtpAa (Chaplin *et al.*, 2019; Ebrahim *et al.*, 2019; Lučić *et al.*, 2020a). As this network is essential for efficient Compound I formation in DtpA (Lučić *et al.*, 2020a) its absence demonstrates that such mechanism cannot occur in DtpB and an alternative must be sought. Thus, $\text{Fe}^{\text{IV}}\text{-DtpB}$ was structurally inspected.

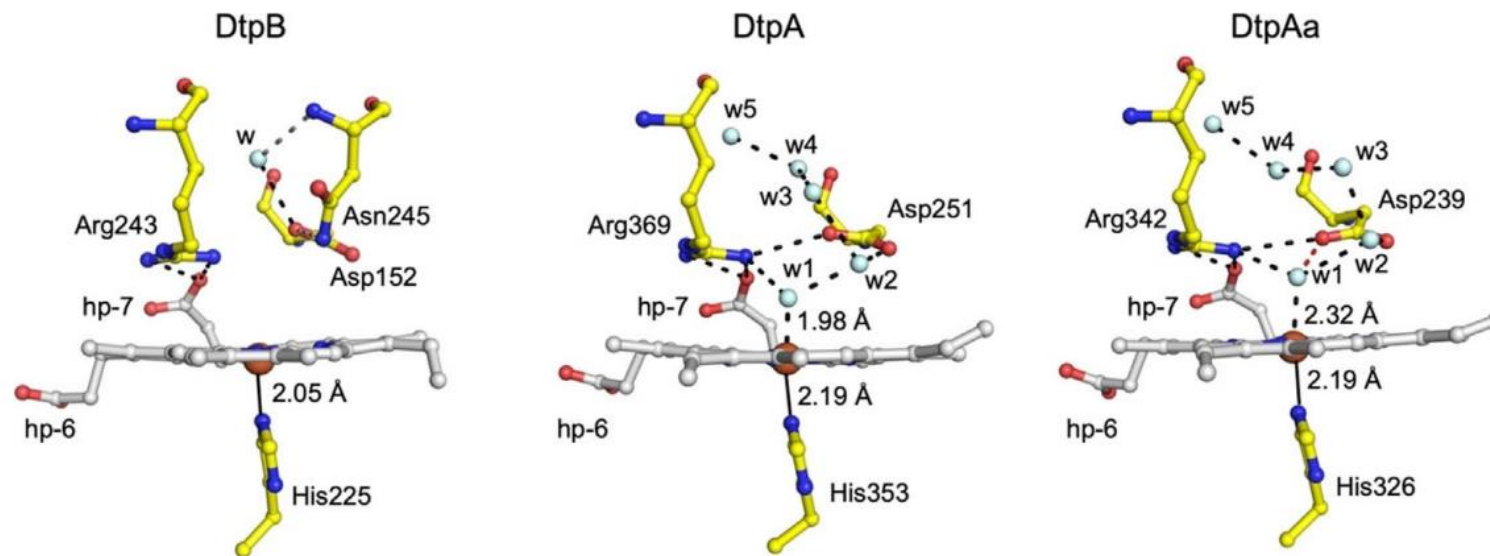


Figure 4.13. The SFX haem site structure of Fe^{III}-DtpB and comparison with the redox state validated Fe^{III}-DtpA (Chaplin *et al.*, 2019) and Fe^{III}-DtpAa (Ebrahim *et al.*, 2019) structures. Water molecules (w) are depicted as cyan spheres, hp refers to haem propionate groups and H-bond interactions are shown as dashed lines. In DtpAa the red dashed line indicates an additional H-bond to w1 that is absent in DtpA - a feature that influences Compound I formation (Lučić *et al.*, 2020a).

Upon soaking of DtpB crystals in H₂O₂, three approaches were used to measure Compound I DtpB structure. Two redox-state validated structures were obtained, one using zero-dose SFX approach and the other using low-dose (11.3 kGy) 100 K composite approach. Additionally, dose series using SSX were collected, however, accumulated dose in the first SSX structure (dose 1) has already surpassed 40 kGy required to reduce 50% of haem-Fe (Pfanzagl *et al.*, 2020a) and thus, does not represent a redox validated structure. The effect of dose accumulation measured using dose series will be discussed later.

Compared to the Fe^{III}-DtpB, Compound I structures reveal an additional feature: oxygen atom bound to the haem-Fe (Berglund *et al.*, 2002; Casadei *et al.*, 2014; Chreifi *et al.*, 2016; Gumiero *et al.*, 2011; Meharena *et al.*, 2010; Stone *et al.*, 2005; Yosca *et al.*, 2016). The formation of Compound I in DtpB coincides with the formation of a new H-bond network centred around the oxo group which accepts H-bonds from the amino group of Asn245 and the Nⁿ¹ atom of Arg243. Utilizing nitrogen atoms as H-bond donors to the oxo group is a feature in the Fe^{IV}=O structures of CcP and ascorbate peroxidase (APX) (Chreifi *et al.*, 2016; Gumiero *et al.*, 2011), where an indole ring N^ε atom of a Trp and a N^ε atom of the distal Arg (as opposed to the Nⁿ¹ atom in DtpB) act as donors. For the N^ε atom of the Arg to H-bond to the oxo in CcP and APX its side chain must adopt an “in” conformation as opposed to the “out” conformation observed in the Fe^{III} structure (Bonagura *et al.*, 2003; Gumiero *et al.*, 2011). No Arg side chain switching is observed for DtpB, which is fixed in position by H-bonds from the O1 atom of haem propionate-7 to the Nⁿ¹ atoms in both the Fe^{III} and Fe^{IV}=O states. These H-bonding interactions together with the porphyrin- π cation radical withdrawing electron density from the oxo group, will make the protonation of the Fe^{IV}=O difficult.

Given that protonation is a precursor for the oxo species to act as a potent oxidant, the combination of Arg and Asn as H-bonding donors must tune the pK_a of the oxo in DtpB to result in a stable, unreactive Compound I. Compound I $t_{1/2}$ times for the bacterial DyPs from *Rhodococcus jostii* RHA1 (Singh *et al.*, 2012) and *Bacillus subtilis* (Mendes *et al.*, 2015b), which both possess a distal Asn, are reported to be 540 s and 3.2 h, respectively. Therefore, the structures of the $Fe^{IV}=O$ DtpB illustrate that the interaction of the Asn with the oxo group must, amongst other factors, serve to stabilize Compound I.

The reactivity of the ferryl species is controlled by protonation. Assigning them as protonated or unprotonated can be implied indirectly by the Fe-O bond length, which is often used to determine bond order *i.e.* single or double bond and thus protonation state. For Chain A, a Fe^{IV} -O bond length of 1.65 Å is present, in both the SFX and 100 K composite structures. This bond length falls within the expected range for a $Fe^{IV}=O$ species and is in line with the most reliable bond lengths (*i.e.* X-ray structures agree with spectroscopy) determined for Compound I species in proteins (1.63 to 1.73 Å) (Berglund *et al.*, 2002; Casadei *et al.*, 2014; Chreifi *et al.*, 2016; Gumiero *et al.*, 2011; Meharena *et al.*, 2010; Stone *et al.*, 2005; Yosca *et al.*, 2016). In the other five chains, variation in the Fe-O bond length (1.70 to 1.89 Å) at both room temperature and 100 K is evident.

Lengthening of the Fe^{IV} -O bond can indicate the formation of an Fe^{IV} -OH or Fe^{III} -OH species (Behan and Green, 2006; Green, 2006). For an Fe^{IV} -OH species an Fe-O bond distance determined through spectroscopic approaches lies between 1.76-1.82 Å (Newcomb *et al.*, 2008; Stone *et al.*, 2006), whereas Fe^{III} -OH is longer > 1.85 Å (Green,

2006). In peroxidases and globins with histidine-ligated haem, no spectroscopic evidence for a $\text{Fe}^{\text{IV}}\text{-OH}$ Compound II species has been reported, in accord with the chemistry of peroxidases (*i.e.* one-electron oxidation of substrates as opposed to C-H bond activations as is the case in cytochrome P450s). However, the observation of positive nuclear density next to the Fe-O bond in the neutron structure of APX Compound II supports a hydroxide species (Kwon *et al.*, 2016). A Fe-O bond distance of 1.88 Å has been determined and the investigators assign this species as a $\text{Fe}^{\text{IV}}\text{-OH}$ (Kwon *et al.*, 2016). More recently a XFEL study (100 K) with APX Compound II reveals a Fe-O bond distance of 1.87 Å (Kwon *et al.*, 2021a) and thus confirming the distance obtained by neutron (Kwon *et al.*, 2016). These zero dose structural studies suggest that the Compound II species generated in APX could be an outlier amongst peroxidases, in that an $\text{Fe}^{\text{IV}}\text{-OH}$ species is formed. However, this view contrasts to spectroscopy data obtained with EXAFS and Mössbauer (Ledray *et al.*, 2020), and more recently NRVS (Nuclear Resonance Vibrational Spectroscopy) (Ledray *et al.*, 2021) where an Fe-O bond distance of 1.68 Å for APX Compound II is determined, consistent with an unprotonated $\text{Fe}^{\text{IV}}\text{=O}$ species (Green, 2006). Thus, a disagreement between spectroscopy data and zero dose structures exists.

For DtpB the heterogeneity in the Fe-O bond lengths is difficult to explain. X-ray induced reduction would appear unlikely considering the low absorbed dose for the 100 K structure (11.3 kGy) and that the SFX approach safeguards against site-specific radiation damage occurring. Furthermore, the *in situ* microspectrophotometry measurements of the crystal after exposure reveal no evidence for a mixed valence species (Lučić *et al.*, 2020b). However, the increase in bond lengths would suggest a partial onset of reduction of the $\text{Fe}^{\text{IV}}\text{=O}$ species. It may be that endogenous reductants

that depend on local environment which differ in each chain could be causing these changes. Thus, further investigation through the acquisition of dose series data was conducted (*i.e.* by feeding electrons into the system via radiolysis) in hope to shed light into the heterogeneity of Fe-O bond lengths observed amongst different DtpB chains.

First of all, it is important to note once more that the dose 1 structure already represents a mixed valence species as the total accumulated dose exceeds 40 kGy (dose increment is 48.4 kGy). This agrees with lengthening of the Fe-O bond, now measured to be between 1.86 Å and 1.96 Å for dose 1, due to reduction of Fe^{IV}=O. With further dose increase, further bond elongation is evident, suggesting that now a higher percentage of total haem-Fe is reduced, and it continues to increase until electron density from oxo group disappears. Dose dependent elongation differs among the chains with Chain B being the most susceptible and Chain C the most resistant to radiation damage. Such variability might be caused by difference in solvent percentage in local environment of each haem, with one haem being more solvent accessible than the other.

Unanswered questions still remain. Variability of Fe-O bond length in zero-dose structure, where haem reduction is no longer an issue, is difficult to explain. A recent report presents evidence that Fe-O bond is flexible and can be moderated by variables such as axial ligand, local charge, temperature, secondary coordination sphere and in particular hydrogen bonding (Kwon *et al.*, 2021). Subtle differences in local environment of each haem, for example caused by accessibility, might moderate Fe-O bond length. Fe-O bond's ability to flex could be prerequisite for efficient catalytic turnover of some enzymes. The longer bond in Compound II APX may be essential for facilitating of proton movement in and out of the active site (Kwon *et al.*, 2021). In

contrast, in CcP, which has an almost identical haem active site as the APX, a rigid Fe-O bond is found which coincides with CcP not needing a shuttle mechanism that transfers protons from substrate to the ferryl haem (Kwon *et al.*, 2021). Thus, formation of ferryl intermediates is incredibly fine-tuned and defines the enzyme functionality. In the following Chapter, such intricacies will be studied and a detailed mechanism of Compound I and II formation in DtpB will be explored.

Chapter Five

Exploring the catalytic mechanism of a B-type dye-decolorizing peroxidase from *Streptomyces lividans*

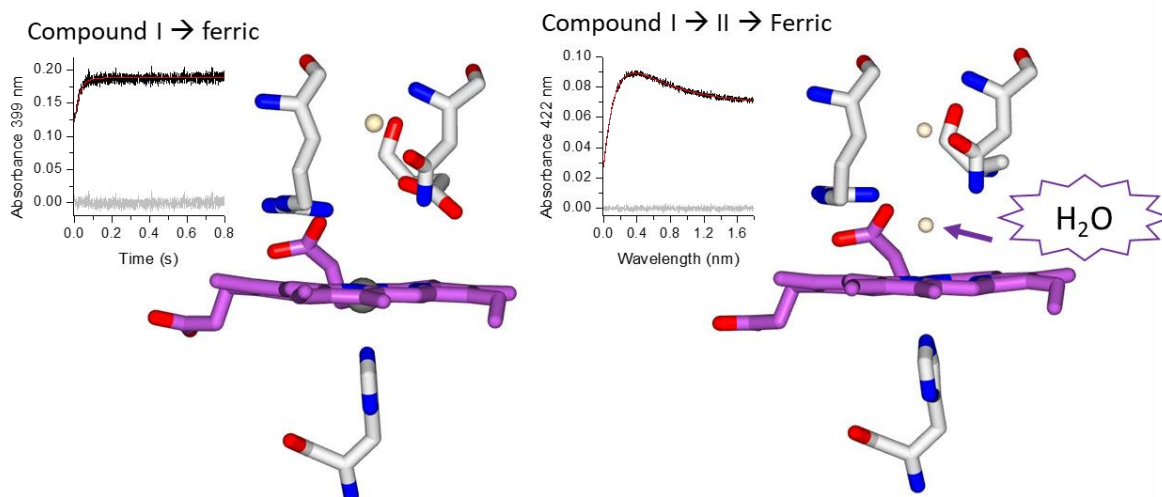


Figure 5. Absence of water molecule in the haem environment affects the DtpB chemistry. Compound II formation in DtpB requires a proton coupled electron transfer to the ferryl haem and is faster in DtpB variants, which possess a water molecule in the active site, than in WT that has a “dry” site.

Some of the results presented in this Chapter have been published in:

M. Lučić, D. A. Svistunenko, M. T. Wilson, A. K. Chaplin, B Davy, A. Ebrahim, D. Axford, T. Tosha, H. Sugimoto, S. Owada, F. S. N. Dworkowski, I. Tews, R. Owen, M. A. Hough and J. A. R. Worrall. Serial femtosecond zero dose crystallography captures a water-free distal haem site in a dye-decolourising peroxidase to reveal a catalytic role for an arginine in $\text{Fe}^{\text{IV}}=\text{O}$ formation. *Angewandte Chemie*, 2020, doi:10.1002/anie.202008622

5.1. Introduction

A distinguishing feature of DyPs is the presence of a distal haem pocket Asp residue (Sugano *et al.*, 2007) in place of a His residue found in non-mammalian peroxidases (Sugano, 2009; Sugano *et al.*, 2007). The distal His plays a prominent role in enhancing the rate of Compound I formation (Erman *et al.*, 1993; Howes *et al.*, 1997; Rodriguez-Lopez *et al.*, 2001). In addition to the His, a conserved distal pocket Arg is indirectly involved in Compound I formation (Hiner *et al.*, 2002; Rodriguez-Lopez *et al.*, 2001). The distal Arg is also conserved amongst DyP members. Studies on a handful of DyPs have provided evidence to indicate that the Arg is directly involved in Compound I formation, implying a catalytic role as a proton acceptor and donor (Lučić *et al.*, 2020b; Mendes *et al.*, 2015a; Singh *et al.*, 2012), whereas in other DyPs the Asp has been reported to act as the acid-base catalyst (Chen *et al.*, 2015; Lučić *et al.*, 2020a; Pfanzagl *et al.*, 2019; Shrestha *et al.*, 2017; Sugano *et al.*, 2007). Thus, there would appear to be a mechanistic variation in Compound I formation amongst DyPs and the question of why Asp or Arg is selected to facilitate proton transfer and rate enhancement of O-O fission amongst DyP members is not fully understood.

In this Chapter, the role of the distal haem pocket residues in the catalytic mechanism of DtpB has been probed through determining zero dose SFX structures of distal pocket variants, together with spectroscopic and kinetic data to reveal how Arg is “selected” by certain DyPs to act as a base catalyst for Compound I formation. Furthermore, this Chapter also focuses on Compound I reduction and gives insight into how “dry” or “wet” haem pocket can influence catalytic mechanism by affecting proton coupled electron transfer efficiency.

5.2. Experimental procedures

5.2.1. Site-directed mutagenesis

Single amino acid substitutions were created using the QuikChange protocol (Stratagene). The pET28*dtpB* was used as template to create mutations that would result in the D152A, N245A and R243A mutants, using primers listed in Table 5.1. For construction of the D152A/N245A (DM), the pET28*dtpB* plasmid containing the D152A mutation was used as template together with the N245A primers. A PCR mix consisting of the respective primers (75 ng/μL), the template (15 ng/μL), 10 mM dNTPs (Fermentas), *Pyrococcus furiosus* (*Pfu*) Turbo polymerase (Agilent), 10 x *Pfu* buffer (Agilent), 8% DMSO and deionised H₂O was prepared and subjected to the following PCR cycle; 95 °C for 3 min; 16 cycles of 95 °C for 1 min, 62 °C for 1 min (D152A and DM) or 64 °C for 1 min (N245A) or 54 °C for 1 min (R243A) and 72 °C for 8 min; 72 °C for 15 min. Clones were corroborated for the presence of the desired mutation by DNA sequencing (Eurofins).

Table 5.1. Mutagenic primer pairs used to generate D152A, N245A, R243A and D152A/N245A DtpB mutations.

Mutation	Primer
D152A	F: 5'-CTCGGTTTCGTCGCCGGCACGGAGAAC-3'
	R: 5'-GTTCTCCGTGCCGGCGACGAAACCGAG-3'
N245A	F: 5'-GAGATCCTGCGGGACGCCATGCCCTTCGGGTC-3'
	R: 5'-GACCCGAAGGGCATGGCGTCCCGCAGGATCTC-3'
R243A	F: 5'-CGATCTGGAGATCCTGGCGGACAACATGCCCTTC-3'
	R: 5'-GAAGGGCATGTTGTCCGCCAGGATCTCCAGATCG-3'

5.2.2. Over-expression and purification

DtpB and the variants were over-expressed in *E. coli* BL21 (DE3) cells and purified applying protocols used for the wild-type DtpB (see Chapter four). Following purification, the enzymes were stored at $-20\text{ }^{\circ}\text{C}$ in 20 mM sodium phosphate buffer, 300 mM NaCl pH 7.0.

5.2.3. Sample preparation

DtpB and the variants were exchanged into a desired buffer using a PD-10 column (Generon) and concentrated using centrifugal ultrafiltration devices (Vivaspin GE Healthcare). Buffers used were 50 mM sodium acetate pH 5.0, 150 mM NaCl; 20 mM sodium phosphate 300 mM NaCl, pH 7.0 and a mixed buffer system comprising of 10 mM Tris, 10 mM MES, 10 mM MOPS, 10 mM sodium acetate, 200 mM potassium chloride with the pH adjusted between values of 4 and 8 as required. Enzyme concentration was determined by UV-visible spectroscopy (Varian Cary 60 UV-visible spectrophotometer) using an extinction coefficient (ϵ) at 280 nm of $111,450\text{ M}^{-1}\text{ cm}^{-1}$ (See Chapter four). H_2O_2 solutions were prepared from a stock (Sigma-Aldrich) with the final concentration determined spectrophotometrically using an $\epsilon = 43.6\text{ M}^{-1}\text{ cm}^{-1}$ at 240 nm (Gasteiger *et al.*, 2003). Potassium ferrocyanide ($\text{K}_4[\text{Fe}(\text{CN})_6]$) (Sigma-Aldrich) concentrations were also determined using absorbance spectroscopy using $\epsilon = 1.046\text{ M}^{-1}\text{ cm}^{-1}$ at 420 nm. The required deuterated buffers were prepared in 99.9% D_2O (Sigma). Highly concentrated enzymes, $\text{K}_4[\text{Fe}(\text{CN})_6]$ and H_2O_2 stocks were diluted directly in D_2O and left to equilibrate in the D_2O solutions for ~ 1 h before analysis.

5.2.4. Stopped-flow absorption spectroscopy

Transient kinetics of the interaction of H₂O₂ with ferric DtpB and variants and reduction of Compound I intermediate were performed using a SX20 stopped-flow spectrophotometer (Applied Photophysics, UK) equipped with a diode-array multi-wavelength unit and thermostatted to 25 °C. Compound I formation was monitored at pH values ranging between 4.0 and 8.0 or 4.5 and 8.0 for the DM. Enzyme solutions (10 μM before mixing) were prepared in the appropriate buffer and mixed with a series of H₂O₂ concentrations (ranging from 20–5000 μM before mixing, depending on enzyme used). Compound I reduction was monitored at pH 5.0 (or 5.8 for D152A and DM) and pH 7.0. Compound I was prepared by adding one equivalent of H₂O₂ or D₂O₂ to the WT and D152A and then mixed with an excess of K₄[Fe(CN)₆] (20–10 000 μM before mixing, depending on pH). To monitor the Compound I reduction in N245A and DM, enzyme was pre-loaded with one equivalent of H₂O₂ or D₂O₂ and rapidly transferred to the stopped-flow working syringe, before rapidly mixing with an excess of K₄[Fe(CN)₆] (20–10 000 μM before mixing, depending on pH). The overall spectral transitions were monitored and fitted to models in the Pro-K software (Applied Photophysics, UK) to yield pseudo-first order rate constants for Compound I formation and where appropriate reduction.

5.2.5. Crystallisation of DtpB variants

Microcrystals of ferric D152A and N245A DtpB variants were grown under batch conditions by mixing in microfuge tubes a 1:1 v/v ratio of a solution containing 6 mg/mL protein in 20 mM sodium phosphate, 300 mM NaCl pH 7.0 with a precipitant solution consisting of 150 mM MgCl₂, 150 mM HEPES, 20% PEG 4000 with the pH adjusted to 7.5, to give a final volume of 200 μL. Microcrystals (~100 x 20 μm) grew

at room temperature within a week. Prior to shipping to SACLA the microcrystal suspension was spun down and nearly all the mother-liquor containing buffer and precipitant solution removed. The resulting crystal pellet (~ 200 μL) was then combined from several batches (in total 1-2 mL of crystal slurry) into one microfuge tube and shipped to SACLA with a small amount (~20 μL) of mother-liquor layered on top of the pellet.

5.2.6. Serial femtosecond X-ray crystallography

SFX data were measured at SACLA beamline BL2 EH3 at room temperature using an X-ray energy of 9.99 keV, a pulse length of 10 fs, beam size 1.39 x 1.30 μm and a repetition rate of 30 Hz by beamline scientists at SACLA. The microcrystal pellet was dispersed into hydroxyethyl cellulose matrix (HEC) (Sugahara *et al.*, 2017) in ratio 1:1 and homogenized using two syringes connected to each other prior to loading into a high-viscosity cartridge-type (HVC) injector developed at SACLA (Shimazu *et al.*, 2019). Diffraction patterns were recorded using a multiport CCD detector with eight sensor modules (Kameshima *et al.*, 2014). The crystals in cellulose matrix were extruded at a flow rate of 0.011 ml min⁻¹ from a nozzle of 125 μm diameter. SFX data were processed by Dr. Anastasiia Shilova (Diamond Light Source) using the CHEETAH pipeline (Barty *et al.*, 2014) and CrystFEL program (White *et al.*, 2016).

The structures were refined using Refmac5 (Murshudov *et al.*, 1997) in the CCP4i2 suite (Potterton *et al.*, 2018) with the ferric wild-type DtpB SFX (PDB code 6YRJ (Lučić *et al.* 2020b)) used as an initial model. Model building between refinement cycles was performed in Coot (Emsley *et al.*, 2010). Riding hydrogen atoms were added during refinement. The structures were validated using the tools within Coot

(Emsley *et al.*, 2010). A summary of data collection and refinement statistics are given in Table 5.2 and 5.3. Estimates of bond length errors were derived using the Online_DPI server (Kala Sekar *et al.*, 2015) based on the estimated coordinate error as previously described (Gurusaran *et al.*, 2013).

Table 5.2. SFX X-ray crystallography data processing for the DtpB D152A and N245A variants in space group $P2_12_12_1$. Values in parenthesis refer to the outermost resolution shell. The effective absorbed X-ray dose for the SFX structures is assigned as zero due to the femtosecond duration of the X-ray pulse. As is standard practice for SFX data, (White *et al.*, 2012) the metrics R_{split} and $CC_{1/2}$ are used to assess data quality and resolution limit in place of conventional crystallographic metrics such as R_{merge} or $I/\text{sd}(I)$.

	D152A	N245A
Wavelength (Å)	1.13	1.13
Effective absorbed X-ray dose (kGy)	0	0
Unit cell dimensions (Å)	86.9, 121.8, 199.5	86.9, 121.8, 199.5
Resolution (Å)	32.08-2.00	31.65-2.00
Number of reflections	94783	124109
R_{split}	0.240 (0.955)	0.285 (0.985)
$CC_{1/2}$	0.907 (0.398)	0.878 (0.369)
Multiplicity	635 (431)	627 (469)
Completeness (%)	100 (100)	100 (100)
Wilson B-factor (Å ²)	7.4	-0.3

Table 5.3. Refinement and validation statistics for the room temperature SFX X-ray crystallography of the DtpB D152A and N245A variants. Values in parenthesis refer to the outermost resolution shell.

	D152A	N245A
Number of reflections	94783	124109
Resolution (Å)	32.08-2.00	31.65-2.00
R_{work}	0.219	0.234
R_{free}	0.266	0.287
RMSD bond lengths (Å)	0.010	0.010
RMSD bond angles (°)	1.7	1.7
Solvent atoms	846	868
Ramachandran most favoured (%)	96	97

5.3. Results

5.3.1. Spectral characteristics

DtpB has an electronic absorbance spectrum consistent with a high-spin ferric haem species, which upon addition of one-equivalent H_2O_2 , leads to decrease in the Soret band intensity and a blue wavelength shift (for detailed description see Chapter 4). These spectral changes are characteristic of a Compound I species with porphyrin π -cation radical. The D152A, N245A and the DM variants display electronic absorption spectra similar to ferric WT DtpB and behave in the same way upon addition of one-equivalent H_2O_2 (Figure 5.1). Table 5.4 compares peak maxima wavelengths between the WT DtpB and respective variants.

Although removal of D152 or N245 did not affect the spectral changes induced upon addition of H_2O_2 to the ferric protein, the N245 variant resulted in a decreased Compound I stability going from hours in WT/D152A to minutes in the N245A and DM variants (Figure 5.2). X-ray structures of ferryl DtpB (see Chapter 4) reveal a H-bonding interaction with the oxo group of the $\text{Fe}^{\text{IV}}=\text{O}$ and the amide side chain of N245. Thus, the destabilisation of Compound I in the N245A/DM variants could arise from the loss of this H-bonding interaction.

Addition of one molar equivalent of H_2O_2 to the ferric R243A variant does not instantaneously lead to Compound I formation. Instead, the electronic absorbance spectrum reveals a slow bleaching overtime of the ferric state (Figure 5.3).

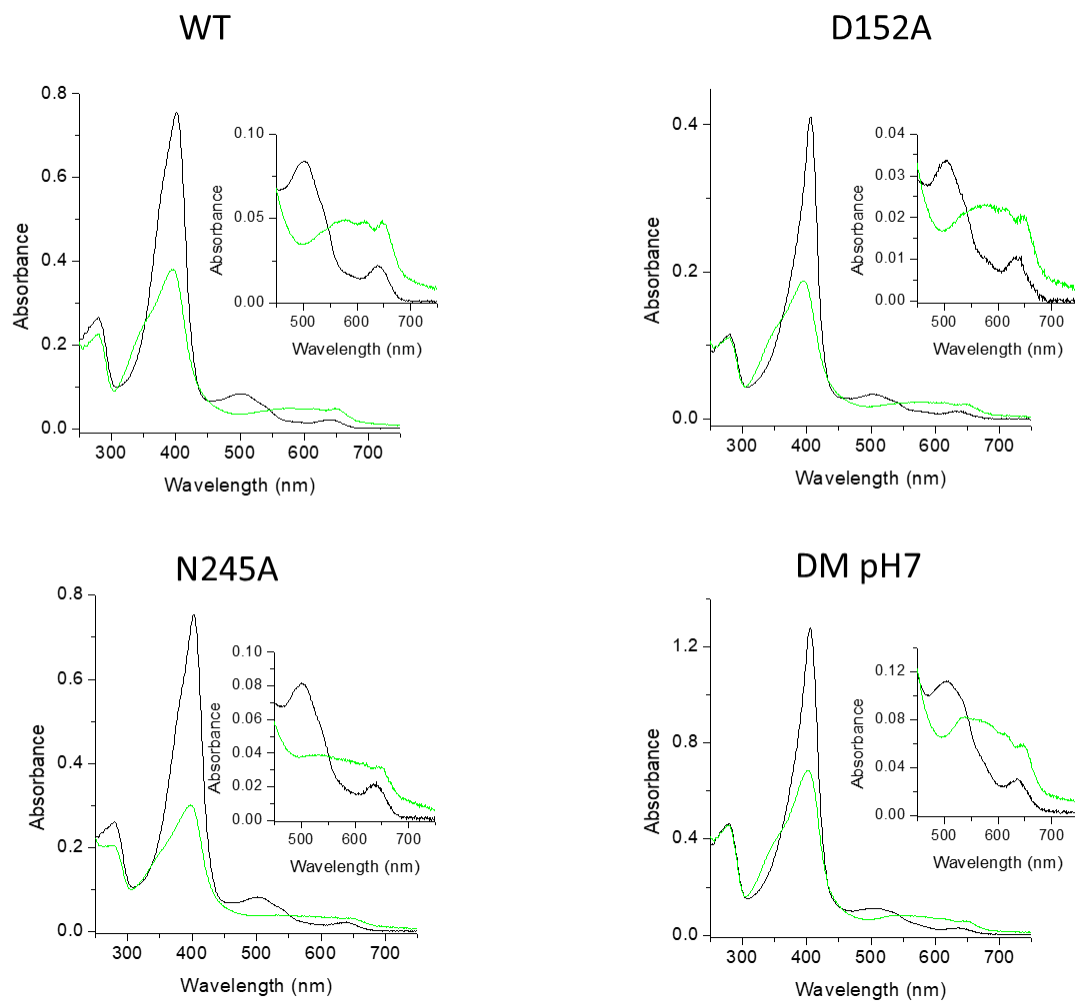


Figure 5.1. Electronic absorbance spectra of DtpB WT and the D152A, N245A and DM variants. The spectra were recorded at pH 5.0 for the WT, D152A and N245A or at pH 7.0 for the DM. Wavelength absorbance maxima are reported in Table 5.4. Insets represent the magnified Q-band region. On addition of one molar equivalent H_2O_2 , a Compound I spectrum is formed (green).

Table 5.4. Wavelength absorbance maxima for DtpB and variants measured at pH 5.0 or pH 7.0 for the DM. Compound II values are taken from global fitting of the spectral transitions upon mixing Compound I with $K_4[Fe(CN)_6]$ in a stopped-flow spectrophotometer at 25 °C.

<i>Protein</i>	<i>Ferric (nm)</i>	<i>Compound I (nm)</i>	<i>Compound II (nm)</i>
<i>WT</i>	400, 502, 638	398, 577, 612, 648	
<i>D152A</i>	406, 502, 638	395, 576, 609, 649	416, 525, 555
<i>N245A</i>	403, 501, 637	398, 575, 613, 649	413, 525, 558
<i>DM*</i>	405, 501, 637	403, 573, 613, 648	413, 525, 552
<i>R243A</i>	404, 502, 625	-	-

*Spectra measured at pH 7

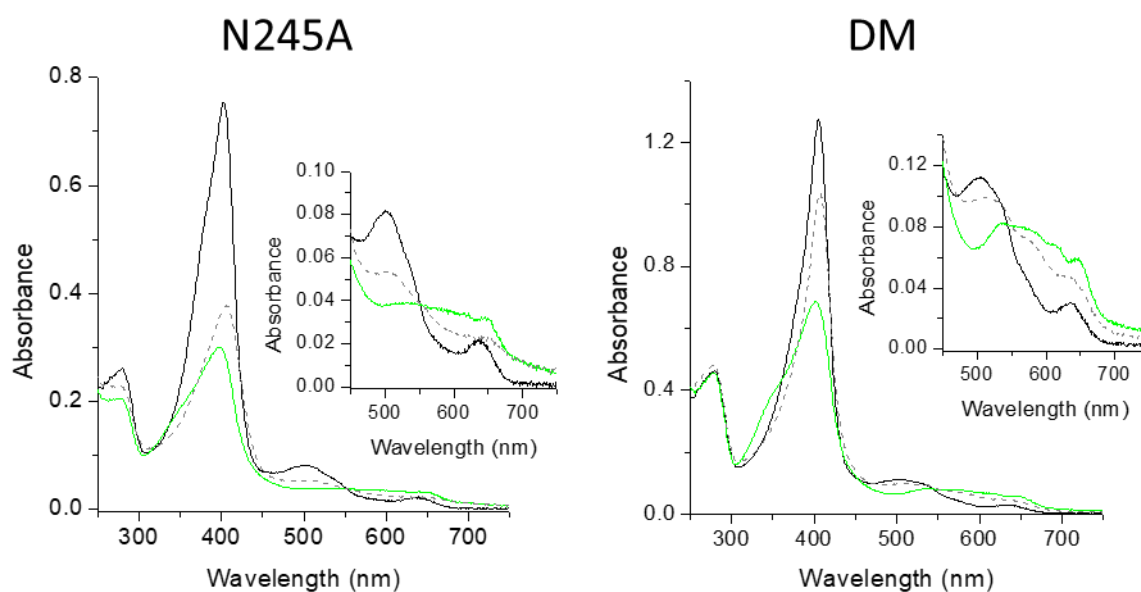


Figure 5.2. Electronic absorbance spectra of the N245A and DM DtpB variants at pH 5.0 and 7.0, respectively, showing reaction of the ferric enzyme with H_2O_2 . The black spectrum represents the ferric species that transitions to Compound I upon addition of H_2O_2 (green) and after 10 min the Compound I species has started to decay back towards a spectrum with ferric species properties (dashed line).

R243A

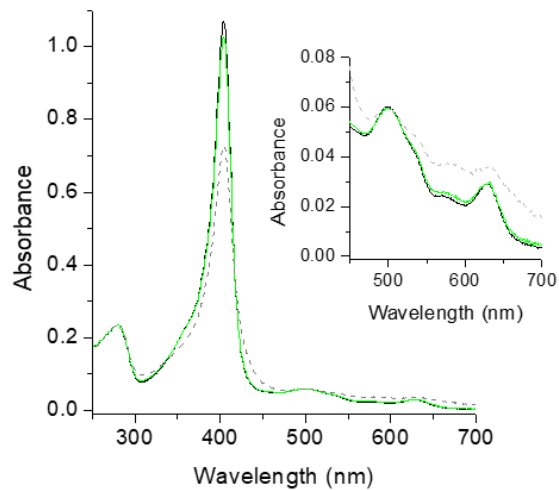


Figure 5.3. Electronic absorbance spectra of the R243A variant of DtpB measured at pH 5.0. Wavelength absorbance maxima are reported in Table 5.4. Inset represents magnified Q-band region. Addition of one molar equivalent H₂O₂ to the ferric enzyme (black) does not lead to instantaneous Compound I formation (green spectrum still corresponds to the ferric enzyme) but a slow decay (dashed line) over 45 min.

5.3.2. Compound I formation is enhanced by the distal Arginine in DtpB

On mixing DtpB WT with H₂O₂, a single spectral transition is observed consistent with transition from ferric haem to Compound I. The rate of Compound I formation was assessed at pH 5.0 and 7.0 and shows a linear dependence of pseudo-first order rate constants obtained from the global fitting of the spectral data with increasing H₂O₂ concentration (Figure 5.4). Second-order rate constants determined at pH 5.0 and 7.0 were $2.7 \times 10^5 \pm 0.1 \text{ M}^{-1} \text{ s}^{-1}$ and $4.7 \times 10^4 \pm 0.1 \text{ M}^{-1} \text{ s}^{-1}$, respectively (Table 5.5). The pH dependence of Compound I formation was further assessed in a pH range between 4.0 and 8.0 by mixing Fe^{III}-DtpB with 50-200 μM H₂O₂ (Figure 5.5). Pseudo-first order rate constants were obtained from global fitting enabling second-order rate constants to be determined for each pH value. The pH profile reveals an initial plateau between pH 4.0 and 6.5 followed by a decrease in rate as the pH is increased from 6.5 to 8.0 (Figure 5.5). This behaviour indicates a single ionisation process with apparent pK_a value of 6.8 ± 0.2 determined from fitting the data in Figure 5.4.

The rates of Compound I formation of Asp/Asn variants have also been assessed at pH 5.0 and 7.0 and are reported in Table 5.5. As observed for the WT DtpB, the Compound I formation rate is linearly dependent on increasing H₂O₂ concentration (Figure 5.3). At pH 5.0, only the DM exhibits a ~10-fold decrease in the rate, while removal of either the Asp or the Asn residue does not individually affect the rate (Table 5.5). The single variants also follow the trend of the WT DtpB, with Compound I formation being faster at acidic pH (Figure 5.4). Discrepancy between the rate at pH 5.0 and 7.0 is more apparent in WT and the N245A variant (Figure 5.4). Removal of the Asp in D152A and DM has resulted in similar Compound I

formation rates at pH 5.0 and 7.0. Thus, the pH dependence of Compound I formation rate was assessed for a wide range of pH values for each variant to check whether D152A mutation shifted the optimal pH for the reaction. Removal of D152 and/or N245 residues shifts the pH profile to now reveal two ionisation processes (Figure 5.5) with apparent pK_{a1} and pK_{a2} values reported in Table 5.5, which were determined from fitting the data to a two proton ionisation equilibria equation (Equation 5.1)

$$k_{\text{obs1}} = k_0 + \frac{\Delta k_1(10^{pH-pK_{a1}}) + \Delta k_2(10^{2pH-pK_{a1}-pK_{a2}})}{1 + (10^{pH-pK_{a1}}) + (10^{2pH-pK_{a1}-pK_{a2}})} \quad (5.1)$$

where k_{obs1} is the observed pseudo-first order rate constant, k_0 rate of the protonated form at zero pH and, Δk is the difference in rate between protonated and unprotonated forms. The first ionisation process is similar to that assigned to the deprotonation of the peroxide bound to the haem-iron in A-type DyPs and will be discussed later. The second pK_{a2} corresponds to the ionisation process also detected in the WT ($pK_a = 6.8 \pm 0.2$), thus a common acidic ionisation equilibrium is present which could possibly be assigned to an ionizable protein residue. In this respect the only shared residue in the distal pocket of WT and variants is the Arg that has been implicated in acting as an acid–base catalyst across the DyP sub-families.

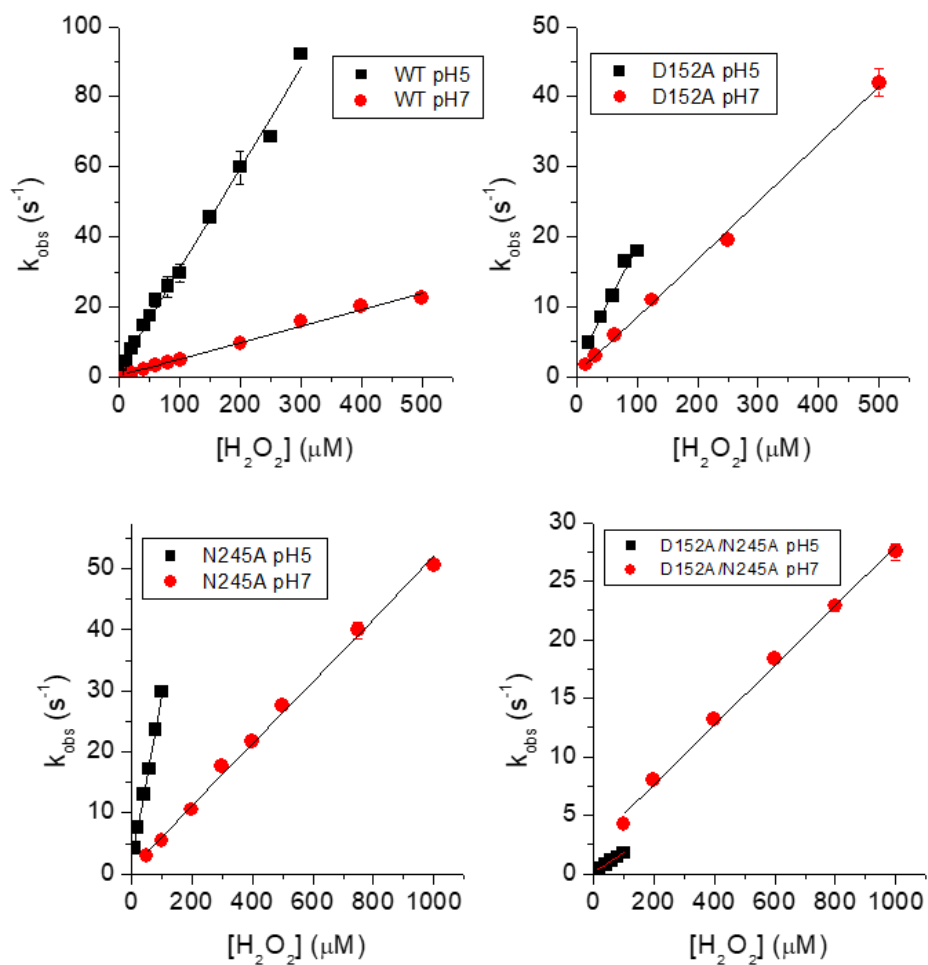


Figure 5.4. Detection of Compound I in WT DtpB and variants using stopped-flow absorption spectroscopy (pH 5.0 and 7.0 at 25 °C). Pseudo first-order rate constants (k_{obs1}) plotted against increasing $[\text{H}_2\text{O}_2]$. The data points are fitted to a linear function to obtain a second-order rate constant. Error bars are present, albeit too small to be visible.

Table 5.5. Second-order rate constants (k) and ionisation equilibrium parameters (pK_a) for Compound I formation in WT DtpB and variants.

<i>Protein</i>	k_{pH5} ($M^{-1} s^{-1}$)	k_{pH7} ($M^{-1} s^{-1}$)	pK_{a1}	pK_{a2}
<i>WT</i>	$2.7 \times 10^5 \pm 0.1$	$4.7 \times 10^4 \pm 0.1$	-	6.8 ± 0.2
<i>D152A</i>	$1.7 \times 10^5 \pm 0.1$	$8.2 \times 10^4 \pm 0.2$	5.6 ± 0.1	6.7 ± 0.1
<i>N245A</i>	$2.8 \times 10^5 \pm 0.1$	$5.1 \times 10^4 \pm 0.1$	5.2 ± 0.6	6.4 ± 0.2
<i>DM</i>	$1.7 \times 10^4 \pm 0.02$	$2.5 \times 10^4 \pm 0.1$	6.0 ± 0.7	6.5 ± 1.0
<i>R243A</i>	-	-	-	-

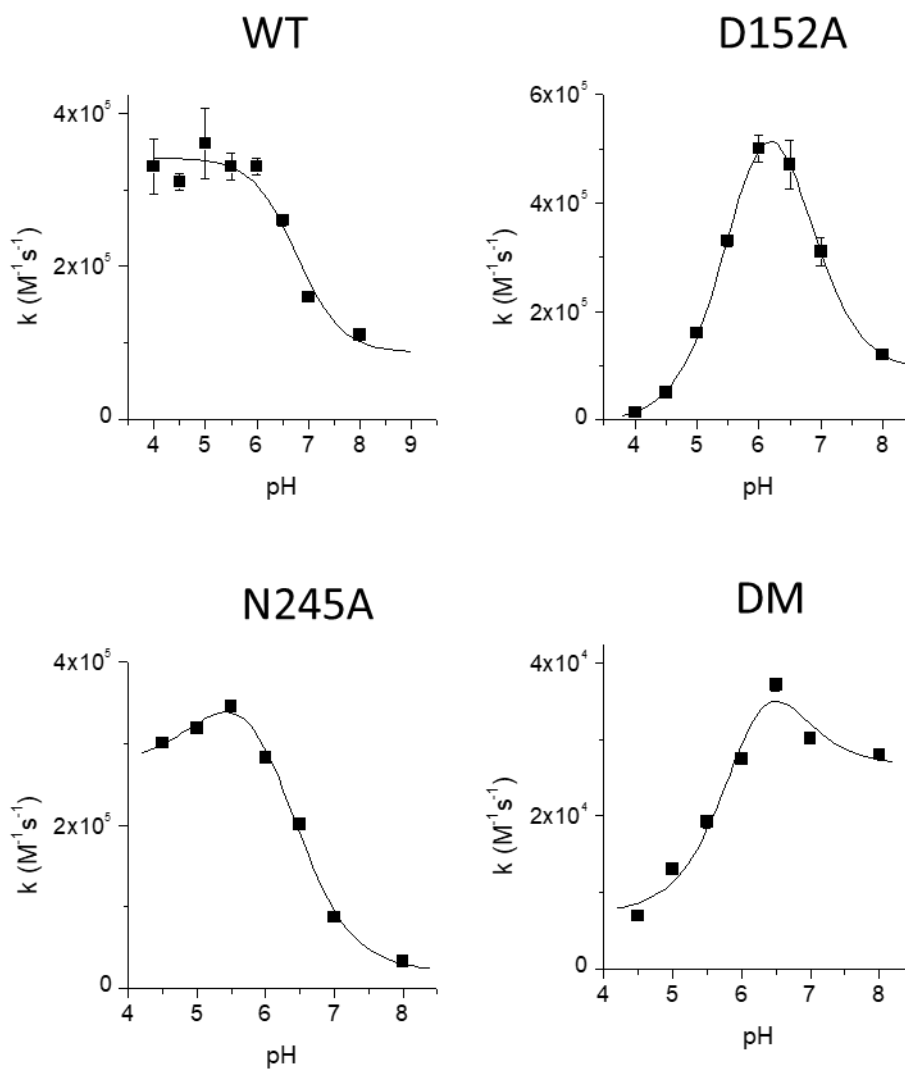


Figure 5.5. The pH dependence of Compound I formation in WT DtpB and variants. Second-order rate constants (k) plotted against pH obtained from stopped-flow measurements at a constant $[\text{H}_2\text{O}_2]$ between 50 μM and 200 μM (see Experimental Procedures).

Removal of the R243 residue from the distal haem pocket slows Compound I formation and destabilises it. Global analysis of the spectral transitions on mixing the R243A variant with H₂O₂ concentrations ranging between 250–2500 mM using stopped-flow, revealed that Compound I slowly formed, and this, unlike the WT, decayed over many minutes to re-form the ferric species. This process is very inefficient, with Compound I species bleaching quickly, making the determination of Compound I formation rate too difficult and pH dependence experiments impossible. However, it seems to confirm that the distal Arg is paramount for efficient and rapid Compound I formation in DtpB.

5.3.3. A “Dry” distal site moderates Compound II formation

Compound I in DtpB is a very stable species that in the absence of an external reductant decays back to the resting ferric state after approximately 3 hours without any detectable spectral features of an intermediate that can be assigned to a Compound II species. To further investigate the kinetics of Compound I reduction in the presence of a one-electron reductant, the small inorganic redox complex, K₄[Fe(CN)₆], was chosen. Using stopped-flow spectrophotometry, Compound I of WT DtpB was mixed with increasing concentrations of K₄[Fe(CN)₆]. A single spectral transition was observed that corresponds to reduction of Compound I to the ferric haem species (Figure 5.6). A linear dependence of pseudo-first order rate constants on increasing K₄[Fe(CN)₆] concentration was observed from the global fitting of the spectral data with increasing (Figure 5.7) at both pH 5.0 and 7.0, allowing for a second-order rate constant of $2.1 \times 10^4 \pm 0.1 \text{ M}^{-1} \text{ s}^{-1}$ and $4 \times 10^2 \pm 0.2 \text{ M}^{-1} \text{ s}^{-1}$ at pH 5.0 and pH 7.0, respectively, to be determined.

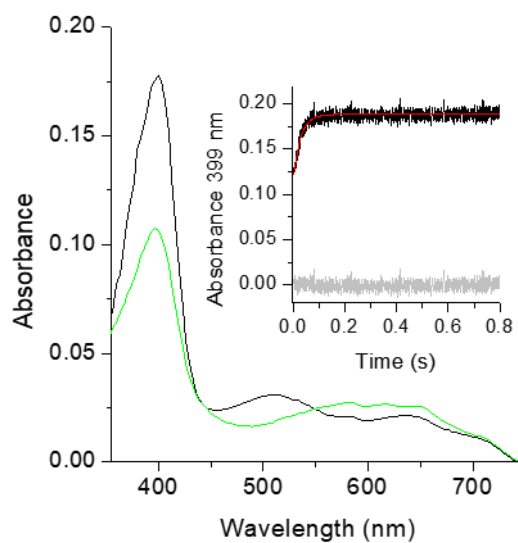


Figure 5.6. Compound I reduction in WT DtpB. Spectra obtained from global fitting of the observed spectral transitions upon mixing 1000 μM $\text{K}_4[\text{Fe}(\text{CN})_6]$ with Compound I enzyme at pH 5.0 using stopped-flow absorption spectroscopy (25 $^\circ\text{C}$). The haem species were identified by global analysis; black-ferric and green-Compound I. Inset shows a magnified kinetic trace at 399 nm wavelength along with its fit (red) and residual to model $a \rightarrow b$.

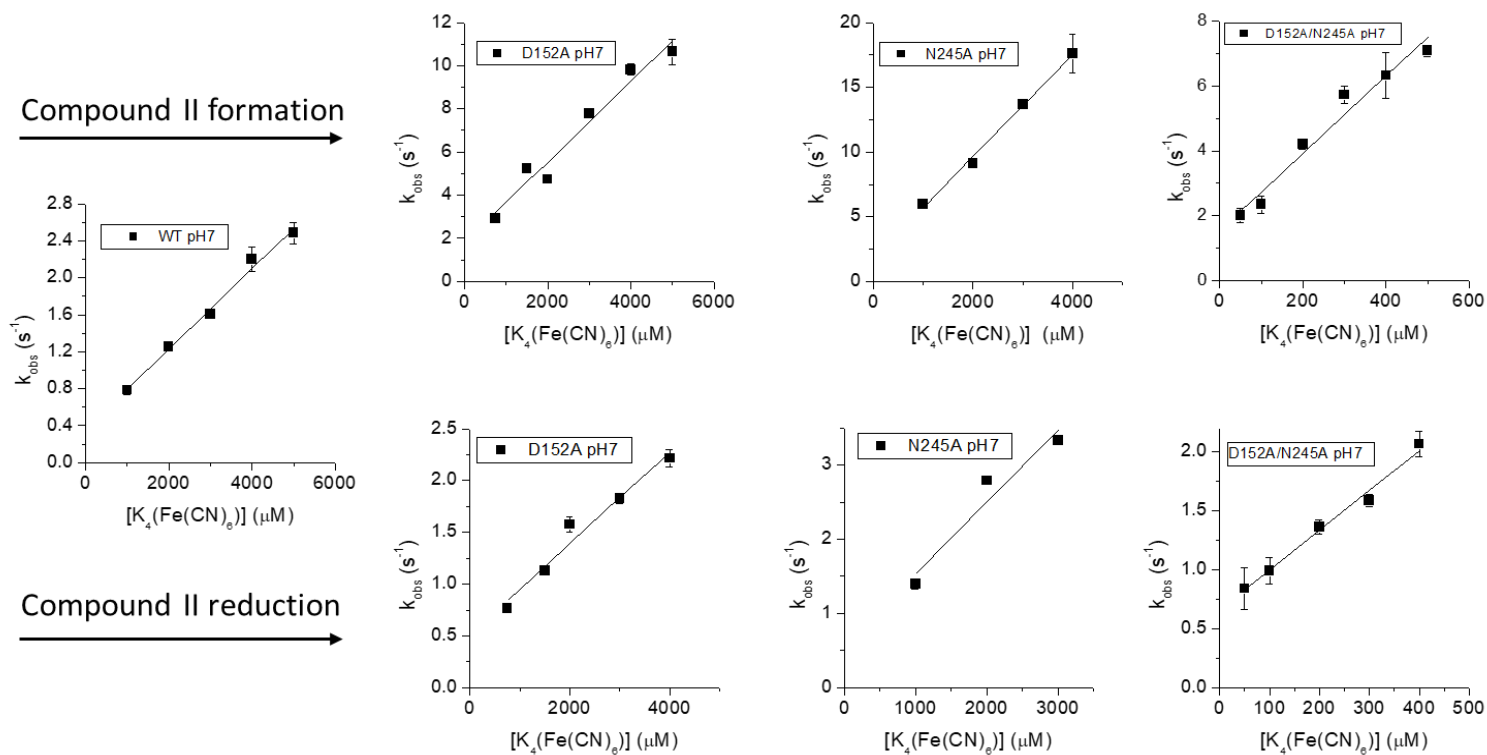


Figure 5.7. Kinetics of Compound II formation and reduction (pH 7 and 25 °C). Pseudo first-order rate constants (k_{obs}) plotted against $[K_4(Fe(CN)_6)]$. The data points are fitted to a linear function to obtain a second-order rate constant. The Compound II intermediate can be detected in all variants and thus two second-order rate constants were determined; Compound II formation (top row) and Compound II reduction (bottom row).

In a similar fashion to WT DtpB, Compound I reduction rates were assessed for the distal Asp and Asn variants. As D152A and DM display a higher optimal pH for Compound I formation (Figure 5.5), the reduction rates were determined at pH 5.8 and 7.0 instead of pH 5.0 and 7.0 as conducted for WT DtpB. On mixing Compound I with $K_4[Fe(CN)_6]$, two spectral transitions were now observed (Figure 5.8). Global analysis of the full spectral data showed that these phases could be assigned firstly to the reduction of Compound I to Compound II, distinguishable by red shift in Soret wavelength and the appearance of α and β bands of equal intensity, and secondly reduction of Compound II to the ferric state (Figure 5.8). Both reactions were found to be linearly dependent on $K_4[Fe(CN)_6]$ concentration (Figure 5.7), enabling for second-order rate constants to be calculated for each step (Table 5.7). For all three variants, rates are ~10-fold higher in the optimum pH area, which is pH 5.0 for N245A and pH 5.8 for D152A and DM variant (Table 5.6).

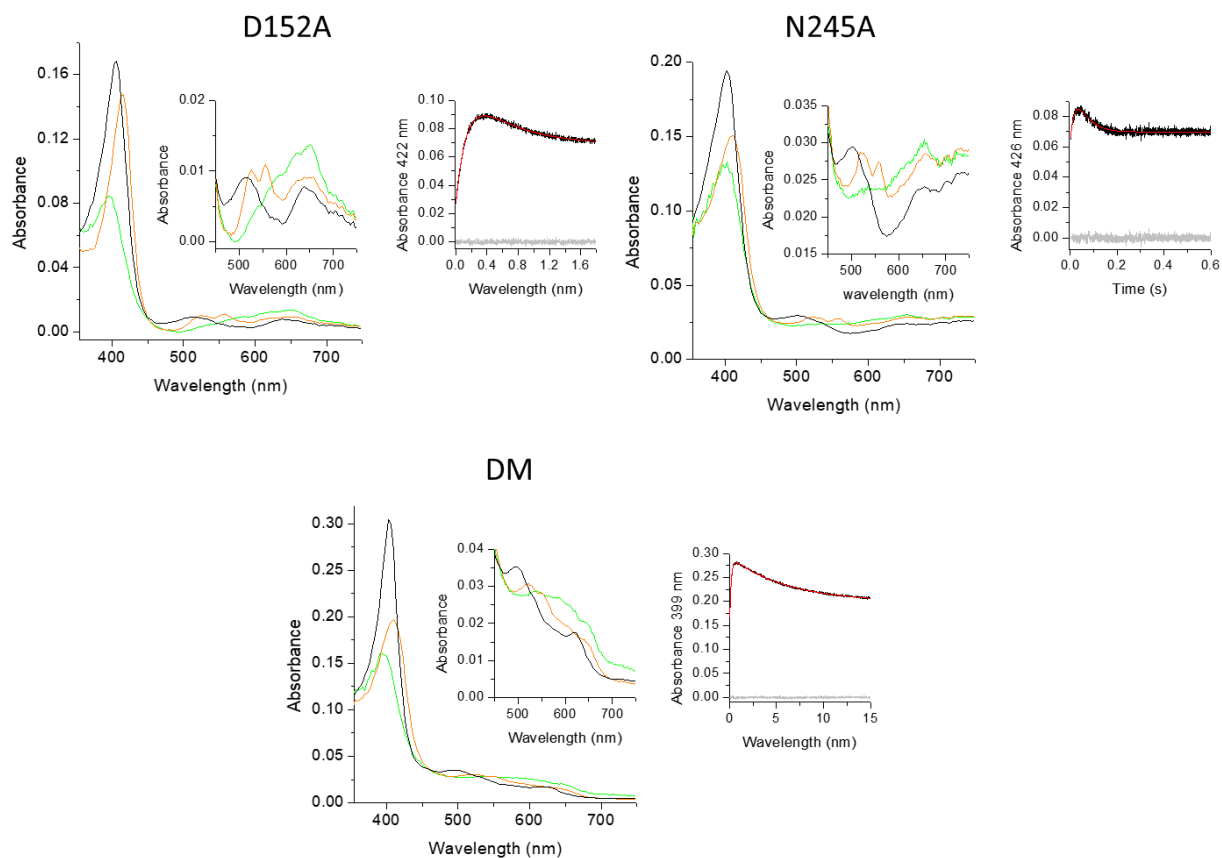


Figure 5.8. Detection of Compound II in DtpB variants using stopped-flow absorption spectroscopy (25 °C). Spectra obtained from global fitting of the observed spectral transitions upon mixing $K_4[Fe(CN)_6]$ (1000 μM or 100 μM for DM only) with Compound I enzyme at pH 5.0 (N245A) or pH 5.8 (D152A and DM). The haem species were identified by global analysis; black-ferric, green-Compound I and red-Compound II. Insets show magnified Q-band region (left) and kinetic traces (right) at selected wavelength along with their fits (red) and residuals to models described in the text (see section 5.3.3).

Table 5.6. Second-order rate constants of Compound II formation and reduction obtained from stopped-flow measurements for DtpB distal Asp and distal Asn variants at pH 5.0/5.8 and 7.0 (see main text).

<i>Protein</i>	$k_{pH5/5.8}$	k_{pH7}	$k_{pH5/5.8}$	k_{pH7}
	($M^{-1} s^{-1}$)			
	Compound II formation		Compound II reduction	
<i>D152A</i>	$2.7 \times 10^4 \pm 0.1$	$1.9 \times 10^3 \pm 0.2$	$3.4 \times 10^3 \pm 0.2$	$4.4 \times 10^2 \pm 0.5$
<i>N245A</i>	$1.3 \times 10^5 \pm 0.2$	$3.9 \times 10^3 \pm 0.2$	$5.6 \times 10^4 \pm 0.6$	$9.7 \times 10^2 \pm 2.4$
<i>DM</i>	$8.5 \times 10^4 \pm 1.0$	$1.2 \times 10^4 \pm 0.1$	$1.3 \times 10^4 \pm 0.1$	$3.5 \times 10^3 \pm 0.2$

5.3.4. Compound II formation is proton-coupled

To investigate proton involvement in Compound I and II formation, the system (enzyme, H₂O₂ and substrate) was exchanged into D₂O (see section 2.3.9 for a detailed description). If a kinetic isotope effect (KIE) is present upon exchange to D₂O (manifested as decrease or, rarely, an increase of reaction rate), then proton involvement in the rate limiting step can be deduced. This was investigated through monitoring of reaction rates using a stopped-flow spectrophotometer and comparing them to the second-order rates determined in a proton environment.

Firstly, Compound I formation was investigated at pD 5.0 and 7.0 with WT DtpB. As Compound I formation is associated with the breakage and formation of an O-H bond, then using D₂O₂ will reveal if these steps are rate limiting the reaction. A linear dependence of k_{obs1} on increasing [D₂O₂] was observed with WT DtpB, enabling a second-order rate constant (k_{D}) to be calculated for Compound I formation at pD 5.0 and 7.0 of $3 \pm 0.3 \times 10^5 \text{ M}^{-1}\text{s}^{-1}$ and $4.2 \pm 0.1 \times 10^4$, respectively (Figure 5.9). The value determined in H₂O ($k_{\text{H}} = 2.7 \pm 0.1 \times 10^5 \text{ M}^{-1}\text{s}^{-1}$ at pH 5.0 and $4.7 \times 10^4 \pm 0.1$ at pH 7.0) and is nearly identical, with $k_{\text{H}}/k_{\text{D}}$ ratio amounting to ~1 indicating no KIE. Thus, it can be deduced that proton movement is not rate limiting Compound I formation in WT DtpB.

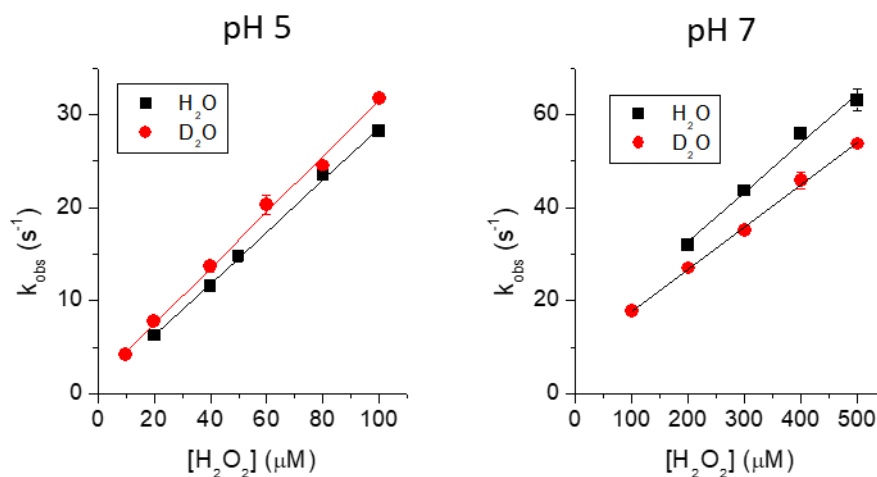


Figure 5.9. Kinetic isotope effect on Compound I formation in DtpB WT at pH 5.0 or 7.0. Pseudo first-order rate constants (k_{obs}) obtained from global fits plotted against peroxide concentration (H_2O_2 or D_2O_2).

Next, reduction of Compound I to Compound II was probed for a KIE. Compound I was formed by adding D_2O_2 to WT DtpB and the D152A variant prior to measurements or *de novo* for N245A and DM. The reaction was monitored using stopped-flow spectrophotometer at pH 7.0 only, as the variants precipitated in pH 5.0 buffer. For the WT enzyme, a single spectral transition was observed, as observed in H_2O environment, corresponding to Compound I reduction to the ferric state. The reaction was found to be linearly dependent on $\text{K}_4[\text{Fe}(\text{CN})_6]$ concentration, allowing second-order rate constant k_D to be calculated $2 \times 10^2 \pm 0.1 \text{ M}^{-1} \text{ s}^{-1}$ (Table 5.7). A k_H/k_D of 2 indicates presence of a KIE in the WT DtpB. Upon addition of $\text{K}_4[\text{Fe}(\text{CN})_6]$ to the variants, two spectral transitions were observed, with Compound II again distinguishable as reported in H_2O . The reactions were linearly dependent on $\text{K}_4[\text{Fe}(\text{CN})_6]$ concentration, and second-order rate constants were calculated and are listed in Tables 5.7 and 5.8. A k_H/k_D of 0.8-1 is reported, consistent with no KIE for the variants.

Table 5.7. Second-order Compound I reduction rates in H₂O and D₂O at pH(D) 7.0. ^a and ^b are rates of Compound I to ferric, while other rates correspond to Compound I going to Compound II.

<i>Protein</i>	k_{H_2O} ($M^{-1} s^{-1}$)	k_{D_2O} ($M^{-1} s^{-1}$)
<i>WT</i>	$4 \times 10^2 \pm 0.2^a$	$2 \times 10^2 \pm 0.1^b$
<i>D152A</i>	$1.9 \times 10^3 \pm 0.2$	$1.9 \times 10^3 \pm 0.1$
<i>N245A</i>	$3.9 \times 10^3 \pm 0.2$	$3.1 \times 10^3 \pm 0.1$
<i>DM</i>	$1.2 \times 10^4 \pm 0.1$	$1.5 \times 10^4 \pm 0.3$

Table 5.8. Compound II reduction rates in H₂O and D₂O at pH(D) 7.0 for the DtpB variants studied.

<i>Protein</i>	k_{H_2O} ($M^{-1} s^{-1}$)	k_{D_2O} ($M^{-1} s^{-1}$)
<i>D152A</i>	$3 \times 10^2 \pm 0.6$	$3 \times 10^2 \pm 0.1$
<i>N245A</i>	$4.5 \times 10^2 \pm 3.2$	$6 \times 10^2 \pm 0.4$
<i>DM</i>	$2.6 \times 10^3 \pm 0.4$	$2.6 \times 10^3 \pm 0.3$

5.3.5. SFX crystal structures of D152A and N245A variants

Zero-dose structures of D152A and N245A variants were obtained at the XFEL facility at SACLA using SFX at room temperature and were determined to 2.00 Å. In both structures a hexamer assembly is present, as reported for the WT in Chapter 4, and each chain of the hexamer assembly houses the haem cofactor.

Unlike WT DtpB, the haem pocket of D152A and N245A variants is “wet” (Figure 5.10). The electron-density map for D152A variant is consistent with the ferric haem being hexa-coordinate, with axial coordination from a proximal His residue, (H225) and a distal H₂O (w1) molecule (Figure 5.10). The distal Fe^{III}-OH₂ bond is long (2.42 ± 0.18 Å) with the w1 molecule participating in a H-bonding interaction with the amide group of the distal N245 (2.82 ± 0.18 Å) (Figure 5.10). An additional w2 molecule resides inside the pocket, which is homologous to H₂O found in the WT DtpB (Figure 4.12). Unlike in the D152A structure, the N245A variant structure reveals a penta-coordinate ferric haem, with w1, which is present, but has shifted such that it no longer directly forms a bonding interaction to the haem-Fe. However, it does participate in a H-bonding interaction with a O^δ atom of the distal Asp (2.85 ± 0.19 Å) (Figure 5.8) and w2. Thus, mutation of either Asp or Asn to an Ala removes the steric impediment to the distal site of DtpB and enables a water molecule to reside in close proximity to the haem in the ferric structure. Structural data for the DM has also been collected during the same remote SACLA visit but has yet to be analysed.

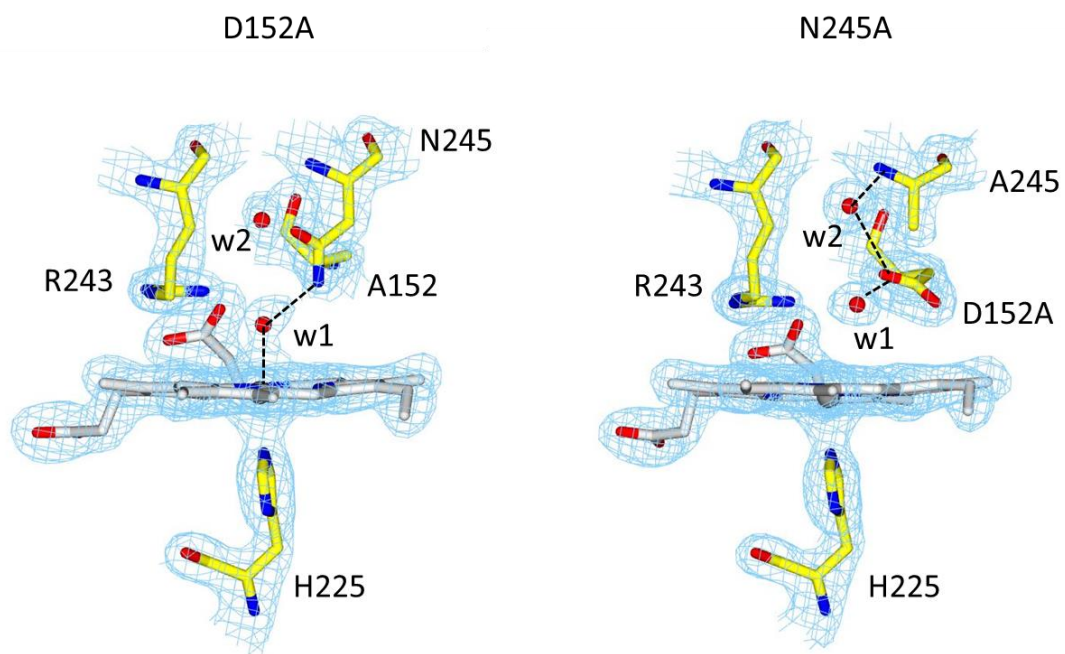


Figure 5.10. Distal pockets of the ferric D152A and N245A variants determined using SFX at room temperature. $2F_o - F_c$ electron density maps (blue) contoured at 1.5σ . The coordinate bond and H-bonds are shown as dashed black lines.

5.4. Discussion

Upon reacting DyPs with H₂O₂ a Compound I catalytic intermediate forms. This is a complex process that requires H₂O₂ to be deprotonated with help of a nearby distal pocket haem residue that acts as a proton acceptor/donor. In the case of non-mammalian peroxidases, the best studied class of peroxidase, the distal His has been recognised to have this role. In Chapter 2, it is discussed that DtpA from *S. lividans* utilizes an H₂O-Asp unit for this purpose, and in Chapter 4 it is outlined that in DtpB there is no direct nor water mediated communication between Fe^{III}-haem and the distal Asp residue. In DtpB, the distal haem pocket is “dry” and thus a different pathway may be used compared to DtpA to form Compound I. A potential alternative to the H₂O-Asp is the distal Arg. Despite the guanidinium group of Arg having a *pK_a* of 13.8 (Fitch *et al.*, 2015) and therefore is protonated at neutral pH, several enzymes (Guillén Schlippe and Hedstrom, 2005; Hwang *et al.*, 2007; Pankhurst *et al.*, 2006; Tedeschi *et al.*, 2001), including metalloenzymes (Evans *et al.*, 2016; Kwon *et al.*, 2020), are reported to use Arg as a catalytic base. Furthermore, several neutron structures provide evidence for the existence of neutral Arg (guanidine) side chains (Hiromoto *et al.*, 2017; Kwon *et al.*, 2020; Yamaguchi *et al.*, 2009; Yonezawa *et al.*, 2017). To test this structure-based hypothesis, D152A, N245A, DM and R243A variants were created.

The D152A, N245A and DM variants displayed kinetic and spectral properties that are equivalent to those of WT DtpB in Compound I formation. Addition of H₂O₂ to these variants instantaneously lead to formation of a Compound I intermediate albeit with the stability of the Compound I intermediate varying for the N245A and DM variants due to likely loss of a H-bond between the oxo group and the amide of N245. The second-order rates for Compound I formation were calculated to be comparable to the

rate obtained for the WT enzyme. This is in agreement with the structure-based hypothesis suggesting that the D152 has no direct involvement in proton movement during Compound I formation process owing to the absence of its H₂O partner.

In contrast, addition of H₂O₂ to the R243A variant, does not instantaneously lead to Compound I. Removal of the distal Arg slows Compound I formation and renders it highly unstable. Slow acquisition of protons from the haem environment and electrons from the protein (auto-reduction) leads to the slow re-formation of the ferric form. Thus, R243 in DtpB does appear to be essential for Compound I to be formed efficiently. A common structural motif amongst enzymes that utilise Arg as an acid/base catalyst is that the guanidinium group is adjacent to a carboxylate group and solvent accessible (Guillén Schlippe and Hedstrom, 2005). In all DyP structures, the guanidinium group of the distal Arg is buried and H-bonded to the carboxylate group of the inwardly facing haem propionate-7. Furthermore, the guanidinium group is solvent accessible and thus can be considered to bear the hallmarks for a catalytic role. Chemically, it is possible for the neutral guanidine moiety to adopt five tautomeric forms in solution each corresponding to the loss of one of the five nitrogen bonded protons. These tautomers exist in a pH-independent equilibrium and rapidly interconvert via bond rotations and/or proton transfer, with the observed pK_a the sum of the five microscopic acid dissociation constants contributed by each tautomer (Raczyńska *et al.*, 2003). Interactions that can “twist” the planar guanidinium group (charged) to nonplanar (neutral) may perturb the pK_a (Guillén Schlippe and Hedstrom, 2005). In this respect the carboxylate groups of the propionate-7 may limit the access to H-bonds thereby forcing the NH₂ groups into a nonplanar conformation. Thus, the inwardly pointing propionate group serves to impose a steric constraint to modulate the

Arg pK_a . In doing so it is conceivable that only a fraction of the active enzyme will exist at any one time, but providing this fraction is kinetically competent it will be sufficient to drive Compound I formation.

No KIE was determined for Compound I formation with either the WT DtpB or the variants, owing to proton movement being more efficient/rapid than the rate determining step, which is the binding of peroxide to the haem. However, from the pH profiles of WT DtpB and the variants it is evident that Compound I formation is pH dependent. On removal of the Asp and/or the Asn, an acidic pK_a of ~ 5.6 is observed, which is most pronounced in the Asp variant. This pK_a is similar to that assigned to the deprotonation of the peroxide bound to the haem-iron as discussed in Chapter 2. It could be that the pK_a of the bound peroxide is < 4 in the WT as a consequence of the ‘dry’ pocket. By disrupting the Asp-Asn couple, creating a ‘wet’ pocket, and to some extent removing a charge, influences the pK_a of the bound peroxide, so in effect removing the Asp and Asn causes the pH profile to shift to the left relative to the WT profile in Figure 5.5. All variants show a second ionisation equilibrium in common with the WT. In Chapter 2, a second ionisable equilibrium was also observed for DtpAa and the D251A variant of DtpA with a pK_a of ~ 8 . This was assigned to ionisation of a group that competes with the distal Asp for a proton, as a KIE is present in DtpAa and in the D251A DtpA variant, which both do not have an efficient way of forming Compound I (Chapter 2). However, in DtpB, no KIE is detected, but the presence of the second ionisation equilibrium in DtpB could suggest competition between R243 and another ionisable group for a proton and thus leading to a reduction in rate of Compound I formation. As only a fraction of DtpB is capable to form Compound I at any one time, due to the requirement of neutral Arg species, this postulated ionisable

group might be deprotonated at pH ~ 6.8 (the pK_a determined) and compete with the Arg for a proton, but is not rate limiting the reaction as when DtpB is in its active neutral Arg form, it is tuned to efficiently transfer the proton to the Arg.

The involvement of the Arg residue in proton shuttling has been recently reported for the ascorbate peroxidase (APX) (Kwon *et al.*, 2020; Kwon *et al.*, 2021). Compound I of APX abstracts an electron and a proton from ascorbate in a concerted manner (proton coupled electron transfer; PCET) to form Compound II, which then also undergoes a PCET step with an ascorbate molecule to form the Fe^{III}-haem and release of H₂O. The distal Arg in APX has been implicated together with a distal H₂O molecule and the haem propionates to be part of a proton delivery pathway that would require switching of the Arg side chain between the neutral and charged states (Kwon *et al.*, 2020). In DtpB, a continuous H-bond network from bulk solvent to the oxo group involving H₂O channels, both haem propionates and the distal Arg243 exists (Figure 5.11). Thus, a case for a proton transfer pathway to the oxo group can be made, implicating the requirement for Arg243 to deprotonate in DtpB.

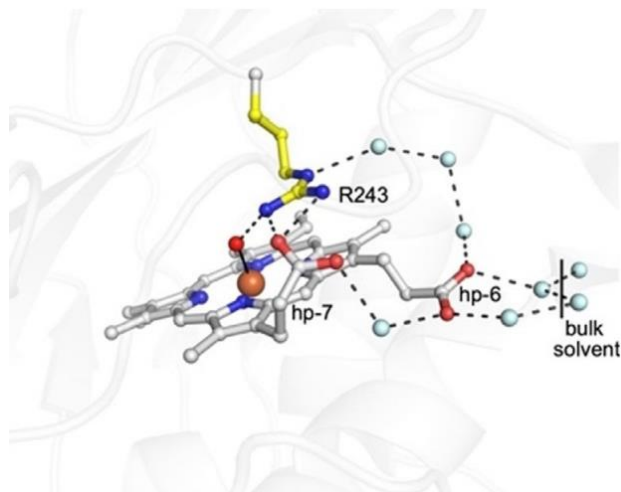


Figure 5.11. Water channels connecting the $\text{Fe}^{\text{IV}}=\text{O}$ to the bulk solvent via the distal R243 and the haem propionates in the SFX structure. Waters (cyan spheres) are positioned within H-bonding range of each other ($\sim 2.8 \text{ \AA}$ dashed lines) and may function as proton transfer pathway.

On mixing Compound I with $\text{K}_4[\text{Fe}(\text{CN})_6]$, an optical transition consistent with Compound I converting to ferric DtpB in a single process with no intermediate is observed (Figure 5.6). This transition is linearly dependent on the $\text{K}_4[\text{Fe}(\text{CN})_6]$ concentration, and yields the second-order rate constants of $2.1 \times 10^4 \pm 0.1 \text{ M}^{-1} \text{ s}^{-1}$ and $4 \times 10^2 \pm 0.2 \text{ M}^{-1} \text{ s}^{-1}$ at pH 5.0 and pH 7.0, respectively. The transition from Compound I to ferric passes through the intermediate Compound II. As the spectral features of this compound were not observed at any $\text{K}_4[\text{Fe}(\text{CN})_6]$ concentration, this rate constant must therefore represent the rate constant for the transition from Compound I to Compound II. Otherwise, Compound II would be populated and spectrally evident. Given that the maximum population of Compound II is $\sim 5\%$ (*i.e.* at or below experimental limit), the

rate constant for Compound II to ferric must be at least $6 \times 10^3 \text{ M}^{-1}\text{s}^{-1}$ at pH 7.0, determined using the equation below.

$$[CmpdI]_{max} = \left(\frac{k_{obs2}}{k_{obs1}} \right)^{\left(\frac{k_{obs2}}{k_{obs1} - k_{obs2}} \right)} \quad (5.2)$$

On repeating the Compound I reduction experiments in D_2O , a distinct KIE of ~ 2 was observed (Table 5.7). This implies that the rate limiting step in the reduction is coupled to a proton uptake. As the rate limiting step is the transition from Compound I to Compound II, then it is this reaction that is coupled to proton uptake. Reduction of Compound I to Compound II requires solely the transfer of an electron to the porphyrin ring and does not have a requirement for a proton. Therefore, the transfer of the electron must itself be rate limited by proton uptake. This is not uncommon in biological electron transfer, where electron addition to a buried site must be accompanied by a proton to ensure electro-neutrality in the transition. Such a constraint is possibly even more demanding when an electron is being added to a ‘dry’ site.

The ‘dry’ distal haem pocket identified in Fe^{III} -haem DtpB remains in the Compound I structure (see Chapter 4). This indicates that the water molecule coproduced on Compound I formation is released from the distal pocket, emphasising the importance of the ease of egress allowed by solvent exposure of the haem site. It has been proposed that the release or retention of the coproduced water molecule upon Compound I formation may influence whether a two-electron reduction of Compound I occurs (a ‘dry’ site; water released) such as in catalases or two one-electron equivalent processes (a ‘wet site; water retained) resulting first in the Compound II intermediate and then the ferric resting state, as in peroxidases (Jones, 2001). This concept of a redox pathway

switching mechanism arose in the early 2000's when more X-ray structures of peroxidases and catalases were becoming available. However, site-specific radiation damage is now known to be a confounding factor in these earlier structures. Thus, despite initial insights into the presence or absence of haem distal pocket water molecules that underpins this redox switching theory, an air of caution should remain as in DyPs, distal pocket waters can move and disappear upon a change of redox state caused by radiation damage (Kekilli *et al.*, 2017; Pfanzagl *et al.*, 2020b). Nevertheless, the 'dry' versus 'wet' theory is compelling, but at the same time has yet to be unequivocally proven.

To advance this discussion, the results of Compound I reduction with the variants are of interest. The rates of reduction of Compound I in the distal pocket variants revealed that in all cases, reduction of Compound I to Compound II was faster than seen in the WT and also faster than reduction of Compound II to ferric (Table 5.7 and 5.8). Thus, in the variants Compound II was almost fully populated and easily recognised as an intermediate between Compound I and the ferric enzyme. Notably, the KIE for reduction of Compound I to Compound II, seen for the WT, is abolished in the variants. This implies, that rate limiting proton uptake is no longer involved in the transition. Reduction of Compound II to ferric, which can now be observed in the variants, depends linearly on $K_4[Fe(CN)_6]$ concentration (Figure 5.7), and had also had no KIE. Together these data suggest that the proton uptake required for H_2O formation in the Compound II to ferric transition is not rate limiting. The SFX structures reveal that distal pocket of the Asp and Asn variants is "wet" (Figure 5.10), and thus it is feasible that a H_2O network could provide a ready source of rapidly available protons for this chemistry. Reduction of Compound I to Compound II requires a concerted moving of

an electron from substrate to porphyrin radical with a proton from the environment. In a “wet” pocket, this proton transfer is efficient as protons for this chemistry are available inside the pocket. In a “dry” pocket the proton transfer, and ultimately Compound II formation, becomes the rate limiting step. By disrupting the Asp/Asn couple in the variants, water can now enter the site (Figure 5.10), the constraint on proton uptake is relieved and thus the Compound I reduction to Compound II is faster than in the WT and the KIE is abolished. In contrast, by disrupting this couple, the rate of Compound II reduction is decreased in the variants compared to WT, even though protons are more readily available. Thus the presence of the Asp/Asn couple in DtpB not only regulates the optimal pH of Compound I formation but also enhances greatly the transition of Compound II to the ferric form.

A picture which emerges that is consistent with this data is that there is a proton coupled electron-transfer to Compound I in WT DtpB. The uptake of the proton is rate limiting and, protonates directly the $\text{Fe}^{\text{IV}}=\text{O}$ group to create a $\text{Fe}^{\text{IV}}\text{-OH}$ species, that decays rapidly to form ferric. In the presence of excess $\text{K}_4[\text{Fe}(\text{CN})_6]$ this process could be very fast and even in the absence of added reductant the autoreduction of protonated Compound II would occur rapidly with the abstraction of an electron from the protein. Thus, the Asp/Asn couple is necessary in DtpB for control of proton uptake that accompanies electron transfer to Compound I as seen from the rate decrease and absence of KIE in Asp/Asn variants. This may be explained if the proton accompanying electron transfer to Compound I protonates the oxo group of Compound II. Such a protonation has been evoked as an explanation for the reactivity of Compound II at lower pH values in globins and free haem (Reeder *et al.*, 2008; Reeder *et al.*, 2002; Reeder and Wilson, 2001; Silaghi-Dumitrescu *et al.*, 2007).

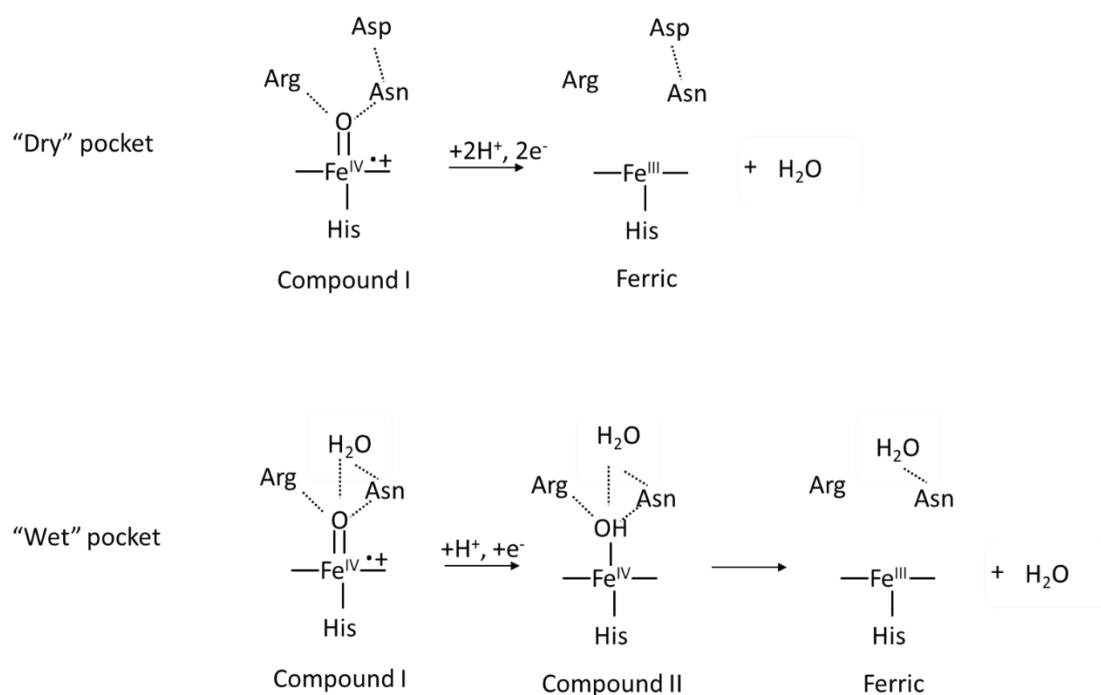


Figure 5.12. The catalytic mechanism of Compound II formation in DtpB based on structural and kinetic data. Compound II formation in DtpB requires a proton coupled electron transfer (PCET) to the ferryl haem resulting in protonated Compound II. Compound II is distinguishable only in the variants, where the pocket is “wet”, as formation of this intermediate is the rate-limiting in “dry” pocket. For detailed description see the main text.

Chapter Six

Summary

This thesis comprises detailed structural and kinetic study aimed towards deciphering mechanistic intricacies of Compound I and II formation in the dye-decolourising peroxidases (DyPs) found in *Streptomyces lividans*. DyPs are the most recently discovered member of the histidine-heme ligated peroxidase superfamily. They have a characteristic Asp residue in distal side of the haem pocket instead of a His which is found in the non-mammalian haem peroxidases. This Asp is paired with an Arg, with the Asp/Arg couple playing a prominent role in Compound I formation. Three DyPs have been identified in *S. lividans*: two A-types (DtpA and DtpAa) and a B-type (DtpB). Rather serendipitously, each DyP has a distinct reactivity with peroxide enabling for the focus of this thesis to be directed towards understanding the basis behind mechanistic variations in *S. lividans* DyPs.

In Chapter 2, a detailed structural and mechanistic characterisation of DtpAa is reported which is then compared with the homologues DtpA. By using X-ray crystallography, stopped-flow kinetics and deuterium kinetic isotope studies, it is shown that both DyPs react with peroxide to form Compound I via a common mechanism, but the reactivity and rate limits that define the mechanism are markedly different between them. DtpA forms Compound I rapidly, while DtpAa is an inefficient peroxidase with 100-fold slower Compound I formation. A validated ferric X-ray structure of DtpAa was determined and compared with the ferric DtpA structure, allowing for the kinetic differences to be attributed to a subtle structural repositioning of the distal haem pocket Asp side chain. Through site-directed mutagenesis, an acid–base catalyst responsible

for proton-transfer to form Compound I is identified to comprise a combination of a water molecule and the distal Asp (referred to as a water-Asp unit) (Figure 6.1). A mechanism for Compound I formation in which the rate limit may be shifted from peroxide binding to proton-transfer and controlled by the position of the distal water-Asp unit and the associated hydrogen-bonded water molecules was proposed and summarised in Figure 6.1.

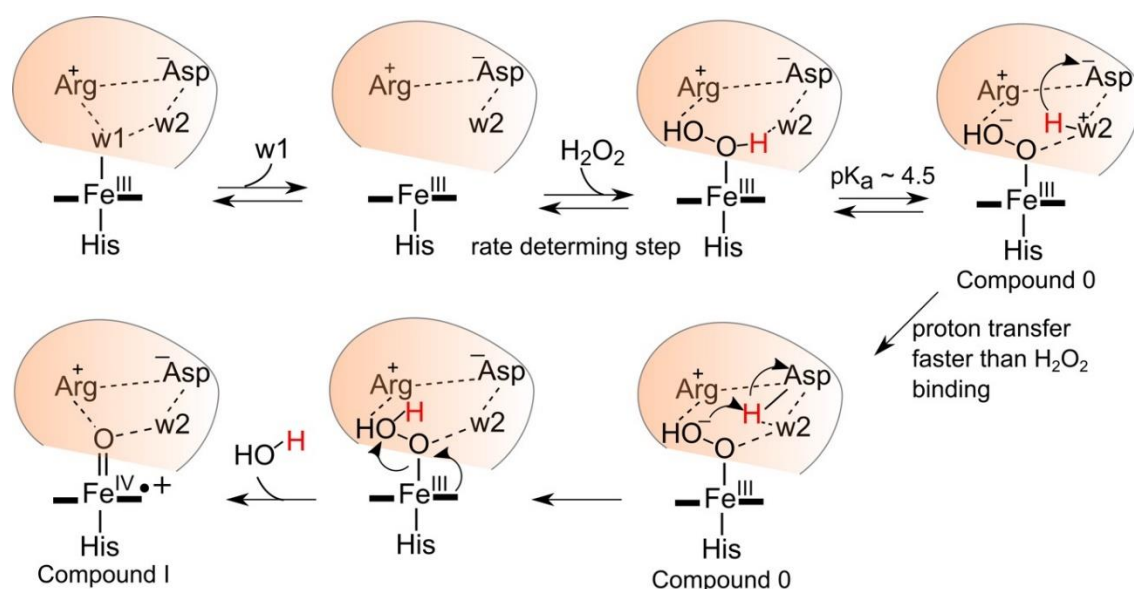


Figure 6.1. The catalytic mechanism of Compound I formation in DtpA based on structural and kinetic data. The H^α proton of the peroxide is shown in red and H-w2⁺ represents a hydronium ion. For a complete description of the individual steps see Chapter 2.

The mechanism of Compound I formation in DtpAa is further explored in Chapter 3, which utilizes Electron Paramagnetic Resonance (EPR) spectroscopy that allows monitoring of formation of transient paramagnetic species, such as Compound I and

tyrosyl and tryptophanyl radicals. Tyr/Trp residues are often positioned in haem enzymes as chains that lead out from the haem to the protein surface, constructing an escape route for radicals formed upon reaction with hydrogen peroxide, *i.e.* Compound I formation (Gray and Winkler, 2018; Gray and Winkler, 2021). Thus, the “destiny” of Compound I can be followed using EPR spectroscopy. Different positioning of Tyr/Trp residues can moderate enzyme reactivity towards a substrate. In DtpA a single Tyr residue was identified as radical site as potential starting point of electron-transfer pathway for substrate oxidation (Chaplin *et al.*, 2019). This Tyr is absent in DtpAa, with Phe found in the homologues position. However, an additional Tyr is present in DtpAa close to the Phe, with its side chain facing in the opposite direction. Effect of Tyr repositioning towards enzyme reactivity was studied using combination of site-directed mutagenesis EPR and stopped-flow studies. Preliminary data shows that kinetics of Compound I and II formation in DtpAa are not influenced by nearby Tyr residues. However, that does not exclude very likely changes in free radical escape routes caused by the mutations which could be identified using EPR spectroscopy. EPR spectra have been measured for DtpAa Tyr variants but remain to be analysed. In DtpAa an additional Tyr was found to have an important role in Compound I formation. This Tyr belongs to a highly conserved aromatic dyad motif previously identified to be disrupted in DtpA (Chaplin *et al.*, 2019). Upon addition of H₂O₂ to the Fe^{III}-DtpAa, a Compound-ES like signal is observed using EPR spectroscopy arising from a Compound I species with a radical on a Trp residue. The presence of Tyr-Trp dyad could account for such signal, with Tyr stabilising the radical on nearby Trp. Thus, further investigation is needed, including construction of “dyad” variants with combination of transient-state kinetic studies.

In Chapter 4, the spotlight is shifted from the A-types towards the B-type DyP (DtpB) from *S. lividans*. It focuses on different methods for capturing of the structures of intact redox states in metalloenzymes, which is critical for assigning the chemistry carried out by the metal in the catalytic cycle. Here, three such approaches have been attempted: *i*) Serial femtosecond X-ray crystallography (SFX), *ii*) Serial synchrotron X-ray crystallography (SSX) and *iii*) low-dose composite (*i.e.* multi-crystal) X-ray crystallography coupled with single crystal spectroscopy. Damage-free (zero dose) structures of the Fe^{III} and Fe^{IV} redox states of DtpB have been determined, with the Fe^{IV}-DtpB structure being the first reported validated Compound I structure of a DyP at room temperature and cryo-cooled temperatures. These structures reveal an additional Asn residue found inside the distal pocket of DtpB with its amide group occupying the spatial position where in the A-type enzymes a water molecule is located and H-bonded to the distal Asp (*i.e.* the water-Asp unit). Thus, DtpB houses a water-free distal haem site, with mechanistic implications which form part of the work presented in Chapter 5.

Chapter 5 is made up of a combination of mutagenesis and kinetic studies coupled with a set of redox state validated SFX structures of two DtpB distal pocket variants. These studies together provide a unique insight into how the distal heme site of DyPs can be tuned to select the Asp or Arg for the rate enhancement of peroxide heterolysis. The ‘dry’ distal haem site identified in Fe^{III}-haem DtpB structure in Chapter 4 reveals that the water mediated Asp mechanism utilised for Compound I formation in DtpA cannot occur in this B-type DyP. However, Compound I in DtpB does form rapidly. Substitution of the three distal heme pocket residues with an Ala has helped to elucidate their roles in Compound I formation in DtpB. Removal of the distal Arg slowed the

reaction and destabilized Compound I, indicating that in DtpB Arg is selected as an acid-base catalyst. A graphical representation of how Arg mediates proton movement on peroxide binding to the Fe^{III}-haem is shown in Figure 6.2.

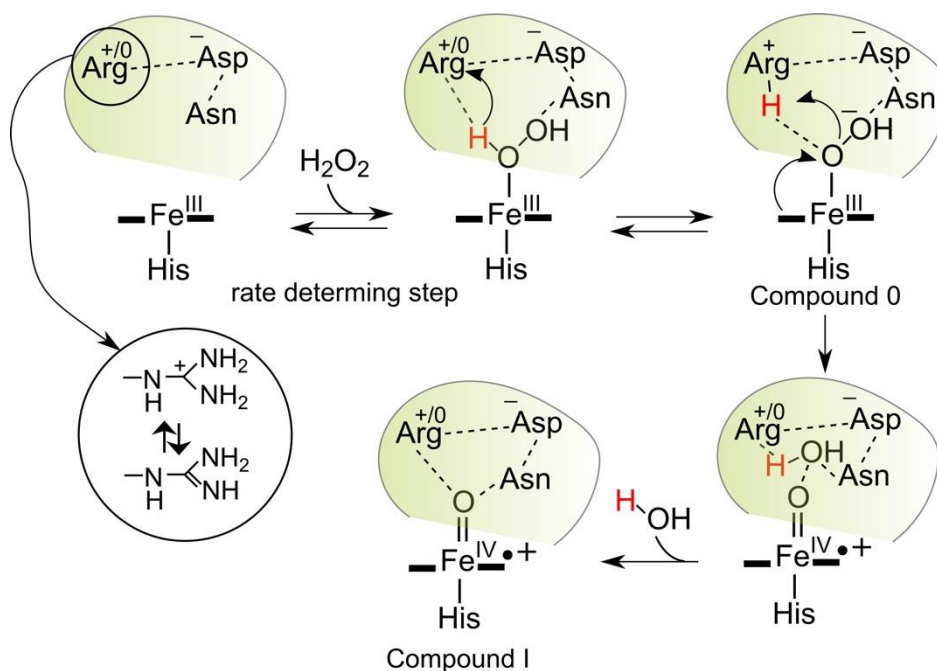


Figure 6.2. The catalytic mechanism of Compound I formation in DtpB based on structural and kinetic data. See Chapter 5 for a discussion of the individual steps.

Chapter 5 also showcases two Fe^{III}-haem structures of the D152A and N245A DtpB variants. They reveal that by mutating distal Asp and Asn to Ala, steric impediment to the formation of a distal water network is removed and a “wet” site is formed. This finding is complemented by stopped-flow data showing that the availability of proton donors (*i.e.* water molecules) increases the rate of Compound II formation. Compound II formation in DtpB requires a proton coupled electron transfer (PCET) to the ferryl haem and is faster in DtpB variants than in WT.

The work described in this thesis demonstrates that subtle differences between highly similar enzymes can greatly affect their catalytic mechanism, highlighting the importance for studying these intricacies and the need to integrate structural and kinetic approaches. Overall, it offers a new framework for understanding different mechanisms of Compound I and II formation adopted by DyPs through combination of redox validated X-ray crystal structures and transient state kinetics. Such comprehensive studies may open new paths towards discovery of DyPs' true substrate(s).

Thus, a challenge for the future researchers would be to obtain a redox state validated structure of Compound II species. Up to this date, no structural studies on a DyP Compound II species are available and approaches to address this would be a next step. Additionally, whilst obtaining 'static' structures of ferryl species are clearly not without challenges, a grand challenge would be to capture the intact structures of the peroxidatic cycle in 'real-time'. In this respect we should keep an eye on the on-going developments in room temperature time resolved X-ray crystallography that open an exciting area to exploit the visualization of structural intermediates in reaction cycles.

References

- Aasa, R., Vanngard, T. and Dunford, H. B. (1975) EPR Studies On Compound-I Of Horseradish-Peroxidase. *Biochimica Et Biophysica Acta*, **391**, 259-264.
- Ahmad, M., Roberts, J. N., Hardiman, E. M., Singh, R., Eltis, L. D. and Bugg, T. D. (2011) Identification of DypB from *Rhodococcus jostii* RHA1 as a lignin peroxidase. *Biochemistry*, **50**, 5096-107.
- Atkins, P. W. a. (2018) Atkins' physical chemistry, Cambridge, UK.
- Baek, H. K. and Vanwart, H. E. (1989) Elementary Steps In The Formation Of Horseradish-Peroxidase Compound-I - Direct Observation Of Compound-0, A New Intermediate With A Hyperporphyrin Spectrum. *Biochemistry*, **28**, 5714-5719.
- Balabin, I. A., Hu, X. and Beratan, D. N. (2012) Exploring biological electron transfer pathway dynamics with the Pathways plugin for VMD. *Journal of computational chemistry*, **33**, 906-910.
- Barty, A., Kirian, R. A., Maia, F. R., Hantke, M., Yoon, C. H., White, T. A. and Chapman, H. (2014) Cheetah: software for high-throughput reduction and analysis of serial femtosecond X-ray diffraction data. *Journal of Applied Crystallography*, **47**, 1118-1131.
- Becker, D., Swarts, S., Champagne, M. and Sevilla, M. D. (1988) An ESR Investigation of the Reactions of Glutathione, Cysteine and Penicillamine Thiyl Radicals: Competitive Formation of $\text{RSO}\cdot$, $\text{R}\cdot$, RSSR , and $\text{RSS}\cdot$. *International Journal of Radiation Biology*, **53**, 767-786.
- Beers, R. F., Jr. and Sizer, I. W. (1952) A spectrophotometric method for measuring the breakdown of hydrogen peroxide by catalase. *J Biol Chem*, **195**, 133-40.
- Behan, R. K. and Green, M. T. (2006) On the status of ferryl protonation. *Journal of Inorganic Biochemistry*, **100**, 448-59.
- Benecky, M. J., Frew, J. E., Scowen, N., Jones, P. and Hoffman, B. M. (1993) EPR and ENDOR detection of compound I from *Micrococcus lysodeikticus* catalase. *Biochemistry*, **32**, 11929-11933.
- Berglund, G. I., Carlsson, G. H., Smith, A. T., Szoke, H., Henriksen, A. and Hajdu, J. (2002) The catalytic pathway of horseradish peroxidase at high resolution. *Nature*, **417**, 463-468.
- Blumberg, W. E., Peisach, J., Wittenberg, B. A. and Wittenberg, J. B. (1968) The electronic structure of protoheme proteins. I. An electron paramagnetic resonance and optical study of horseradish peroxidase and its derivatives. *Journal of Biological Chemistry*, **243**, 1854-1862.
- Bonagura, C. A., Bhaskar, B., Shimizu, H., Li, H., Sundaramoorthy, M., McRee, D. E., Goodin, D. B. and Poulos, T. L. (2003) High-resolution crystal structures and spectroscopy of native and compound I cytochrome c peroxidase. *Biochemistry*, **42**, 5600-5608.
- Burmeister, W. P. (2000) Structural changes in a cryo-cooled protein crystal owing to radiation damage. *Acta Crystallographica Section D*, **56**, 328-41.
- Burton, M. J., Cresser-Brown, J., Thomas, M., Portolano, N., Basran, J., Freeman, S. L., Kwon, H., Bottrill, A. R., Llansola-Portoles, M. J., Pascal, A. A., Jukes-Jones, R., Chernova, T., Schmid, R., Davies, N. W., Storey, N. M., Dorlet, P., Moody, P. C. E., Mitcheson, J. S. and Raven, E. L. (2020) Discovery of a

- heme-binding domain in a neuronal voltage-gated potassium channel. *Journal of Biological Chemistry*, **295**, 13277-13286.
- Casadei, C. M., Gumiero, A., Metcalfe, C. L., Murphy, E. J., Basran, J., Concilio, M. G., Teixeira, S. C., Schrader, T. E., Fielding, A. J., Ostermann, A., Blakeley, M. P., Raven, E. L. and Moody, P. C. (2014) Heme enzymes. Neutron cryo-crystallography captures the protonation state of ferryl heme in a peroxidase. *Science*, **345**, 193-197.
- Chand, S., Ray, S., Wanigasekara, E., Yadav, P., Crawford, J. A., Armstrong, D. W., Rajeshwar, K. and Pierce, B. S. (2018) Improved rate of substrate oxidation catalyzed by genetically-engineered myoglobin. *Archives of Biochemistry and Biophysics*, **639**, 44-51.
- Chaplin, A. K., Chicano, T. M., Hampshire, B. V., Wilson, M. T., Hough, M. A., Svistunenko, D. A. and Worrall, J. A. R. (2019) An Aromatic Dyad Motif in Dye Decolourising Peroxidases Has Implications for Free Radical Formation and Catalysis. *Chemistry – A European Journal*, **25**, 6141-6153.
- Chaplin, A. K., Wilson, M. T. and Worrall, J. A. R. (2017) Kinetic characterisation of a dye decolourising peroxidase from *Streptomyces lividans*: new insight into the mechanism of anthraquinone dye decolourisation. *Dalton Transactions*, **46**, 9420-9429.
- Chapman, H. N., Caleman, C. and Timneanu, N. (2014) Diffraction before destruction. *Philosophical Transactions of the Royal Society B: Biological Sciences*, **369**, 20130313.
- Chapman, H. N., Fromme, P., Barty, A., White, T. A., Kirian, R. A., Aquila, A., Hunter, M. S., Schulz, J., DePonte, D. P., Weierstall, U., Doak, R. B., Maia, F., Martin, A. V., Schlichting, I., Lomb, L., Coppola, N., Shoeman, R. L., Epp, S. W., Hartmann, R., Rolles, D., Rudenko, A., Foucar, L., Kimmel, N., Weidenspointner, G., Holl, P., Liang, M. N., Barthelmess, M., Caleman, C., Boutet, S., Bogan, M. J., Krzywinski, J., Bostedt, C., Bajt, S., Gumprecht, L., Rudek, B., Erk, B., Schmidt, C., Homke, A., Reich, C., Pietschner, D., Struder, L., Hauser, G., Gorke, H., Ullrich, J., Herrmann, S., Schaller, G., Schopper, F., Soltau, H., Kuhnel, K. U., Messerschmidt, M., Bozek, J. D., Hau-Riege, S. P., Frank, M., Hampton, C. Y., Sierra, R. G., Starodub, D., Williams, G. J., Hajdu, J., Timneanu, N., Seibert, M. M., Andreasson, J., Rucker, A., Jonsson, O., Svenda, M., Stern, S., Nass, K., Andrich, R., Schroter, C. D., Krasniqi, F., Bott, M., Schmidt, K. E., Wang, X. Y., Grotjohann, I., Holton, J. M., Barends, T. R. M., Neutze, R., Marchesini, S., Fromme, R., Schorb, S., Rupp, D., Adolph, M., Gorkhover, T., Andersson, I., Hirsemann, H., Potdevin, G., Graafsma, H., Nilsson, B. and Spence, J. C. H. (2011) Femtosecond X-ray protein nanocrystallography. *Nature*, **470**, 73-U81.
- Chen, C., Shrestha, R., Jia, K., Gao, P. F., Geisbrecht, B. V., Bossmann, S. H., Shi, J. and Li, P. (2015) Characterization of Dye-decolorizing Peroxidase (DyP) from *Thermomonospora curvata* Reveals Unique Catalytic Properties of A-type DyPs. *Journal of Biological Chemistry*, **290**, 23447-23463.
- Chen, K. C., Wu, J. Y., Liou, D. J. and Hwang, S. C. J. (2003) Decolorization of the textile dyes by newly isolated bacterial strains. *Journal of Biotechnology*, **101**, 57-68.
- Chreifi, G., Baxter, E. L., Doukov, T., Cohen, A. E., McPhillips, S. E., Song, J., Meharena, Y. T., Soltis, S. M. and Poulos, T. L. (2016) Crystal structure of the pristine peroxidase ferryl center and its relevance to proton-coupled

- electron transfer. *Proceedings of the National Academy of Sciences of the United States of America*, **113**, 1226-1231.
- Contreras, H., Joens, M. S., McMath, L. M., Le, V. P., Tullius, M. V., Kimmey, J. M., Bionghi, N., Horwitz, M. A., Fitzpatrick, J. A. and Goulding, C. W. (2014) Characterization of a Mycobacterium tuberculosis nanocompartment and its potential cargo proteins. *Journal of Biological Chemistry*, **289**, 18279-18289.
- Cowtan, K. (2006) The Buccaneer software for automated model building. 1. Tracing protein chains. *Acta Crystallographica Section D: Structural Biology*, **62**, 1002-1011.
- Davis, I. W., Leaver-Fay, A., Chen, V. B., Block, J. N., Kapral, G. J., Wang, X., Murray, L. W., Arendall, W. B., 3rd, Snoeyink, J., Richardson, J. S. and Richardson, D. C. (2007) MolProbity: all-atom contacts and structure validation for proteins and nucleic acids. *Nucleic Acids Research*, **35**, 375-383.
- de la Mora, E., Coquelle, N., Bury, C. S., Rosenthal, M., Holton, J. M., Carmichael, I., Garman, E. F., Burghammer, M., Colletier, J.-P. and Weik, M. (2020) Radiation damage and dose limits in serial synchrotron crystallography at cryo- and room temperatures. *Proceedings of the National Academy of Sciences*, **117**, 4142-4151.
- Dempsey, J. L., Winkler, J. R. and Gray, H. B. (2010) Proton-coupled electron flow in protein redox machines. *Chemical reviews*, **110**, 7024-7039.
- Dolphin, D., Forman, A., Borg, D. C., Fajer, J. and Felton, R. H. (1971) Compounds I of Catalase and Horse Radish Peroxidase: π -cation Radicals. *Proceedings of the National Academy of Sciences of the United States of America*, **68**, 614-618.
- Dunford, H. B. (1999) *Heme peroxidases*, John Wiley.
- Ebrahim, A., Moreno-Chicano, T., Appleby, M. V., Chaplin, A. K., Beale, J. H., Sherrell, D. A., Duyvesteyn, H. M. E., Owada, S., Tono, K., Sugimoto, H., Strange, R. W., Worrall, J. A. R., Axford, D., Owen, R. L. and Hough, M. A. (2019) Dose-resolved serial synchrotron and XFEL structures of radiation-sensitive metalloproteins. *IUCrJ*, **6**, 543-551.
- Emsley, P., Lohkamp, B., Scott, W. G. and Cowtan, K. (2010) Features and development of Coot. *Acta Crystallographica Section D: Structural Biology*, **66**, 486-501.
- Erman, J. E., Vitello, L. B., Mauro, J. M. and Kraut, J. (1989) Detection Of An Oxyferryl Porphyrin π -cation-radical Intermediate In The Reaction Between Hydrogen-Peroxide And A Mutant Yeast Cytochrome-C Peroxidase - Evidence For Tryptophan-191 Involvement In The Radical Site Of Compound-I. *Biochemistry*, **28**, 7992-7995.
- Erman, J. E., Vitello, L. B., Miller, M. A., Shaw, A., Brown, K. A. and Kraut, J. (1993) Histidine 52 is a critical residue for rapid formation of cytochrome c peroxidase compound I. *Biochemistry*, **32**, 9798-9806.
- Evans, P. R. and Murshudov, G. N. (2013) How good are my data and what is the resolution? *Acta Crystallographica Section D: Structural Biology*, **69**, 1204-1214.
- Evans, R. M., Brooke, E. J., Wehlin, S. A. M., Nomerotskaia, E., Sargent, F., Carr, S. B., Phillips, S. E. V. and Armstrong, F. A. (2016) Mechanism of hydrogen activation by [NiFe] hydrogenases. *Nature Chemical Biology*, **12**, 46-50.

- Fawal, N., Li, Q., Savelli, B., Brette, M., Passaia, G., Fabre, M., Mathé, C. and Dunand, C. (2013) PeroxiBase: a database for large-scale evolutionary analysis of peroxidases. *Nucleic Acids Research*, **41**, 441-444.
- Fitch, C. A., Platzer, G., Okon, M., Garcia-Moreno E., B. and McIntosh, L. P. (2015) Arginine: Its pKa value revisited. *Protein Science*, **24**, 752-761.
- Fraser, J. S., van den Bedem, H., Samelson, A. J., Lang, P. T., Holton, J. M., Echols, N. and Alber, T. (2011) Accessing protein conformational ensembles using room-temperature X-ray crystallography. *Proceedings of the National Academy of Sciences of the United States of America*, **108**, 16247-16252.
- Freeman, S. L., Kwon, H., Portolano, N., Parkin, G., Venkatraman Girija, U., Basran, J., Fielding, A. J., Fairall, L., Svistunenko, D. A., Moody, P. C. E., Schwabe, J. W. R., Kyriacou, C. P. and Raven, E. L. (2019) Heme binding to human CLOCK affects interactions with the E-box. *Proceedings of the National Academy of Sciences of the United States of America*, **116**, 19911-19916.
- Fuchs, M. R., Pradervand, C., Thominet, V., Schneider, R., Panepucci, E., Grunder, M., Gabadinho, J., Dworkowski, F. S., Tomizaki, T., Schneider, J., Mayer, A., Curtin, A., Olieric, V., Frommherz, U., Kotrlé, G., Welte, J., Wang, X., Maag, S., Schulze-Briese, C. and Wang, M. (2014) D3, the new diffractometer for the macromolecular crystallography beamlines of the Swiss Light Source. *Journal of Synchrotron Radiation*, **21**, 340-51.
- Gasteiger, E., Gattiker, A., Hoogland, C., Ivanyi, I., Appel, R. D. and Bairoch, A. (2003) ExPASy: the proteomics server for in-depth protein knowledge and analysis. *Nucleic Acids Research*, **31**, 3784-3788.
- Giessen, T. W. (2016) Encapsulins: microbial nanocompartments with applications in biomedicine, nanobiotechnology and materials science. *Current Opinions in Chemical Biology*, **34**, 1-10.
- Giessen, T. W. and Silver, P. A. (2017) Widespread distribution of encapsulin nanocompartments reveals functional diversity. *Nature Microbiology*, **2**, 17029.
- Gotthard, G., Aumonier, S., De Sanctis, D., Leonard, G., von Stetten, D. and Royant, A. (2019) Specific radiation damage is a lesser concern at room temperature. *IUCrJ*, **6**, 665-680.
- Gray, H. B. and Winkler, J. R. (2018) Living with Oxygen. *Accounts of Chemical Research*, **51**, 1850-1857.
- Gray, H. B. and Winkler, J. R. (2021) Functional and protective hole hopping in metalloenzymes. *Chemical Science*, **12**, 13988-14003.
- Green, M. T. (2006) Application of Badger's rule to heme and non-heme iron-oxygen bonds: an examination of ferryl protonation states. *Journal of American Chemical Society*, **128**, 1902-6.
- Groves, J. T. (2006) High-valent iron in chemical and biological oxidations. *Journal of Inorganic Biochemistry*, **100**, 434-47.
- Guillén Schlippe, Y. V. and Hedstrom, L. (2005) A twisted base? The role of arginine in enzyme-catalyzed proton abstractions. *Archives of Biochemistry and Biophysics*, **433**, 266-278.
- Gumiero, A., Metcalfe, C. L., Pearson, A. R., Raven, E. L. and Moody, P. C. (2011) Nature of the ferryl heme in compounds I and II. *Journal of Biological Chemistry*, **286**, 1260-1268.
- Gurusaran, M., Shankar, M., Nagarajan, R., Helliwell, J. R. and Sekar, K. (2013) Do we see what we should see? Describing non-covalent interactions in protein structures including precision. *IUCrJ*, **1**, 74-81.

- Habib, M. H., Rozeboom, H. J. and Fraaije, M. W. (2019) Characterization of a New DyP-Peroxidase from the Alkaliphilic Cellulomonad, *Cellulomonas bogoriensis*. *Molecules (Basel, Switzerland)*, **24**, 1208.
- Hassanali, A., Giberti, F., Cuny, J., Kuhne, T. D. and Parrinello, M. (2013) Proton transfer through the water gossamer. *Proceedings of the National Academy of Sciences of the United States of America*, **110**, 13723-13728.
- Hedberg, A. and Ehrenberg, A. (1968) Resolution Enhancement of ESR Spectra from Irradiated Single Crystals of Glycine. *The Journal of Chemical Physics*, **48**, 4822-4828.
- Henderson, R. (1995) The potential and limitations of neutrons, electrons and X-rays for atomic resolution microscopy of unstained biological molecules. *Quarterly Reviews of Biophysics*, **28**, 171-193.
- Hillar, A., Peters, B., Pauls, R., Loboda, A., Zhang, H., Mauk, A. G. and Loewen, P. C. (2000) Modulation of the activities of catalase-peroxidase HPI of *Escherichia coli* by site-directed mutagenesis. *Biochemistry*, **39**, 5868-5875.
- Hiner, A. N., Raven, E. L., Thorneley, R. N., Garcia-Canovas, F. and Rodriguez-Lopez, J. N. (2002) Mechanisms of compound I formation in heme peroxidases. *Journal of Inorganic Biochemistry*, **91**, 27-34.
- Hiromoto, T., Meilleur, F., Shimizu, R., Shibasaki, C., Adachi, M., Tamada, T. and Kuroki, R. (2017) Neutron structure of the T26H mutant of T4 phage lysozyme provides insight into the catalytic activity of the mutant enzyme and how it differs from that of wild type. *Protein Science*, **26**, 1953-1963.
- Hofbauer, S., Pfanzagl, V., Michlits, H., Schmidt, D., Obinger, C. and Furtmüller, P. G. (2021) Understanding molecular enzymology of porphyrin-binding $\alpha + \beta$ barrel proteins - One fold, multiple functions. *Biochimica et Biophysica Acta Proteins and Proteomics*, **1869**, 140536.
- Howes, B. D., Rodriguez-Lopez, J. N., Smith, A. T. and Smulevich, G. (1997) Mutation of Distal Residues of Horseradish Peroxidase: Influence on Substrate Binding and Cavity Properties. *Biochemistry*, **36**, 1532-1543.
- Husain, Q. (2010) Peroxidase mediated decolorization and remediation of wastewater containing industrial dyes: a review. *Reviews in Environmental Science and Bio-Technology*, **9**, 117-140.
- Hwang, H. J., Dilbeck, P., Debus, R. J. and Burnap, R. L. (2007) Mutation of Arginine 357 of the CP43 Protein of Photosystem II Severely Impairs the Catalytic S-State Cycle of the H₂O Oxidation Complex. *Biochemistry*, **46**, 11987-11997.
- Ilme, S. (2015) Serial femtosecond crystallography: the first five years. *IUCrJ*, **2**, 246-255.
- Ishikita, H. and Saito, K. (2014) Proton transfer reactions and hydrogen-bond networks in protein environments. *Journal of the Royal Society Interface*, **11**, 20130518.
- Ivancich, A., Dorlet, P., Goodin, D. B. and Un, S. (2001) Multifrequency High-Field EPR Study of the Tryptophanyl and Tyrosyl Radical Intermediates in Wild-Type and the W191G Mutant of Cytochrome c Peroxidase. *Journal of the American Chemical Society*, **123**, 5050-5058.
- Ivancich, A., Jakopitsch, C., Auer, M., Un, S. and Obinger, C. (2003) Protein-based radicals in the catalase-peroxidase of *synechocystis* PCC6803: a multifrequency EPR investigation of wild-type and variants on the environment of the heme active site. *Journal of the American Chemical Society*, **125**, 14093-14102.

- Ivancich, A., Jouve, H. M., Sartor, B. and Gaillard, J. (1997) EPR investigation of compound I in *Proteus mirabilis* and bovine liver catalases: formation of porphyrin and tyrosyl radical intermediates. *Biochemistry*, **36**, 9356-64.
- Jones, P. (2001) Roles of water in heme peroxidase and catalase mechanisms. *Journal of Biological Chemistry*, **276**, 13791-13796.
- Kabsch, W. (2010) XDS. *Acta Crystallographica Section D: Structural Biology*, **66**, 125-132.
- Kala Sekar, D. K., Manickam, G., Satheesh, S. N., Radha, P., Pavithra, S., Tharshan, K. and Helliwell, J. (2015) Online-DPI: A web server to calculate the diffraction precision index for a protein structure. *Journal of Applied Crystallography*, **48**, 939-942.
- Kameshima, T., Ono, S., Kudo, T., Ozaki, K., Kirihara, Y., Kobayashi, K., Inubushi, Y., Yabashi, M., Horigome, T., Holland, A., Holland, K., Burt, D., Murao, H. and Hatsui, T. (2014) Development of an X-ray pixel detector with multi-port charge-coupled device for X-ray free-electron laser experiments. *Review of Scientific Instruments*, **85**, 033110.
- Keegan, R. M. and Winn, M. D. (2008) MrBUMP: an automated pipeline for molecular replacement. *Acta Crystallographica Section D: Structural Biology*, **64**, 119-24.
- Kekilli, D., Moreno-Chicano, T., Chaplin, A. K., Horrell, S., Dworkowski, F. S. N., Worrall, J. A. R., Strange, R. W. and Hough, M. A. (2017) Photoreduction and validation of haem-ligand intermediate states in protein crystals by in situ single-crystal spectroscopy and diffraction. *IUCrJ*, **4**, 263-270.
- Khindaria, A. and Aust, S. D. (1996) EPR detection and characterization of lignin peroxidase porphyrin pi-cation radical. *Biochemistry*, **35**, 13107-13111.
- Kim, S. J. and Shoda, M. (1999) Purification and characterization of a novel peroxidase from *Geotrichum candidum* Dec 1 involved in decolorization of dyes. *Applied and Environmental Microbiology*, **65**, 1029-1035.
- Kwon, H., Basran, J., Casadei, C. M., Fielding, A. J., Schrader, T. E., Ostermann, A., Devos, J. M., Aller, P., Blakeley, M. P., Moody, P. C. E. and Raven, E. L. (2016) Direct visualization of a Fe(IV)-OH intermediate in a heme enzyme. *Nature Communications*, **7**.
- Kwon, H., Basran, J., Devos, J. M., Suardíaz, R., van der Kamp, M. W., Mulholland, A. J., Schrader, T. E., Ostermann, A., Blakeley, M. P., Moody, P. C. E. and Raven, E. L. (2020) Visualizing the protons in a metalloenzyme electron proton transfer pathway. *Proceedings of the National Academy of Sciences*, **117**, 6484-6490.
- Kwon, H., Basran, J., Pathak, C., Hussain, M., Freeman, S. L., Fielding, A. J., Bailey, A. J., Stefanou, N., Sparkes, H. A., Tosha, T., Yamashita, K., Hirata, K., Murakami, H., Ueno, G., Ago, H., Tono, K., Yamamoto, M., Sawai, H., Shiro, Y., Sugimoto, H., Raven, E. L. and Moody, P. C. E. (2021) XFEL Crystal Structures of Peroxidase Compound II. *Angewandte Chemie International Edition*, **60**, 14578-14585.
- Kwon, H., Smith, O., Raven, E. L. and Moody, P. C. E. (2017) Combining X-ray and neutron crystallography with spectroscopy. *Acta Crystallographica Section D: Structural Biology*, **73**, 141-147.
- Ledray, A. P., Krest, C. M., Yosca, T. H., Mitra, K. and Green, M. T. (2020) Ascorbate Peroxidase Compound II Is an Iron(IV) Oxo Species. *Journal of American Chemical Society*, **48**, 20419-20425 .

- Ledray, A. P., Mitra, K. and Green, M. T. (2021) NRVS investigation of ascorbate peroxidase compound II: Observation of Iron(IV)oxo stretching. *Journal of Inorganic Biochemistry*, **224**, 111548.
- Liebschner, D., Afonine, P. V., Baker, M. L., Bunkoczi, G., Chen, V. B., Croll, T. I., Hintze, B., Hung, L. W., Jain, S., McCoy, A. J., Moriarty, N. W., Oeffner, R. D., Poon, B. K., Prisant, M. G., Read, R. J., Richardson, J. S., Richardson, D. C., Sammito, M. D., Sobolev, O. V., Stockwell, D. H., Terwilliger, T. C., Urzhumtsev, A. G., Videau, L. L., Williams, C. J. and Adams, P. D. (2019) Macromolecular structure determination using X-rays, neutrons and electrons: recent developments in Phenix. *Acta Crystallographica Section D: Structural Biology*, **75**, 861-877.
- Liers, C., Bobeth, C., Pecyna, M., Ullrich, R. and Hofrichter, M. (2010) DyP-like peroxidases of the jelly fungus *Auricularia auricula-judae* oxidize nonphenolic lignin model compounds and high-redox potential dyes. *Applied Microbiological Biotechnology*, **85**, 1869-1879.
- Liers, C., Pecyna, M. J., Kellner, H., Worrlich, A., Zorn, H., Steffen, K. T., Hofrichter, M. and Ullrich, R. (2013) Substrate oxidation by dye-decolorizing peroxidases (DyPs) from wood- and litter-degrading agaricomycetes compared to other fungal and plant heme-peroxidases. *Applied Microbiological Biotechnology*, **97**, 5839-49.
- Linde, D., Pogni, R., Canellas, M., Lucas, F., Guallar, V., Baratto, M. C., Sinicropi, A., Saez-Jimenez, V., Coscolin, C., Romero, A., Medrano, F. J., Ruiz-Duenas, F. J. and Martinez, A. T. (2015) Catalytic surface radical in dye-decolorizing peroxidase: a computational, spectroscopic and site-directed mutagenesis study. *Biochemical Journal*, **466**, 253-262.
- Liu, X., Du, Q., Wang, Z., Zhu, D., Huang, Y., Li, N., Wei, T., Xu, S. and Gu, L. (2011) Crystal structure and biochemical features of EfeB/YcdB from *Escherichia coli* O157: ASP235 plays divergent roles in different enzyme-catalyzed processes. *Journal of Biological Chemistry*, **286**, 14922-14931.
- Liu, X., Yuan, Z., Wang, J., Cui, Y., Liu, S., Ma, Y., Gu, L. and Xu, S. (2017) Crystal structure and biochemical features of dye-decolorizing peroxidase YfeX from *Escherichia coli* O157 Asp(143) and Arg(232) play divergent roles toward different substrates. *Biochemical Biophysical Research Communications*, **484**, 40-44.
- Lučić, M., Chaplin, A. K., Moreno-Chicano, T., Dworkowski, F. S. N., Wilson, M. T., Svistunenko, D. A., Hough, M. A. and Worrall, J. A. R. (2020a) A subtle structural change in the distal haem pocket has a remarkable effect on tuning hydrogen peroxide reactivity in dye decolourising peroxidases from *Streptomyces lividans*. *Dalton Transactions*, **49**, 1620-1636.
- Lučić, M., Svistunenko, D. A., Wilson, M. T., Chaplin, A. K., Davy, B., Ebrahim, A., Axford, D., Tosha, T., Sugimoto, H., Owada, S., Dworkowski, F. S. N., Tews, I., Owen, R. L., Hough, M. A. and Worrall, J. A. R. (2020b) Serial Femtosecond Zero Dose Crystallography Captures a Water-Free Distal Heme Site in a Dye-Decolorising Peroxidase to Reveal a Catalytic Role for an Arginine in Fe(IV) =O Formation. *Angewandte Chemie International Edition English*, **59**, 21656-21662.
- Martiel, I., Muller-Werkmeister, H. M. and Cohen, A. E. (2019) Strategies for sample delivery for femtosecond crystallography. *Acta Crystallographica Section D: Structural Biology*, **75**, 160-177.

- Matsui, T., Ozaki, S.-i. and Watanabe, Y. (1999) Formation and Catalytic Roles of Compound I in the Hydrogen Peroxide-Dependent Oxidations by His64 Myoglobin Mutants. *Journal of the American Chemical Society*, **121**, 9952-9957.
- Mauro, J. M., Fishel, L. A., Hazzard, J. T., Meyer, T. E., Tollin, G., Cusanovich, M. A. and Kraut, J. (1988) Tryptophan-191- Phenylalanine, a Proximal-side Mutation in Yeast Cytochrome-C Peroxidase that Strongly Affects the Kinetics of Ferrocycytochrome-c Oxidation. *Biochemistry*, **27**, 6243-6256.
- Mehareenna, Y. T., Doukov, T., Li, H. Y., Soltis, S. M. and Poulos, T. L. (2010) Crystallographic and Single-Crystal Spectral Analysis of the Peroxidase Ferryl Intermediate. *Biochemistry*, **49**, 2984-2986.
- Mendes, S., Brissos, V., Gabriel, A., Catarino, T., Turner, D. L., Todorovic, S. and Martins, L. O. (2015a) An integrated view of redox and catalytic properties of B-type PpDyP from *Pseudomonas putida* MET94 and its distal variants. *Archives of Biochemistry and Biophysics*, **574**, 99-107.
- Mendes, S., Catarino, T., Silveira, C., Todorovic, S. and Martin, L. O. (2015b) The catalytic mechanism of A-type dye-decolourising peroxidase BsDyP: neither aspartate nor arginine is individually essential for peroxidase activity. *Catalysis Science & Technology*, **5**, 5196-5207.
- Moody, P. C. E. and Raven, E. L. (2018) The Nature and Reactivity of Ferryl Heme in Compounds I and II. *Accounts of Chemical Research*, **51**, 427-435.
- Moore, G. R. (1983) Control of redox properties of cytochrome c by special electrostatic interactions. *FEBS Lett*, **161**, 171-175.
- Moreno-Chicano, T., Ebrahim, A., Axford, D., Appleby, M. V., Beale, J. H., Chaplin, A. K., Duyvesteyn, H. M. E., Ghiladi, R. A., Owada, S., Sherrell, D. A., Strange, R. W., Sugimoto, H., Tono, K., Worrall, J. A. R., Owen, R. L. and Hough, M. A. (2019) High-throughput structures of protein-ligand complexes at room temperature using serial femtosecond crystallography. *IUCrJ*, **6**, 1074-1085.
- Murshudov, G. N., Vagin, A. A. and Dodson, E. J. (1997) Refinement of macromolecular structures by the maximum-likelihood method. *Acta Crystallographica Section D: structural Biology*, **53**, 240-255.
- Neutze, R., Wouts, R., van der Spoel, D., Weckert, E. and Hajdu, J. (2000) Potential for biomolecular imaging with femtosecond X-ray pulses. *Nature*, **406**, 752-7.
- Newcomb, M., Halgrimson, J. A., Horner, J. H., Wasinger, E. C., Chen, L. X. and Sligar, S. G. (2008) X-ray absorption spectroscopic characterization of a cytochrome P450 compound II derivative. *Proceedings of the National Academy of Sciences of the United States of America*, **105**, 8179-84.
- Ogola, H. J., Kamiike, T., Hashimoto, N., Ashida, H., Ishikawa, T., Shibata, H. and Sawa, Y. (2009) Molecular characterization of a novel peroxidase from the cyanobacterium *Anabaena* sp. strain PCC 7120. *Appl Environ Microbiol*, **75**, 7509-7518.
- Owen, R. L., Axford, D., Sherrell, D. A., Kuo, A., Ernst, O. P., Schulz, E. C., Miller, R. J. D. and Mueller-Werkmeister, H. M. (2017) Low-dose fixed-target serial synchrotron crystallography. *Acta Crystallographica Section D: Structural Biology*, **73**, 373-378.
- Owen, R. L., Rudiño-Piñera, E. and Garman, E. F. (2006) Experimental determination of the radiation dose limit for cryocooled protein crystals. *Proceedings of the National Academy of Sciences of the United States of America*, **103**, 4912-4917.

- Pankhurst, K. L., Mowat, C. G., Rothery, E. L., Hudson, J. M., Jones, A. K., Miles, C. S., Walkinshaw, M. D., Armstrong, F. A., Reid, G. A. and Chapman, S. K. (2006) A Proton Delivery Pathway in the Soluble Fumarate Reductase from *Shewanella frigidimarina*. *Journal of Biological Chemistry*, **281**, 20589-20597.
- Patterson, W. R., Poulos, T. L. and Goodin, D. B. (1995) Identification of a porphyrin pi-cation-radical in ascorbate peroxidase compound-I. *Biochemistry*, **34**, 4342-4345.
- Peisach, J., Blumberg, W. E., Ogawa, S., Rachmilewitz, E. A. and Oltzik, R. (1971) The effects of protein conformation on the heme symmetry in high spin ferric heme proteins as studied by electron paramagnetic resonance. *Journal of Biological Chemistry*, **246**, 3342-3355.
- Petrus, M. L. C., Vijgenboom, E., Chaplin, A. K., Worrall, J. A. R., van Wezel, G. P. and Claessen, D. (2016) The DyP-type peroxidase DtpA is a Tat-substrate required for GlxA maturation and morphogenesis in *Streptomyces*. *Open Biology*, **6**.
- Pfanzagl, V., Beale, J., Michlits, H., Schmidt, D., Gabler, T., Obinger, C., Djinovi - Carugo, K. and Hofbauer, S. (2020) X-ray induced photoreduction of heme metal centers rapidly induces active-site perturbations in a protein-independent manner. *Journal of Biological Chemistry*, **295**, 13488 - 13501.
- Pfanzagl, V., Bellei, M., Hofbauer, S., Laurent, C., Furtmuller, P. G., Oostenbrink, C., Battistuzzi, G. and Obinger, C. (2019) Redox thermodynamics of B-class dye-decolorizing peroxidases. *Journal of Inorganic Biochemistry*, **199**, 110761.
- Pfanzagl, V., Nys, K., Bellei, M., Michlits, H., Mlynek, G., Battistuzzi, G., Djinovic-Carugo, K., Van Doorslaer, S., Furtmüller, P. G., Hofbauer, S. and Obinger, C. (2018) Roles of distal aspartate and arginine of B-class dye-decolorizing peroxidase in heterolytic hydrogen peroxide cleavage. *Journal of Biological Chemistry*, **293**, 14823-14838.
- Potterton, L., Agirre, J., Ballard, C., Cowtan, K., Dodson, E., Evans, P. R., Jenkins, H. T., Keegan, R., Krissinel, E., Stevenson, K., Lebedev, A., McNicholas, S. J., Nicholls, R. A., Noble, M., Pannu, N. S., Roth, C., Sheldrick, G., Skubak, P., Turkenburg, J., Uski, V., von Delft, F., Waterman, D., Wilson, K., Winn, M. and Wojdyr, M. (2018) CCP4i2: the new graphical user interface to the CCP4 program suite. *Acta Crystallographica Section D: Structural Biology*, **74**, 68-84.
- Poulos, T. L. (2014) Heme Enzyme Structure and Function. *Chemical Reviews*, **114**, 3919-3962.
- Poulos, T. L. and Kraut, J. (1980) A hypothetical model of the cytochrome-c peroxidase cytochrome-c electron-transfer complex. *Journal of Biological Chemistry*, **255**, 322-330.
- Raczyńska, E. D., Cyrański, M. K., Gutowski, M., Rak, J., Gal, J.-F., Maria, P.-C., Darowska, M. and Duczmal, K. (2003) Consequences of proton transfer in guanidine. *Journal of Physical Organic Chemistry*, **16**, 91-106.
- Rahmanpour, R. and Bugg, T. D. (2013) Assembly in vitro of *Rhodococcus jostii* RHA1 encapsulin and peroxidase DypB to form a nanocompartment. *FEBS J*, **280**, 2097-104.
- Rai, H. S., Bhattacharyya, M. S., Singh, J., Bansal, T. K., Vats, P. and Banerjee, U. C. (2005) Removal of dyes from the effluent of textile and dyestuff manufacturing industry: A review of emerging techniques with reference to

- biological treatment. *Critical Reviews in Environmental Science and Technology*, **35**, 219-238.
- Rajagopal, Badri S., Edzuma, Ann N., Hough, Michael A., Blundell, Katie L. I. M., Kagan, Valerian E., Kapralov, Alexandr A., Fraser, Lewis A., Butt, Julea N., Silkstone, Gary G., Wilson, Michael T., Svistunenko, Dimitri A. and Worrall, Jonathan A. R. (2013) The hydrogen-peroxide-induced radical behaviour in human cytochrome c–phospholipid complexes: implications for the enhanced pro-apoptotic activity of the G41S mutant. *Biochemical Journal*, **456**, 441-452.
- Ravelli, R. B. and McSweeney, S. M. (2000) The 'fingerprint' that X-rays can leave on structures. *Structure*, **8**, 315-328.
- Reeder, B. J., Cutruzzola, F., Bigotti, M. G., Hider, R. C. and Wilson, M. T. (2008) Tyrosine as a redox-active center in electron transfer to ferryl heme in globins. *Free Radical Biology and Medicine*, **44**, 274-283.
- Reeder, B. J., Svistunenko, D. A., Sharpe, M. A. and Wilson, M. T. (2002) Characteristics and Mechanism of Formation of Peroxide-Induced Heme to Protein Cross-Linking in Myoglobin. *Biochemistry*, **41**, 367-375.
- Reeder, B. J. and Wilson, M. T. (2001) The effects of pH on the mechanism of hydrogen peroxide and lipid hydroperoxide consumption by myoglobin: a role for the protonated ferryl species. *Free Radical Biology and Medicine*, **30**, 1311-1318.
- Robert, X. and Gouet, P. (2014) Deciphering key features in protein structures with the new ENDscript server. *Nucleic Acids Research*, **42**, W320-W324.
- Roberts, J. N., Singh, R., Grigg, J. C., Murphy, M. E., Bugg, T. D. and Eltis, L. D. (2011) Characterization of dye-decolorizing peroxidases from *Rhodococcus jostii* RHA1. *Biochemistry*, **50**, 5108-5119.
- Rodríguez-López, J. N., Lowe, D. J., Hernández-Ruiz, J., Hiner, A. N. P., García-Cánovas, F. and Thorneley, R. N. F. (2001) Mechanism of Reaction of Hydrogen Peroxide with Horseradish Peroxidase: Identification of Intermediates in the Catalytic Cycle. *Journal of the American Chemical Society*, **123**, 11838-11847.
- Rutter, R., Hager, L. P., Dhonau, H., Hendrich, M., Valentine, M. and Debrunner, P. (1984) Chloroperoxidase compound I: electron paramagnetic resonance and Moessbauer studies. *Biochemistry*, **23**, 6809-6816.
- Rutter, R. A. H., Lowell P. (1982) The detection of two electron paramagnetic resonance radical signals associated with chloroperoxidase compound I. *The Journal of biological chemistry*, **257** **14**, 7958-6791.
- Schlichting, I. (2000) Crystallographic Structure Determination of Unstable Species. *Accounts of Chemical Research*, **33**, 532-538.
- Schlichting, I. (2015) Serial femtosecond crystallography: the first five years. *IUCrJ*, **2**, 246-55.
- Schlick, S. and Kevan, L. (1979) Study of g-anisotropy associated with molecular motion in the triphenylmethylperoxy radical: an environmental probe. *The Journal of Physical Chemistry*, **83**, 3424-3429.
- Scholes, C. P. (1969) Hyperfine structure from the four pyrrole nitrogens of heme. *Proceedings of the National Academy of Sciences of the United States of America*, **62**, 428-431.
- Schulz, C. E. and Schirmer, R. H. (1979) *Principles of Protein Structure* Berlin, New York, Springer-Verlag.

- Sharp, K. H., Mewies, M., Moody, P. C. and Raven, E. L. (2003) Crystal structure of the ascorbate peroxidase-ascorbate complex. *Nature Structural Biology*, **10**, 303-307.
- Shimazu, Y., Tono, K., Tanaka, T., Yamanaka, Y., Nakane, T., Mori, C., Terakado Kimura, K., Fujiwara, T., Sugahara, M., Tanaka, R., Doak, R. B., Shimamura, T., Iwata, S., Nango, E. and Yabashi, M. (2019) High-viscosity sample-injection device for serial femtosecond crystallography at atmospheric pressure. *Journal of applied crystallography*, **52**, 1280-1288.
- Shrestha, R., Huang, G., Meekins, D. A., Geisbrecht, B. V. and Li, P. (2017) Mechanistic Insights into Dye-Decolorizing Peroxidase Revealed by Solvent Isotope and Viscosity Effects. *Acs Catalysis*, **7**, 6352-6364.
- Silaghi-Dumitrescu, R., Reeder, B. J., Nicholls, P., Cooper, C. E. and Wilson, M. T. (2007) Ferryl haem protonation gates peroxidatic reactivity in globins. *Biochemical Journal*, **403**, 391-395.
- Singh, R. and Eltis, L. D. (2015) The multihued palette of dye-decolorizing peroxidases. *Archives of Biochemistry and Biophysics*, **574**, 56-65.
- Singh, R., Grigg, J. C., Armstrong, Z., Murphy, M. E. and Eltis, L. D. (2012) Distal heme pocket residues of B-type dye-decolorizing peroxidase: arginine but not aspartate is essential for peroxidase activity. *Journal of Biological Chemistry*, **287**, 10623-10630.
- Sivaraja, M., Goodin, D. B., Smith, M. and Hoffman, B. M. (1989) Identification by ENDOR Of Trp191 as the free-radical site in cytochrome-c peroxidase Compound ES. *Science*, **245**, 738-740.
- Spence, J. C. H. (2014) Approaches to time-resolved diffraction using an XFEL. *Faraday Discussions*, **171**, 429-438.
- Stolz, A. (2001) Basic and applied aspects in the microbial degradation of azo dyes. *Applied Microbiology and Biotechnology*, **56**, 69-80.
- Stone, K. L., Behan, R. K. and Green, M. T. (2005) X-ray absorption spectroscopy of chloroperoxidase compound I: Insight into the reactive intermediate of P450 chemistry. *Proceedings of the National Academy of Sciences of the United States of America*, **102**, 16563-16565.
- Stone, K. L., Behan, R. K. and Green, M. T. (2006) Resonance Raman spectroscopy of chloroperoxidase compound II provides direct evidence for the existence of an iron(IV)-hydroxide. *Proceedings of the National Academy of Sciences of the United States of America*, **103**, 12307-12310.
- Strittmatter, E., Liers, C., Ullrich, R., Wachter, S., Hofrichter, M., Plattner, D. A. and Piontek, K. (2013) First crystal structure of a fungal high-redox potential dye-decolorizing peroxidase: substrate interaction sites and long-range electron transfer. *The Journal of biological chemistry*, **288**, 4095-4102.
- Sugahara, M., Nakane, T., Masuda, T., Suzuki, M., Inoue, S., Song, C., Tanaka, R., Nakatsu, T., Mizohata, E., Yumoto, F., Tono, K., Joti, Y., Kameshima, T., Hatsui, T., Yabashi, M., Nureki, O., Numata, K., Nango, E. and Iwata, S. (2017) Hydroxyethyl cellulose matrix applied to serial crystallography. *Scientific Reports*, **7**, 703.
- Sugano, Y. (2009) DyP-type peroxidases comprise a novel heme peroxidase family. *Cellular and Molecular Life Sciences*, **66**, 1387-1403.
- Sugano, Y., Muramatsu, R., Ichiyangi, A., Sato, T. and Shoda, M. (2007) DyP, a unique dye-decolorizing peroxidase, represents a novel heme peroxidase family. *Journal of Biological Chemistry*, **282**, 36652-36658.

- Sugawara, K., Igeta, E., Amano, Y., Hyuga, M. and Sugano, Y. (2019) Degradation of antifungal anthraquinone compounds is a probable physiological role of DyP secreted by *Bjerkandera adusta*. *AMB Express*, **9**, 56.
- Sutter, M., Boehringer, D., Gutmann, S., Günther, S., Prangishvili, D., Loessner, M. J., Stetter, K. O., Weber-Ban, E. and Ban, N. (2008) Structural basis of enzyme encapsulation into a bacterial nanocompartment. *Nature Structural Molecular Biology*, **15**, 939-947.
- Svistunenko, D. A. (2001) An EPR study of the peroxy radicals induced by hydrogen peroxide in the haem proteins. *Biochimica et Biophysica Acta (BBA) - Protein Structure and Molecular Enzymology*, **1546**, 365-378.
- Svistunenko, D. A. and Cooper, C. E. (2004) A new method of identifying the site of tyrosyl radicals in proteins. *Biophysical Journal*, **87**, 582-595.
- Svistunenko, D. A., Davies, N., Brealey, D., Singer, M. and Cooper, C. E. (2006) Mitochondrial dysfunction in patients with severe sepsis: an EPR interrogation of individual respiratory chain components. *Biochimica et Biophysica Acta*, **1757**, 262-272.
- Svistunenko, D. A., Reeder, B. J., Wankasi, M. M., Silaghi-Dumitrescu, R.-L., Cooper, C. E., Rinaldo, S., Cutruzzola, F. and Wilson, M. T. (2007) Reaction of *Aplysia limacina* metmyoglobin with hydrogen peroxide. *Dalton Transactions*, 840-850.
- Tang, Y., Mu, A., Zhang, Y., Zhou, S., Wang, W., Lai, Y., Zhou, X., Liu, F., Yang, X., Gong, H., Wang, Q. and Rao, Z. (2021) Cryo-EM structure of *Mycobacterium smegmatis* DyP-loaded encapsulin. *Proceedings of the National Academy of Sciences of the United States of America*, **118**, e2025658118.
- Tazhigulov, R. N., Gayvert, J. R., Wei, M. and Bravaya, K. B. (2019) eMap: A Web Application for Identifying and Visualizing Electron or Hole Hopping Pathways in Proteins. *The Journal of Physical Chemistry B*, **123**, 6946-6951.
- Tedeschi, G., Ronchi, S., Simonic, T., Treu, C., Mattevi, A. and Negri, A. (2001) Probing the Active Site of l-Aspartate Oxidase by Site-Directed Mutagenesis: Role of Basic Residues in Fumarate Reduction. *Biochemistry*, **40**, 4738-4744.
- Uervirojnangkoorn, M., Zeldin, O. B., Lyubimov, A. Y., Hattne, J., Brewster, A. S., Sauter, N. K., Brunger, A. T. and Weis, W. I. (2015) Enabling X-ray free electron laser crystallography for challenging biological systems from a limited number of crystals. *eLife*, **4**, e05421.
- Vidossich, P., Fiorin, G., Alfonso-Prieto, M., Derat, E., Shaik, S. and Rovira, C. (2010) On the Role of Water in Peroxidase Catalysis: A Theoretical Investigation of HRP Compound I Formation. *The Journal of Physical Chemistry B*, **114**, 5161-5169.
- Wariishi, H., Dunford, H. B., Macdonald, I. D. and Gold, M. H. (1989) Manganese peroxidase from the lignin-degrading basidiomycete *Phanerochaete chrysosporium* - Transient state kinetics and reaction-mechanism. *Journal of Biological Chemistry*, **264**, 3335-3340.
- Weik, M., Ravelli, R. B., Kryger, G., McSweeney, S., Raves, M. L., Harel, M., Gros, P., Silman, I., Kroon, J. and Sussman, J. L. (2000) Specific chemical and structural damage to proteins produced by synchrotron radiation. *Proceedings of the National Academy of Sciences of the United States of America*, **97**, 623-628.
- Welinder, K. G. (1992) Superfamily of plant, fungal and bacterial peroxidases. *Current Opinion in Structural Biology*, **2**, 388-393.

- Welinder, K. G., Mauro, J. M. and Norskovlauritsen, L. (1992) Structure of plant and fungal peroxidases. *Biochemical Society Transactions*, **20**, 337-340.
- White, T. A., Kirian, R. A., Martin, A. V., Aquila, A., Nass, K., Barty, A. and Chapman, H. N. (2012) CrystFEL: a software suite for snapshot serial crystallography. *Journal of Applied Crystallography*, **45**, 335-341.
- White, T. A., Mariani, V., Brehm, W., Yefanov, O., Barty, A., Beyerlein, K. R., Chervinskii, F., Galli, L., Gati, C., Nakane, T., Tolstikova, A., Yamashita, K., Yoon, C. H., Diederichs, K. and Chapman, H. N. (2016) Recent developments in CrystFEL. *Journal of Applied Crystallography*, **49**, 680-689.
- Winkler, J. R. and Gray, H. B. (2011) *Electronic Structures of Oxo-Metal Ions*, Berlin, Ger.
- Winter, G. (2010) xia2: an expert system for macromolecular crystallography data reduction. *Journal of Applied Crystallography*, **43**, 186-190.
- Winter, G., Waterman, D. G., Parkhurst, J. M., Brewster, A. S., Gildea, R. J., Gerstel, M., Fuentes-Montero, L., Vollmar, M., Michels-Clark, T., Young, I. D., Sauter, N. K. and Evans, G. (2018) DIALS: implementation and evaluation of a new integration package. *Acta Crystallographica Section D: Structural Biology*, **74**, 85-97.
- Yamaguchi, S., Kamikubo, H., Kurihara, K., Kuroki, R., Niimura, N., Shimizu, N., Yamazaki, Y. and Kataoka, M. (2009) Low-barrier hydrogen bond in photoactive yellow protein. *Proceedings of the National Academy of Sciences*, **106**, 440-444.
- Yee, E. F., Dzikovski, B. and Crane, B. R. (2019) Tuning Radical Relay Residues by Proton Management Rescues Protein Electron Hopping. *Journal of American Chemical Society*, **141**, 17571-17587.
- Yonezawa, K., Shimizu, N., Kurihara, K., Yamazaki, Y., Kamikubo, H. and Kataoka, M. (2017) Neutron crystallography of photoactive yellow protein reveals unusual protonation state of Arg52 in the crystal. *Scientific Reports*, **7**, 9361.
- Yosca, T. H., Langston, M. C., Krest, C. M., Onderko, E. L., Grove, T. L., Livada, J. and Green, M. T. (2016) Spectroscopic Investigations of Catalase Compound II: Characterization of an Iron(IV) Hydroxide Intermediate in a Non-thiolate-Ligated Heme Enzyme. *Journal of American Chemical Society*, **138**, 16016-16023.
- Yoshida, T. and Sugano, Y. (2015) A structural and functional perspective of DyP-type peroxidase family. *Archives of Biochemistry and Biophysics*, **574**, 49-55.
- Zeldin, O. B., Gerstel, M. and Garman, E. F. (2013) RADDOS-3D: time- and space-resolved modelling of dose in macromolecular crystallography. *Journal of Applied Crystallography*, **46**, 1225-1230.